A comparison between the SLaMA method and NLFEA for 2D and 3D analyses of masonry structure.

By Nidal Ennali

September 7, 2020

Delft University of Technology, ARCADIS

Thesis committee:

prof.dr.ir.J.G.Rots TU DELFT
dr.F.Messali TU DELFT
ir.S.Pasterkamp TU DELFT
ir.M.Bettonvil ARCADIS
ir.G.van Engelen ARCADIS

A comparison between the SLaMA method and NLFEA for 2D and 3D analyses of masonry structure.

By Nidal Ennali

September 7, 2020

Delft University of Technology, ARCADIS

Thesis committee:

prof.dr.ir.J.G.Rots TU DELFT
dr.F.Messali TU DELFT
ir.S.Pasterkamp TU DELFT
ir.M.Bettonvil ARCADIS
ir.G.van Engelen ARCADIS

I. SUMMARY

Each year, the province of Groningen experiences many induced earthquakes due gas extraction, which has been ongoing since 1963. The earthquakes cause damage to the buildings situated in the Groningen area, and they constitute a potential danger for the safety of the residents. These buildings are typically unreinforced masonry structures which are designed without knowledge of the presence of seismic activity in this area.

It is therefore essential develop and use assessment methods that are on one end reliable and accurate, but on the other hand allow to perform a large number of assessments of the vulnerability of the buildings in a short time. In other words, the assessment of all the buildings requires a quick and reliable assessment method. Such an assessment method should offer a strong understanding of the occurring failure mechanism during an earthquake, an acceptable prediction of the ground acceleration at which the collapse of the building may occur (maximum base shear force) and the displacement capacity of unreinforced masonry (URM) building.

The NPR9998 recommends four seismic assessment approaches, which differ in complexity and assessment time needed to be performed. The most comprehensive and time-consuming assessment method is the NLTHA (nonlinear time history analysis), which includes both the dynamic and nonlinear effects. In practice, this method is used only in special cases, such as in the case of monumental buildings. A simpler approach is the NLPO (nonlinear pushover) analysis, which is static and considers the nonlinear properties of the structure. An NLPO is less time consuming than an NLTHA, even when the finite element method (FEM) is considered.

A more simplified approach is the Simple Lateral Mechanism Analysis (SLaMA). This method is a simplified mechanism-based analytical approach. If the SLaMA method predicts realistically conservative global capacities, it could serve as an effective alternative assessment method for URM buildings, and especially to the NLPO FEM analysis. This study focusses on the comparison between the SLaMA method and the NLPO FEM analysis. Therefore, this study aims to answer the following research question:

Could the SLaMA method be a realistically conservative and effective alternative to the NLPO FEM analysis in making a seismic assessment for two-storey unreinforced masonry buildings?

To answer the main research question, 10 wall models and two URM building models have been analysed using the two considered assessment methods. The 10 walls were analysed via 2D analyses, and the two buildings via 3D analyses. The primary focus lies in the definition of the capacity curves of the models for each method, namely in the determination of the maximum base shear force, the displacement capacities and the predicted failure mechanisms. The global capacities predicted by both methods are compared, and the differences are discussed. Each of the analysed models (walls and buildings) differs in some specific aspect (e.g. masonry type, presence of lintels, floor type or loading condition) to study the influence of these aspects on the comparison between the predictions of the SLaMA method and the NLPO FEM analyses. The NLPO FEM analyses were performed with the software DIANA 10.3.

The comparison of the results of both assessment methods reveals that the SLaMA method predicts conservative base shear forces compared with the NLPO FEM analysis. Furthermore, the masonry type and loading condition

did not affect the difference between the maximum base shear force and the failure mechanism predicted by the two methods.

The two buildings differ mainly for the floor type: the first building has reinforced concrete (RC) floors, whereas the second timber floors. As regards the displacement capacity of the URM building with RC floors, the SLaMA method was conservative compared with the NLPO FEM analysis with respect to the prediction of both the base shear and the displacement capacity of the building. The ratio of the SLaMa results and the NLPO FEA results vary between 0.42-0.75 for the displacement capacity and 0.40-0.47 for the prediction of the base shear force.

In the case of the URM building with timber floors, the ultimate displacement reached with the NLPO FEM analysis was not reliable and no comparison was possible: the analyses did not reach the ultimate displacement, as a result of the instability of the numerical solving method used in the modal pushover analysis.

The comparison between the predicted global failure mechanisms is based on the type of failure and on the location of the structural elements that fail. The results of both methods reveal that the location of the failure mechanism differs in many of the models analysed. The SLaMA method identifies always a soft storey mechanism, and it is therefore limited in predicting failure at different floors of a building. For this reason, the analyst must consider the acceleration at the different storey levels to interpret the results in a proper manner. If the ratio between the accelerations is close to 1, it could be concluded that both levels will fail. If this ratio is significantly higher than 1, only the floor with the lowest acceleration will undergo failure. The last statement is confirmed by almost all the models, except for the Casestudy-3D-model 2 with timber floors; in this case, there was a significant difference in the participating mass, which influenced the predicted failure mechanism.

An analysis of the predicted failure mechanism for the single structural elements revealed that the SLaMA method can frequently predict the same failure type of a FEM analysis. The main difficulty of the SLaMA method lies in the prediction of hybrid failure type (a combination of shear and flexure). Once more, when the shear capacities of the different failure modes are close one to another, the analyst must interpret the results in a proper manner. In that situation the engineer must consider a combination of failure modes; this apply to both piers and spandrels.

In conclusion, the SLaMA method could be a realistically conservative and effective alternative to the NLPO FEM analysis in predicting the maximum base shear force. The displacement capacity predicted using the SLaMA method is validated only for buildings with RC floors. This predicted SLaMA method was realistically conservative compared with the ultimate displacement achieved using the NLPO FEM analysis. The SLaMA method is overall suitable for obtaining a quick understanding of the behaviour of an URM building. However, it requires a proper evaluation of the analyses to identify properly the type and the location of the failure mechanisms. For this reason, this method could be valuable to be applied before using a more complex assessment method.

II. ACKNOWLEDGEMENT

This study has been carried out in collaboration with the supervisors at TU-Delft and Arcadis. I wish to thank my supervisors and committee members Francesco Messali, Jan Rots, Sander Pasterkamp, Martijn Bettonvil and Gerard van Engelen for their support during this research period. Special thanks for Francesco Messali for guiding and helping me with challenging problems that I faced during answering the research questions. The critical feedback and quick responses of Francesco Messali in particular, were highly appreciated. I would also like to thank Erwin Dam, Gerard van Engelen and Martijn bettonvil for giving me the chance to graduate at Arcadis and for their supervision during this period. In addition, I want to thank Piet van Bezu and Coen van der Vliet for sharing their specialist knowledge. Furthermore, I gratefully acknowledge Jan Rots for helping me to find this great research topic and for his supervision and guidance.

This research has been conducted parallel to the research of Anass El Kouri. Both studies were focussed on a different aspect of the SLaMA method. And therefore I want to thank Anass El Kouri for working together and for motivating me during this research.

Finally, I wish to thank my family, friends and colleagues for their support during this thesis project.

1 TABLE OF CONTENT

I. Summary i

II. Acknowledgement iii

2 Introduction 1

2.1 Context of study 1

2.2 Objectives 1

2.3 Report structure 2

3 Literature study 4

3.1 SLaMA method 4

3.2 Nonlinear pushover finite element analysis (DIANA) 16

4 Descriptions of the case studies and methodology 23

4.1 Overview of the analysed walls/buildings 24

4.2 Description of the assessment approach 28

4.3 Material properties 33

5 Results of the 2D analyses 37

5.1 NLPO FEA (DIANA) results 38

5.2 SLaMA results 45

5.3 Comparison between the SLaMA and DIANA NLPO FEA results 48

6 Results of the 3D analyses 51

6.1 3D NLPO FEA (DIANA) results 51

6.2 3D SLaMA results 61

6.3 Comparison between the SLaMA and NLPO FEA results 63

7 Discussion 66

8 Conclusion 78

9 Recommendations 82

10 Bibliography 83

11 Appendix A: Simple model 1: Full DIANA NLPO FEM analysis 85

12 Appendix B: Simple model 1: Full SLaMA calculations 88

13 Appendix C: Simple model 2: Full DIANA NLPO FEM analysis 89

14 Appendix D: Simple model 2: Full SLaMA calculations 92

15 Appendix E: Simple model 3: Full DIANA NLPO FEM analysis 93

16 Appendix F: Simple model 3: Full SLaMA calculations 96

17 Appendix G: Simple model 4: Full DIANA NLPO FEM analysis 97

18 Appendix H: Simple model 4: Full SLaMA calculations 99

19 Appendix I: Simple model 5: Full DIANA NLPO FEM analysis 100

20 Appendix J: Simple model 5: Full SLaMA calculations 102

21 Appendix K: Simple model 6: Full DIANA NLPO FEM analysis 103

22 Appendix L: Simple model 6: Full SLaMA calculations 106

Appendix M: CASE STUDY- 2D-1A: Full DIANA NLPO FEM analysis 107
Appendix N: CASE STUDY- 2D-1B: Full DIANA NLPO FEM analysis 109
Appendix O: CASE STUDY- 2D-1A/B: Full SLaMA calculations..... 111
Appendix P: CASE STUDY- 2D-2A: Full DIANA NLPO FEM analysis..... 112
Appendix Q: CASE STUDY- 2D-2B: Full DIANA NLPO FEM analysis 114
Appendix R: CASE STUDY- 2D-2A/B: Full SLaMA calculations..... 116
Appendix S: Case study-3D-Model-double rc-floors Full DIANA NLPO FEM analysis..... 117
Appendix T: Case study-3D assessment phase: Full SLaMA calculations 159
Appendix U: Discussion- Changing axial force SM1..... 163
Appendix V: Discussion- Changing axial force CASE STUDY- 2D-1A..... 166
Table List..... 167
Figure List 169

2 INTRODUCTION

2.1 CONTEXT OF STUDY

Since 1963, the extraction of gas has been ongoing in Groningen. This has caused (human) induced earthquakes over the recent decades. The first induced earthquake occurred in 1991, and in recent years, induced seismicity has considerably increased throughout this region. These incidents represent a great danger for the built environment because the buildings are primarily unreinforced masonry structures. These structures are vulnerable to seismic activity due to their slender walls, weak wall-floor connections and use of cavity walls.

Since the 2011 earthquake in Christchurch, New Zealand, it has been difficult to assess many buildings within a limited timeframe. Both the NLPO FEA (nonlinear pushover finite element analysis) and the NLTHA (nonlinear time history analysis) are time-consuming methods used for the seismic assessment of these buildings. The other problem was that most of the buildings that had been damaged after the earthquake were unreinforced masonry buildings (URM) buildings. Therefore, a need existed for a quicker assessment method for URM buildings. Such a quicker method was presented as the SLaMA method , as described in the New Zealand guidelines part C2 (NZSEE, 2017). The seismic behaviour of the unreinforced masonry buildings in New Zealand is described in the New Zealand guidelines part C8 (NZSEE, 2017). In 2018, this SLaMA method was adopted in the Dutch guidelines NPR9998.

Previously, the NPR9998 recommended that the NLTHA method be used to assess the seismic capacity of a building. However, this method is highly complex and requires much computational time. Therefore, this method depends on many assumptions that must be made by the engineer. Today, the NPR9998 recommends the NLPO FE analysis for in-plane assessment and the NLKA method for out-of-plane assessment. These methods are validated by the TU Delft and the EU centre (Craig MUIR, 2018). The SLaMA method is another NLPO method which is recommended by the NPR9998 for determining the in-plane capacity of a wall.

2.2 OBJECTIVES

KNOWLEDGE GAPS

The main knowledge gaps could be summarised as follows:

The SLaMA method for URM buildings has not been comprehensively compared/validated with other computational methods, such as the NLPO and NLTHA FE analyses, or with experiments. The results that should be compared consist primarily of the global capacities (maximum base shear force and displacement capacity) and the predicted failure mechanisms.

AIM OF RESEARCH

The aim of this research is to determine whether the SLaMA method could be a realistically conservative and effective method for determining the global capacity of a URM building subjected to seismic loading. Furthermore, it seeks to learn whether the SLaMA method can be an alternative for the NLPO FEA and NLTHA for a specific type of building. In such a case, the SLaMA method would save much time when assessing this type of building.

RESEARCH QUESTION

Could the SLaMA method be a realistically conservative and effective alternative for the NLPO FEM analysis to make a seismic assessment for two-storey unreinforced masonry buildings?

RESEARCH SUB-QUESTIONS

- *What are the global capacities and predicted failure mechanisms of the analysed two-storey unreinforced masonry buildings based on the 2D/3D NLPO FEM analyses and the SLaMA method?*

- *Does the SLaMA method predict conservative global capacities and the same governing failure modes for the two-storey unreinforced masonry buildings compared with the 2D/3D NLPO FEM analyses?*

- *What is the influence of the masonry type, floor type and loading condition on the comparison between the global capacity and the failure mechanism predicted by the SLaMA method and the NLPO FEM analysis?*

2.3 REPORT STRUCTURE

This total report consists of the five main parts, namely the literature study, 2D assessment phase, 3D assessment phase, results and appendices. Each of these main parts are further elaborated below.

LITERATURE STUDY

The purpose of the literature review is to determine what has already been investigated and what has yet to be investigated regarding the SLaMA method. In addition, the literature research was conducted to obtain better insight into the material behavior of unreinforced masonry, the in-plane seismic response of an URM wall, the available material models within a finite element program and equivalent frame program, the available seismic assessment tools (SLaMA method/ NLPO FE analysis), and various modelling approaches. The relevant information for this research which was obtained from the literature study is presented in Chapter 2: Literature study.

DESCRIPTIONS OF THE CASE STUDIES AND METHODOLOGY

The analysed walls and buildings which are assessed during the 2D and 3D assessment phases are introduced and presented in Chapter 3: Methodology and case studies. This overview provides the masonry types, floor type, loading type and material properties of each specific wall/building. Chapter 3: Methodology and case studies describes the two main assessment methods, namely the SLaMA method and the NLPO FEM analysis. The descriptions of the methods clearly reveal the approaches and assumptions that are applied in assessing the walls/buildings during both the 2D and 3D assessment phases.

RESULTS OF THE 2D AND 3D ANALYSES

The 2D assessment phase consists of the seismic assessments of six simple wall models and four practical wall models. The simple models are not practical URM walls, as situated in Groningen; rather, they are simply analysed for study purposes. The other four wall models are more practical URM walls and have the same geometry as the experimental house EUC-BUILD 6 tested for the NAM by the EUROCENTRE. The only difference is the loading conditions on these walls. Each model differs in certain aspects, such as loading condition, floor types and masonry types. These models were assessed using both the NLPO FEM analysis and the SLaMA method.

The global capacities and predicted failure mechanisms were collected and compared with one another. This phase focussed primarily on the comparison between both assessment methods and the influence of the floor type, masonry type and loading condition on that comparison. The geometrical irregularities have been studied by Anass el Kouri and are therefore beyond the scope of my research.

The 3D assessment phase focussed on the comparison of both seismic assessments of the 3D building models. Two 3D building models were analysed using the NLPO FE analysis within DIANA. The two models have the same geometry and loading condition but differ in terms of floor type. One model consists of a two-storey URM

building with timber floors, while the other model is the same building but with reinforced concrete floors. The main objectives of the 3D assessment phase are to determine the differences between the SLaMA analysis and the FEM analysis and determine the influence of the floors on that comparison.

Therefore, for each model, a pushover curve was determined with both the 3D/2D NLPO FEM analyses and the SLaMA method. For the SLaMA method, the pushover curve was translated into an acceleration curve, from which the expected failure mechanism was determined. The maximum principal strain was analysed to determine the decisive failure mechanism resulting from the 3D/2D FEM analyses. At the end of the 3D and 2D assessment phases, an overview is provided of the comparison between the results of both assessment methods.

Discussion

All the results of the 2D and 3D assessment phases are presented and analysed in Chapter 4&5: Results. The two used seismic assessment methods were compared with each other, and the results are discussed in Chapter 6: Discussion. A possible explanation for the difference between both methods is reported and discussed in that chapter, as well. Further recommendations for improving the SLaMA method are noted in the chapter 'Recommendations'. The conclusion supplies the answers to all the research questions and finally answers the main research question.

Conclusion and Recommendations

The results and discussion provide the information necessary to answer the research sub-questions, which leads to an answer to the main research question. These answers are then explained and presented in Chapter 7: Conclusion.

This study identifies some limitations of the SLaMA method and the NLPO FEA (DIANA). Possible improvements in both methods must be studied to make the methods less conservative. Chapter 8: Recommendations provides a list of improvements which could be studied in future research.

Appendices

The appendices consist of comprehensive assessments of the SLaMA method and the NLPO FEA (DIANA)for all the analysed walls and buildings. This elaborated NLPO FEM results reveal the intermediate steps of the full DIANA FEM analysis. Chapter 4&5: Results presents only the relevant results of the assessments for the walls and buildings. The relevant results are selected based on the research question that must be answered.

3 LITERATURE STUDY

In this section the important literature concerning this research has been described. It should be noted that (parts of) this literature study has been done in cooperation with Anass El kouri with the consent of our committee members.

3.1 SLAMA METHOD

The SLaMA method is an analytical approach for making a seismic assessment of buildings. This method was first used in New Zealand, where this method was applied for several building. The SLaMA method is normally applied to provide an initial estimation of the global capacity of a building subjected to a seismic load. This initial estimation primarily determines the type of assessment necessary to follow the SLaMA assessment. The assessment method that follows from this first estimation could be the NLPO or NLTHA, both of which are considered to be reliable and validated methods for unreinforced masonry buildings (URM buildings).

TOTAL OVERVIEW SLAMA METHOD

This part consists of a short summary of the SLaMA method as described in **NZSEE C8** (NZSEE, 2017) and the **NPR9998** (NEN, 2018), specified to unreinforced masonry.

Step 1: Assess the structural configuration and load paths to identify key structural elements, potential structural weaknesses (SWs) and severe structural weaknesses (SSWs). (NZSEE, 2017)

Unreinforced masonry buildings consist of boundary walls, walls and the diaphragm. The diaphragm can be a ceiling, floor or foundation. Depending on the material, the diaphragm could differ in terms of stiffness.

The wall elements within an URM building could be divided into wall elements with penetration and wall elements without penetration. For the assessment, the orientation of the wall is important, as well. Walls can be oriented parallel or perpendicular to the plane of loading.

These elements within an URM building must be analysed by consulting the plans/blueprint and details. When analysing, special notice must be given regarding the structural configuration, load paths, potential structural weaknesses and severe structural weakness. An analysis of these structural elements is part of the first step of the SLaMA method.

Step 2: Assess the capacity of the diaphragm/wall connection to determine whether the diaphragm is capable of transferring lateral load to the walls. (NZSEE, 2017)

In the second step, it is necessary to analyse the detailed drawings of the connections between the diaphragm and the wall. The capacity of the connection between the diaphragm and the wall depends on the decisive failure mode.

Step 3: Determine the out-of-plane response and the out-of-plane capacity using the NLKA-method.

The next phase of the SLaMA method requires determining the out-of-plane response of a wall element loaded with a face load. Both the NZSEE (NZSEE, 2017) and the NPR9998 (NEN, 2018) use the same method to determine these out-of-plane responses. This method is based on an NLKA approach, a nonlinear kinematic analysis. This method leads to a conservative value for the resistance of this wall. The method is generally applicable to masonry walls oriented in a normal manner. Walls that are oriented in a complex geometry must be analysed using a different method.

Step 4: Determine the in-plane response and the in-plane resistance to the possible failure modes.

Before analysing the behaviour of the wall loaded in plane, two different wall types must be described. First, there are walls with penetrations, which consist of the pier elements and spandrel elements. The pier elements are the wall parts between the penetrations, while the spandrels elements are the wall part above the penetrations. The other wall type are walls without any penetration.

The in-plane capacity of the URM walls or piers could be determined based on the governing failure mechanism.

The following failure mechanisms are considered when analysing the in-plane capacity of the URM walls or pier elements. The derivation of the formulas is provided in the following section of this chapter.

- Diagonal tensile
- In-plane rocking/toe crushing
- Bed-joint sliding
- Slip plane sliding
- URM spandrel failure

Step 5: Determine the probable inelastic behaviour of elements by comparing the probable member capacities and evaluating the hierarchy of strength.

In this step of the SLaMA method, it is necessary to compare the strengths of the different components in a URM wall. The inelastic behaviour of every component must be analysed, and finally, the hierarchy of strength could be determined. The following components must be considered in this step:

- Wall loaded out of plane
- Wall without penetrations loaded in plane
- Spandrels
- Piers
- Foundation
- Diaphragm

Step 6: Assess the sub-system inelastic mechanisms by extending local to global behaviour. (NZSEE, 2017)

The global capacity represents the strength and deformation capacity of a total building. In the assessment of the global capacity, only the primary structure is considered. The primary structure consists of the diaphragm and the walls loaded in plane. In the case of the cantilever wall system, the walls loaded out of plane should also be considered in this assessment.

The diaphragms distribute the lateral force to the wall loaded in plane, and these diaphragms could be flexible or rigid. A flexible diaphragm can be modelled in a 3D analysis or 2D analysis, while a rigid diaphragm could result in an eccentricity due to the varying rigidities of the walls. This results in torsion and thereby an additional lateral force due to shear stresses.

Step 7: Form a view of the potential governing mechanism and calculate the probable base shear and global displacement capacity. (NZSEE, 2017)

The global displacement capacity and the probable base shear could be calculated based on the stiffness of the diaphragm and the shear/deformation capacity of the governing structural element (spandrels, piers, foundation, and so on). The governing structural element is the element which has the lowest capacity due to the occurrence of a plausible failure mechanism.

Step 8: Determine equivalent SDOF system, seismic demand and %NBS. (NZSEE, 2017)

In this step, the structure must be schematised as a SDOF system. The steps to determine the effective mass and effective height are described in greater detail in the following section. Based on the SDOF model, the %NBS could be determined. Additionally, the procedure to determine the seismic demand is described in the NZSEE C8 ((NZSEE, 2017).

IN PLANE BEHAVIOUR MASONRY

This study focusses primarily on the in-plane behaviour of masonry. Therefore, it is interesting to study the derivation of the shear capacities for each failure mechanism.

ROCKING FAILURE

Rocking failure is a mechanism that occurs due to the tilting of the pier. The failure mechanism is a stable mechanism, so it does not result in an immediate collapse of the piers. Rocking of the pier will occur until the toe crushes due to compression stresses. The shear capacity is derived based on the assumption that the compressive stress at the base of a pier that undergoes rocking has a parabolic distribution. Subsequently, this parabolic distribution is assumed to be rectangular with a correction factor of 0.85. There will be a difference in the assumed compression energy and actual compressive energy. Another assumption in this derivation is that the bed joint tensile strength is neglected. The Figure below presents the assumed mechanical model which has been used by Calvi and Magenes (MAGENES, 1997) to derive this shear capacity. This formula is adopted by both the NPR9998 and the NZSEE-C8.

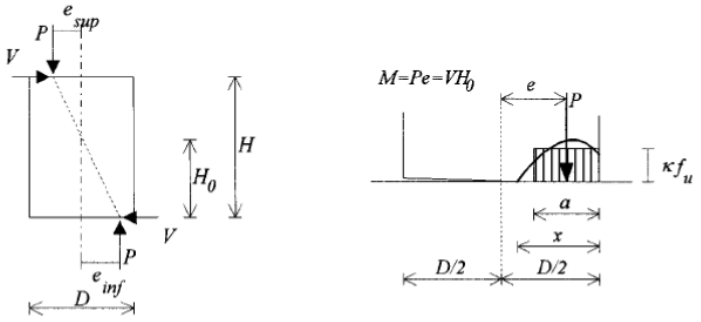

FIGURE 1: ASSUMED MECHANICAL MODEL ROCKING FAILURE (MAGENES, 1997)

$P = \ Normal\ force\ in\ N$

$f_u = Compressive\ strength\ in\ N/m^2$

$t = \ thickness\ of\ the\ pier\ in\ m$

$L = \ Length\ of\ the\ pier\ in\ m$

$\sigma_y = average\ compressive\ stress\ at\ the\ top\ of\ the\ pier$

$f_{ma;m} = average\ compressive\ strength\ of\ the\ masonry$

$h_0 = Effective\ heigth\ of\ the\ pier\ depended\ on\ the\ boundary\ conditions\ of\ the\ piers.$

$$e_{slama} = \frac{L}{2} - a = \frac{L}{2} - \frac{P}{0.85 \cdot f_u \cdot t}$$

$$V_r = P \cdot \frac{L}{2 \cdot h_0} \cdot (1 - 1.15 \cdot \frac{\sigma_y}{f_{ma;m}})$$

SHEAR FAILURE

In addition to the rocking failure mechanism, there also exists shear failure. Two different forms of shear failure exist, namely diagonal cracking and sliding. Shear failure considering diagonal cracking is a complex failure mechanism to describe in a single formula. Calvi and Magenes (MAGENES, 1997) derived an expression for this type of failure mechanism, which has been adopted by the NPR9998 and the NZSEE C8.

The starting point for this derivation is the following Mohr-Coulomb criterion:

$\tau_u = c + \mu \cdot \sigma_v$

$\tau_u = ultimate\ shear\ failure$

$c = cohesion$

$\mu = friction\ coefficient$

$\sigma_v = average\ axial\ stress\ due\ to\ the\ axial\ force\ on\ the\ pier$

$P = axial\ force\ at\ the\ top\ of\ the\ pier$

In this case, diagonal cracking is the associated failure of a mortar bed and head joint. In addition, diagonal cracking could be caused by cracking through the bricks if the mortar is stronger than the bricks.

The shear capacity of a pier failing due to diagonal cracking is determined based on the assumption that the shear stress distribution is uniform, resulting in the following formula:

$$V_d = \tau_u \cdot D \cdot t\ = (c + \mu \cdot \sigma_v) \cdot D \cdot t = D \cdot t \cdot \left(c + \mu \cdot \frac{P}{D \cdot t}\right)$$

The expression above describes the shear capacity under the assumption that no cracking develops due to flexure. This assumption could result in the overestimation of the shear capacity. The effect is included by calculating the uncracked length at both ends of the pier. Furthermore, the tensile bed joint strength is neglected in the derivation for the uncracked length. Moreover, the compressive stress distribution is assumed to be linear or constant. With these main assumptions, the following formula has been derived. This formula is in the same manner adopted by the NPR 9998 and the NZSEE C8.

$$D' = 3 \cdot (\frac{1}{2} - \frac{V}{P} \cdot \frac{H_0}{D}) \cdot D$$

$$V_d = D \cdot t \cdot \frac{1.5 \cdot c + \mu \cdot p}{1 + 3 \cdot \frac{c \cdot \alpha_v}{p}}$$

$D' = uncracked\ section\ length$

$p = compressive\ stress\ at\ the\ top\ of\ the\ pier$

$$\alpha_v = shear\ ratio = \frac{H_0}{D}$$

The other approach for determining the diagonal cracking is due to exceeding the conventional tensile strength of the masonry by the principal stresses in the pier. This failure mechanism is one of the most undesirable failure mechanisms, as it results in rapid-strength degradation (brittle failure mode). Calvi and Magenes (MAGENES, 1997) created a formula that describes the shear capacity in the case that this failure mode is decisive. The formula

is based on tests, whereby a horizontal load is applied on an unreinforced masonry pier under a double clamped condition (TOMAZEVIC, 1997).

$$V_d = \frac{f_{tu} \cdot D \cdot t}{b} \cdot \sqrt{1 + \frac{p}{f_{tu}}}$$

$f_{tu} = conventional\ tensile\ strength$

$D = length\ of\ the\ pier$

$p = compressive\ stress\ due\ to\ the\ axial\ force$

$b = parameter\ depending\ on\ the\ aspect\ ratio$

It must be noted that the NPR9998 states that for most regular Dutch masonry, this failure mode could be neglected. In the 2D and 3D assessment phases, this failure mode is considered, through which it could be determined whether this statement is valid.

The NPR9998 (NEN, 2018) considers shear capacity in the case of the sliding failure mode with the first formula. Another failure mode that must be considered is the case that the combination of compression stresses and shear stresses results in splitting of the bricks while the friction is sufficiently large to avoid sliding. The NPR9998 formulates this limit state in the following manner:

$$V_r \leq 0.1 \cdot f_b \cdot D' \cdot t_p$$

$f_b = compressive\ strength\ of\ the\ brick$

$D' = uncracked\ section\ length\ , length\ of\ the\ compression\ zone$

$t_p = thickness\ of\ the\ pier$

DISPLACEMENT CAPACITY

The drift capacity of the rocking failure mode could be determined using the following empirical formula developed in the paper of Messali (F. Messali, 2017). This formula is derived based on the data obtained from laboratory tests of clay and calcium silicate URM walls. The tests were made by the TU Delft and EUROCENTRE commissioned by the NAM (Nederlandse aardolie maatschappij). This research on the drift limit reveals that the displacement capacity of URM piers depends primarily on the axial load ratio and aspect ratio. Other properties of URM piers, such as the boundary condition, wall height, thickness, and head and bed joint typologies do not significantly influence the displacement capacity (F. Messali, 2017).

$$\theta_{R,NC,f} = 0.0135 \cdot (1 - 2.6 \cdot \frac{\sigma_y}{f_{ma;m}}) \cdot (\frac{h_{ref}}{hp}) \cdot \sqrt{\frac{h_p}{l_p}}$$

$h_p = height\ of\ the\ pier$

$l_p = length\ of\ the\ pier$

$\sigma_y = axial\ stress\ at\ the\ top\ of\ the\ pier$

$f_{ma;m} = mean\ compressive\ strength$

Bed joint sliding or diagonal stair stepped sliding are stable failure modes. Therefore, when the initial cracking begins, the pier would not immediately collapse. Due to this ductile failure mode, the pier will have a considerable

displacement capacity, even when initial cracks begin to develop. Based on several studies regarding the displacement capacity of a pier undergoing sliding, the following force-drift diagram has been recommended for piers undergoing sliding failure. This force-drift diagram is adopted by both the NPR9998 (NEN, 2018) and the NZSEE C8 (NZSEE, 2017).

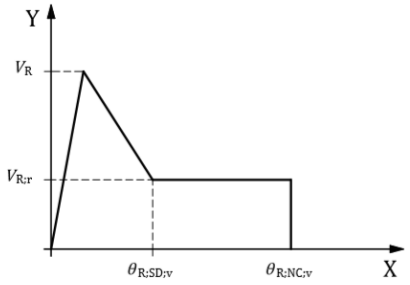

FIGURE 2: FORCE-DRIFT DIAGRAM ACCORDING TO THE NPR9998

The maximum shear capacity can be calculated using the sliding formula provided by Calvi and Magenes (MAGENES, 1997). To determine the residual shear capacity, the cohesion of the masonry may be neglected.

$$V_R = D \cdot t \cdot \frac{1.5 \cdot c + \mu \cdot p}{1 + 3 \cdot \frac{c \cdot \alpha_v}{p}}$$

$$V_{R,r} = D \cdot t \cdot \mu \cdot p$$

The following drift limits are suggested by the NZSEE C8 and the NPR9998:

$$\theta_{R;SD;v} = 0.003$$

$$\theta_{R;ND;v} = 0.0075$$

SPANDREL SHEAR CAPACITY

For a spandrel, two different failure types could be distinguished, namely shear failure and flexural failure. This part describes only the capacity formulas of rectangular spandrels without the effect of lintels. Only formulas applicable to the case studies are analysed in the following chapter.

SHEAR FAILURE

The shear capacity of rectangular spandrels is formulated on the assumption that the spandrel consists of an elastic homogeneous material with a parabolic shear stress distribution along the height of the spandrel. The shear capacity could be found by integrating the shear stress distribution along the height of the spandrel, which results in the following formulation for head and bed joint sliding occurring in a spandrel (Beyer, 2011):

$$V_{cr,s} = \frac{2}{3} \cdot \tau_{max} \cdot h_{sp} \cdot t_{sp}$$

$$\tau_{max} = c + \mu \cdot p_{sp}$$

$$V_{cr,s} = \frac{2}{3} \cdot (c + \mu \cdot p_{sp}) \cdot h_{sp} \cdot t_{sp}$$

$$\tau_{max} = maximum\ shear\ stress\ along\ the\ height\ of\ the\ spandrel, in\ N/mm^2$$

$$\mu = friction\ of\ the\ masonry$$

$p_{sp} = axial\ stress\ at\ the\ spandrels$

$c = cohesion\ of\ the\ masonry, in\ N/mm^2$

Shear failure of the spandrels can occur in two ways. One is that the shear cracks develop through the bed and head joints. Meanwhile, the other shear failure type is that the cracks develop through the bricks rather than the bed and head joints. Another failure type occurs for masonry that consists of strong mortar and the weak bricks; the shear capacity corresponding to this final failure type can be determined based on the following formula of the NZSEE C8 and the NPR9998.

$$V_s = f_{dt} \cdot \beta_{sp} \cdot \sqrt{1 + \frac{p_{sp}}{f_{dt}}} \cdot h_{sp} \cdot t_{sp}$$

$$f_{dt} = 0.5 \cdot c + f_a \cdot \mu$$

$$\begin{cases} \frac{l_{sp}}{h_{sp}} > 1.5, & \beta_{sp} = 0.67 \\ \frac{l_{sp}}{h_{sp}} < 1.0, & \beta_{sp} = 1.0 \end{cases}$$

$l_{sp} = length\ of\ the\ spandrel$

$h_{sp} = height\ of\ the\ spandrel$

$f_{dt} = diagonal\ tensile\ strength\ of\ masonry, in\ N/mm^2$

The residual shear capacity when shear failure occurs can be neglected if the lintels are not considered. The NPR9998 and the NZSEE reveal the effect of the lintels of the residual shear capacity.

FLEXURE FAILURE

The shear capacity in the case that a flexure failure behavior is governing depends on the tensile strength of the head joints and the interlocking of the bed joints. The tensile strength of the head joints could be approximated using the following expression (Beyer, 2011):

$$f_{hj} = \frac{c}{2 \cdot \mu}$$

$c = cohesion\ in\ N/mm^2$

$\mu = friction\ coefficient$

The equivalent tensile strength resulting from the interlocking of the bed joints has been formulated based on the assumption that the shear stress along the bed joint is uniformly distributed. The stress perpendicular to the bed joints and the cohesion of the bed joints contribute to the equivalent tensile strength of the spandrel. The equivalent tensile strength is the sum of the tensile strength of the head joint and the interlocking of the bed joint:

$$f_t = f_{hj} + f_{bj}$$

$$f_t = 1.3 \cdot (c + 0.5 \cdot \mu \cdot \sigma_v) + \frac{c}{2 \cdot \mu}$$

Based on the assumption that the stress is linearly distributed along the height of the spandrel, the bending moment and the shear capacity can be calculated using the following simple formulas:

$$M_{fl} = (f_t + p_{sp}) \cdot \frac{h_{sp}^2 \cdot b_{sp}}{6}$$

$$V_{fl} = (f_t + p_{sp}) \cdot \frac{h_{sp}^2 \cdot b_{sp}}{3 \cdot l_{sp}}$$

The residual flexure shear capacity is determined based on the developed diagonal compressive strut. Therefore, the compressive strength in the horizontal direction would be the normative in the determination of the residual shear capacity. Furthermore, the tensile strength of the head joint and the cohesion of the bed joint tend to approach zero after the peak capacity has been reached. Therefore, these properties could be neglected in the derivation of the residual shear capacity. After cracking, the compression zone height will decrease until h_c.The compressive strength in the horizontal direction f_{hm} is 50% of the compressive strength of masonry (Beyer, 2011).

$$h_c = \frac{P_{sp}}{0.85 \cdot f_{hm} \cdot b_{sp}}$$

Based on this compression zone, the residual shear capacity can be determined using the following expression of the NPR9998:

$$V_{fl,r} = \frac{p_{sp} \cdot h_{sp}^2 \cdot b_{sp}}{l_{sp}} \cdot (1 - \frac{p_{sp}}{0.85 \cdot f_{hm}})$$

$f_{hm} = compressive\ strength\ in\ the\ horizontal\ direction$

$p_{sp} = axial\ stresses\ due\ to\ restraint\ elongation\ of\ the\ sprandrel\ or\ prestressing$

$l_{sp} = length\ of\ the\ spandrel$

$h_{sp} = height\ of\ the\ spandrel$

$b_{sp} = thickness\ of\ the\ spandrel$

Axial stresses on the spandrel would be generated due to the restraint of the elongation upon spandrel deformation. These stresses must be considered when calculating the residual shear capacity due to flexural failure. Additionally, these stresses can be calculated using the following formula stated in the NPR9998:

$$p_{sp} = (1 + \beta_{sp}) \cdot f_{dt} \cdot \frac{l_{sp}}{\sqrt{l_{sp}^2 + h_{sp}^2}}$$

$f_{dt} = diagonal\ tension\ strength\ of\ the\ masonry$

An important point to consider is that all the formulas concerning the spandrel shear capacity exclude the effect of the lintels, since the effect of the lintels is beyond the scope of this study.

The following force-drift diagram for the spandrel is recommended by both the NSCEE C8 and the NPR9998. This diagram is based on much research concerning the displacement capacity of spandrels.

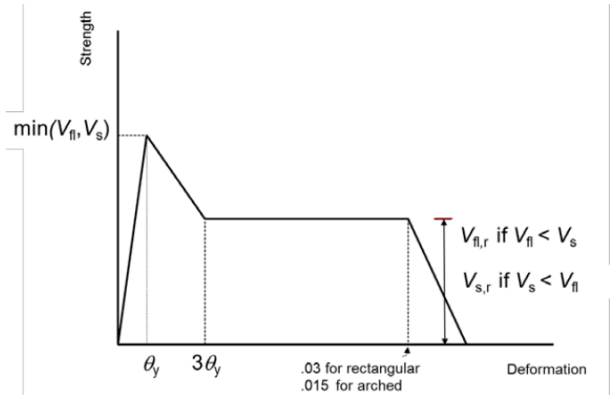

FIGURE 3: FORCE-DRIFT DIAGRAM ACCORDING TO THE NPR9998

FLOORS

The floors of an unreinforced masonry building play an important role in seismic assessment. The type of floor influences both the in-plane and out-of-plane behaviour of URM walls. The floors transfer the seismic load (shear) from the face-loaded walls to the in-plane walls. The floors could be categorised into two main types: rigid floors and flexible floors. These two types differ primarily in their in-plane stiffness. If the floor is rigid, this allows the structure to redistribute the seismic force to the parallel-loaded walls and therefore resists the shear force and torsional shear force applied on the floor. Reinforced concrete floors are generally assumed to behave rigidly due to the large amount of reinforcement. An infinitely flexible floor results in an independent in-plane behaviour of the parallel-loaded wall. Timber floors are categorised as flexible floors because of their relatively low in-plane shear stiffness. The in-plane stiffness of timber floors depends on the connection between the timber planks and timber beams. The strength of the nails that are needed to connect the timber planks and the timber beams appears to be the decisive factor in determining the in-plane stiffness. The Figure below illustrates the influence of the nail-connection on the in-plane deformation of the timber floor.

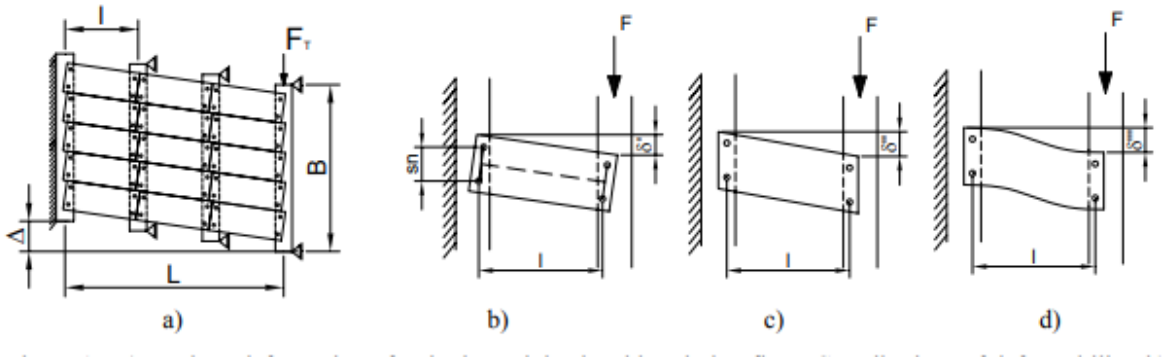

FIGURE 4: TIMBER BEAM-PLANK CONNECTION: B-RIGID DEFORMATION, C-SHEAR DEFORMATION AND D-FLEXURAL DEFORMATION. (A. BRIGNOLA & S. PODESTÀ, 2008)

The NPR9998 recommends in-plane stiffness based on the condition of the floor and the orientation of the beams and planks. A flexible floor has a high displacement capacity, which causes the in-plane stiffness to be the critical property for the out-of-plane capacity of the face-loaded masonry wall. When an unreinforced masonry building consists of timber, the in-plane loaded walls could be considered to behave separately in the SLaMA assessment.

FLANGE CONTRIBUTION

The in-plane behaviour of unreinforced masonry changes when the flanges are considered. The flanges are the parts of the out-of-plane loaded wall that contribute to the in-plane behaviour of the in-plane wall. However, it is difficult to determine exactly which part of this out-of-plane wall contributes to this in-plane behavior. Moon suggested a method of determining which part of the flange contributes to the in-plane behavior. The suggested approach is based on experimental results presented in the paper by Yi (Yi, 2006) and Moon (Moon F. , 2004).

Moon (Moon F. Y., 2006) categorised the flanges into three definitions: the compression flange, global tension flange and component tension flange.

- Compression flange: the portion of the out-of-plane wall that resists compressive stresses generated by the rocking of the adjacent pier.
- Global tension flange: the portion of the out-of-plane wall that is lifted by global rocking.
- Component tension flange: the portion of the out-of-plane wall that is **lifted** by local pier rocking, which can occur at both the tension and compression sides of a building structure.

Compression Flanges

The compression flange occurs at the side of the pier where compressive stresses are developed at the base of the pier. The length of the compressive flange is approximated to be six times the thickness of the specific pier that undergoes rocking behaviour. The compressive flange significantly influences the rotational displacement of the specific pier. The rocking and sliding strength of the adjusted pier does not change due to the compressive flange.

Global Tension Flanges

The global tension flange is the part of the out-of-plane wall which is tilted up due to the global rocking of the in-plane wall. The global tension flange can be considered by applying additional weight to the adjusted pier. The vertical stresses at the top of this pier would subsequently increase due to the contribution of this flange. The shear strength and the governing failure mode of the specific pier would be influenced when considering this flange. Moon (Moon F. Y., 2006) suggested in his paper that the contributing flange part could be determined based on the assumption of crack development at an angle of less than 45 degrees. Therefore, this flange part is the area enclosed by a 45-degree crack until the centerline of the out-of-plane wall; see the Figure below.

Component Tension Flanges

The component tension flange is the part of the out-of-plane wall which is tilted upwards due to the local rocking of the in-plane wall (rocking of the piers). The component tension flange could be considered by applying additional weight to the adjusted pier. The vertical stresses at the top of this pier would subsequently increase due to the contribution of this flange. The shear strength and the governing failure mode of the specific pier would be influenced when considering this flange. Moon (Moon F. Y., 2006) suggested in his paper that the contributing flange part could be determined based on the assumption of crack development at an angle of less than 45 degrees. Therefore, this flange part is the area enclosed by a 45-degree crack until the centerline of the out-of-plane wall; see the Figure below. Moon (Moon F. Y., 2006) concluded from his experiment that the 45-degree crack development is a conservative assumption. The part in which the global tension flange and the local tension overlap must be neglected in the calculation of the in-plane capacity of the total structure.

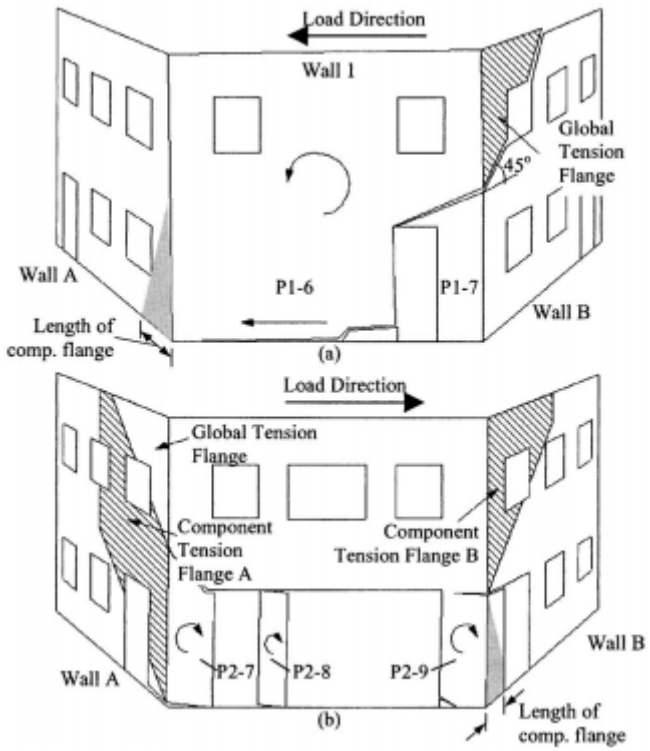

FIGURE 5: OVERVIEW OF THE DIFFERENT TYPE OF FLANGES (FRANKLIN L.MOON, 2006)

EFFECTIVE HEIGHT OF THE PIERS

The rocking failure mode is strongly dependent on the effective height of the piers and the boundary conditions due to the presence of lintels and spandrels. The boundary conditions of the piers could be considered double clamped in the case of weak spandrels and strong piers. The cantilevered boundary conditions can be considered in the case of the weak piers and the strong spandrels. When the piers behave cantilevered, the total height of the pier should be taken into account when calculating the shear capacity of the pier.

It is challenging to determine the effective height of a weak pier in the presence of strong spandrels. Moon (Moon F. Y., 2006) proposed a method in which this effective height could be determined in the case fixed-fixed boundary conditions of the pier. This approach shows that the effective heights of the piers are dependent on the geometry of the in-plane loaded wall and the loading direction. The effective height approach is based on the development of the compression strut. The compression strut will follow the steepest angle or a 45 degree angle. The Figure below shows the effective heights of the piers in an in-plane loaded wall when there are doors and windows present (Moon F. , 2004).

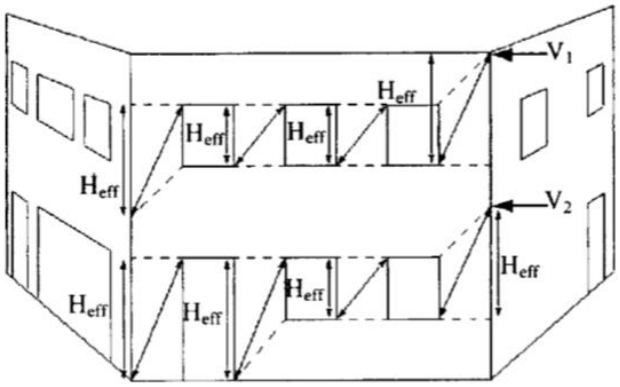

FIGURE 6: EFFECTIVE HEIGTH APPROACH (MOON F. Y., 2006)

3.2 NONLINEAR PUSHOVER FINITE ELEMENT ANALYSIS (DIANA)

The nonlinear static pushover analysis (NLPO) is a seismic assessment method which could be applied to unreinforced masonry buildings. The NLPO analysis is good assessment method for determining the seismic safety of the structure and predicting the damage pattern in the masonry walls of floors. The NLPO could be applied for structures with a complex geometry and for structures consisting of nonlinear material properties. The assessment procedure is also recommended by the NPR9998. This section describes the general procedure to apply the NLPO FE analysis within DIANA.

STRUCTURAL EIGENVALUE ANALYSIS

Part of the NLPO analysis is the structural eigenvalue analysis. The primarily goal of the structural eigenvalue analysis is to determine the natural frequencies, the eigenmodes and the participating masses. The properties can obtained by solving the following equation of motion for undamped free vibrations:

$$\boldsymbol{M}\ddot{u} + \boldsymbol{K}u = 0$$

$$\boldsymbol{M} = mass\ matrix$$

$$\boldsymbol{K} = stiffness\ matrix$$

The assumed solutions for the equations of motion for undamped free vibrations consist of the eigenvector and the corresponding natural frequencies. The following solution can be assumed:

$$u = \varphi \cdot \sin(\omega \cdot t)$$

$$\varphi = eigenvector$$

$$\omega = natural\ frequency$$

Substituting this assumed solution into the equation of motion results in the following equation:

$$-\omega^2 \cdot \boldsymbol{M} \cdot \varphi \cdot \sin(\omega \cdot t) + \boldsymbol{K} \cdot \varphi \cdot \sin(\omega \cdot t) = 0$$

$$(-\omega^2 \cdot \boldsymbol{M} + \boldsymbol{K}) \cdot \varphi = \boldsymbol{0}$$

The determinant of the left-hand side must be equal to zero to obtain nontrivial solutions:

$$Det(-\omega^2 \cdot \boldsymbol{M} + \boldsymbol{K}) = \boldsymbol{0}$$

The eigenvalues that follow from the equation above are related to the natural frequencies with the following formula:

$$f_i = \frac{\omega_i}{2\pi}$$

The main output of the structural eigenvalue analysis are the natural frequencies, the eigenmodes and the corresponding participating/effective masses. These properties are needed for the modal pushover analysis.

MODAL PUSHOVER ANALYSIS

The information obtained from the structural eigenvalue analysis is used in the modal pushover analysis. The critical eigenmode should be determined from the results of the eigenvalue analysis and specified in the pushover analysis. This decisive eigenmode determines the type of loading pattern that would simulate the inertia forces that result from the ground motion during an earthquake. However, the actual loading pattern during an earthquake is not constant and depends on time.

In the application of the nonlinear pushover analysis, a fixed loading pattern is assumed. The assumed fixed lateral loading pattern is proportional to the critical normalised modal shape and effective mass in the analysed direction. Within DIANA (DIANA FEA, 2014), this distribution is calculated using the following formula:

$$f_{pushover} = \sum_{j} a \cdot \boldsymbol{M} \cdot \varphi_i \cdot x_j$$

$a = specified\ acceleration$

$\boldsymbol{M} = mass\ matrix$

$\varphi_i = normalised\ critical\ eigenmodel/eigenvector$

$x_j = analysed\ direction\ vector$

In general, the fixed loading pattern is applicable primarily for structures that have a dominant eigenmode and therefore are not sensitive to higher-order modes (Krawinkler, 1998). Different approaches for the loading pattern are presented to improve the seismic assessment of a building. However, in this study, the aforementioned loading pattern is applied in both assessment methods. Therefore, this literature study is limited to this fixed loading pattern.

MATERIAL MODELS FOR MASONRY

The way masonry is modelled is an important aspect in the modal pushover analysis of URM buildings/walls. This section describes the material models that can be used when modelling masonry walls, concrete and timber floors.

ENGINEERING MASONRY MODEL

The engineering masonry model is a recently developed material model for masonry in DIANA. This model was developed by DIANA FEA and the Technical University of Delft. The figures and equations in this chapter are taken from (Schreppers, Garofano, Messali, & Rots, 2017). The model is primarily used for modelling the failure of masonry walls (2D plane stress elements) or masonry structures (3D curved shell elements). Important characteristics of the engineering masonry model are as follows:

- The material model is a total-strain-based continuum model
- Tensile, shear and compression failure modes
- Four in-plane crack directions are possible: x,y and two diagonal directions with a predefined angle.
- Orthotropic
- X-direction aligned with the bed joints and y-direction aligned with the head joints
- If diagonal cracks do not occur, the model acts as an orthotropic material with a Poisson's ratio of zero (no coupling between the stiffness of the normal components and the in-plane shear component)

Furthermore, the engineering masonry model regards the following failure mechanisms:

- Tensile cracking of the bed and head joints
    - Secant nonlinear unloading and reloading
- Compressive crushing normal to the bed and head joints

    - Nonlinear non-secant unloading and reloading
- Cracking normal to the diagonal cracks
    - When a crack is opening, the tensile and shear stress are reduced. When a crack is closing, the model has a linear stiffness equal to the initial stiffness.
    - The behaviour of the diagonal crack can be unrealistic for slender walls. The diagonal cracking can then be deactivated.
- Frictional shear sliding
    - Shear stresses calculated using Coulomb friction.
- Out-of-plane shear failure
    - Out-of-plane shear stiffness components are considered to be linear elastic, except when the option of out-of-plane shear failure is selected. In such a case, Coulomb friction is used.

CRACKING BEHAVIOUR

The stresses in an element are defined by the strains in the x- and y-directions and the maximum strain value $\alpha_{tensile}$ achieved during the loading history. The corresponding stress at $\alpha_{tensile}$ is expressed as $\sigma_{rf,tensile}$. Via the maximum value of the strain, the secant unloading behaviour is determined. The tensile stress-strain curve is described by determining the ultimate strain with the tensile strength f_t , crack energy G_{ft} and crack bandwidth of the element h. The ultimate tensile strain occurs when the crack is fully open and no stress transfer is possible. This is determined using the following formula:

$$\varepsilon_{ult} = \frac{2G_{ft}}{hf_t}$$

The following Figure describes the tensile behaviour of the engineering masonry model:

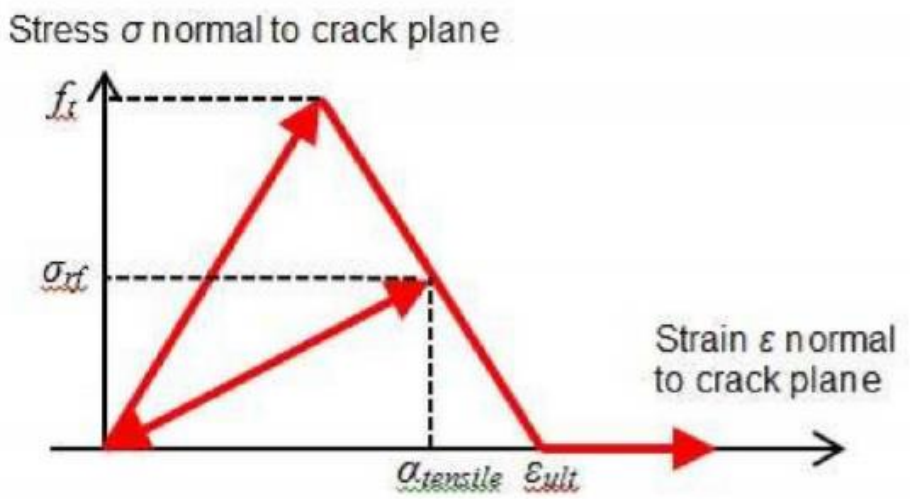

FIGURE 7: CRACKING BEHAVIOUR ENGINEERING MASONRY MODEL (SCHREPPERS, GAROFANO, MESSALI, & ROTS, 2017)

The compressive stresses of an element in the x- and y-directions are defined by the strain and the minimum strain value α_{comp} achieved during the loading history. The corresponding stress is expressed as $\sigma_{rf,compressive}$. The compressive stress-strain curve is described by determining the ultimate strain with the compressive strength f_c, crack energy G_c and factor n. The factor n is used to determine the strain ε_{peak} at compressive strength using the following formula:

$$n = \frac{E\varepsilon_{peak}}{f_c}$$

The stress-strain curve is comprised of a parabolic curve until reaching the compressive strength and a linear softening curve until reaching 10% of the compressive strength. The ultimate strain ε_{ult} is equal to the strain corresponding to a zero stress level, determined using the following formula:

$$\varepsilon_{ult} = \varepsilon_{peak} + \max\left[0, \frac{2G_c}{hf_c} - \frac{f_c}{A^2E} - \frac{A+1}{A}(\varepsilon_{peak} - \frac{f_c}{E})\right]$$

where h is the crack bandwidth, and A is defined as following:

$$A = \left(\frac{E\varepsilon_{peak}}{f_c}\right)^{\frac{1}{3}}$$

The Figure below illustrates the crushing behaviour of the engineering masonry model:

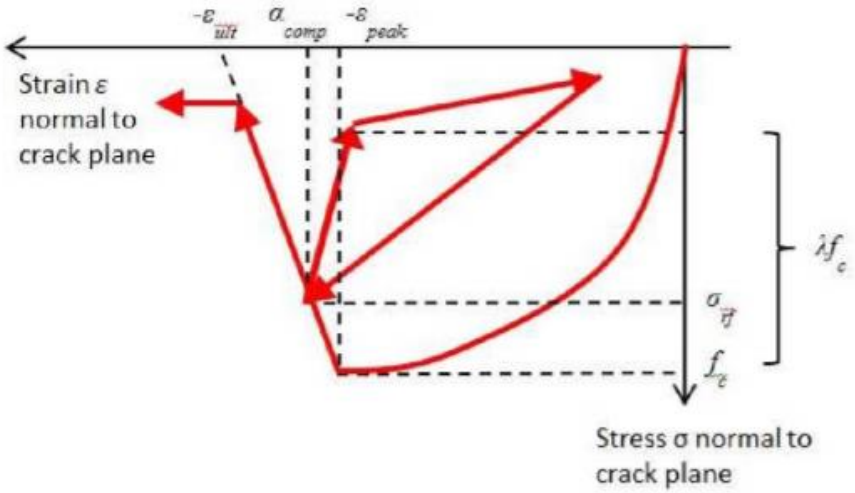

FIGURE 8: COMPRESSIVE BEHAVIOUR OF ENGINEERING MASONRY MODEL (SCHREPPERS, GAROFANO, MESSALI, & ROTS, 2017)

In the Figure, λ represents the unloading factor. The factor can obtain values between 1 and 0, in which $\lambda = 1$ corresponds to secant unloading to the origin with stiffness $\frac{\sigma_{rf,compressive}}{\alpha_{comp}}$, and $\lambda = 0$ corresponds to unloading to zero stress with the initial stiffness and secant stiffness. For $\lambda = 0$, unloading with the initial stiffness is applied until the compressive stress is equal to $\lambda\sigma_{rf,compressive}$. The secant stiffness is then applied until the origin is reached. Reloading the curve goes with a straight line to the last loading extreme point. The secant stiffness is defined as follows:

$$E_{sec} = \frac{\lambda \sigma_{rf,compressive}}{\alpha_{comp} - \frac{\lambda \sigma_{rf,compressive}}{E}}$$

SHEAR BEHAVIOUR

The in-plane shear stress τ is defined by the shear strain γ and the stress σ_{yy} normal to the bed joint. The shear stress $|\tau|$ cannot exceed the maximum stress τ_{max}, which is formulated according to the Coulomb friction criterion as follows:

$$\tau_{max} = \max\left[0, c - \sigma_{yy}\tan(\varphi)\right]$$

where c is the cohesion of friction, and φ is the friction angle of the masonry. The shear stress-strain curve is presented in the Figure below:

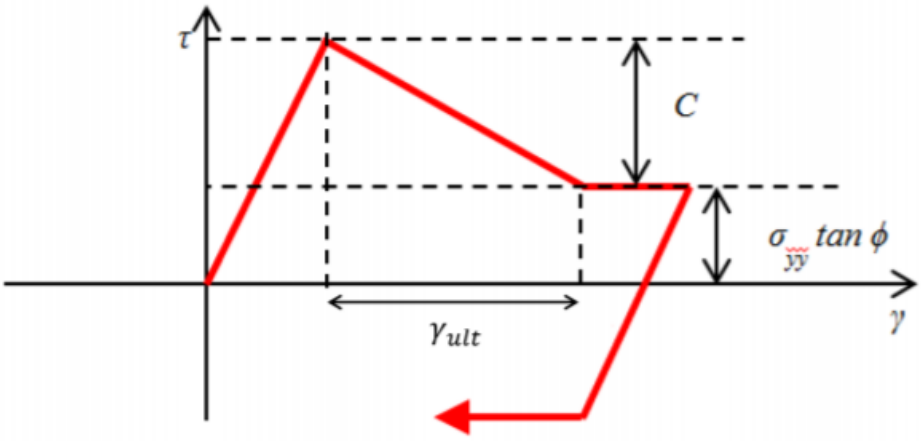

FIGURE 9: SHEAR BEHAVIOUR OF ENGINEERING MASONRY MODEL (SCHREPPERS, GAROFANO, MESSALI, & ROTS, 2017)

The Figure above depicts a linear relationship between the shear strain and stress until $\tau_{\max}$ is reached. The cohesion then decreases until the cohesion reaches zero at a total shear strain of γ_{ult}, which is defined as follows:

$$\gamma_{ult} = \frac{2G_{fs}}{h * c} - \frac{c}{G}$$

where h is the crack bandwidth, G_{fs} is the shear energy and G is the shear modulus. Last, when an integration point is cracked ($\alpha_{tension} > \frac{f_t}{E}$), the cohesion is reduced to zero.

HEAD JOINT FAILURE OPTIONS

The engineering masonry model has four options for considering the failure of the head joint in the DIANA model. The user must select one of the following four head joint failure options:

1. Head joint failure not considered: In this option, the model does not consider diagonal cracks. Only cracking and crushing normal to the bed joint and the Mohr-Coulomb criterion are evaluated.
2. Direct input head joint tensile strength: In this option, the cracking and crushing normal to the head joint are also considered. The tensile strength in both directions and the compressive strength in one direction which is used in both directions must be explicitly defined by the user. Once again, diagonal cracks are not considered.
3. Diagonal staircase cracks: The failure of the head-joint is assumed to occur as part of a diagonal staircase crack. In this option, in addition to cracking and crushing normal to the bed joint and shear failure, the cracking and shear release of the diagonal staircase cracks are also considered. The user must define the angle with the bed joint of the staircase crack, the bed joint tensile strength and the frictional shear stress in the bed joint.

4. Tensile strength head joint defined by friction: This is similar to point 2, but now the tensile strength is calculated based on the friction shear stress in the bed joint. A minimum tensile strength of the head joint can also be explicitly defined. The effect of a highly overburdened load can be considered in this option.

TOTAL STRAIN CRACK MODEL

The total strain crack model is a constitutive model based on the total strain and is developed according to the modified compression field theory (Vecchio & Collins, 1986). The total strain crack model offers three different constitutive models based on the crack orientation: fixed, rotating and combined. The difference lies in the different evaluations of the stress-strain relationships of the three variants. For the fixed crack orientation, the stress-strain relationship is evaluated in a fixed coordinate system. For the rotating crack orientation, it is evaluated in the principal directions of the strain vector. Finally, for the combined crack orientation, a limit value for the total strain directs whether the crack orientation changes from rotating to fixed. For this research, the focus is only on the rotating strain crack model.

The total strain crack model requires several material input parameters. These are the linear elastic material properties, the parameters for the tensile behaviour and the parameters for the compressive behaviour. The tensile behaviour can be modelled using a variety of approaches. The following functions are based on fracture energy:

- Linear softening curve
- Exponential softening curve
- Nonlinear softening curve by Hordijk
- Nonlinear tension softening according to CEB-FIP Model Code 1990
- Nonlinear softening according to fib Model Code for Concrete structures 2010
- Nonlinear softening according to JSCE

Other tensile curves are as follows:

- Constant tensile behaviour
- Linear behaviour based on ultimate strain
- Multilinear behaviour
- Brittle behaviour
- Tensile failure model for fiber reinforced concrete (CEB-FIP)
- User-supplied

The compressive behaviour can be modelled with a number of predefined curves. These predefined curves are as follows:

- Constant curve
- Brittle curve
- Thorenfeld curve
- Linear hardening curve
- Multilinear curve
- Saturation hardening curve
- Parabolic curve
- Eurocode 2 1992-1-2 and Eurocode 4 1994-1-2
- Maekawa cracked concrete curves
- CEB-FIP Model Code 1990
- Fib Model Code for concrete structures 2010
- Hognestad parabola
- Eurocode 2 EN1992-1-1

The above curves have a secant unloading behaviour, except the Maekawa cracked concrete curves, which follow a nonlinear unloading behaviour.

For this study, the following tensile and compression curves were selected:

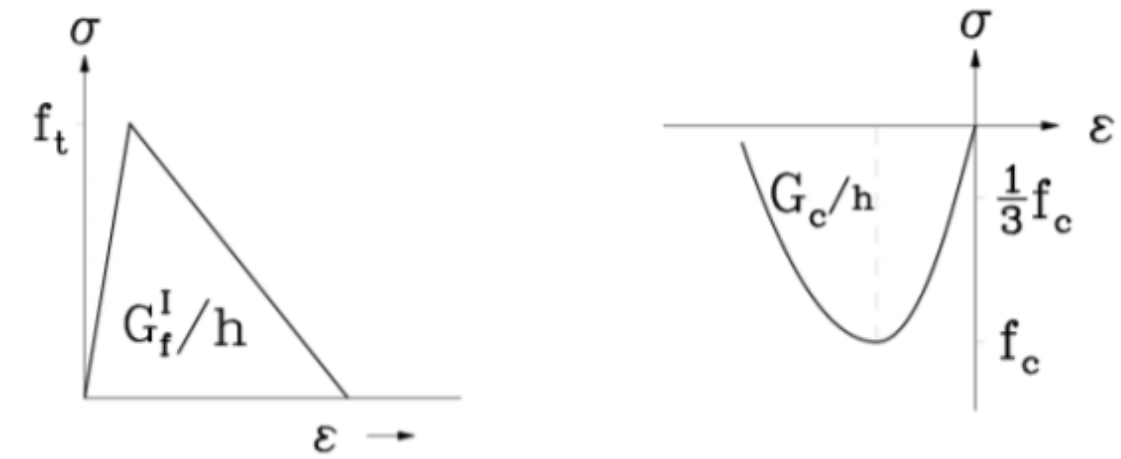

FIGURE 10: LINEAR TENSILE SOFTENING CURVE (LEFT) AND PARABOLIC COMPRESSION CURVE (RIGHT) (DIANA FEA)

4 DESCRIPTIONS OF THE CASE STUDIES AND METHODOLOGY

This chapter describes the approach that is used to answer the main research questions. The approach consists of seismic assessments for different models, starting with simple 2D models and ending up with two different 2D case study model. In every model some changes are made to determine the influence of these changes to the comparison between the two seismic assessment methods. After the 2D assessment phase, two 3D case study buildings are analysed with the same two assessment methods.

The seismic assessments will be done in accordance to the SLaMA method and NLPO (Nonlinear pushover assessment) FEM analysis as described in the NPR9998. These assessments are mainly focussed on the in-plane behaviour of the wall- models. This study is mainly focused of the influence of masonry type, floor types and loading type. The influence of the geometry and the openings percentage is out of the scope of this research. The influence of this parameter is studied by Anass El kouri, and his conclusions will be mentioned in this report.

4.1 OVERVIEW OF THE ANALYSED WALLS/BUILDINGS

In this 2D assessment phase 10 models have been analyzed with both assessment approaches as described above. The first 6 models are the simple model with the same geometry but different masonry type, floor type and loading. It is not a typical front façade common in the Netherlands, but it is just a model that will be used for study purposes. This simple model has already been analyzed by Milani and Akhaveissy (A.H.Akhaveissy, 2013).The Figures below show the geometry and the loading condition of each simple model.

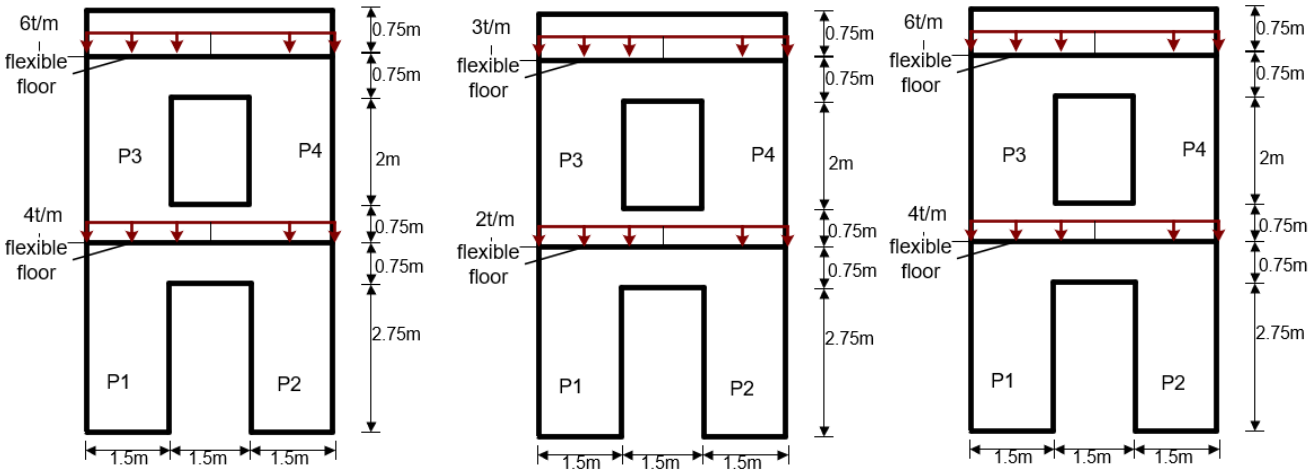

FIGURE 11: SM 1-CLAY<1945, SM2, SM- CLAY>1945 *FROM LEFT TO RIGHT*

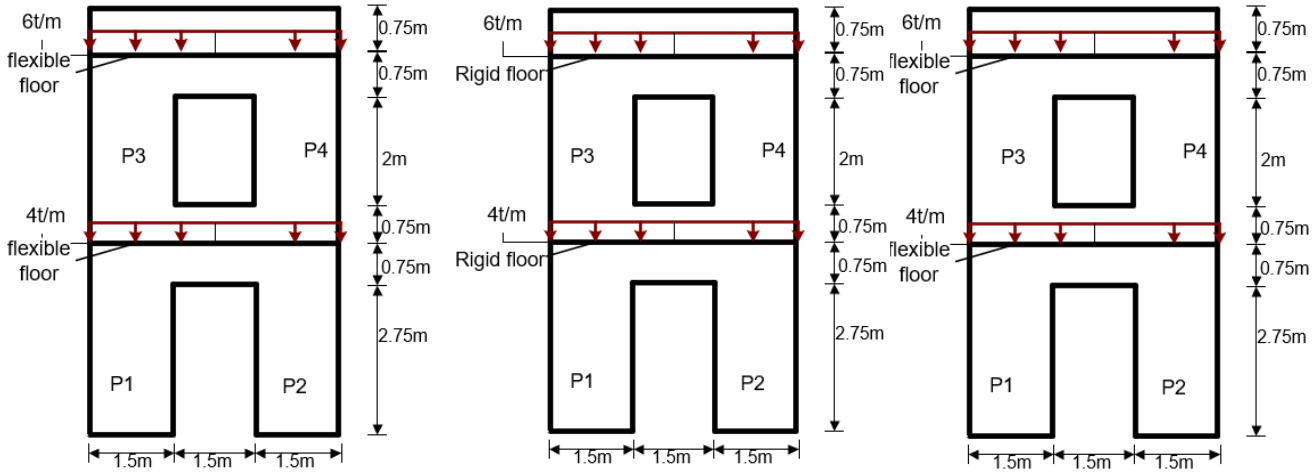

FIGURE 12: SM4 CS<1985, SM5, SM6- CLAY- TENSILE CASE FROM LEFT TO RIGHT

The last four case study models that have been analysed are the two different walls (with openings) of the EUROCENTRE –BUILDING 6 (M. Miglietta, 2019). The Figures below show the geometry of the two different models. The last two models are the same models but with the lintels modelled specifically instead of neglecting them.

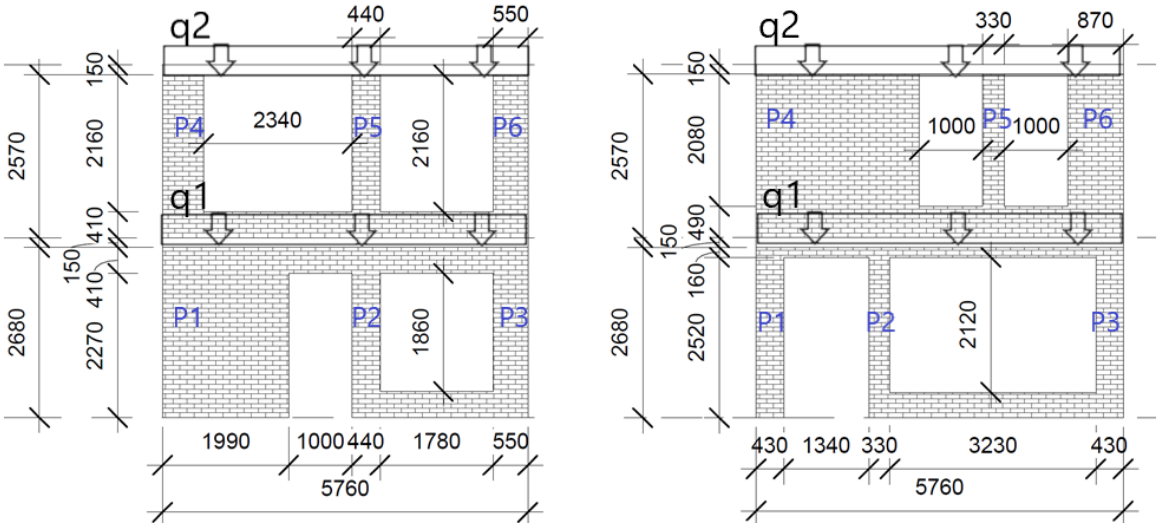

FIGURE 13: CASE STUDY-2D-1A , CASE STUDY-2D-2A

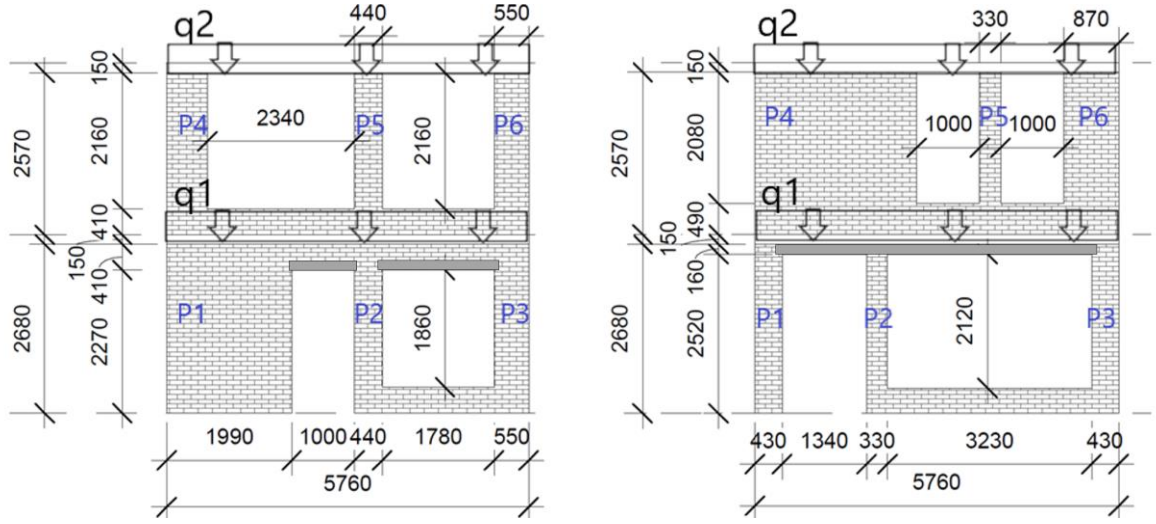

FIGURE 14: CASE STUDY-2D-1B , CASE STUDY-2D-2B

After the 2D assessment phase, the 3D assessment of two buildings follows. In this phase, two models are analyzed, and the capacity of these models is calculated using the SLaMA method and the DIANA FEA. This phase is primarily intended to determine the influence of the floors. The influence of floors is easier to determine by means of a 3D analysis than with a 2D analysis. In the 3D FEM analysis, the entire floor is modeled with all specifications. It is a challenge to model the floors as realistically as possible. But the analysis can give a good view of the influence of the floors on the difference in capacity and expected failure mechanism between the SLaMA method and NLPO DIANA FEA.

The two models analyzed in this phase have the same geometry, material properties and the same load. The only difference between the two models is that **Casestudy-3D-Model-double RC-floors** has concrete reinforced floors and **Casestudy-3D-Model-double timber-floors** has timber floors for both levels. The geometry of these models is comparable to the geometry of the test house EUC-BUILD-6, which has been tested by the eurocentre for the NAM (M. Miglietta, 2019). See below an overview of both models.

Casestudy-3D-Model-double RC-floors	Casestudy-3D-Model-double timber-floors
Clay pre 1945 masonry	Clay pre 1945 masonry
16 bags of 400 kg placed at second floor	16 bags of 400 kg placed at second floor
RC-floors for both levels	Timber floors for both levels

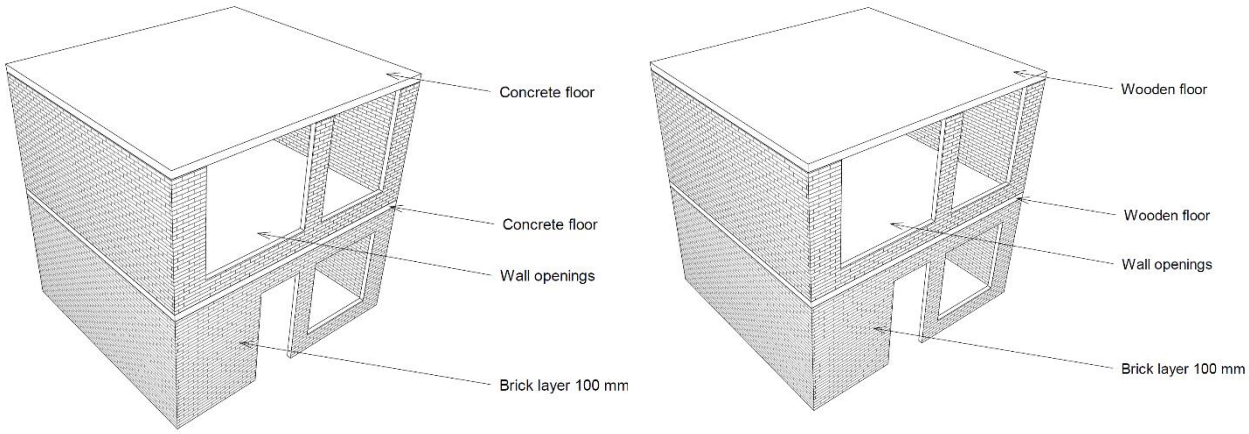

FIGURE 15: 3D MODELS CONCRETE FLOOR, TIMBER FLOOR *FROM LEFT TO RIGHT*

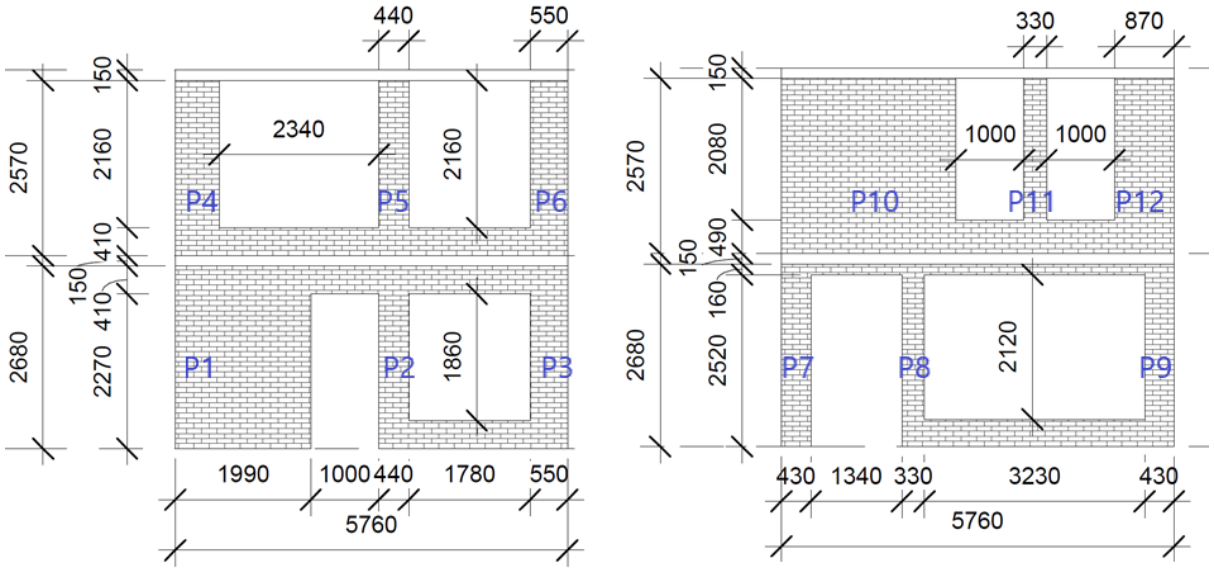

FIGURE 16: PIER LOCATIONS 3D MODEL

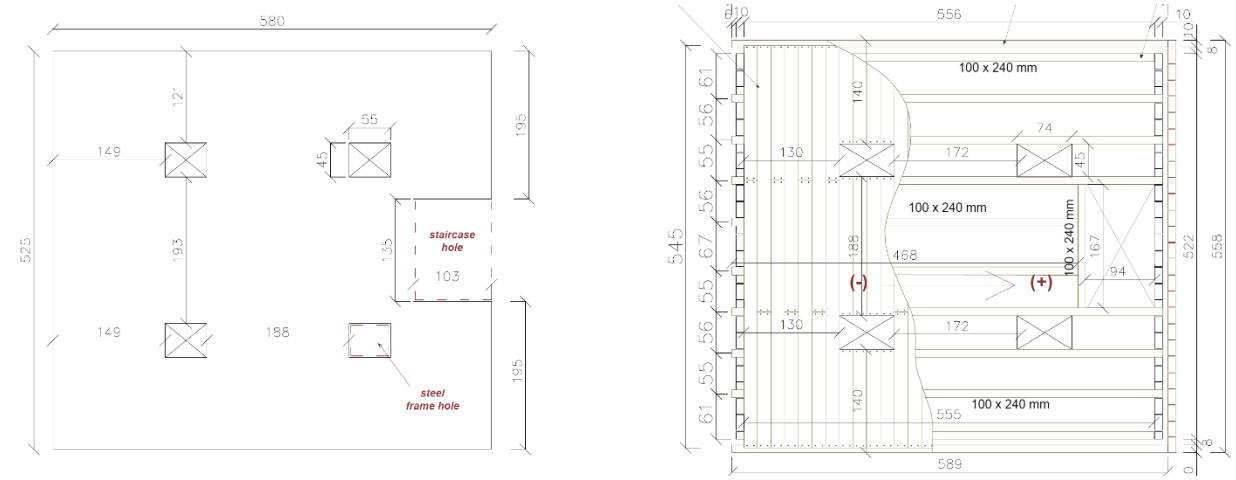

FIGURE 17: FLOOR PLANS, EUCENTRE EXAMPLES (M. MIGLIETTA, 2019)

4.1.1 OVERVIEW OF THE ANALYSED WALLS/ BUILDINGS AND THE VARIATIONS

The table below shows an overview of the different models that will be analysed and the different specifications. Each model differs in one specific aspect, and this could be floor type, masonry type and applied load. The material properties of each masonry type are further specified in section "Material properties". In this way, the influence of the differences in the assessments could be determined.

Models	Floor type	Applied load	Masonry type
SM1	Flexible floor	$q_1 = 6t/m$, $q_2 = 4t/m$	Clay-pre 1945
SM2	Flexible floor	$\boldsymbol{q_1 = 3t/m}$, $\boldsymbol{q_2 = 2t/m}$	Clay-pre 1945
SM3	Flexible floor	$q_1 = 6t/m$, $q_2 = 4t/m$	**Clay-post 1945**
SM4	Flexible floor	$q_1 = 6t/m$, $q_2 = 4t/m$	**CS-pre 1985**
SM5	**Rigid floor/ RC floor**	$q_1 = 6t/m$, $q_2 = 4t/m$	Clay-pre 1945
SM6	Flexible floor	$q_1 = 6t/m$, $q_2 = 4t/m$	**Clay-pre 1945- Different tensile strength**
Case study-2D-1A	Flexible floor	$q_1 = 1.65kN/m$, $q_2 = 2.65kN/m$	Clay-pre 1945
Case study- 2D-2A	Flexible floor	$q_1 = 1.65kN/m$, $q_2 = 2.65kN/m$	Clay-pre 1945
Case study-2D-1B (lintels)	Flexible floor	$q_1 = 1.65kN/m$, $q_2 = 2.65kN/m$	Clay-pre 1945
Case study-2D- 2B (lintels)	Flexible floor	$q_1 = 1.65kN/m$, $q_2 = 2.65kN/m$	Clay-pre 1945
Casestudy-3D-Model-double RC-floors	**Rigid floor/ RC floor**	16 bags of 400 kg placed at second floor	Clay-pre 1945
Casestudy-3D-Model-double timber-floors	Flexible floor	16 bags of 400 kg placed at second floor	Clay-pre 1945

4.2 DESCRIPTION OF THE ASSESSMENT APPROACH

This section describes the two methods which have been used to assess the presented buildings and walls.

4.2.1 SLAMA METHOD AND THE APPLIED ASSUMPTIONS

The SLaMA assessment is done based on the SLaMA method as described in the NPR9998:2018 Appendix G. The total approach for this method is summarized in the literature study. The full SLaMA calculation of each model could be found in the appendix. This main report shows only the most import results from the SLaMA method. These are the results which are necessary to answer the main research questions. The main steps that have been applied in this method are briefly mentioned in the sections below.

EFFECTIVE HEIGHT

It is needed to compute the effective height of the piers based on the direction of the compressive strut to determine which part of the pier contributes to seismic resistance of the wall. The approach to compute de effective height is outlined in the NPR9998:2018 and proposed by Moon (Moon F. Y., 2006). This approach could be applied both for the 2D assessment as the 3D assessment phase.

THE AXIAL FORCE ON THE PIERS

The axial force on the pier is an important input value for the SLaMA method. Both the SLaMA method and the DIANA FE model must have the same starting axial force to make the comparison fair. The SLaMA method allows to choose an axial force which is more representative with the condition at failure of the piers. But this will require a nonlinear fem analysis ,and that would make the method unnecessary. Therefore this analysis uses the axial force at the top of the piers under static conditions.

The axial force on the piers is determined based on the first step within DIANA. In this step the self-weight and the loads from floors are applied. The normal force is determined by integrating the regression polynomial of the stresses, which fits through DIANA results.

BOUNDARY CONDITIONS OF THE PIERS

It is essential to determine the boundary conditions of the piers. Within the SLaMA method two options are possible, firstly the pier behaves cantilevered and secondly the pier has double clamped boundary conditions. To determine which kind of boundary conditions are applicable in the specific situation, the following procedure is used:

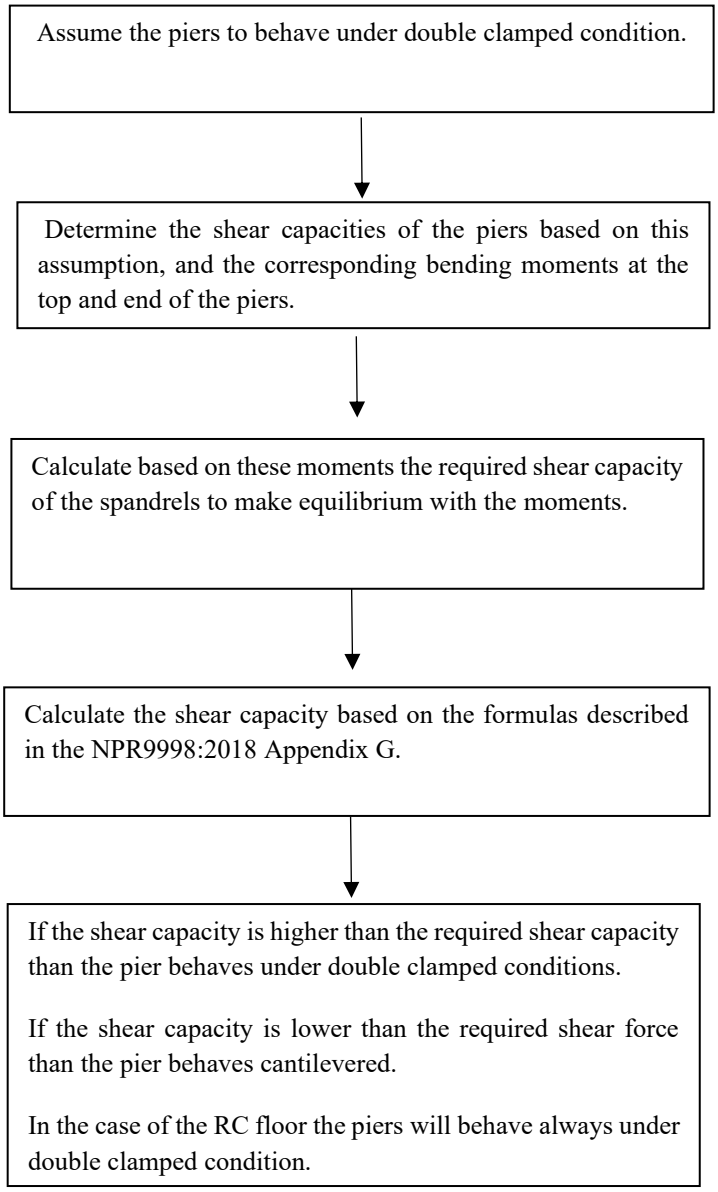

SHEAR CAPACITY OF THE PIERS

The shear capacity of the piers needs to be recalculated based on the obtained boundary conditions. These shear capacities are determined based on the formulas described in the NPR9998:2018 Appendix G section G9.2.3 and G9.2.2 equations G30, G29a. and b. The critical shear capacity of a pier corresponds to the lowest value of the shear capacities, which corresponds to a specific failure mechanism.

PUSHOVER CURVE SLAMA CALCULATION

The pushover curve is constructed for each floor. In the case of the 2D assessment, the shear capacity of each floor is the sum of the shear capacities of all the piers at this floor. The displacement capacity of each wall is determined based on the drift capacity of the piers that corresponds to critical failure type and also depended on the 50% drop of the shear capacity of the whole wall.

The SLaMA method used in this 3D analysis is comparable to the method used in the 2D analysis. The main difference lies in the cooperation between the in-plane loaded walls. In the 3D SLaMA calculation, the capacities of the piers in the in-plane walls can be summed up together when analyzing buildings with RC floors. Because this rigid floor gives the in plane loaded walls similar displacements.

In the case of timber floors the displacement of each single wall is not the same as the displacement of the center of the floor. That is way for timber floors the single wall are analyzed independently. Another difference is that the effect of flanges is taken into account when determining in plane capacity of the walls. The flange effect is considered in the way Moon (Moon F. Y., 2006)described it. See chapter 2 literature study-flange contribution for a comprehensive description of the contributing flange effects.

ACCELERATION

The acceleration curve is constructed by dividing pushover curve of each floor by contributing effective masses that corresponds to the specific floor. These effective masses could be found in the full SLaMA calculation of each model in the appendix. This main report shows only the resulting acceleration curve.

MAXIMUM BASE SHEAR FORCE

The resulting acceleration curve shows the acceleration of the different levels. The lowest acceleration is critical one and is used to determine the global base shear force of the whole structure, that is taken equal to the acceleration multiplied by the total effective masses of the building.

4.2.2 NONLINEAR PUSHOVER FINITE ELEMENT ANALYSIS AND THE MODELLING ASSUMPTIONS

Each wall/building was analysed using the NLPO FEA within DIANA. The models were modelled with specific assumptions, and the results can be found in the full DIANA FE analysis in the appendix. This main report describes only the relevant results of the DIANA NLPO FEA.

MODELLING ASSUMPTIONS (DIANA)

MASONRY

The masonry is modelled using the engineering masonry model. The material model consists of four options, all of which are considered. The four options are further explained in Chapter 2: Literature study- engineering masonry model. For the 2D cases, no significant difference was found between those four options. The material model in the presented results considers the 'diagonal staircase' option.

For the 3D cases, the masonry is modelled using the engineering masonry model with the the 'diagonal staircase' option, the 'head joint tensile strength not considered' option and the 'direct input head joint tensile strength' option applied to these models. These options are abbreviated using the following terminology: DS options, HJ option and direct option.

The masonry in the 2D cases consists of plane stress elements, while in the 3D cases, it consists of quadrilateral curved shell elements. The material properties for modelling the masonry corresponds with the material properties used in the SLaMA assessment. These material properties are listed in the tables of Chapter 3: Methodology and case studies section 3.3 material properties.

FLOORS

The RC floor in the 2D case is modelled with the plane stress elements with a thickness of 0.15 m and an out-of-plane thickness that corresponds to the part of the floor that contributes to the rotational stiffness (1.5 m). The reinforcement is modelled with rebar elements with a diameter of 12 mm. In the 3D case, the complete RC floors are modelled with quadrilateral curved shell elements. The concrete properties are considered with the total-strain-based crack model and considers the rotating crack model with the tensile softening behaviour (fib fiber reinforced concrete CMOD model) and the parabolic compressive behavior. Reinforcement bars are modelled with embedded rebar elements with a diameter of 12 mm and a spacing of 240 mm.

The timber floors in the 2D cases are simulated with beam elements with the stiffness of the floors and a thickness of 0.24 m. Meanwhile, the timber floors in the 3D model consist of timber beams and timber planks. The timber beams are modelled as 3D beam elements and the planks as a single sheet of regular curved shell elements with a thickness of 17 mm. The timber beams are connected to the out-of-plane walls with a spacing of 240 mm and are rigidly connected to the planks. Linear isotropic timber properties have beams assigned to the timber beams and orthotropic timber properties to the timber planks.

LOADS

The applied load on the floors was modelled with beam elements by changing the density of the beam until the gravity load of the beams corresponds to the load applied at the floor. This was performed for both the 2D and 3D assessment phases.

As mentioned previously, all the loads are considered to be seismic masses with densities and dimensions which corresponds to the value of the load. This is because modal pushover analysis considers only the masses, resulting in a more realistic participating mass. The pushover load is applied to the entire structure via the modal pushover tool in DIANA.

MESH

Quadratic plane stress elements and linear plane stress elements were applied by meshing this structure. Both quadrilateral and triangular elements were applied. Both choices were based on the convergence behaviour of these analyses. The mesh sizes vary between 0.1 mm and 0.2 mm and depend on the computational time and the convergence behaviour of the specific model.

ANALYSES

The first analysis that was conducted on this model is the structural eigenvalue analysis. This analysis is further elucidated in Chapter 2: Literature study- structural eigenvalue analysis. The primary goal of this analysis is to determine the critical eigenmode that corresponds to the highest participating mass in the analysed direction. This is the main input parameter for the modal pushover load which, together with the self-weight, is considered in the structural nonlinear analysis. In the mentioned analysis, both geometrical and physical nonlinearity are considered.

The step size selected in the assessments vary from 0.0001– 0.01 depending on the specific model. These step sizes are selected based on the computational time and the convergence behaviour of the specific model. In particular, the energy convergence norm of 0.0001 was selected. Moreover, the numerical solving method for the second analysis is the secant method that uses the arc length control approach.

4.3 MATERIAL PROPERTIES

There are different masonry types considered for each different model. This part of this report gives an overview of the material properties for the different masonry types. The material properties are equally used in both the SLaMA calculations as in the DIANA FE analysis. These properties are in accordance with the NPR9998:2018, the properties that are used by the engineers at Arcadis and properties determined in the article of Jafari (Jafari, 2017).

CLAY MASONRY -PRE 1945

The material properties applied for the clay masonry-pre 1945 are all assumed based on the expertise of the engineers at Arcadis.

TABLE 1: MATERIAL PROPERTIES CLAY MASONRY-PRE 1945

Material properties	**Description**	
Ex	Young's modulus in x-direction	$2.5 * 10^9\ N/m^2$
Ey	Young's modulus in y-direction	$5.0 * 10^9\ N/m^2$
G	Shear modulus	$2.0 * 10^9\ N/m^2$
θ	Angle between the bed-joint and the stair-case diagonal stair-case-cracks	$0.785\ rad$
ftx	Tensile strength in x-direction	$0.2 * 10^6\ N/m^2$
fty	Tensile strength in y-direction	$0.067 * 10^6\ N/m^2$
Gfty	Tensile fracture energy in y-direction	$7\ N/\ m$
fcy	Compressive strength in y-direction	$5.67 * 10^6\ N/m^2$
Gfcy	Compressive fracture in y-direction	$6667\ N/\ m$
ϕ	Friction angle	$0.543\ rad$
C	Cohesion coefficient	$0.2 * 10^6\ N/m^2$
Gfs	Shear fracture energy	$67\ N/\ m$
ρ	Density	$1900\ kg/m^3$

CLAY MASONRY-POST 1945

These material properties are mainly based on the porperties suggested by the NPR9998:2018. Only the young's modulus in both directions are taken from the research of Samira Jafari (Jafari, 2017).

TABLE 2: MATERIAL PROPERTIES CLAY MASONRY-POST 1945

Material properties	**Description**	
Ex	Young's modulus in x-direction	$5.47 * 10^9\ N/m^2$
Ey	Young's modulus in y-direction	$9.4 * 10^9\ N/m^2$
G	Shear modulus	$2.5 * 10^9\ N/m^2$
θ	Angle between the bed-joint and the stair-case diagonal stair-case-cracks	$0.785\ rad$
ftx	Tensile strength in x-direction	$0.55 * 10^6\ N/m^2$
fty	Tensile strength in y-direction	$0.2 * 10^6\ N/m^2$
Gfty	Tensile fracture energy in y-direction	$10\ N/\ m$
fcy	Compressive strength in y-direction	$17.7 * 10^6\ N/m^2$
Gfcy	Compressive fracture in y-direction	$15000\ N/\ m$
ϕ	Friction angle	$0.6435\ rad$
C	Cohesion coefficient	$8.73 * 10^4\ N/m^2$
Gfs	Shear fracture energy	$200\ N/\ m$
ρ	Density	$1900\ kg/m^3$

CALCIUM SILICATE-PRE 1985

These material properties are mainly based on the porperties suggested by the NPR9998:2018. Only the young's modulus in both directions are taken from the research of Samira Jafari (Jafari, 2017)

TABLE 3: MATERIAL PROPERTIES CALCIUM SILICATE-PRE 1985

Material properties	**Description**	
Ex	Young's modulus in x-direction	$2.33 * 10^9\ N/m^2$
Ey	Young's modulus in y-direction	$3.5 * 10^9\ N/m^2$
G	Shear modulus	$3.0 * 10^9\ N/m^2$
θ	Angle between the bed-joint and the stair-case diagonal stair-case-cracks	$0.785\ rad$
ftx	Tensile strength in x-direction	$0.65 * 10^6\ N/m^2$
fty	Tensile strength in y-direction	$0.4 * 10^6\ N/m^2$
Gfty	Tensile fracture energy in y-direction	$10\ N/\ m$
fcy	Compressive strength in y-direction	$7 * 10^6\ N/m^2$
Gfcy	Compressive fracture in y-direction	$17000\ N/\ m$
ϕ	Friction angle	$0.548\ rad$
C	Cohesion coefficient	$0.25 * 10^4\ N/m^2$
Gfs	Shear fracture energy	$100\ N/\ m$
ρ	Density	$1900\ kg/m^3$

CLAY-PRE 1945- DIFFERENT TENSILE STRENGTH

These are the material properties that have been used to determine the influence of the tensile strength in y-direction and tensile fracture energy. These two properties are ten times smaller than that of the Clay-pre 1945. The other are properties are the same as the properties of the Clay-pre 1945 and are assumed based on the expertise of the engineers at Arcadis.

TABLE 4: MATERIAL PROPERTIES CLAY-PRE 1945- DIFFERENT TENSILE STREGNTH

Material properties	**Description**	
Ex	Young's modulus in x-direction	$2.5 * 10^9\ N/m^2$
Ey	Young's modulus in y-direction	$5.0 * 10^9\ N/m^2$
G	Shear modulus	$2.0 * 10^9\ N/m^2$
θ	Angle between the bed-joint and the stair-case diagonal stair-case-cracks	$0.785\ rad$
ftx	Tensile strength in x-direction	$0.2 * 10^6\ N/m^2$
fty	Tensile strength in y-direction	$\mathbf{0.067 * 10^5\ N/m^2}$
Gfty	Tensile fracture energy in y-direction	$\mathbf{0.7\ N/\ m}$
fcy	Compressive strength in y-direction	$5.67 * 10^6\ N/m^2$
Gfcy	Compressive fracture in y-direction	$6667\ N/\ m$
ϕ	Friction angle	$0.534\ rad$
C	Cohesion coefficient	$0.2 * 10^6\ N/m^2$
Gfs	Shear fracture energy	$67\ N/\ m$
ρ	Density	$1900\ kg/m^3$

5 RESULTS OF THE 2D ANALYSES

The results of the 2D assessment phase are presented in this chapter. These are the results of the DIANA NLPO FEA and the SLaMA assessment of the walls/buildings presented in chapter Methods. The results relevant to answering the research questions are presented in this chapter. The more comprehensive results (of four different load steps) are presented in the appendices for each specific model. These results are discussed in the following chapter, in which these discussion points are divided into the 2D assessment phase and the 3D assessment phase.

5.1 NLPO FEA (DIANA) RESULTS

This section presents the most important FEM results of all the analysed models. The full DIANA NLPO FEA can be found in the appendix corresponding to each specific model. The appendix provides the results of four different load steps. The results presented in this chapter are the participating masses, eigenmodes, maximum horizontal deflection, maximum principal strains at the last load step, observed failure mechanisms and pushover curves.

5.1.1 RESULTS: STRUCTURAL EIGENVALUE ANALYSIS

The first analysis is the structural eigenvalue analysis, which is required to determine the critical eigenmode and eigen frequency. The eigenmode with the greatest participating mass in the y-direction is the critical eigenmode. The table below presents the participating masses of all the models that have been analysed during this 2D assessment phase. The Figures below display the corresponding eigenmodes of the analysed models.

TABLE 5: PARTICIPATING MASSES

Model:	Participating mass in x-direction
SM1	81%
SM2	79%
SM3	82%
SM4	83%
SM5	84%
SM6	81%
Case study-2D-1A,1B	56%
Case study-2D-2A,2B	90%

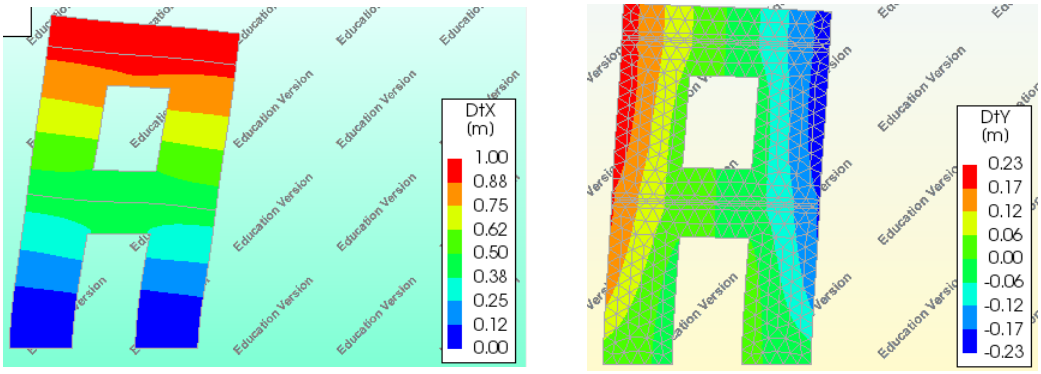

FIGURE 18: EIGENMODE SM1 UNTILL SM4,SM6 (LEFT) AND EIGENMODE SM5 (RIGHT)

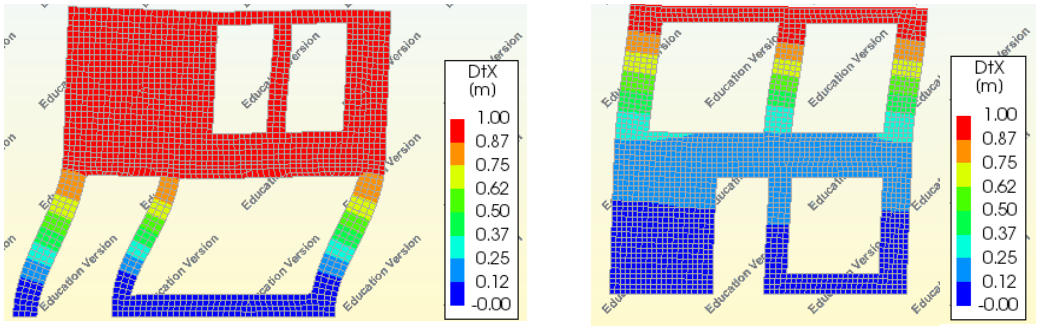

FIGURE 19:EIGENMODE CASESTUDY 2D-1A & 1B(LEFT) AND EIGENMODE CASESTUDY 2D-2A & 2B (RIGHT)

5.1.2 RESULTS: STRUCTURAL NONLINEAR ANALYSIS

This subsection contains the results of the structural nonlinear analysis. In this case, the relevant obtained results are the horizontal deflection, maximum principal strain, observed failure mechanism and the pushover curve. These are the results which will be compared with the results of the SLaMA method. The comparison between both methods is discussed in Chapter 6: Discussion.

HORIZONTAL DEFLECTION

The ultimate displacement reached with the NLPO FEM analysis is presented for each model in the results below. These displacements were reached the moment the divergence of the numerical solving method began to occur.

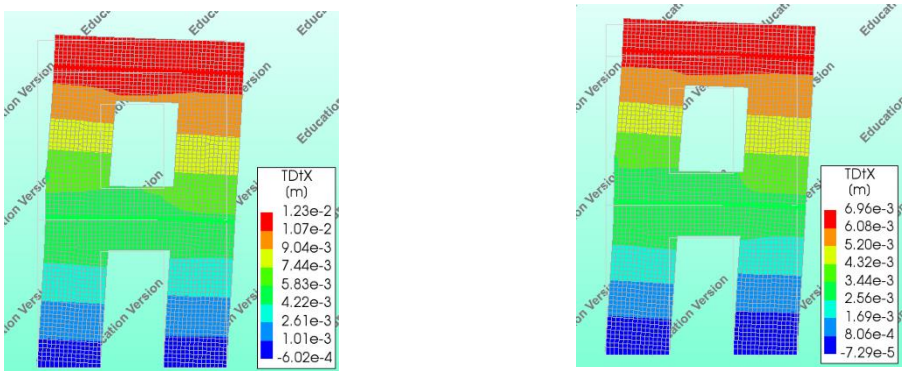

FIGURE 20:SM1-ULTIMATE DISPLACEMENT(LEFT) AND SM2-ULTIMATE DISPLACEMENT (RIGHT)

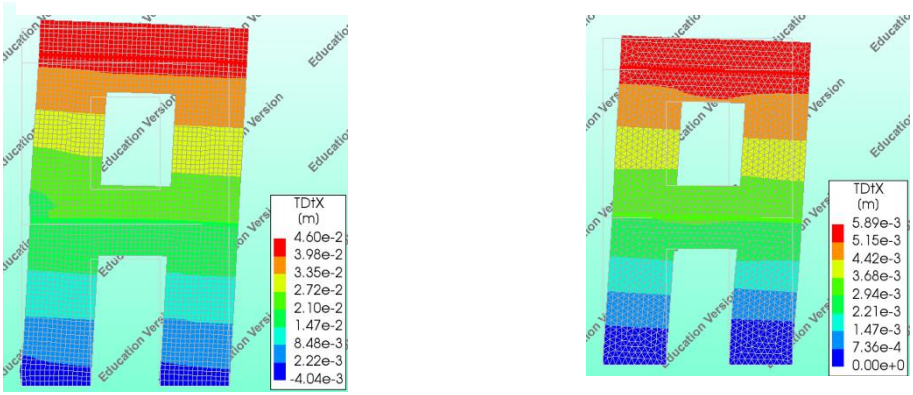

FIGURE 21:SM3-ULTIMATE DISPLACEMENT(LEFT) AND SM4-ULTIMATE DISPLACEMENT (RIGHT)

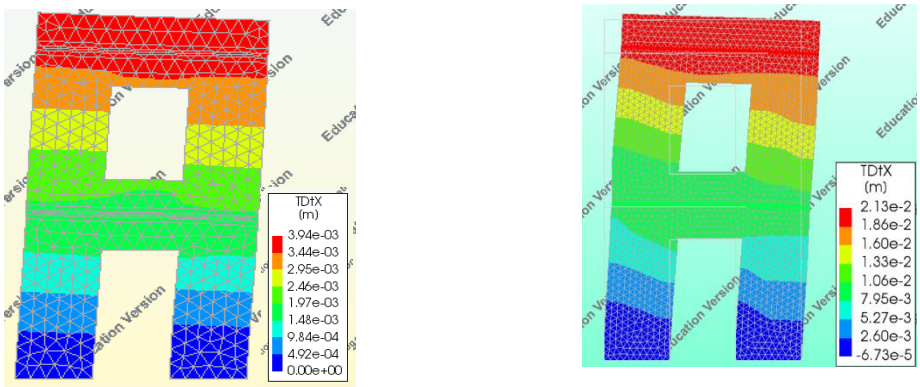

FIGURE 22: SM5-ULTIMATE DISPLACEMENT (LEFT) AND SM6-ULTIMATE DISPLACEMENT(RIGHT)

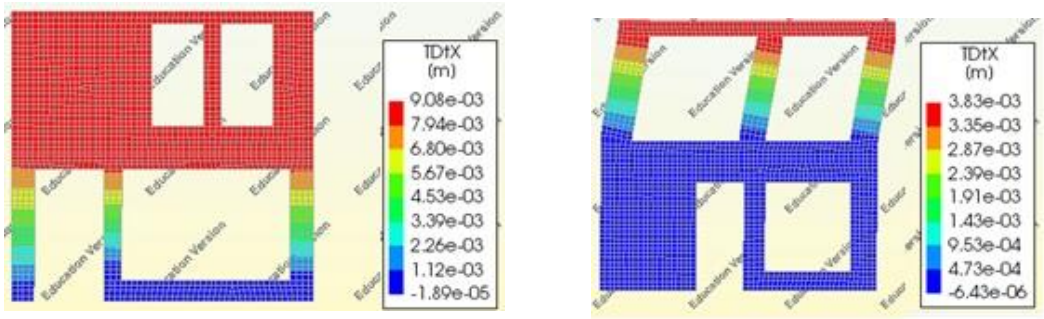

FIGURE 23: CASESTUDY 2D-1A-ULTIMATE DISPLACEMENT (LEFT) AND CASESTUDY 2D-2A-ULTIMATE DISPLACEMENT(RIGHT)

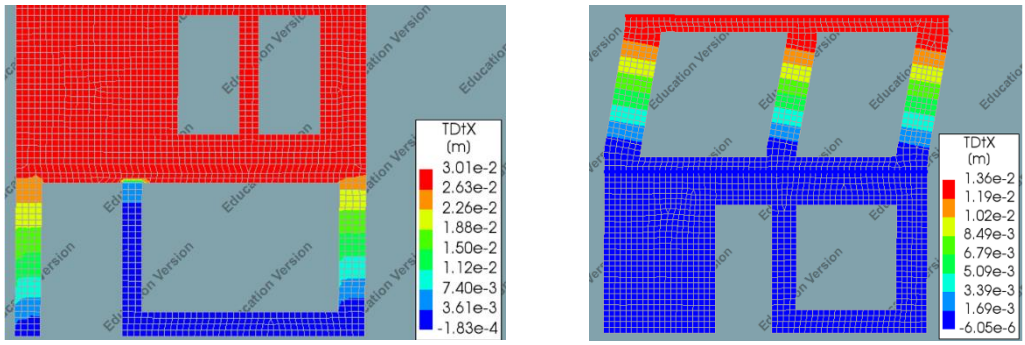

FIGURE 24: CASESTUDY 2D-1B-ULTIMATE DISPLACEMENT (LEFT) AND CASESTUDY 2D-2B-ULTIMATE DISPLACEMENT (RIGHT)

MAXIMUM PRINCIPAL STRAIN

The maximum principal strain plot of each model provides a solid indication of the development of the cracking patterns during the pushover curve. The Figures below display only the results from the last loading step.

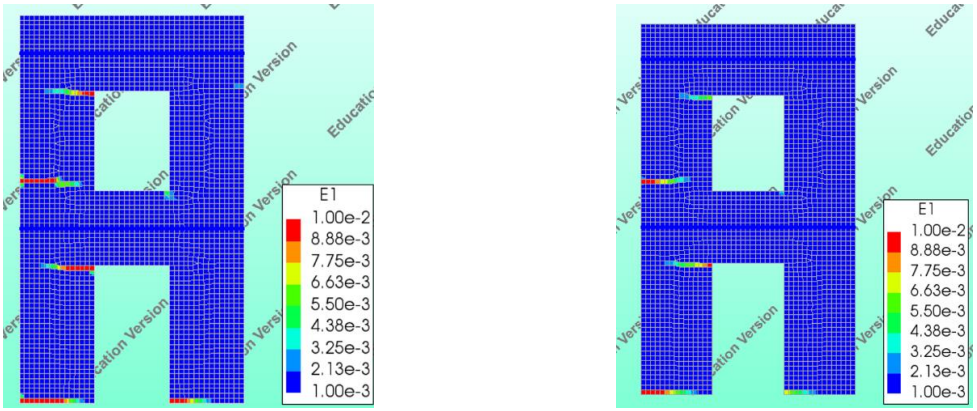

FIGURE 25: SM1-MAXIMUM PRINCIPAL STRAIN (LEFT) AND SM2-MAXIMUM PRINCIPAL STRAIN (RIGHT)

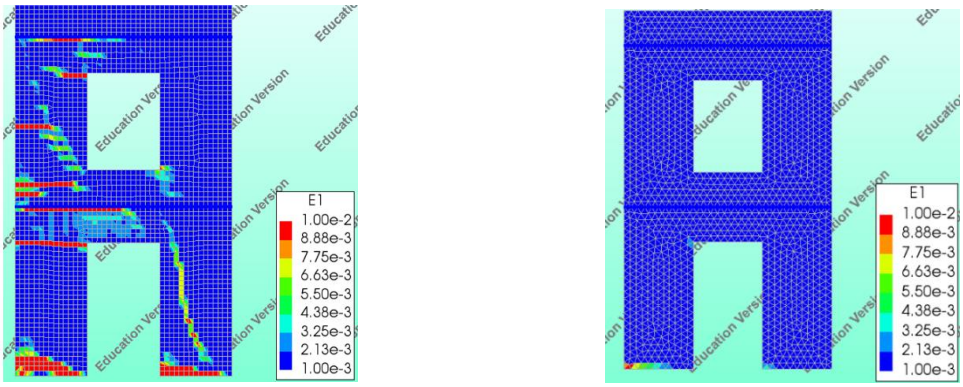

FIGURE 26: SM3-MAXIMUM PRINCIPAL STRAIN (LEFT) AND SM4-MAXIMUM PRINCIPAL STRAIN (RIGHT)

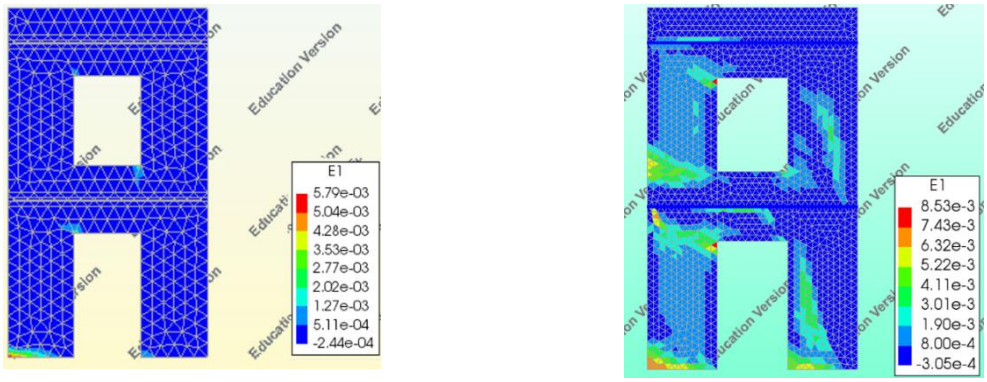

FIGURE 27: SM5-MAXIMUM PRINCIPAL STRAIN (LEFT) AND SM6-MAXIMUM PRINCIPAL STRAIN (RIGHT)

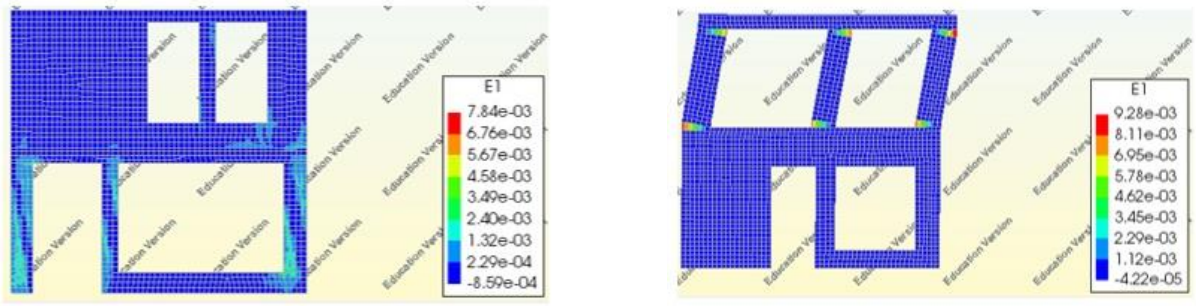

FIGURE 28: CASESTUDY 2D-1A MAXIMUM PRINCIPAL STRAIN (LEFT) AND CASESTUDY 2D-2A-MAXIMUM PRINCIPAL STRAIN (RIGHT)

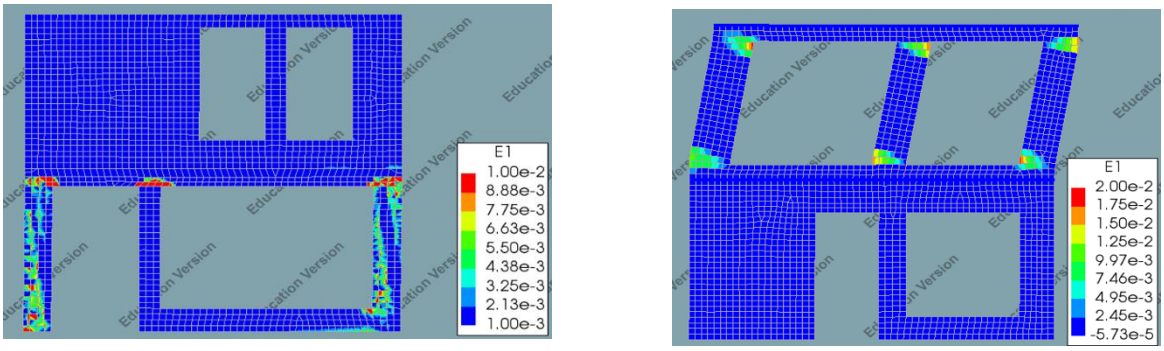

FIGURE 29: CASESTUDY 2D-1B MAXIMUM PRINCIPAL STRAIN (LEFT) AND CASESTUDY 2D-2B-MAXIMUM PRINCIPAL STRAIN (RIGHT)

OBSERVED FAILURE MECHANISM

The observed failure mechanism is determined by analysing the maximum principal strains. The failure mode of each pier of a specific model is described below.

Simple model 1 and simple model 2 display the same failure mechanism. The failure mechanism developed during this pushover assessment is primarily the rocking of pier 1 and pier 3. Since this pushover analysis is applied in only one direction and the wall is symmetric, it could be concluded that also piers 2 and 4 will undergo rocking behaviour in the case of cyclic loading.

Simple model 3 presents the rocking of pier 1 and pier 2, but there is also some shear failure observed for pier 2 and pier 3. The observed shear failure could be the result of a lower cohesion compared with SM1 and SM2.

The failure mechanism occurring in simple model 4 is rocking of the piers at the ground level. No specific failure occurred at piers 3 and 4. The difference in failure mechanism with SM1 could be explained by the difference in the compression fracture energy, which is an important property of the rocking failure mode.

The model with the reinforced concrete floor (SM5) reveals rocking failure of piers 1 and 2. The analysis stopped soon after the divergence of the numerical solving method began. Therefore, it could not be concluded whether piers 3 and 4 will also fail due to rocking.

The failure mechanism developed during this pushover assessment of SM6 is a combination of rocking and shear failure of all the piers. There is clear influence of the tensile strength and tensile fracture energy on the failure type that occurs during the pushover assessment.

Both case study models reveal realistic failure mechanisms occurring at a specific floor:

- CASE STUDY-2D-1A: The failure mechanism that develops during this pushover assessment is the rocking of the piers at the first floor.
- CASE STUDY-2D-1B: The failure mechanism that develops during this pushover assessment is the rocking of piers 7 and 9.
- CASE STUDY-2D-2A/2B: The failure mechanism that develops during this pushover assessment is the rocking of the piers at the second floor.

PUSHOVER CURVES

The graph below shows the pushover curve that is obtained from the results of the analysis in DIANA.

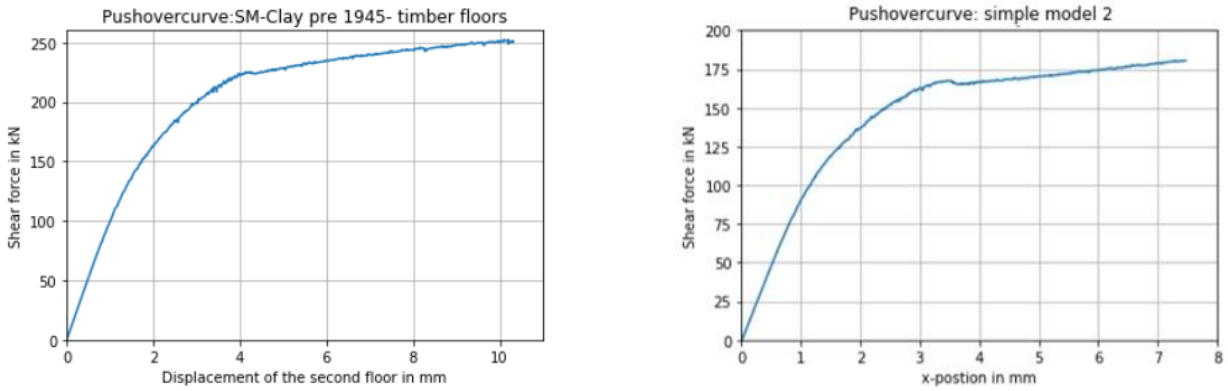

FIGURE 30: PUSHOVER CURVE SM1 AND SM2 *LEFT TO RIGHT*

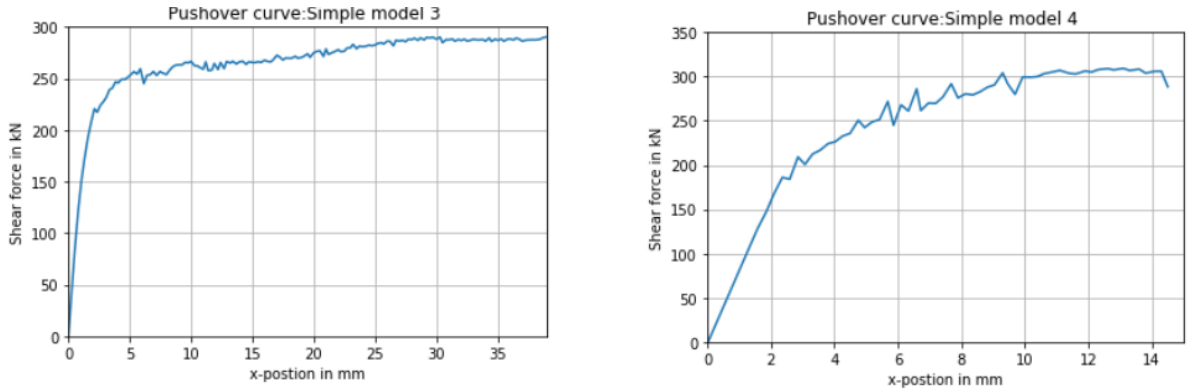

FIGURE 31: PUSHOVER CURVE SM3 AND SM4 *LEFT TO RIGHT*

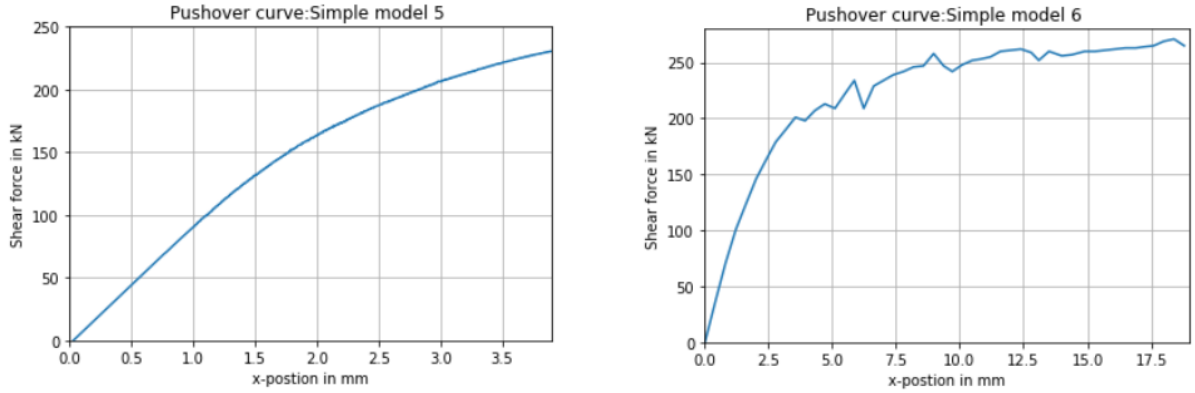

FIGURE 32: PUSHOVER CURVE SM5 AND SM6 *LEFT TO RIGHT*

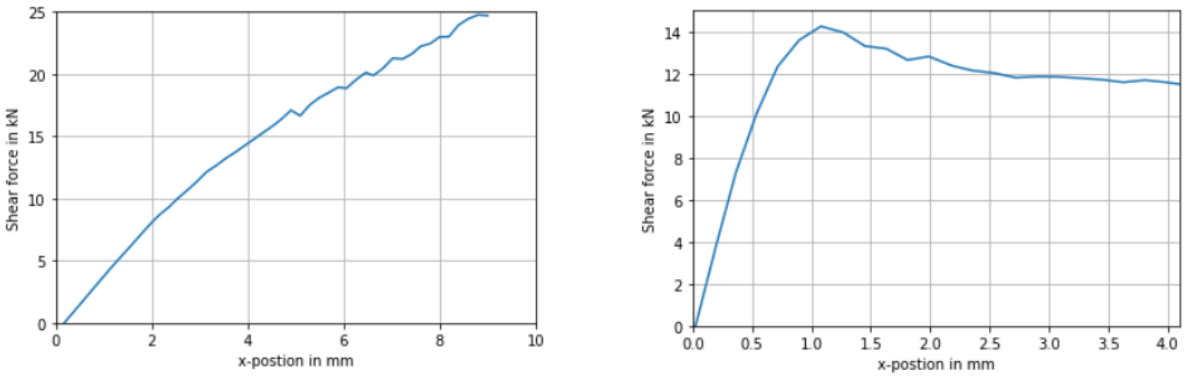

FIGURE 33: PUSHOVER CURVE CASE STUDY 2D-1A, CASESTUDY 2D-2A, *LEFT TO RIGHT*

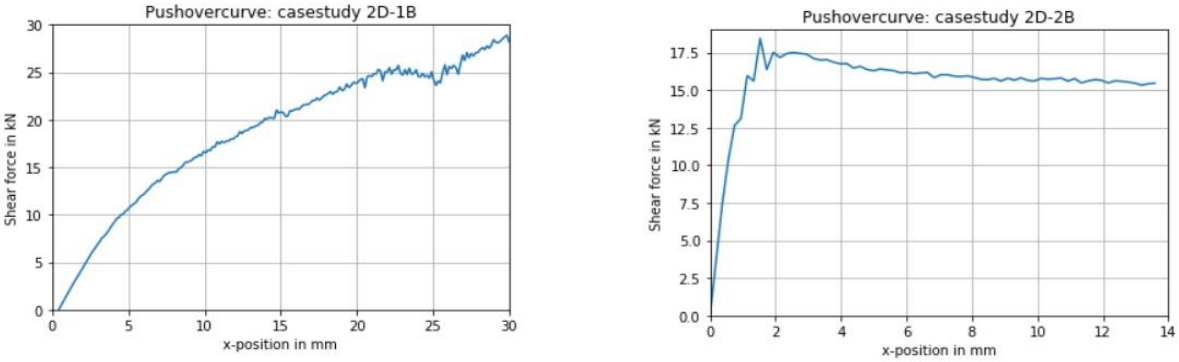

FIGURE 34: PUSHOVER CURVE CASE STUDY 2D-1B, CASESTUDY 2D-2B, *LEFT TO RIGHT*

5.2 SLaMA RESULTS

This section contains the results of the SLaMA calculation for all the analysed models. The full SLaMA calculation can be found in the appendix. Only the acceleration curves, predicted failure mechanisms and maximum base shear are presented in this chapter.

5.2.1 ACCELERATION CURVES

The graphs below show the acceleration curves that are obtained from the SLaMA calculations.

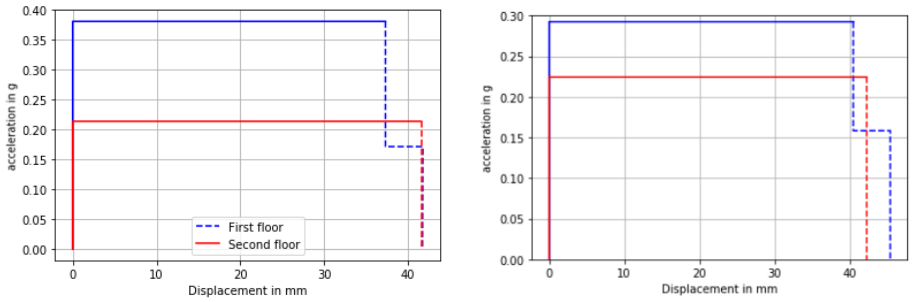

FIGURE 35: ACCELERATION CURVES SM1,SM2 *LEFT TO RIGHT*

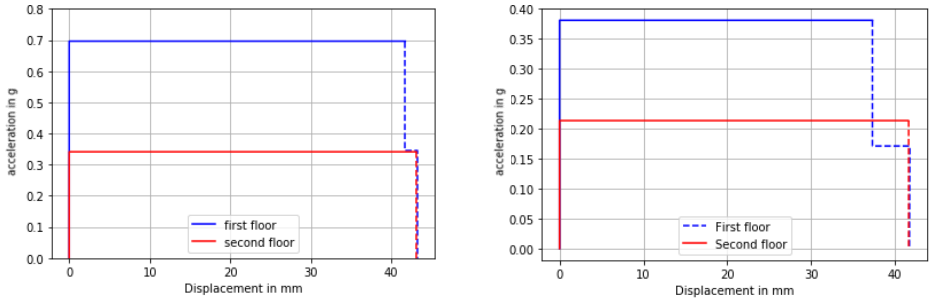

FIGURE 36: ACCELERATION CURVES SM3,SM4 *LEFT TO RIGHT*

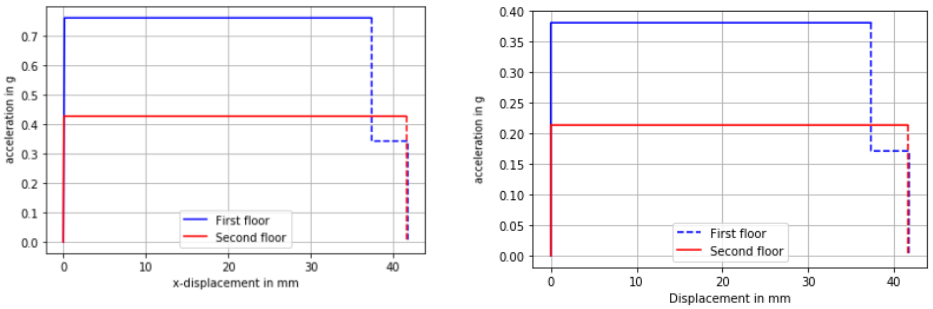

FIGURE 37: ACCELERATION CURVES SM5,SM6 *LEFT TO RIGHT*

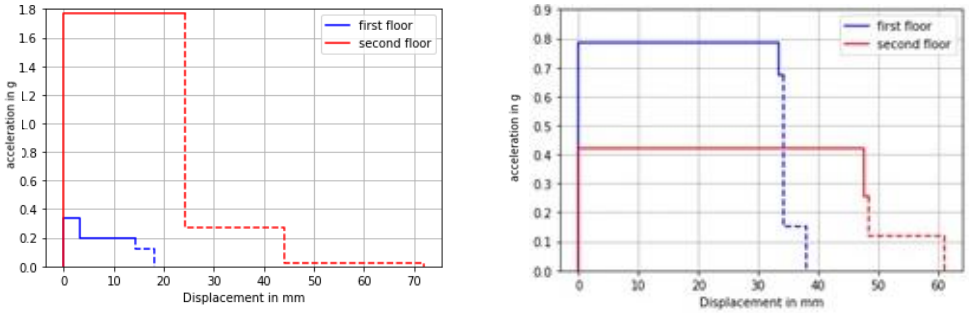

FIGURE 38: ACCELERATION CURVES CASE STUDY 2D-1A, CASESTUDY 2D-2A, *LEFT TO RIGHT*

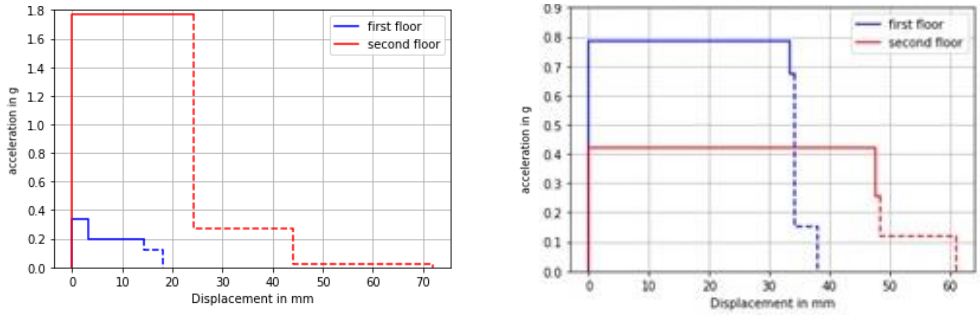

FIGURE 39: ACCELERATION CURVES CASE STUDY 2D-1B, CASESTUDY 2D-2B, *LEFT TO RIGHT*

5.2.2 MAXIMUM BASE SHEAR FORCE AND PREDICTED FAILURE MECHANISM

The table below shows the maximum base shear force and the predicted failure mechanisms determined with the SLaMA method.

TABLE 6: MAXIMUM BASE SHEAR FORCE AND PREDICTED FAILURE MECHANISMS

Model	Maximum base shear force	Predicted failure mechanisms
SM1	76.35 kN	Rocking of the piers at the second floor.
SM2	53.39 kN	Rocking of the piers at the second floor.
SM3	122.0 kN	Rocking of the piers at the second floor.
SM4	76.70 kN	Rocking of the piers at the second floor.
SM5	152.70 kN	Rocking of the piers at the second floor.
SM6	76.35 kN	Rocking of the piers at the second floor.
Case study-2D-1A	8.3 kN	Rocking of the piers at the first floor.
Case study-2D- 2A	9.3 kN	Rocking of the piers at the second floor.
Case study-2D-1B	8.3 kN	Rocking of the pier 7 &9.
Case study-2D- 2B	9.3 kN	Rocking of the piers at the second floor.

5.3 COMPARISON BETWEEN THE SLAMA AND DIANA NLPO FEA RESULTS

This section presents the comparison between the results calculated using the SLaMA method and those using the DIANA NLPO FEA. The ratio is defined as the result of the SLaMA divided by the result of the DIANA NLPO FEA and indicates the difference between both results. The differences between the results of both assessment methods are discussed in Chapter 6: Discussion.

5.3.1 BASE SHEAR FORCE

The results of the 2D assessment phase reveal that the SLaMA method predicts a conservative base shear force compared with the DIANA NLPO FEA. The range of the ratios between the predicted base shear force obtained using the SLaMA method and the base shear force obtained using the DIANA NLPO FEA varies from 0.26 to 0.78; these ratios are presented in the table below. Different reasons could be used to explain the difference in the base shear forces predicted by both methods. The main reasons for these conservative results are the redistribution of the axial load and the determination of the boundary conditions of the piers. Both reasons are explained in detail in Chapter 6: Discussion.

TABLE 7: COMPARISON MAXIMUM BASE SHEAR FORCE

Model	SLaMA	DIANA NLPO FEA	Ratio
SM1	76.35 kN	250 kN	0.31
SM2	53.39 kN	175 kN	0.31
SM3	122.0 kN	288 kN	0.42
SM4	76.70 kN	300 kN	0.26
SM5	152.70 kN	230 kN	0.66
SM6	76.35 kN	250 kN	0.31
Case study-2D-1A	8.3 kN	25 kN	0.33
Case study- 2D-2A	9.3 kN	12 kN	0.78
Case study-2D-1B	8.3 kN	27 kN	0.31
Case study- 2D-2B	9.3 kN	15.5 kN	0.63

There are differences in the ratios between the analysed models. A large difference exists between the ratios of SM5 (simple model with RC concrete floors) and SM1 (simple model with timber floors). The primary reason is the difference of the assumed boundary conditions in the SLaMA calculations. This point is further elaborated in the discussion chapter.

The amount of loading, presence of lintels and the masonry type do not significantly influence the ratios. Small differences in the ratio could be explained by the sensitivity of the different material properties in both analyses. Cohesion, compressive fracture energy and compressive strength are properties which yield the small difference in the ratios of the models with different masonry types.

The ratios of case study-2D-1A/B are less conservative compared with those of case study-2D-2A/B. A possible reason could the difference in the participating masses assumed in the SLaMA and the NLPO FEM analysis for the case study-2D-1A/B.

5.3.2 PREDICTED FAILURE MECHANISM

The table below displays the comparison between the predicted failure mechanism with the assessment methods. This comparison in divided into the type of failure mechanism and the position of the failure. The predicted failure mechanism with the SLaMA method, in most cases, differs from the failure mechanisms predicted by the NLPO FEM analysis. In all cases, the type of failure is correctly predicted, but the location of the failure differs in some cases, especially when the NLPO FFEM analysis predicts failure at different storeys. The SLaMA method is able to predict failure at only one specific floor. Another reason is that the SLaMA method predicts only one type of failure, while the DIANA NLPO FE analysis can predict a combination of failure mechanisms. This could occur due to the redistributions of the axial forces, resulting in a different failure type in the latter stage of the pushover analysis. Both reasons and possible solutions are further explained in Chapter 6: Discussion.

TABLE 8: COMPARISON PREDICTED FAILURE MECHANISMS

Model	SLaMA	DIANA NLPO FEA	Comparison-type failure	Comparison-location of the failure
SM1	Rocking of the piers at the second floor.	Rocking of all the piers.	Good agreement	Poor agreement
SM2	Rocking of the piers at the second floor.	Rocking of all the piers.	Good agreement	Poor agreement
SM3	Rocking of the piers at the second floor.	Rocking of all the piers. Shear failure of pier 2 and 3.	Poor agreement	Poor agreement
SM4	Rocking of the piers at the second floor.	Rocking of the piers at the first floor.	Good agreement	Poor agreement
SM5	Rocking of the piers at the second floor.	Rocking of the piers at the first floor.	Good agreement	Poor agreement
SM6	Rocking of the piers at the second floor.	Rocking and shear failure of all the piers.	Poor agreement	Poor agreement
Case study-2D- 1A	Rocking of the piers at the first floor.	Rocking of the piers at the first floor.	Good agreement	Good agreement
Case study-2D- 2A	Rocking of the piers at the second floor.	Rocking of the piers at the second floor.	Good agreement	Good agreement
Case study-2D- 1B	Rocking of the pier 7 &9.	Rocking of the piers at the first floor.	Good agreement	Poor agreement
Case study-2D- 2B	Rocking of the piers at the second floor.	Rocking of the piers at the second floor.	Good agreement	Good agreement

5.3.3 DISPLACEMENT CAPACITY

The table below presents the displacement capacities computed using the SLaMA method and the ultimate displacement obtained from the Daina FEM analysis. It must be mentioned that the ultimate displacements obtained from the DIANA FE analysis are, for all the models, dependent on the convergence behaviour of the analysis. All these analyses stopped due to the divergence of the numerical solving method. No indication is offered that this divergence is the result of the collapse of the structure, which causes the displacement capacities to be incomparable with each other.

TABLE 9: COMPARISON DISPLACEMENT CAPACITY

Model	SLaMA	DIANA NLPO FEA
SM1	41 mm	10 mm
SM2	41 mm	7 mm
SM3	41 mm	35 mm
SM4	38 mm	31 mm
SM5	38 mm	4 mm
SM6	38 mm	19 mm
Case study-2D-1A	12 mm	9 mm
Case study-2D-2A	46 mm	4 mm
Case study-2D-1B	12 mm	30 mm
Case study-2D-2B	46 mm	14 mm

6 RESULTS OF THE 3D ANALYSES

6.1 3D NLPO FEA (DIANA) RESULTS

Two models were analysed, and the only property in which these models differed was the floor type. This allows the influence of the floors to be properly investigated. Foremost, it investigates differences in the governing eigenmode and the related participating mass. This analysis primarily considers the normative eigenmode in the y-direction, after which the maximum principal strain at the different loading steps is examined. With these results, the occurring failure mechanism can be determined. In addition, the pushover curve obtained from this analysis is studied, and the displacement capacity and maximum base shear force are determined from this pushover curve. Each model is modeled three times with various material models. This chapter presents only the results relevant to answering the research questions. These results are obtained from the last loading step when the numerical solving method was still converging. See the appendix for the extended version of the results.

6.1.1 RESULTS: STRUCTURAL EIGENVALUE ANALYSIS-3D-MODEL-DOUBLE RC-FLOORS

The first model consists of reinforced concrete floors for both levels. Initially, this model was analysed with the structural eigenvalue analysis. The results were analysed, and the governing eigenmode in the y-direction was determined based on the participating masses. The Figure below displays the governing eigenmode of this structure. This eigenmode is similar for all three engineering masonry model options.

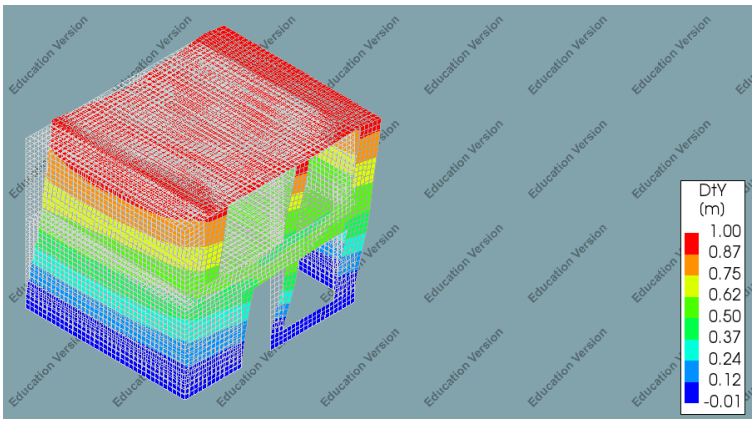

FIGURE 40: EIGENMODE 1, 84% PARTICIPATING MASS

6.1.2 RESULTS: STRUCTURAL NONLINEAR ANALYSIS-3D-MODEL-DOUBLE RC-FLOORS

In the next phase of this assessment, the structure was analysed with the model pushover analysis in the direction of the governing eigenmode. The results below present only the last step of this analysis. These results consist of the displacement, maximum principal strain and the pushover curve. To view all the extracted results, see appendix.

DISPLACEMENT

The Figures below present the displacement in the y-direction of model-3D-double RC floors-DS (left), model model-3D-double RC floors -HJ (middle) and model- model-3D-double RC floors -Direct(right). These are the displacement profiles of the last loading step when the analysis was still converging. These results reveal the displacement capacities of the unreinforced masonry building.

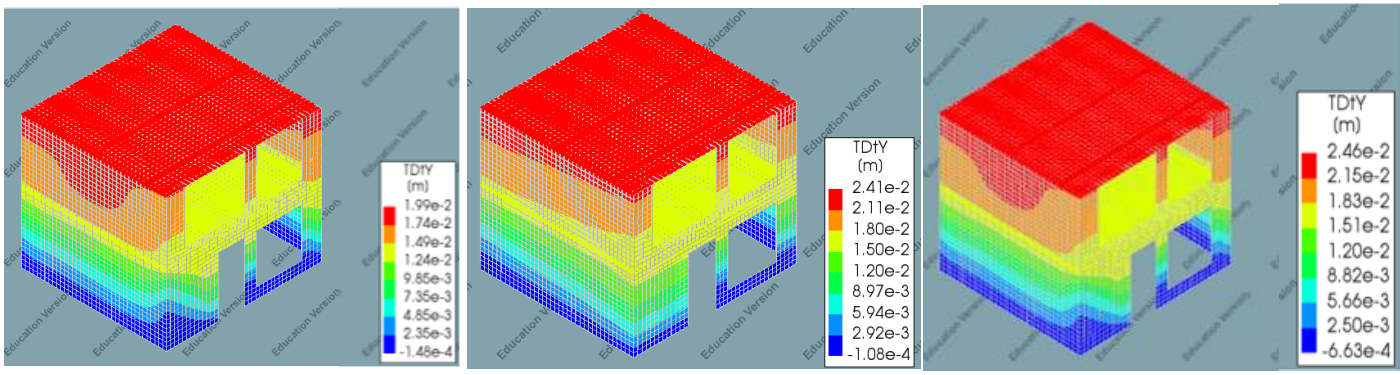

FIGURE 41: DISPLACEMENT IN THE Y-DIRECTION OF MODEL-3D-DOUBLE RC FLOORS-DS (LEFT), MODEL MODEL-3D-DOUBLE RC FLOORS -HJ (MIDDLE) AND MODEL- MODEL-3D-DOUBLE RC FLOORS -DIRECT(RIGHT).

MAXIMUM PRINCIPAL STRAINS

The Figures below display the results of the maximum principal strain of the last step of the analysis when convergence was still occurring. The maximum principal strain provides good insight into the crack pattern that would occur during a similar loading. Therefore, the local failure mechanisms could be observed from these results. The left Figures display the results of the analysis of model-3D-double RC floors -DS, the middle Figures display the results of model-3D-double RC floors -HJ and the right Figures display the results of model- model-3D-double RC floors-Direct. The Figures below do not clearly present the principal stain pattern occurring at the concrete slab, due to the chosen scale of the contour plot used to present these results. The floors were analysed, and the occurring strains, cracks and damages were not significantly high compared with in the masonry walls.

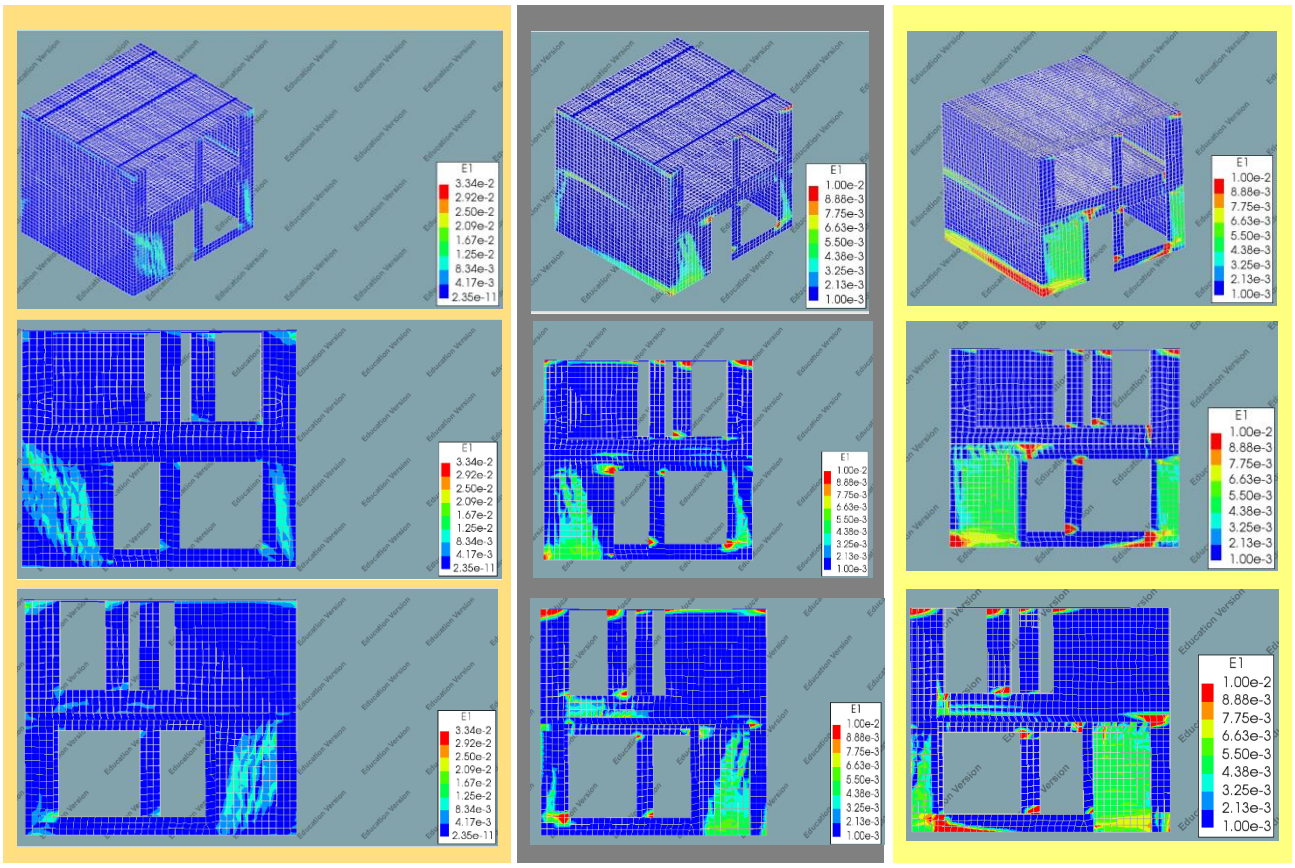

FIGURE 42: MODEL-3D-DOUBLE RC FLOORS-DS-OPTION (LEFT), MODEL-3D-DOUBLE RC FLOORS-HJ-OPTION (MIDDLE), MODEL-3D-DOUBLE RC FLOORS- DIRECT-OPTION (RIGHT)

PUSHOVER CURVE

The Figure below displays the pushover curves of 3D-Model-double RC floors-DS(left), 3D-Model-double RC floors-HJ(middle) and 3D-Model-double RC floors -Direct (right). At the last loading, divergence occurred, which is why this loading step is not included in the pushover curve. The pushover curves present both the displacement capacity and the maximum base shear force.

.

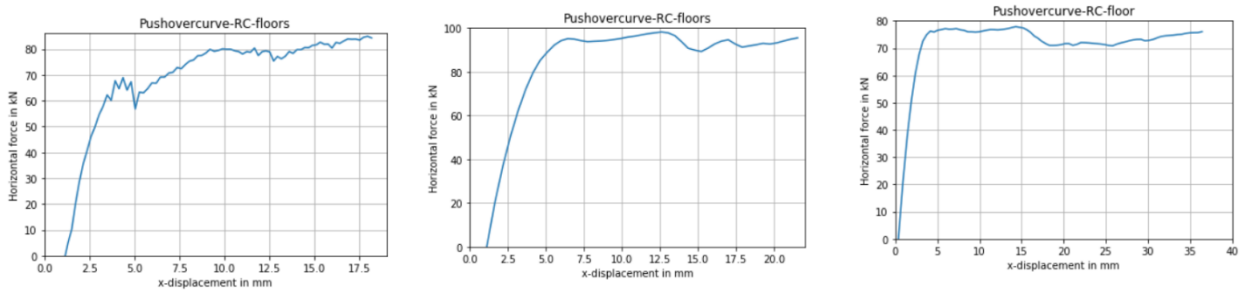

FIGURE 43: PUSHOVER CURVE 3D-MODEL-DOUBLE RC- DS,HJ &DIRECT LEFT TO RIGHT

6.1.3 SUMMARIZED RESULTS-3D-MODEL-DOUBLE RC-FLOORS

The tables below show the summarized results (predicted failure mechanisms, base shear force and the displacement capacity) of all the NLPO FE analyses.

TABLE 10: PREDICTED FAILURE MECHANISM

Model	Pier no.	Predicted failure mechanism
3D-Model-double RC floors-DS	Pier 1	Shear failure
	Pier 2	Rocking failure
	Pier 3	Shear failure
	Pier 4	No failure
	Pier 5	No failure
	Pier 6	No failure
	Pier 7	No failure
	Pier 8	No failure
	Pier 9	Rocking failure
	Pier 10	No failure
	Pier 11	Rocking failure
	Pier 12	Rocking failure
3D-Model-double RC floors-HJ	Pier 1	Shear failure
	Pier 2	Rocking failure
	Pier 3	Shear failure
	Pier 4	No failure
	Pier 5	Rocking failure
	Pier 6	Rocking failure
	Pier 7	Rocking failure
	Pier 8	No failure
	Pier 9	Rocking/shear failure
	Pier 10	No failure
	Pier 11	Rocking failure
	Pier 12	Rocking failure
3D-Model-double RC floors-Direct	Pier 1	Rocking/shear failure
	Pier 2	Rocking failure
	Pier 3	Rocking/shear failure
	Pier 4	No failure
	Pier 5	Rocking failure
	Pier 6	Rocking failure
	Pier 7	Rocking failure
	Pier 8	Rocking failure
	Pier 9	Rocking/shear failure
	Pier 10	No failure
	Pier 11	Rocking failure
	Pier 12	Rocking failure

Model	Maximum base shear force	Displacement capacity
3D-Model-double RC floors- DS	81 kN	19.9 mm
3D-Model-double RC floors- HJ	90 kN	24.1 mm
3D-Model-double RC floors- Direct	76 kN	36.4 mm

6.1.4 RESULTS: STRUCTURAL EIGENVALUE ANALYSIS-3D-MODEL-DOUBLE TIMBER FLOORS

The next model differs in one specific aspect, namely the floor type. This model consists of two timber floors rather than reinforced concrete floors. This model was analysed with three different engineering masonry models with the DS-option, HJ-option and Direct-option. The timber floor consists of timber beams and timber planks. The timber planks are modelled as one regular curved shell sheet. This sheet has orthotropic timber properties, recommended by the NPR9998. The planks are rigidly connected to the timber beams, which are again rigidly connected to the face-loaded walls. The Figure below presents the governing eigenmode in the y-direction and the participating mass resulting from the structural eigenvalue analysis.

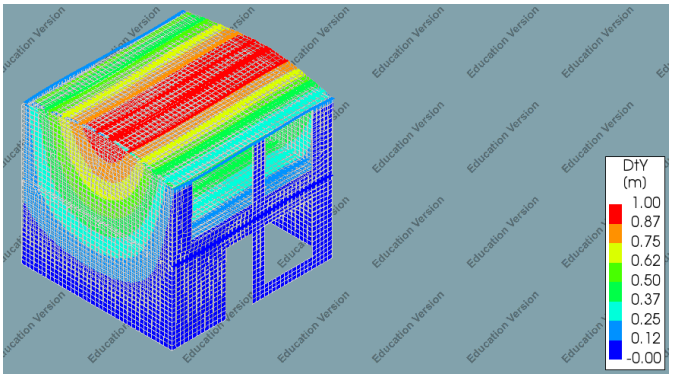

FIGURE 44: EIGENMODE 3D-MODEL-DOUBLE TIMBER FLOORS, 54% PART. MASS

6.1.5 RESULTS: STRUCTURAL NONLINEAR ANALYSIS-3D-MODEL-DOUBLE TIMBER FLOORS DISPLACEMENT

The Figures below present the displacement in y-direction of 3D-Model-double timber floors -DS (left), 3D-Model-double timber floors -HJ (middle) and Model-double timber floors -Direct (right). These are the displacement profiles of the last step when the analysis was still converging. These results reveal the displacement capacities of the unreinforced masonry building. There is a significant difference between the ultimate displacement reached in the two analyses.

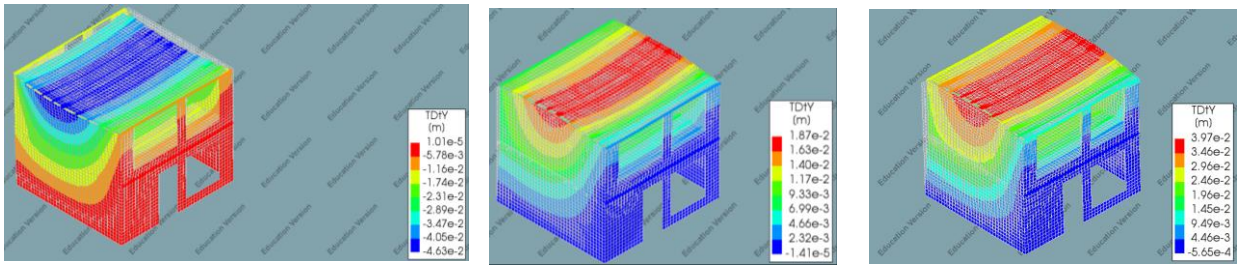

FIGURE 45: 3D-MODEL-DOUBLE TIMBER FLOORS-DS(LEFT), 3D-MODEL-DOUBLE TIMBER FLOORS-HJ (MIDDLE), 3D-MODEL-DOUBLE TIMBER FLOORS-DIRECT (RIGHT)

MAXIMUM PRINCIPAL STRAIN

The Figures below present the results of the maximum principal strain of the last step of the analysis when convergence was still occurring. The maximum principal strain provides good insight into the crack pattern that would occur during a similar loading. Therefore, the local failure mechanisms could be observed from these results. The results reveal significantly high strains of and damages to the timber floors. These high strains of the floors are misleading and not realistic; they are the result of the reduced stiffness, which results in a higher deformation due to the gravity loading of the planks. A possible modelling solution could be to assign zero density to the timber planks and apply a loading to the timber beams that is similar to the weight of the planks. In doing so, the reduced stiffness of the planks would not influence the strains and damages at the floors. The left Figures display the results of the analysis of 3D-model-double timber floors -DS, the middle Figure displays the results of 3D-model-double timber floors -HJ and the right Figures display the results of 3D-model-double timber floors -Direct.

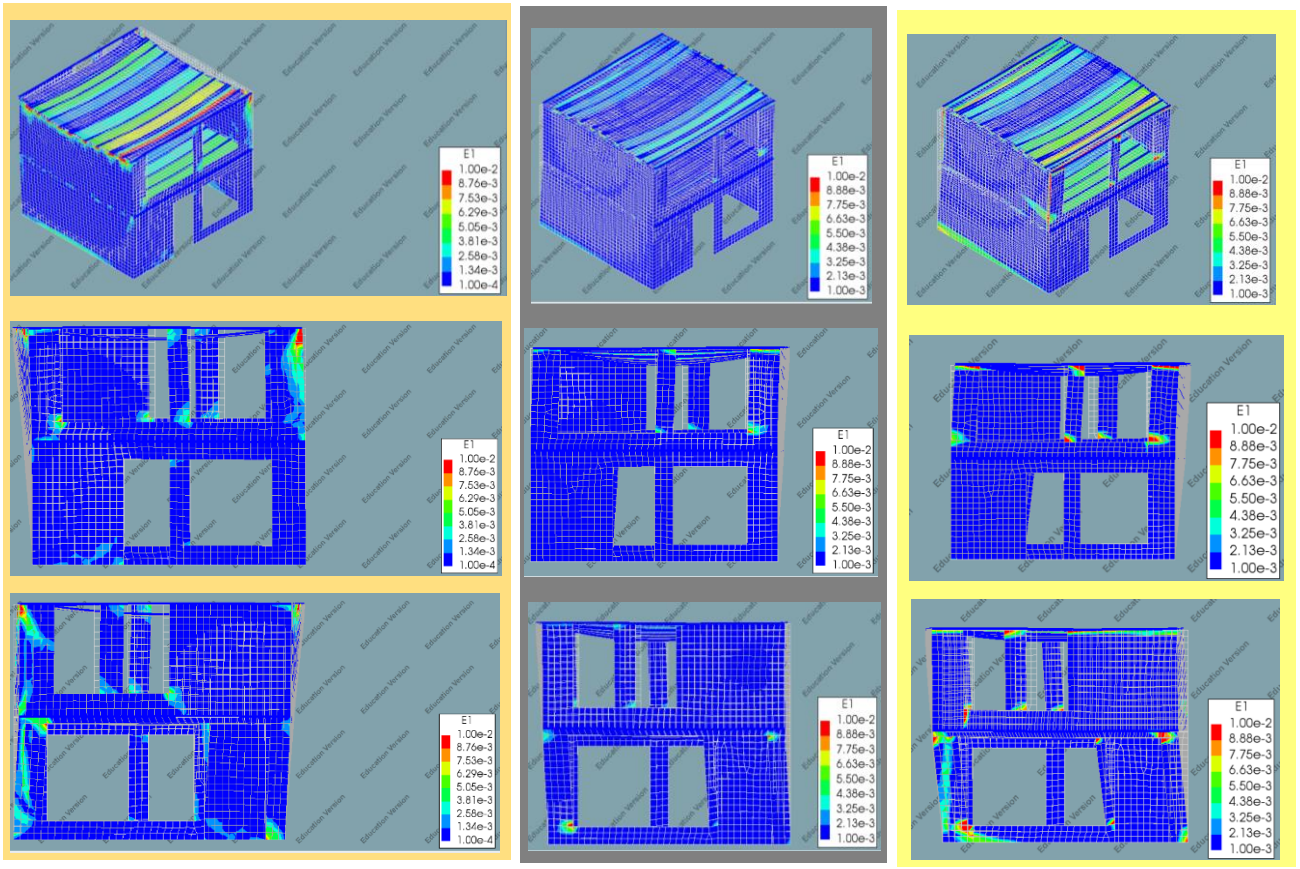

FIGURE 46: 3D-MODEL-DOUBLE TIMBER FLOORS -DS (LEFT), 3D-MODEL-DOUBLE TIMBER FLOORS-HJ(MIDDLE), 3D-MODEL-DOUBLE TIMBER FLOORS-DIRECT (RIGHT)

PUSHOVER CURVE

The Figure below show the pushover curves of 3D-Model-double timber floors-DS(left), 3D-Model-double timber floors -HJ(middle) and 3D-Model-double timber floors -Direct (right). At the last loading divergence occurred, and that is the reason that this loading step is not included in the pushover curve. The pushover curves show both the displacement capacity and the maximum base shear force.

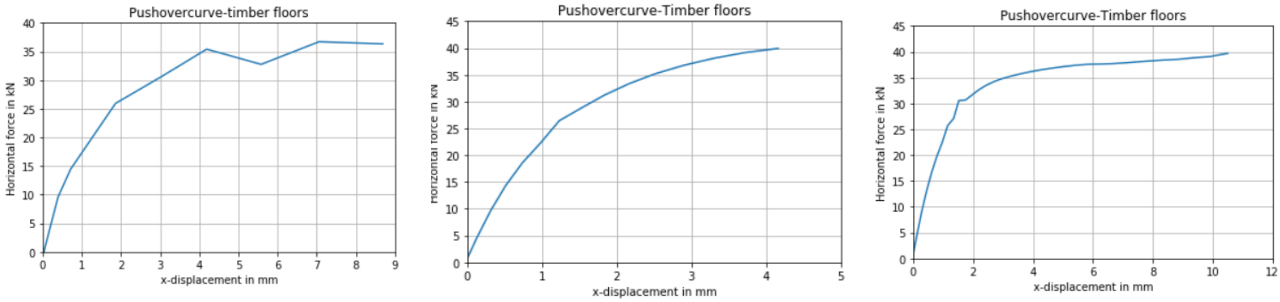

FIGURE 47: PUSHOVER CURVE 3D-MODEL-DOUBLE TIMBER FLOORS -DS, HJ, DIRECT LEFT TO RIGHT

6.1.6 SUMMARIZED RESULTS-3D-MODEL-DOUBLE TIMBER FLOORS

The table below shows the summarized results (predicted failure mechanisms, base shear force and the displacement capacity) of all the NLPO FE analyses.

TABLE 11: SUMMURIZED RESULTS OF 3D-MODEL-DOUBLE TIMBER FLOORS

Model	Pier no.	Predicted failure mechanism
3D-Model-double timber floors - DS	Pier 1	No failure
	Pier 2	No failure
	Pier 3	No failure
	Pier 4	Rocking failure
	Pier 5	Rocking failure
	Pier 6	Rocking failure
	Pier 7	Rocking failure
	Pier 8	Rocking failure
	Pier 9	Rocking/shear failure
	Pier 10	No failure
	Pier 11	Rocking failure
	Pier 12	Shear failure
3D-Model-double timber floors -HJ	Pier 1	No failure
	Pier 2	No failure
	Pier 3	No failure
	Pier 4	No failure
	Pier 5	Rocking failure
	Pier 6	Rocking failure
	Pier 7	Rocking failure
	Pier 8	No failure
	Pier 9	Rocking failure
	Pier 10	No failure
	Pier 11	Rocking failure
	Pier 12	Rocking failure

3D-Model-double timber floors - Direct	Pier 1	No failure
	Pier 2	No failure
	Pier 3	No failure
	Pier 4	Rocking failure
	Pier 5	Rocking failure
	Pier 6	Rocking failure
	Pier 7	Rocking failure
	Pier 8	Rocking failure
	Pier 9	Rocking/shear failure
	Pier 10	No failure
	Pier 11	Rocking failure
	Pier 12	No failure

Model	Maximum base shear force	Displacement capacity
3D-Model-double timber floors - DS	35 kN	8.5 mm
3D-Model-double timber floors -HJ	40 kN	4.2 mm
3D-Model-double timber floors - Direct	39 kN	10.5 mm

6.2 3D SLaMA RESULTS

This section provides an overview of the results of the SLaMA calculation for both unreinforced masonry buildings that were analysed in the DIANA NLPO FE assessment. The SLaMA approach followed in this assessment is similar to the approach used in the 2D assessment phase. The effective heights of the piers were determined based on the effective height approach used by Moon (Moon F. Y., 2006). The axial force at the top of the piers is extracted from FEM results after applying the self-weight on the structure. Therefore, the starting point of both assessment methods is equal. The flange contribution was considered in both SLaMA calculations in the manner that Moon proposed. Chapter 4: Literature study explains the effective height approach and the way in which the flange contribution is considered in the SLaMA calculation. This chapter provides an overview of the most important results of the SLaMA method. See the appendix for a more extensive representation of these results.

PUSHOVER CURVES AND THE MAXIMUM BASE SHEAR FORCE

The Figures below display the pushover curves and the acceleration curves of both unreinforced masonry buildings. The left Figures present the results of the unreinforced masonry building with the concrete reinforced floors, while the right Figures present the results of the unreinforced masonry building with the timber floors. The pushover curve is determined for each specific floor and is translated to the acceleration curve by dividing the pushover curve by the effective contributing masses.

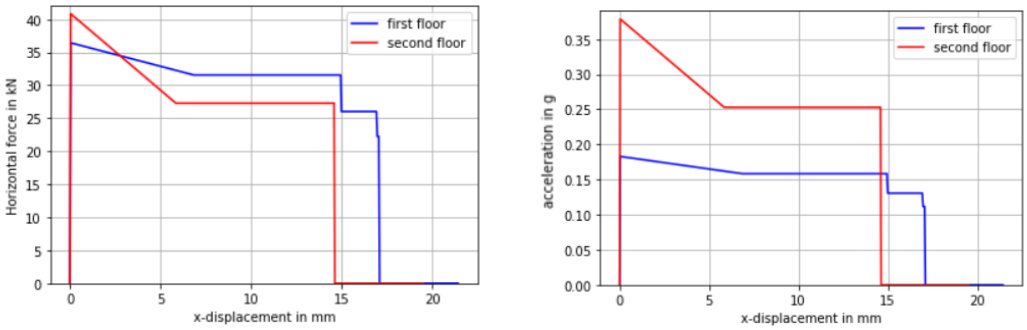

FIGURE 49: PUSHOVER CURVE 3D-MODEL-DOUBLE RC FLOORS (LEFT) AND THE ACCELERATION CURVE 3D-MODEL-DOUBLE RC-FLOORS (RIGHT)

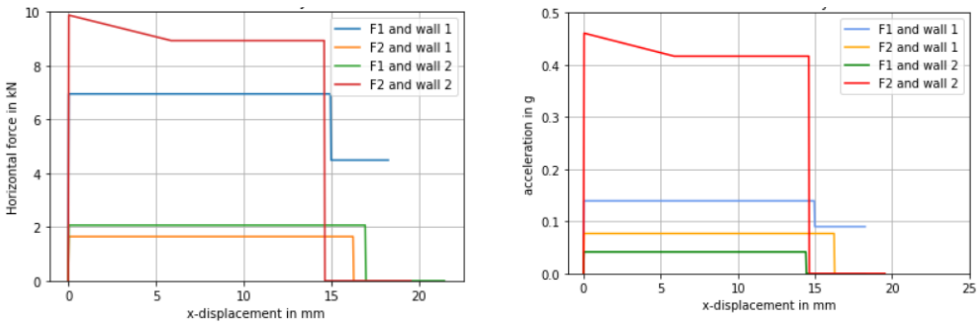

FIGURE 48: PUSHOVER CURVE 3D-MODEL-DOUBLE TIMBER FLOORS (LEFT) AND THE ACCELERATION CURVE 3D-MODEL-DOUBLE TIMBER-FLOORS (RIGHT)

PREDICTED FAILURE MECHANISM AND THE MAXIMUM BASE SHEAR

The critical acceleration of the total structure corresponds to the acceleration of the first floor of both unreinforced masonry buildings. Therefore, the piers at the first level undergo failure. The specific failure type for each pier is listed in the table below. The maximum base shear force is determined based on the critical acceleration of the first floor and the corresponding effective mass. The table below displays the maximum base shear force of each unreinforced masonry building. The displacement capacity predicted by the SLaMA method is determined based on the 50% shear capacity drop of the piers and is presented in the table below.

TABLE 12: PREDICTED FAILURE MECHANISM

Model	Pier no.	Level	Predicted failure mechanism
3D-Model-double RC-floors	Pier 1	1	Shear failure
	Pier 2	1	Rocking failure
	Pier 3	1	Rocking failure
	Pier 4	2	No failure
	Pier 5	2	No failure
	Pier 6	2	No failure
	Pier 7	1	Rocking failure
	Pier 8	1	Rocking failure
	Pier 9	1	Rocking failure
	Pier 10	2	No failure
	Pier 11	2	No failure
	Pier 12	2	No failure
3D-Model-double timber floors	Pier 1	1	No failure
	Pier 2	1	No failure
	Pier 3	1	No failure
	Pier 4	2	Rocking failure
	Pier 5	2	Rocking failure
	Pier 6	2	Rocking failure
	Pier 7	1	Rocking failure
	Pier 8	1	Rocking failure
	Pier 9	1	Rocking failure
	Pier 10	2	No failure
	Pier 11	2	No failure
	Pier 12	2	No failure

TABLE 13: MAXIMUM BASE SHEAR FORCE AND THE DISPLACEMENT CAPACITY

Model	Maximum base shear force	Displacement capacity
3D-Model-double RC-floors	36 kN	15 mm
3D-Model-double timber floors	5.9 kN	14.6 mm

6.3 COMPARISON BETWEEN THE SLAMA AND NLPO FEA RESULTS

This section further explores the comparison between the SLaMA results and the DIANA NLPO FEA results. The predicted failure mechanism, base shear force and displacement capacity are the specific results that are compared. The DIANA NLPO FEA was performed using three different material models. These analyses are compared in this chapter.

PREDICTED FAILURE MECHANISM

The predicted failure mechanisms resulting from the two assessment methods are listed in the table below. The obtained failure mechanism was specified for each pier. The global failure mechanism predicted using the SLaMA method of the URM building with the RC floors is the failure of the piers at the first floor. Pier 1 will undergo shear failure, while the other piers at the first floor will fail due to rocking. The results of the unreinforced masonry building with RC floors reveal a similar failure mechanism predicted by the NLPO FEM analysis for piers 1, 2, 4, 7, 8 and 10. The difference in the predicted failure mechanisms could be explained with the same reasoning as mentioned in the 2D results.

TABLE 14: COMPARISON PREDICTED FAILURE MECHANISM

Model	Pier	Level	Predicted failure mechanism- SLaMA	Predicted failure mechanism FEM- HJ	Predicted failure mechanism FEM- DS	Predicted failure mechanism FEM-Direct
3D-Model - double RC-floors	Pier 1	1	Shear failure	Shear failure	Shear failure	Rocking/shear failure
	Pier 2	1	Rocking failure	Rocking failure	Rocking failure	Rocking failure
	Pier 3	1	Rocking failure	Shear failure	Shear failure	Rocking/shear failure
	Pier 4	2	No failure	No failure	No failure	No failure
	Pier 5	2	No failure	Rocking failure	No failure	Rocking failure
	Pier 6	2	No failure	Rocking failure	No failure	Rocking failure
	Pier 7	1	Rocking failure	Rocking failure	No failure	Rocking failure
	Pier 8	1	Rocking failure	No failure	No failure	Rocking failure
	Pier 9	1	Rocking failure	Rocking/shear failure	Rocking failure	Rocking/shear failure
	Pier 10	2	No failure	No failure	No failure	No failure
	Pier 11	2	No failure	Rocking failure	Rocking failure	Rocking failure
	Pier 12	2	No failure	Rocking failure	Rocking failure	Rocking failure

The table below provides an overview of the predicted failure mechanism of each pier in the URM buildings with timber floors. The SLaMA method predicted the rocking failure of pier 4 to pier 9. The maximum principal strains resulting from the NLPO FEM analysis reveal similar results for the failure at pier 1 to pier 8 and pier 10.

The NLPO FEM analysis predicts a combination of shear and rocking failure at pier 9, while the SLaMA method predicts rocking failure for this specific pier. The combination of shear and rocking failure could be explained by the redistribution of the axial force or the use of the material model. Predicting shear failure for a slender pier appears to be a limitation of the applied material model for modeling masonry. The same reasoning could be applied for the shear failure predicted at slender pier 12. The explanations are further elaborated upon in the following chapter (Discussion).

TABLE 15: COMPARISON PREDICTED FAILURE MECHANISM

Model	Pier	Level	Predicted failure mechanism- SLaMA	Predicted failure mechanism FEM- HJ	Predicted failure mechanism FEM- DS	Predicted failure mechanism FEM- Direct
3D-Model-double timber floors	Pier 1	1	No failure	No failure	No failure	No failure
	Pier 2	1	No failure	No failure	No failure	No failure
	Pier 3	1	No failure	No failure	No failure	No failure
	Pier 4	2	Rocking failure	No failure	Rocking failure	Rocking failure
	Pier 5	2	Rocking failure	Rocking failure	Rocking failure	Rocking failure
	Pier 6	2	Rocking failure	Rocking failure	Rocking failure	Rocking failure
	Pier 7	1	Rocking failure	Rocking failure	Rocking failure	Rocking failure
	Pier 8	1	Rocking failure	No failure	Rocking failure	Rocking failure
	Pier 9	1	Rocking failure	Rocking failure	Rocking/shear failure	Rocking/shear failure
	Pier 10	2	No failure	No failure	No failure	No failure
	Pier 11	2	No failure	Rocking failure	Rocking failure	Rocking failure
	Pier 12	2	No failure	Rocking failure	Shear failure	No failure

The table below presents the maximum base shear force predicted by the two assessment methods. The SLaMA method predicts a highly conservative maximum base shear force compared with the DIANA FEM analysis. The SLaMA method for the URM building with the timber floor yields a lower ratio for the difference of the base shear force than does the building with the RC floors. This ratio is defined as the SLaMA results divided by the FEM results.

Therefore, the assumed double-clamped boundary conditions for URM buildings with timber floors appear to be more realistic. The low ratio of the URM buildings with timber floors could be explained by several modelling assumptions applied in the analysed models. Examples include the connection of the out-of-plane wall with the in-plane loaded wall, the beam-wall connections and the beam-plank connections. The effect of these modelling assumptions is explained in the following chapter. Another reason could be the difference in the participating masses calculated in both methods.

TABLE 16: COMPARISON MAXIMUM BASE SHEAR FORCE

Model	Maximum base shear force-SLaMA	Maximum base shear force FEM HJ	Maximum base shear force FEM DS	Maximum base shear force FEM Direct	Ratio
3D-Model-double RC-floors	36 kN	90kN	81kN	76 kN	[0.40-0.47]
3D-Model-double timber floors	5.9 kN	40kN	35kN	39 kN	[0.15-0.17]

The displacement capacities predicted by the assessment methods are listed in the table below. The displacement capacities resulting from the FEM analysis are determined based on the final loading step of the pushover analysis. Therefore, these results could be comparable to the SLaMA results for the ultimate displacement. The results indicate conservative ultimate displacements predicted by the SLaMA method compared with the FEM results when assessing buildings with RC floors. The ultimate displacement reached with the FEM analysis appears to be realistic, as the analysis stopped when a full diagonal crack developed over the height of piers 3 and 9. Therefore, it could be concluded that this analysis stopped due to the physical collapse of the structure. This FEM analysis predicts a displacement capacity of 19.9 mm, while the SLaMA method predicts a displacement capacity of 15 mm. This comparison reveals that the SLaMA method is a conservative method in predicting the displacement capacity for URM buildings with RC floors.

There is no clear indication that the analysed URM building with timber floors predicts realistic displacement capacities compared with the SLaMA displacement capacity. In this case, the ultimate displacement strongly depends on the modelling assumptions of the timber floors. These are similar assumptions, as mentioned above.

TABLE 17: COMPARISON DISPLACEMENT CAPACITY

Model	Displacement capacity - SLaMA	Displacement capacity - FEM HJ	Displacement capacity - FEM DS	Displacement capacity - FEM Direct	Ratio
3D-Model-double RC-floors	15 mm	24 mm	20 mm	36.4 mm	[0.42-0.75]

3D-Model-double timber floors	14.6 mm	4.2 mm	8.5 mm	10.5 mm	[1.40-3.40]

7 DISCUSSION

BASE SHEAR FORCE

The results of both the 2D and 3D assessment phases reveal that the SLaMA method predicts a conservative base shear force compared with the DIANA NLPO FEA. The range of the ratios between the predicted base shear force obtained using the SLaMA method and the base shear force obtained using the DIANA NLPO FEA varies from 0.26 to 0.78. These align with the results presented in the study of Anass el Kouri. Different reasons could be used to explain the difference in the base shear forces predicted by both methods. The main reasons for these conservative results are the changing axial load and the determination of the boundary conditions of the piers.

REDISTRIBUTION AXIAL FORCE

CHANGING AXIAL LOAD AT THE TOP OF THE PIER

The axial force used within the SLaMA method calculations is determined under the static loading condition. In such a case, the load from the self-weight and the loads from the floors are used to calculate the axial loads at the top of the piers.

The pushover analysis within DIANA considers the frame effect, which means that the axial applied force on the piers changes with every step in the analysis. To observe the influence of this effect, all nodal distributed normal forces at the top of the piers were plotted. A polynomial function that fits through these results was determined via polynomial regression. This function was integrated to determine the normal force and the eccentricities of this force.

Table 18 below displays the resultant of the changing distributed normal force of simple model 1 in four steps in the pushover analysis within DIANA. Note that these are the forces at the top of the piers without the self-weight of the piers at the ground floor. The following section presents the axial force at the base of the pier (including self-weight).

The table reveals the resultant compression force due to integrating the compression stresses and the resultant tensile force due to integrating the tensile stresses at the top of the piers. The eccentricities reveal the coordinates at which these forces are concentrated. The origin of the coordinate system is positioned at the lower left corner of pier 1 of simple model 1. This change in the normal distributed forces at the top of the piers is similar for all the simple models.

TABLE 18: CHANGING AXIAL FORCE AT THE TOP OF THE PIERS OF SIMPLE MODEL 1

Pier 1	**Normal force-compression**	**Eccentricity**	**Normal force-tension**	**Eccentricity**
Step 2	-261.4kN	0.74 m	-	-
Step 150	-63.74kN	0.29 m	9.7kN	1.12m
Step 300	-45.6kN	0.086 m	22.0kN	0.83 m
Step 500	-45.1kN	0.063m	30.2kN	0.80 m

Pier 2	**Normal force-compression**	**Eccentricity**	**Normal force-tension**	**Eccentricity**
Step 2	-247.2kN	3.81 m	-	-
Step 150	-318.6 kN	3.84 m	-	-
Step 300	-320.7kN	4.00 m	-	-
Step 500	-305.4kN	4.00 m	-	-

Pier 3	Normal force-compression	Eccentricity	Normal force-tension	Eccentricity
Step 2	-57.9 kN	0.83 m	-	-
Step 150	-50.6kN	0.26 m	24.6kN	1.19 m
Step 300	-52.6 kN	0.10 m	35.9kN	0.93 m
Step 500	-49.4kN	0.08 m	34.2kN	0.92 m

Pier 4	Normal force-compression	Eccentricity	Normal force-tension	Eccentricity
Step 2	-57.9kN	3.67 m	-	-
Step 150	-69.8 kN	3.38 m	8.2kN	4.34 m
Step 300	-64.3 kN	3.35 m	8.7kN	4.26 m
Step 500	-56.3 kN	3.29 m	6.0kN	4.14 m

It is clear that the axial forces on top of piers 1 and 3 decrease in every step of the pushover assessment. Therefore, the shear capacity of the piers likewise decreases in every step. The axial force at the top of pier 2 and pier 4 increases in every step of the analysis. Therefore, the shear capacity of pier 2 and pier 4 needed to increase.

The same approach was used in the first case study-2D-1A. The table below presents the changing distributed normal force at the top of the piers of Case study-1. The appendix provides the plots of the distributed normal forces at the top of each specific pier.

TABLE 19: CHANGING AXIAL FORCE AT THE TOP OF THE PIERS OF CASE STUDY-2D-1A

		Step 2	Step 20	Step 31	Step 44	Shear capacity
Pier 1	**Compression**	-12079 N	-17245 N	-18571 N	-21421 N	Decrease
	Tension	0 N	+13154N	+18760 N	+26332 N	
Pier 2	**Compression**	-15860.8 N	-25680 N	-30085 N	-38121 N	Increase
	Tension	0 N	+5750 N	+9745 N	+16070 N	
Pier 3	**Compression**	-15411 N	-28973.8 N	-33839 N	-40710.5 N	Increase
	Tension	0 N	+12026 N	+17783.3 N	+24840.5 N	
Pier 4	**Compression**	-8623.7 N	-8336.12 N	-8581.7 N	-8421 N	Decrease
	Tension	0 N	+419.01 N	+840.9 N	1054.2 N	
Pier 5	**Compression**	-2435.64 N	-5454.09 N	-6410.45 N	-7453.0 N	Decrease
	Tension	+1421.64 N	+4070.02 N	+5174.9 N	+6682.8 N	
Pier 6	**Compression**	-4886.2 N	-6440.5 N	-7248.7 N	-8520.5 N	Increase
	Tension	+387.35 N	+1634.4 N	+2261.65 N	+3195.9 N	

The piers that contribute the most to the seismic capacity of the structure are pier 1 through pier 3. The table above reveals that the shear capacity of pier 1 decreases in every step, while the shear capacity of piers 2 and 3 increases in every step. Note that the presented table provides only the force at the top of the piers and therefore neglects the self-weight of the piers at the ground floor.

CHANGING COMPRESSION FORCE AT THE BASE OF THE PIER

In addition to the varying normal force due to the tilting of the floor, a difference exists between the assumed normal stress distributions at the base of the piers. The eccentricity assumed within the SLaMA method can be calculated using the following formula:

$P = \ normal\ force\ in\ N$

$f_u = compressive\ strength\ in\ N/m^2$

$t = \ thickness\ of\ the\ pier\ in\ m$

$L = \ length\ of\ the\ pier\ in\ m$

$$e_{slama} = \frac{L}{2} - a = \frac{L}{2} - \frac{P}{0.85 \cdot f_u \cdot t}$$

This formula is derived based on the assumption that the compressive stress at the base of a pier that undergoes rocking considers a parabolic distribution. This parabolic distribution is subsequently assumed to be rectangular with a correction factor of 0.85.

Table 20 below presents the differences in eccentricities and normal forces between both methods. The eccentricities are indicated in a coordinate system with an origin at the lower left corner of pier 1. Especially piers 2 and 4 of simple model 1 exhibit some difference between the eccentricities assumed in the SLaMA and the calculated eccentricity in the DIANA model; however, these differences are not too high. Moreover, the axial forces determined using both methods demonstrate significant differences.

TABLE 20: AXIAL FORCE AT THE BASE OF THE PIERS OF SIMPLE MODEL 1

Step 500	**Pier 1**	**Pier 2**	**Pier 3**	**Pier 4**
SLaMA eccentricity	1.474 m	4.474 m	1.494 m	4.494 m
FEM eccentricity	1.478 m	4.345 m	1.471 m	3.992 m
SLaMA normal force-C	247207.63N	247228.85 N	57945.06 N	57944.13 N
FEM normal force-C	62252.39 N	685421.61 N	42282.61 N	256087.39 N
Decrease/ Increase	-75%	+177.24 %	-27%	+342%

To determine the influence of the changing normal force at the base of the pier, the SLaMA calculation was performed again with the normal force determined by the FEM analysis. It is understandable that the normal force at the base of piers 1 and 3 decreases and that the normal force at the base of piers 2 and 4 increases. This results in an increase of the shear capacities of piers 2 and 4 and a decrease in the shear capacities of piers 1 and 3.

The table below shows the new shear capacities of the piers in simple model 1.

TABLE 21: NEW CALCULATED SHEAR CAPACITIES OF THE PIERS AT SIMPLE MODEL 1

	Shear capacity	**Drift capacity**	**Failure mechanism**
Pier 1	15311.25 N	0.012	Rocking
Pier 2	207735.61 N	0.014	Rocking
Pier 3	20395.9 N	0.015	Rocking
Pier 4	123529.85 N	0.015	Rocking

Using these new shear capacities, the accelerations have been calculated.

$$a_{first} = \frac{Vfirst = 223.04}{0.7 \cdot m_{2,eff} + 0.3 \cdot m_{1,eff}} = 0.6239\ g$$

$$a_{second} = \frac{Vsecond = 143.93}{0.7 \cdot m_{2,eff}} = 0.55\ g$$

The maximum base shear force is calculated based on the critical acceleration of the second floor. This acceleration is multiplied by the effective masses.

$$V_{base\ shear} = 0.55\ g \cdot (0.7 \cdot m_{2,eff} + 0.3 \cdot m_{1,eff})$$

$$V_{base\ shear} = 196.62\ kN$$

TABLE 22: NEW SLAMA CALCULATION BASED ON THE CHANGING AXIAL FORCES

SLaMA	DIANA NLPO FEA	Difference
76.35 *kN*	250 *kN*	−69.5%
196.62 *kN*	250 *kN*	−21.3%

The new calculation reveals that the changing compressive force at the base of the pier significantly influences the difference of the maximum base shear forces. This previous statement holds merely for this specific analysed model. There are walls in which this effect of varying normal force is cancelled out due to the geometry, loading condition and distribution of masses. It is equally possible that the changing normal force would result in a different failure type for some specific cases. The Figure below illustrates the shear capacity as a function of the normal force:

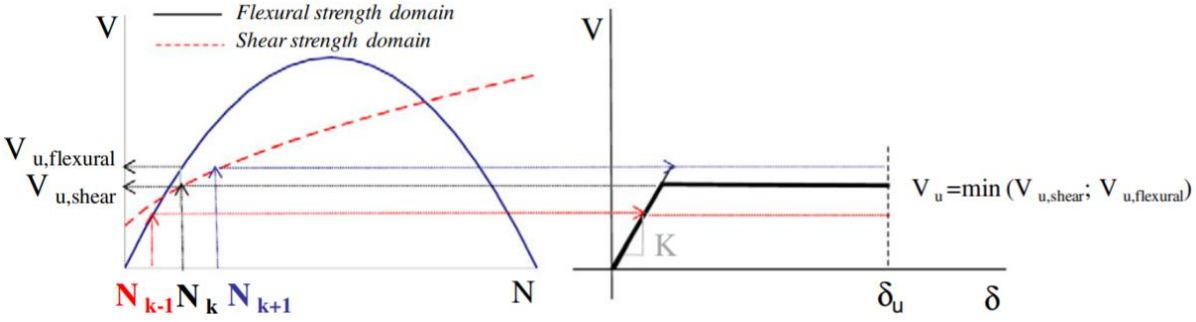

FIGURE 50: SHEAR CAPACITY AS FUNCTION OF AXIAL FORCE AT THE OF THE PIER (LAGOMARSINO, 2013)

The effect of the changing normal forces at the top and base of the piers is observed for all the analysed models, in both the 2D and 3D phases.

The overall shear capacity greatly depends on the changing axial force at the top and base of the piers. These changing forces could result in a decrease or an increase of the overall shear capacity. This primarily depends on the position of the piers, which determines the net increase/decrease of the shear capacity. This effect is completely neglected in the SLaMA approach, as described in the NPR9998:2018. Including this effect could present an improvement in the SLaMA method and would result in a more realistic seismic capacity (see quick calculation).

One possible way to include this frame effect is to assume the floor to be a rigid body and be supported by the piers, which could be assumed to behave like a slender beam. The rotation and horizontal displacement of the

floor during a pushover analysis could be coupled to the rotation of the piers which support the floor. Assigning nonlinear properties to the piers (e.g. zero tension strength of the bed joint) and using the coupling of the rotation/displacement of the floor to the rotation/displacement of the pier results in a set of equations which could be solved using different software packages. The solution method requires additional research and must be validated.

BOUNDARY CONDITIONS

The boundary conditions of the piers determined using the SLaMA method are limited to two options. The first option is to assume that the pier behaves cantilevered, and the second option is to assume the pier is double clamped. In most cases, it is apparent that both options are inapplicable. The real boundary condition of the pier lies between being cantilevered and being double clamped.

This is a clear limitation of the SLaMA method and bears a significant influence on the calculation of the base shear force. The DIANA NLPO FEA determines the boundary conditions based on the material properties and the used material model. The boundary conditions would be more realistic in this case.

The results of the simple models in the 2D assessment phase demonstrate a clear double clamped behaviour when studying the maximum principal strain and the cracking pattern of the FEM results. No spandrel failure is observed, while the piers undergo rocking failure. However, the piers of the similar models are considered to behave cantilevered in the SLaMA calculation, based on the procedure of determining the boundary conditions.

An alternative approach to determine the boundary conditions is proposed in the study of Anass el Kouri, which is carried out in parallel to this study and in collaboration with it. This new approach determines the boundary conditions of the piers which can lie between the cantilevered and double clamped boundary conditions. This approach is currently applicable to only one-storey buildings. Further research is required is to extend this method.

In the 3D assessment phase, two models were analysed, one with the reinforced concrete floors and the other one with the timber floors. In the case of RC floors, the piers are assumed to behave as double clamped due to the high stiffness of this floor. This assumption appears to be realistic in the case of RC floors.

The ratio of the base shear force in the case of timber floors appears to be much lower than the ratio of the model with the RC floors. The SLaMA method assumes, in the case of the timber floors, that these floors are fully flexible and do not contribute to the rotational stiffness of the piers. The FEM analysis reveals that the floors could contribute to the boundary condition of the piers as a result of the modelling assumptions for the timber floor. Therefore, the FEM analysis overestimates the maximum shear capacity. This point is further elaborated upon in the section concerning the influence of the floor type.

INFLUENCE OF THE LOADING

Varying the loading conditions has no significant influence on the seismic capacity of the structure. No difference exists between the ratios of the base shear force of the SM1 and SM2, while the loading differs between models. In addition, no significant change in the ratio of the displacement capacity was observed. The predicted failure mechanisms with both methods reveal similar results (rocking of the piers).

INFLUENCE OF THE MASONRY TYPE

Changing the masonry type has a limited influence on the difference between the base shear force predicted with the SLaMA method and that predicted with the DIANA NLPO FEA. In simple model 3, the masonry type is changed from clay pre 1945 to clay post 1945. This variation results in a reduction in the error between the base shear force predicted by both methods. The main difference lies in the determination of the boundary conditions of the piers. In this case, the boundary conditions are determined to be double clamped due to the strong spandrels. The material properties that affect the strength of the spandrel are the friction and cohesion. The notable difference between the cohesion of clay pre 1945 and clay post 1945 explains the reduction in the difference. The increase in cohesion does not result in a different failure mechanism.

Changing the masonry type from clay pre 1945 to calcium silicate pre 1985 led to an increase in the difference between the SLaMA method and the DIANA NLPO FEA. This increase could be explained by the influence of the compressive strength and the compressive energy on both assessment methods, which are the material properties which are higher than the properties of the clay pre 1945. The engineering masonry model considers a parabolic compressive curve, while the formula for the rocking capacity considers a rectangular distribution. Because of these assumptions, the maximum base shear force predicted by the DIANA NLPO FEA is more sensitive to compressive strength compared with the SLaMA method. The increase in the compressive energy and compressive strength does not change the predicted failure mechanism.

The influence of the bed joint tensile strength and the tensile fracture energy were analysed using simple model 6. The material properties of simple model 6 are similar to the clay pre 1945 masonry, with a single difference in the tensile strength and tensile fracture energy. Both material properties are considered to be 10 times lower than the clay pre 1945 masonry. The resulting ratio between the SLaMA base shear force and the FEM base shear force remains similar to the ratio of simple model 1.

Therefore, changing the material properties in this way has no influence on the ratio for the prediction of the base shear force. Altering the tensile properties in this way results in the same ultimate strain as simple model 1; therefore, both models predict the same base shear force. The predicted failure mechanism with the FEM analysis changes from rocking to a combination of rocking and shear. Varying the tensile properties affects only the predicted failure mechanism.

INFLUENCE OF THE FLOOR TYPE

2D ASSESSMENT PHASE

The difference between the base shear force determined using both methods is lower for SM5 than for SM1. This is because the SLaMA method assumes double clamped boundary conditions for the piers in the case of a reinforced concrete floor. This assumption yields a much higher shear capacity than in the case of the cantilevered behaviour of the piers.

The FEM results reveal no significant difference in the predicted base shear force when comparing the same model with a different floor type. The base shear force of the model with the RC floors (SM5) is 230 kN and has a displacement capacity of 4 mm. This pushover analysis was stopped after the convergence criterion was not met. On the other hand, the base shear force of the model with the timber floors (SM1) is 250 kN and has a displacement capacity of 10 mm. These similar results for the different floor types suggest that the floor type does not significantly influence the FEM results under the conditions of the 2D analysis.

These results are somehow misleading, as the 3D assessment phase reveals that there is evident influence of the floor type on the results. The minor difference between the FEM results could be explained by the presence of the strong spandrels. The maximum principal strains reveal that the piers behave under double clamped boundary conditions for the model with the timber floors. Therefore, analysing the same model with the RC floors would not result in a significant difference in the predicted failure mechanism and base shear force.

In the presence of a weak spandrel, the effect of the floor type would be more visible in the results. A 2D model does not generate valuable results in the case that the floor type has a significant influence. It is difficult to determine the stiffness and contributing part of the floor to the in-plane capacity of the wall. Moreover, modelling the contributing part with a 2D plane stress element would not describe the realistic behaviour of the floor during a pushover assessment. Therefore, when the floor type significantly influences the results, the 3D pushover analysis would be more valuable.

3D ASSESSMENT PHASE

The difference between the base shear force predicted by the SLaMA method and the DIANA NLPO FEA of the URM building with timber floors is much higher than the difference of the same URM building with RC floors. One possible explanation is that the SLaMA method considers the piers in the in-plane wall to behave fully cantilevered. This assumption provides the most conservative shear capacities of the in-plane walls. Therefore, the floors are assumed to not influence the rotational stiffness of the connection between the spandrel and pier. Meanwhile, in the FEM analysis, the timber floor has some influence on the rotational stiffness of the spandrel-pier connection.

When analysing the details of the timber floors and their connections to the walls, it could be observed that the floor is a one-way spanned floor. The floor planks are rigidly connected to the timber beams, which are again rigidly connected to the out-of-plane walls. The out-of-plane walls can resist and therefore influence the displacement of the in-plane loaded walls. In this way, the timber floor influences the deformed shape of the piers. However, in practise, the timber floor does not significantly influence the boundary conditions of the piers. These conditions are primarily determined based on the presence of lintels and spandrels. It could therefore be concluded that the FEM analysis results in an overestimated shear capacity of the in-plane loaded walls.

Another point which could be mentioned is the method for modelling the floor, beginning from the connection between the out-of-plane walls and the timber floor beams. This beam-wall connection is modelled as a rigid connection, which is not the case in practise. In practise, these connections are more likely to be hinged connections. This modelling choice could lead to an overestimated interaction between the walls and the in-plane deformation of the floor. This could consequently lead to an increase in the in-plane stiffness of the floor and therefore an increase in the base shear force.

To determine the influence of the beam-wall connection, a simple one-storey model was analysed using two methods, namely the structural eigenvalue analysis and the modal pushover analysis. Only the self-weight was applied to this model, and the masonry and floors were modelled in the same manner as the models of the 3D assessment phase. The beam-wall connection in this first model was modelled as a rigid connection, while in the second model, this connection was modelled as a hinged connection (using tyings). The Figures below illustrate the simple model which was used to determine the influence of the beam-wall connection. The resulting base shear force for the model with a rigid beam-wall connection is $V_B = 26\ kN$, and the corresponding displacement capacity is 36 mm.

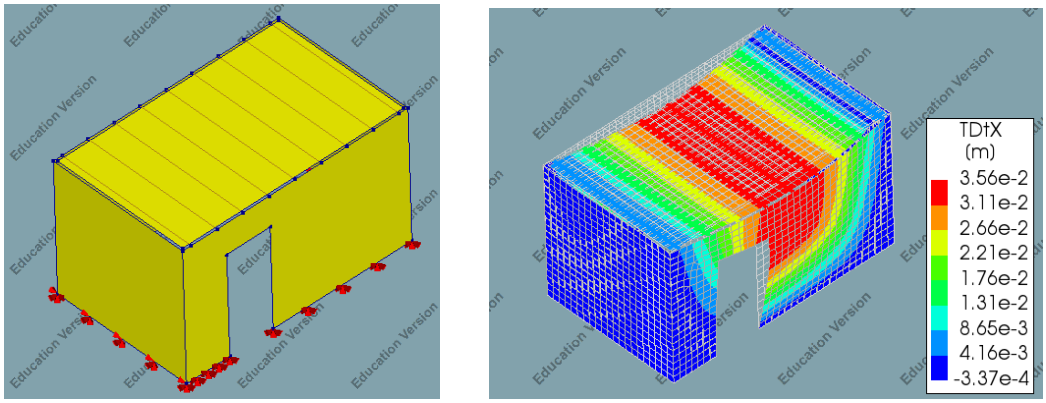

FIGURE 51: MODEL WITH RIGID BEAM-WALL CONNECTION

The Figures below display the same model with a hinged beam-wall connection in the second model. The resulting base shear force for the model with a hinged beam-wall connection is $V_B = 21\ kN$, and the corresponding displacement capacity is 33 mm.

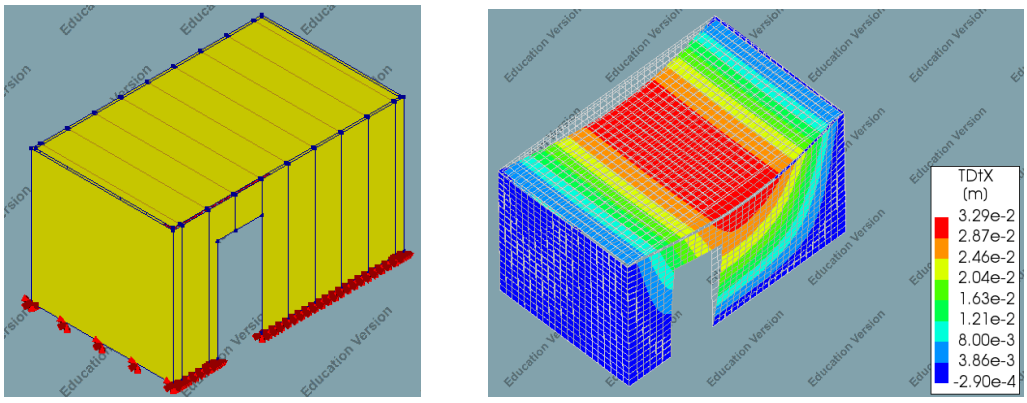

FIGURE 52: MODEL WITH HINGED BEAM-WALL CONNECTION

This quick check demonstrates a clear influence of the beam-wall connection on the displacement capacity and maximum base shear force. Modelling the connection as hinged instead of rigid results in a reduction of almost 20% of the maximum base shear force and a reduction of 10% of the displacement capacity. Therefore, it could be concluded that the predicted base shear force of $V_B = 40\ kN$ is an overestimation, as the connection is modelled rigidly. Applying the reduction factor (20%) would result in a maximum base shear force of $V_B = 32\ kN$.

The connection between the timber planks and the timber beams is likewise modelled as a rigid connection. This assumption can influence the deformation of the floor, as the floor would behave more stiffly than in the case of a hinged connection between the beams and planks. The beam-plank connection is, in practise, closer to a hinged

connection than a rigid one. The stiffer behaviour would result in a less cantilevered behaviour of the piers, as well. Reducing the in-plane stiffness results in a decrease in the maximum base shear force and displacement capacity (in-plane wall). Floors with a low in-plane stiffness are less capable of distributing the seismic load equally over the in-plane walls, resulting in a reduction of the maximum base shear force and ultimate displacement. Further research is required to determine the reduction factor of the in-plane stiffness due to the hinged connection between the timber planks and beams.

These last two explanations appear to be possible reasons for the significant difference in the base shear force between the two assessment methods of the URM building with timber floors. The DIANA NLPO FEA overestimates the maximum base shear force due to the modelling approach, while the SLaMA method underestimates the maximum base shear force by neglecting the stiffness of the floor.

The results indicate that the SLaMA predicts more a conservative base shear force in the case of timber floors than for a building with an RC floor. The SLaMA method assumes double clamped boundary conditions of the piers in the case of reinforced concrete floors. These assumptions appear to simulate a realistic influence of the floor on the pier boundary conditions.

PREDICTED FAILURE MECHANISM

The predicted failure mechanism with the SLaMA method is, in most cases, different from the failure mechanisms predicted by the DIANA NLPO FEA. This difference could be observed during both the 2D assessment phase and the 3D assessment phase. Two possible reasons explain this difference, namely the limitation of the SLaMA method and the influence of the material model within the FEM analysis.

The limitation of the SLaMA method is that this method is capable of predicting the failure mechanism at only one specific floor, namely the floor that corresponds to the lowest and thereby critical acceleration. If both accelerations are close to each other, it would be difficult to determine what kind of failure mechanism would occur. When the difference between the accelerations is small, it could be concluded that both floors would fail. This was confirmed by almost all the analysed models, save for the Casestudy-3D-Model with the timber floors.

The accelerations of the levels in this model are significantly different, and therefore, the SLaMA method predicts the failure occurring at one specific level. This contrasts with the DIANA NLPO FEA of this model, which predicts failure occurring at both levels of the building. The primary reason is the difference in participating mass: The SLaMA method assumes a participating mass of 83%, while the DIANA NLPO FEA considers a participating mass of 54%. This difference in participating masses could be the result of the modelling assumptions in DIANA or the assumption of the effective masses in the SLaMA. The modal pushover analysis is less reliable in the case that the structure is sensitive to higher-order eigenmodes.

Another limitation is that the SLaMA is unable to predict the combination of rocking and shear failure. This contrasts with the DIANA NLPO FEA, which can predict the combination of rocking and shear failure depending on the material model used for masonry. In the case that the SLaMA method and the FEM analysis predict failure at the same pier, it is common that the same failure type is predicted.

INFLUENCE OF THE MATERIAL MODEL

The masonry in all the FEM analyses was modelled with the engineering masonry model. The engineering masonry model could be applied with four different options, which differ in how to involve the head joint failure. The models in the 2D assessment phase consider the masonry with the engineering masonry model: the diagonal staircase option. Analysing simple model 1 with the four options reveals that the influence of the selected option is negligible when comparing the base shear force, displacement capacity and failure mechanism. All the simple models reveal rocking to be the governing failure mechanism, and this failure type is considered in all options in the same manner.

The 3D DIANA NLPO FEA of both unreinforced masonry buildings was conducted with three different material models. The specific difference lies in modelling the masonry of the walls. The masonry in the first model was modelled with the engineering masonry model ‘diagonal staircase’ option/DS option, the masonry in the second model was modelled with the engineering masonry model ‘head joint failure not considered’ option/HJ option, and the masonry in the last model was modelled with the engineering masonry model ‘direct input head joint tensile strength’/direct option.

The FEM results of the URM building with reinforced concrete floors and timber floors reveal that the HJ option predicts a higher base shear force capacity than the other options. There is not a large difference between the pushover curve resulting from all the options.

When considering the predicted failure mechanism of the URM building with RC floors, it appears that the models do not predict the same failure mechanism. The model with the diagonal staircase option predicts no rocking of piers 5, 6 and 7, while the models with the HJ option and the direct option predict the rocking of these specific piers. A possible explanation for this could be that the model with the DS option did not reach the displacement of the model with the HJ option, and so the failure of these piers did not occur. For all the other piers, the models of the HJ option and the DS option predict the same local failure mechanisms.

When comparing the predicted failure mechanisms of the model with the HJ option and those with the direct option, it could be observed that piers 1, 3 and 8 exhibit different failure mechanisms. These piers reveal an extra rocking failure mode in the case of the direct option. These differences in the predicted failure mechanism could be explained by the fact that the direct option considers crushing perpendicular to the bed joints and head joints, while the HJ option considers the crushing perpendicular to only the bed joints.

The FEM results of the URM building with timber floors reveal different failure mechanisms of four piers. The model with the HJ option predicts no failure of piers 4 and 8, while the model with the DS option predicts that these piers would undergo rocking failure. A possible explanation lies in the maximum in-plane deformation of the timber floor in the diagonal staircase option, which is considerably higher than the deformation with the HJ option. Therefore, it is possible that the HJ option did not reach this rocking failure of these piers.

The other difference in the predicted failure mechanism is that the model with the DS option predicts a shear failure of piers 9 and 12, while the model with the HJ joint failure predicts a rocking failure mode of these piers. The DS option has already proven to be reliable in predicting the shear failure of wide piers. Unfortunately, this option sometimes predicts a shear failure of slender piers, such as piers 9 and 12; this is not realistic, and therefore, the failure mechanism predicted by the HJ option is more realistic.

DISPLACEMENT CAPACITY

The SLaMA method predicts a higher displacement capacity than the DIANA NLPO FEA in the 2D assessment phase. The main explanation for this lies in the convergence behaviour of the analysis for the models in this phase. The divergence of the numerical solving method could be caused by the collapse of the structure or the numerical instability of the solving method. The ultimate displacement achieved with the FEM analyses cannot be considered the displacement capacity for the total structure; therefore, the SLaMA method could not be validated with the DIANA NLPO FEA based on this study for the 2D assessment phase.

The displacement capacities resulting from the FEM analysis in the 3D phase are determined based on the final loading step of the pushover analysis. Therefore, these results are comparable to the SLaMA results for the ultimate displacement. The results indicate conservative ultimate displacements predicted by the SLaMA method compared with the FEM results when assessing buildings with RC floors. The ultimate displacement reached with the FEM analysis appears to be realistic, as the analysis stopped when a full diagonal crack was developed over the height of piers 3 and 9. Therefore, it could be concluded that this analysis stopped due to the physical collapse of the structure. This FEM analysis predicts a displacement capacity of 19.9 mm, and the SLaMA method predicts a displacement capacity of 15 mm. This comparison reveals that the SLaMA method is a conservative method in predicting the displacement capacity for the URM buildings with RC floors.

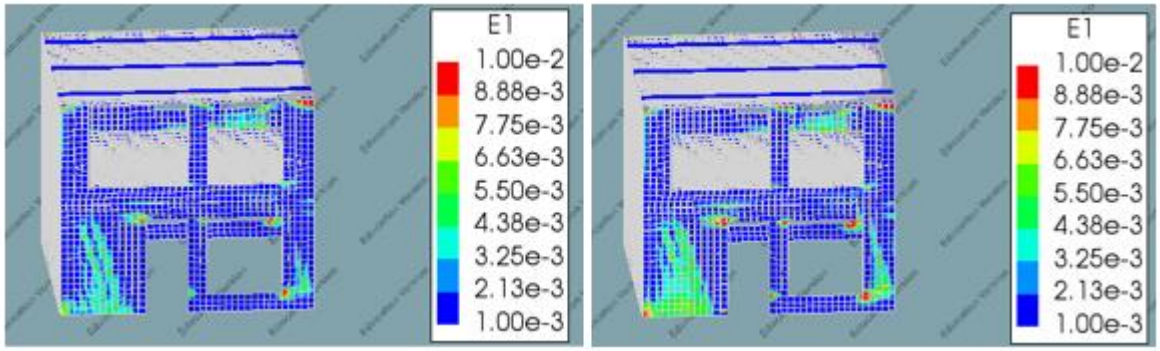

FIGURE 53: FINAL STEP IN THE PUSHOVER ANALYSIS OF THE 3D MODEL WITH RC-FLOORS

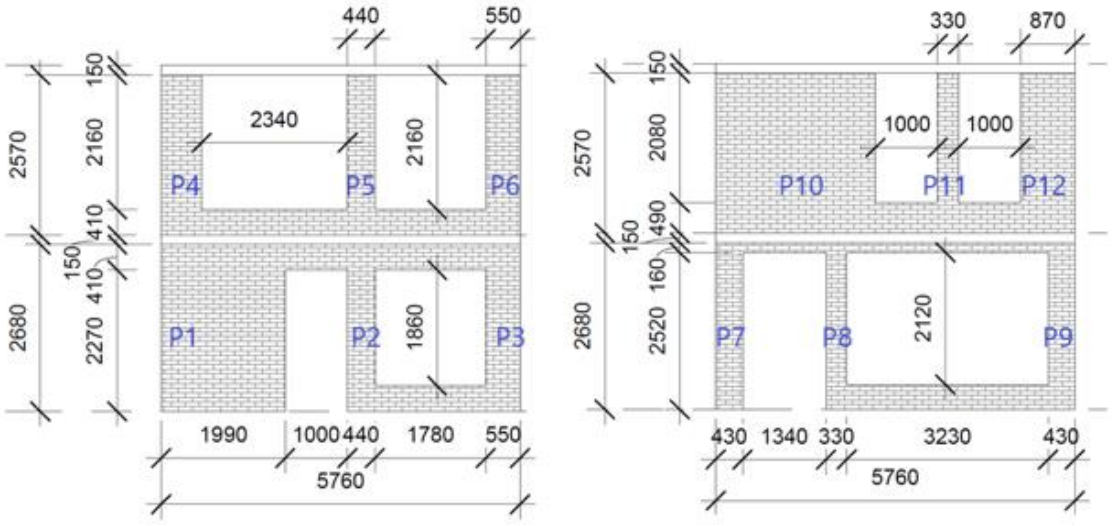

FIGURE 54: SIDEVIEW 3D MODEL WITH RC-FLOORS

In the case of buildings with timber floors, the SLaMA overestimates the displacement capacity compared with the FEM results. This overestimation could be the result of the previously mentioned modelling assumptions for the timber floors. This floor is modelled more stiffly than in practise, which results in a lower displacement capacity. Another possible reason could be the effect of the determined failure type; the drift capacities are determined based on the governing failure type. Nevertheless, if the shear capacities of the different failure types are close to one another, it would be challenging to determine the occurring failure mechanism. This choice is crucial for the drift capacity considered in the calculations of the displacement capacities.

8 CONCLUSION

The aim of my research was to find out whether the SLaMA could be realistically conservative and an effective method to determine the global capacity of a building subjected to seismic loading. And if the SLaMA method can be an alternative for the FEM NLPO analysis for a specific type of building. In that case the SLaMA method would save a lot of time when assessing unreinforced masonry buildings. The study aims to answer to sub-research questions and finally the main research question.

These questions have been answered by analysing 12 models of a two-storey URM building with both the SLaMA method and the NLPO FEM analysis. Each model differs in some specific aspect, such as the loading condition, floor type or masonry type. Ten models were analysed during the 2D assessment phase, and two models were analysed during the 3D assessment phase. Therefore, the influence of these specific aspects was studied properly. The main research questions are answered in this concluding chapter.

1. ***What are the global capacities and predicted failure mechanisms of the analysed two-storey unreinforced masonry buildings based on the 2D/3D NLPO FEM analyses and the SLaMA method?***

In general, this question could not be answered for all existing two-storey unreinforced masonry buildings. Therefore, the answer to this question will be limited to the analysed models in this study.

The global capacities are defined as the maximum base shear forces and the displacement capacities of the analysed models determined using both assessment methods. The displacement capacity in some cases could not be estimated with the NLPO FEM analysis. Because the analysis in these specific cases stopped due to instability of the numerical solving method, and not due to the physical collapse of the structure. The results are presented by the pushover curves and in several tables in Chapter 2D and 3D assessment phase results.

The failure mechanisms predicted by the NLPO FEM analysis were specified by analysing the maximum principal strains during the pushover analysis. The failure modes determined using the SLaMA method are based on the acceleration curves and the lowest shear capacities. The critical shear capacities determine the type of failure occurring in the piers. In addition, the acceleration curves specify the location of the failure (which level). The predicted failure mechanisms of the analysed models are summarised in several tables in section 6.3 and 7.3.

2. ***Does the SLaMA method predict conservative global capacities and the same governing failure modes for the two-storey unreinforced masonry buildings compared with the 2D/3D NLPO FEM analyses?***

In all cases, the SLaMA is a highly conservative method for predicting the maximum base shear force. The ratios between the SLaMA base shear force and the FEM base shear force vary throughout the range of 0.23 to 0.78. This conclusion is confirmed also by the study conducted by Anass El Kouri, which reveals that the range varies from 0.33 to 0.75. The conservative ratios could be explained by several factors which are mentioned in the discussion part. The primary reasons for these conservative ratios are as follows:

- Lack of including the force redistribution-at the top and base of the piers during a pushover analysis. The effect of the redistribution of the force is completely neglected in the SLaMA method.

- The simplified method for determining the boundary condition of the piers and the limitation of this method in determining a boundary condition which lies between the cantilevered and double clamped conditions.

- Influence of the material model used for modelling masonry in the FEM pushover analysis. The results of the 3D analyses shows that the use of different options in the engineering masonry model results in small difference in the predicting of the maximum base shear force.

- Influence of the modelling assumptions for modelling the timber floors. Especially the beam-wall and the beam-plank connection have an influence on the prediction of the maximum base shear force. Modelling the beam-wall connection hinged make the SLaMA prediction less conservative. The same holds for modelling the beam-plank connection hinged (reducing in-plane stiffness).

- Effect of the participating masses assumed in both assessment methods.

The displacement capacities resulting from the SLaMA calculations reveal an overall conservative result compared with the 3D DIANA NLPO FE analysis of the models with the RC floors. The displacement capacities of the 3D DIANA NLPO FE analyses are comparable because these analyses stopped at the final loading step once divergence began to occur. The divergence of this analysis was likely caused by the physical collapse of the structure due to the total failure of piers 3 and 9.

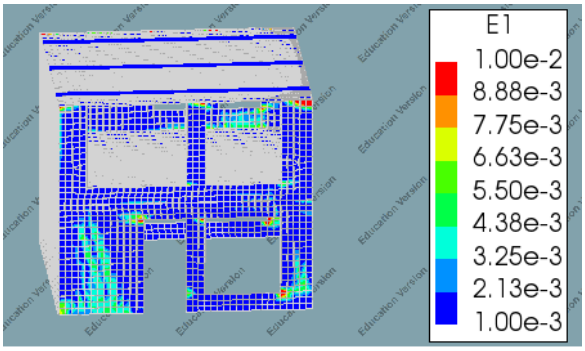

FIGURE 55: ONE STEP BEFORRE FINAL STEP IN THE PUSHOVER ANALYSIS OF THE 3D MODEL WITH RC-FLOORS

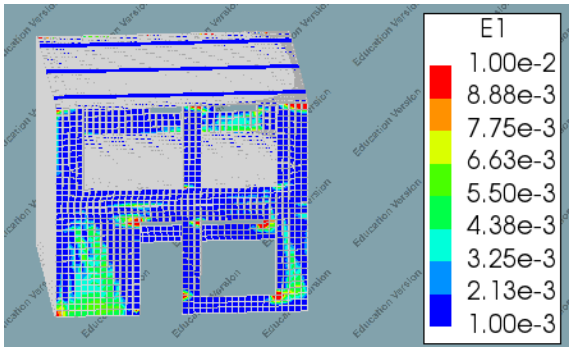

FIGURE 56: FINAL STEP IN THE PUSHOVER ANALYSIS OF THE 3D MODEL WITH RC-FLOORS

The 2D FEM analyses were not applicable for comparing the displacement capacities, since these analyses were stopped due to divergence of the numerical solving method. The main explanation for this lies in the convergence behaviour of the analysis for the models with the timber floors. The divergence of the numerical solving method could be caused by the collapse of the structure or the numerical instability of the solving method. There is no indication for the total collapse of the structure in the case of the models with timber floors. Therefore, these displacement capacities predicted by the NLPO FEM analysis are unreliable. The same reasoning holds for the displacement capacity of the 3D model with timber floors.

The failure mechanisms resulting from the SLaMA method are not the same as the failure mechanism resulting from the DIANA NLPO FE analyses for most of the analysed models. The specific failure types of the piers are typically in accordance with the DIANA NLPO FEA results. The SLaMA method is limited in predicting one specific failure type; therefore, a combination of failure types at one pier could not be predicted by the SLaMA method.

However, the problem lies in the position of these failure mechanisms. The SLaMA method determines the failure mechanism based on the critical acceleration curve of a specific floor. Therefore, the SLaMA method predicts only the failure occurring at one specific floor. The DIANA pushover analysis could predict failure occurring at both floors during a pushover analysis.

The predicted failure mechanism resulting from the SLaMA method could be valuable with the correct interpretation. When the acceleration curves of both floors are close to each other, it could be concluded that a combination of the failure would occur at both levels. Excluding failure occurring at one floor would be a misinterpretation of the results. Moreover, in the case that the accelerations significantly differ, the correct failure mechanism could be predicted by the SLaMA method. This method is overall conservative in predicting the global capacities, and with critical interpretation, the same failure mechanism as the FEM analysis could be predicted in most cases.

3. ***What is the influence of the masonry type, floor type and loading condition on the comparison between the global capacity and the failure mechanism predicted by the SLaMA method and the NLPO FEM analysis?***

This study reveals that the masonry type and loading condition have no significant influence on the global capacities and predicted failure mechanisms. The displacement capacities and predicted failure mechanisms are overall the same. The only differences lie in the resulting base shear force ratios, which vary in the range of 0.26 to 0.42. These variations are due to the sensitivity of the assessment methods for some material properties, such as compressive fracture energy, compressive strength and cohesion. Some of these properties could change the boundary condition, which could significantly influence the maximum base shear force.

The results of the 3D assessment phase present a significant influence of the floor type on the global capacities. The ratio of the maximum base shear force in the case of RC floors is much higher than in the case of timber floors. It could therefore be concluded that the SLaMA method is better at calculating the base shear force of buildings with RC floors than the buildings with timber floors. This influence is also visible in the results of the 2D assessment phase.

The floor type also influences the displacement capacity ratio. This ratio is defined as the ultimate SLaMA displacement divided by the ultimate FEM displacement. The ratios reveal that the SLaMA predicts conservative results in the case of buildings with RC floors. In contrast, the ratios for buildings with timber floors present an overestimation of the SLaMA method for displacement capacity. But the displacement capacity reached with the NLPO FEM analysis is not a reliable properties , and is dependent on the modelling assumptions.

Modelling assumptions for timber floors influence the displacement ratios and base shear force ratios. The beam-wall connection, plank-beam connection and in-plane stiffness influence the global capacities predicted by the NLPO FEM analysis.

The floor type has no specific influence on the different predicted failure mechanisms by both assessment methods. These differences could be explained by the answer to the previous research question.

4. ***Could the SLaMA method be a realistically conservative and effective alternative to the NLPO FEM analysis in making a seismic assessment of a two-storey unreinforced masonry building?***

Maximum base shear force

In all cases, the SLaMA method is a conservative method in predicting the maximum base shear force. The range of the base shear force ratios lies between 0.23 and 0.78, which makes the question difficult to answer. The term 'realistically' is subjective and based on the interpretation of the engineer. It depends on the ratio to determine whether this method is realistically conservative.

In general, the SLaMA method appears to be realistically conservative when assessing unreinforced masonry buildings with reinforced concrete floors independent of the masonry type and loading condition. In this case, the maximum base shear force ratios lie between 0.4 and 0.66. In the case of URM buildings with timber floors, the SLaMA would be too conservative in predicting the maximum base shear force, since the ratios vary between 0.23 and 0.78. The ratios depend upon the modelling assumptions within the DIANA NLPO FEA. Therefore, the real ratios will be higher, which could cause the SLaMA method to be less conservative.

Displacement capacity

The 3D assessment results reveal a realistically conservative displacement capacity of the URM buildings with RC floors compared with the FEM result, while with timber floors, the SLaMA method reveals an overestimated displacement capacity. The main reasons are the difference in the participating masses and the modelling assumptions within DIANA. Another reason is the convergence behaviour of the numerical solving method. The analysis was stopped after divergence began to occur, which concerns the instability of the numerical method. Therefore, the displacement capacities predicted using the SLaMA method could not be validated for URM buildings with timber floors, only for URM buildings with RC-floors.

Predicted failure mechanism

Analysing the predicted failure mechanism reveals that the SLaMA method can frequently predict the same failure type. The main difficulty of the SLaMA method lies in the prediction of the combined failure type. When the shear capacities of the different failure modes are close to one another, the engineer must interpret the results in a proper manner. Thus, the engineer must consider a combination of failure types occurring at the piers/spandrels.

The SLaMA method is limited in predicting failure occurring at different floors of a building. The same principal holds for this limitation: The engineer must analyse the acceleration to interpret the results in a proper manner. If the ratio between the accelerations is close to 1, it could be concluded that both levels would fail. Meanwhile, if this ratio is significantly higher than 1, the floor with the lowest acceleration would fail. The last statement is confirmed by almost all the models, save for the Casestudy-3D-model with timber floors. In that case, a significant difference existed in the participating mass, which influenced the predicted failure mechanism.

In conclusion, the SLaMA method could be a realistically conservative and effective alternative to the NLPO FEM analysis when assessing URM buildings with RC floors. The SLaMA method appears to be too conservative in predicting the maximum base shear for URM buildings with timber floors.

The displacement capacity predicted using the SLaMA method is validated only for RC floors. This predicted SLaMA method was realistically conservative compared with the ultimate displacement achieved using the NLPO FEM analysis. The displacement capacity for URM buildings with timber floors could not be validated based on this study.

The SLaMA method is overall a suitable method for obtaining a quick understanding of the behaviour of an URM building. This method could be valuable to apply before using a more complex assessment method.

9 RECOMMENDATIONS

This study identifies some limitations of the SLaMA method and the DIANA NLPO FEA. This part describes some recommendations which follow from this study and the study by Anass El kouri. Both studies were conducted in parallel and in cooperation with each other. Therefore, the recommendations resulting from these studies are combined in this chapter.

- Further research is required to determine how to include (in a simple manner) the effect of the varying axial load at the top and base of the piers within the SLaMA method. Combining a simplified equivalent frame method with the SLaMA method could be a possible solution.
- A new procedure is needed to determine the boundary conditions of the piers in the in-plane loaded walls. Including the boundary conditions that lie between the double clamped boundary condition and the cantilevered boundary condition would result in a less conservative prediction when using the SLaMA method.
- Further improvements in modelling the timber floors in the NLPO FEM analysis must be studied for the timber floor to behave more realistically.
- More research is needed to determine at which difference in shear capacities the combined failure type occurs. It is clear that one specific failure type would occur when the difference in shear capacity is significant. How small must this difference be to adopt the combined failure mechanism within the SLaMA method?
- The SLaMA method must be improved to determine the location of the failure mechanism. When assessing buildings with multiple floors, it would be difficult to determine which floor would fail first. The SLaMA is able to predict failure at only one specific floor, and therefore, this method must be extended to predict failure at additional floors.
- Further research is required to determine the reduction factor, which could be applied in the FEM analysis, for the in-plane stiffness due to the hinged connection between the timber planks and the beam and the hinged connection between the beam and the wall.
- The effective mass, as calculated within the SLaMA method, must be validated for URM buildings with timber floors. The results reveal a significant difference in the participating mass (DIANA) and the assumed effective mass (SLaMA).

10 BIBLIOGRAPHY

A. Brignola & S. Podestà, S. P. (2008). *In-plane stiffness of wooden floor* . Genoa: 2008 NZSEE CONFERENCE.

A.H.Akhaveissy, G. (2013). *Pushover analysis of large scale unreinforced masonry structures by means of a fully 2D non-linear model.* Construction and Building Materials.

Beyer, K. (2011). *Peak and residual strengths of brick masonry spandrels.* Switzerland: ELSEVIER.

DIANA FEA. (2014). *6.4 Modal Pushover Analysis*. Retrieved from dianafea: https://dianafea.com/manuals/d95/Analys/node74.html

F. Messali, J. R. (2017). *In-plane drift capacity at near collapse of rocking unreinforced calcium silicate and clay masonry piers.* Delft.

Jafari, S. R. (2017). *Characterizing the material properties of dutch unreinforced masonry.* Delft: Elsevier.

Krawinkler, H. &. (1998). *Pros and cons of a pushover analysis of seismic performance evaluation.* Engineering structures.

Lagomarsino, S. P. (2013). *TREMURI program: An equivalent frame model for the nonlinear seismic analysis of masonry buildings.* Elsevier.

M. Miglietta, L. M. (2019). *FULL-SCALE SHAKING TABLE TEST ON A DUTCH URM CAVITY-WALL TERRACED-HOUSE END UNIT – EUC-BUILD-6.* Pavia: EUCENTRE.

MAGENES, G. C. (1997). *IN-PLANE SEISMIC RESPONSE OF BRICK MASONRY WALLS.* Pavia.

Moon, F. (2004). *Seismic strengthening of low-rise unreinforced masonry buildings.* Atlanta: Georgia Institute of Technology.

Moon, F. Y. (2006). *Recommendations for Seismic Evaluation and Retrofit of Low-Rise URM Structures.* JOURNAL OF STRUCTURAL ENGINEERING.

NEN. (2018). *NPR9998.*

NOORTMAN, F. (2019). *APPLICABILITY OF THE PUSHOVER METHOD FOR THE SEISMIC ASSESSMENT OF URM STRUCTURES IN GRONINGEN.* TU Delft.

NZSEE. (2017). *Unreinforced Masonry Buildings C8.*

Schreppers, G., Garofano, A., Messali, F., & Rots, J. (2017). *DIANA Validation report for Masonry modelling.*

TOMAZEVIC, M. K. (1997). *SEISMIC BEHAVIOUR OF CONFINED MASONRY WALLS.* Slovenia.

Vecchio, F., & Collins, M. (1986). *The modified compression field theory for reinforced concrete elements subjected to shear.* ACI Journal.

Yi, T. M. (2006). *Lateral Load Tests on a Two-Story Unreinforced Masonry Building.*

APPENDIX

By Nidal Ennali

September 7, 2020

Delft University of Technology, ARCADIS

Thesis committee:

prof.dr.ir.J.G.Rots TU DELFT
dr.F.Messali TU DELFT
ir.S.Pasterkamp TU DELFT
ir.M.Bettonvil ARCADIS
ir.G.van Engelen ARCADIS

11 APPENDIX A: SIMPLE MODEL 1: FULL DIANA NLPO FEM ANALYSIS

RESULTS: STRUCTURAL EIGENVALUE ANALYSIS

The first analysis that has been made is the structural eigenvalue analysis. This analysis is required to determine the critical Eigen mode and Eigen frequency. The Eigen mode with the highest participating mass is the critical Eigen mode. In this case Eigen mode 1 is the governing Eigen mode and corresponds to a participating mass percentage 80.96%. The Figure below shows first five Eigen modes and their participating masses.

TABLE 23: GOVERNING EIGEN MODE AND THE PARTICIPATING MASS

MODE	FREQUENCY	EFF.MASS TX	PERCENTAGE	CUM.PERCENT
1	0.73718E+01	0.62040E+05	0.80956E+02	0.80956E+02

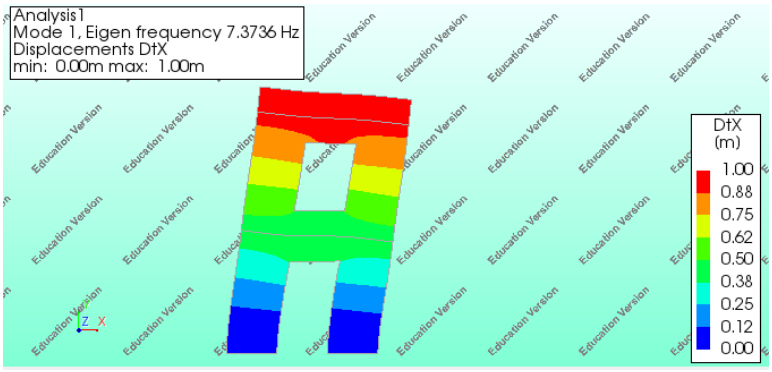

FIGURE 57: THE GOVERNING EIGEN MODE

RESULTS: STRUCTURAL NONLINEAR ANALYSIS

This part contains the results of the structural nonlinear analysis. The relevant obtained results in this case, are the horizontal deflection, maximum principal strain, observed failure mechanism and the pushover curve.

Horizontal DEFLECTION

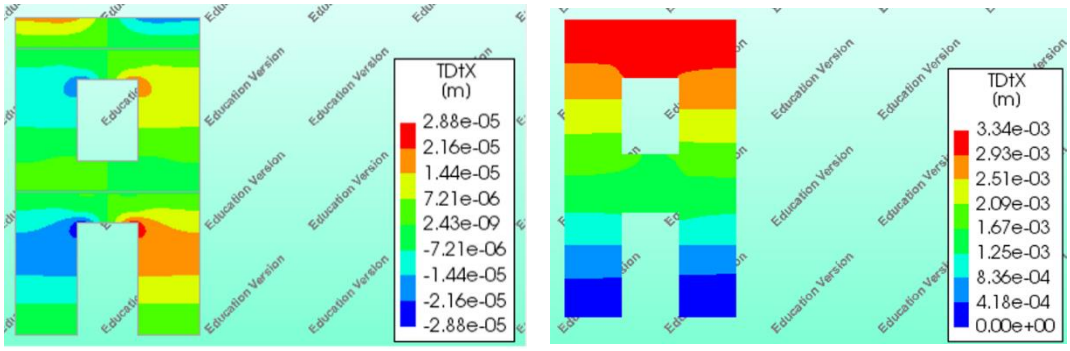

FIGURE 58: HORIZONTAL DEFLECTION STEP 1 (LEFT) , HORIZONTAL DEFLECTION STEP 150 (RIGHT)

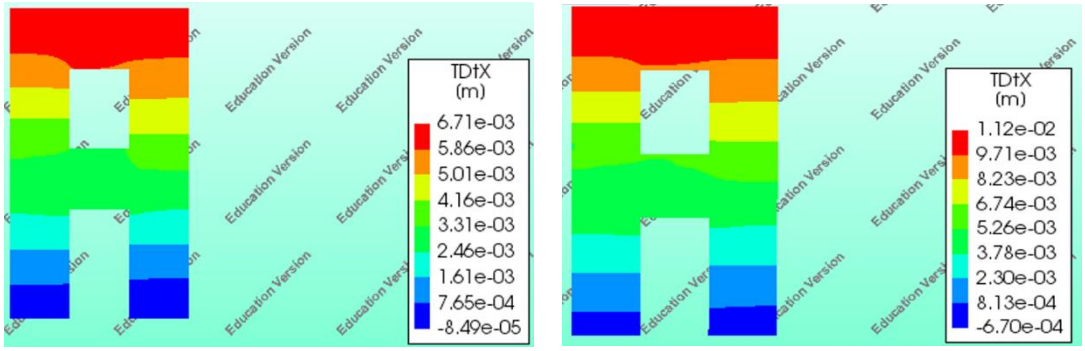

FIGURE 59: HORIZONTAL DEFLECTION STEP 300 (LEFT) , HORIZONTAL DEFLECTION STEP 500 (RIGHT)

MAXIMUM PRINCIPAL STRAIN

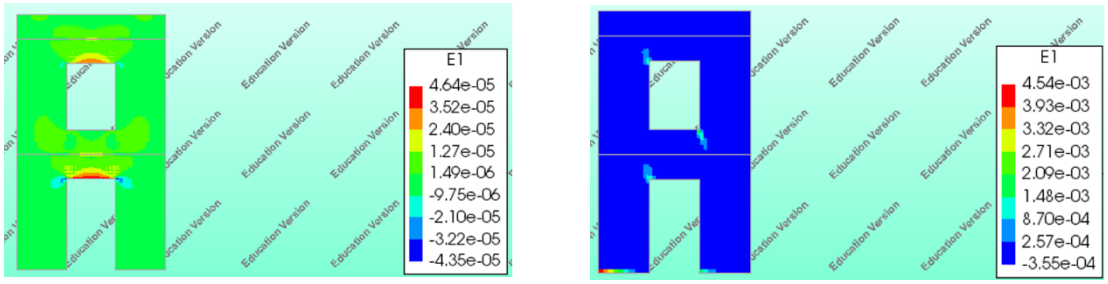

FIGURE 60: MAXIMUM PRINCIPAL STRAIN-LOAD STEP 1 (LEFT) , MAXIMUM PRINCIPAL STRAIN-LOAD STEP 150 (RIGHT)

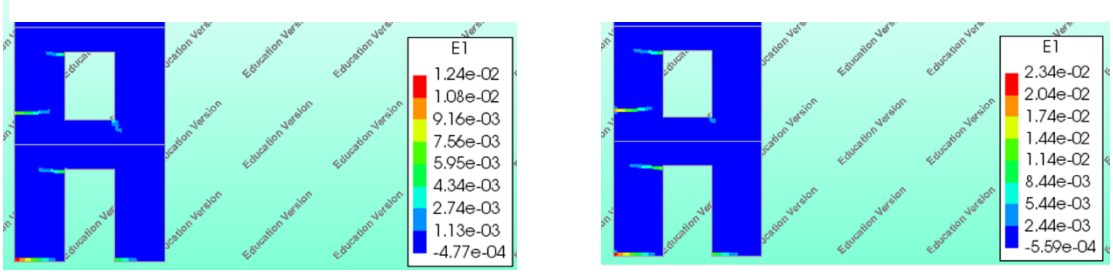

FIGURE 61: MAXIMUM PRINCIPAL STRAIN-LOAD STEP 300 (LEFT) , MAXIMUM PRINCIPAL STRAIN-LOAD STEP 500 (RIGHT)

OBSERVED FAILURE MECHANISM

The failure mechanism that is developed during this pushover assessment is mainly the rocking of pier 1 and pier 3. Because this pushover analysis is only applied in one direction and the wall is symmetric, it could be concluded that also pier 2 and 4 will undergo rocking behaviour in the case of the cyclic loading.

PUSHOVER CURVE: SIMPLE MODEL 1

The graph below shows the pushover curve that is obtained from the results of the analysis in DIANA.

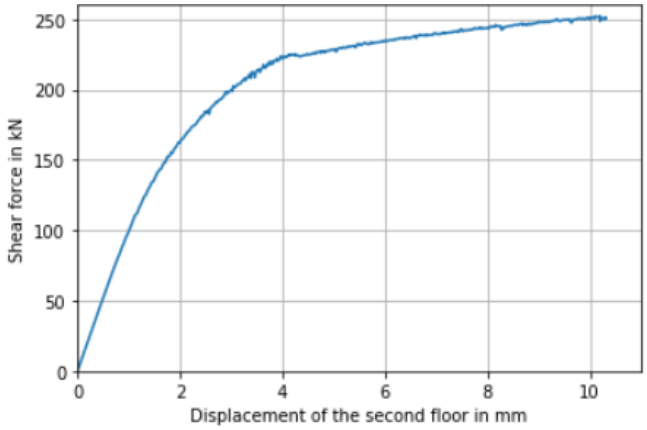

FIGURE 62:PUSHOVER CURVE SIMPLE MODEL 1

12 APPENDIX B: SIMPLE MODEL 1: FULL SLAMA CALCULATIONS

SHEAR CAPACITY OF THE PIERS

The table below shows the shear capacities, drift capacities and the failure mechanisms of each pier.

TABLE 24: OVERVIEW SHEAR AND DRIFT CAPACITY OF EACH PIER

	Shear capacity	Drift capacity	Failure mechanism
Pier 1	61244.98 N	0.012	Rocking
Pier 2	74929.41 N	0.014	Rocking
Pier 3	27950.98N	0.015	Rocking
Pier 4	27950.73 N	0.015	Rocking

PUSHOVER CURVE

The graph below shows the pushover curve that is obtained from the SLaMA calculations.

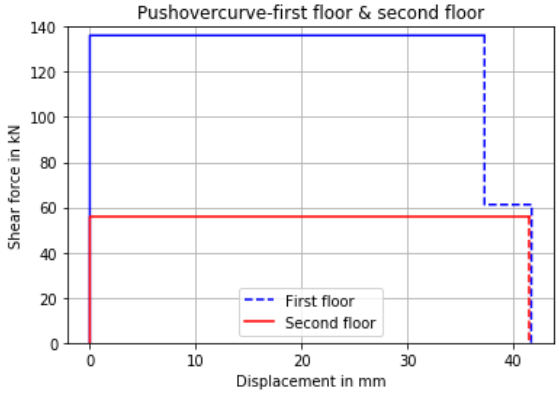

FIGURE 63:PUSHOVER CURVE SIMPLE MODEL 1

ACCELERATION CURVE

The graph below shows the acceleration curve that is obtained from the SLaMA calculations.

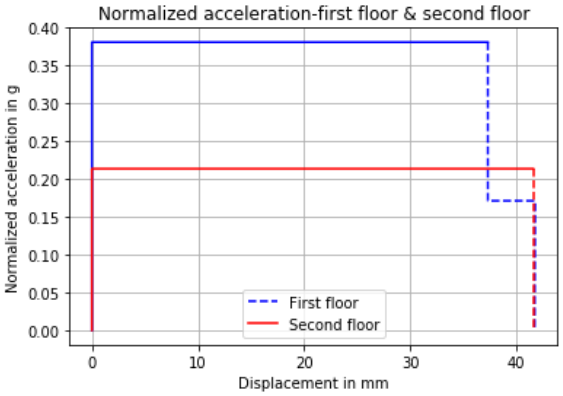

FIGURE 64: ACCELERATION CURVE SIMPLE MODEL 1

MAXIMUM BASE SHEAR FORCE

The maximum base shear force is calculated based on the critical acceleration of the second floor. This acceleration is multiplied by the effective masses.

$$V_{base\ shear} = 0.2135742237\ g \cdot (0.7 \cdot m_{2,eff} + 0.3 \cdot m_{1,eff})$$

$$V_{base\ shear} = 76.35\ kN$$

13 APPENDIX C: SIMPLE MODEL 2: FULL DIANA NLPO FEM ANALYSIS

RESULTS: STRUCTURAL EIGENVALUE ANALYSIS

The first analysis that has been made is the structural eigenvalue analysis. This analysis is required to determine the critical Eigen mode and Eigen frequency. The Eigen mode with the highest participating mass is the critical Eigen mode. In this case Eigen mode 1 is the governing Eigen mode and corresponds to a participating mass percentage 78.65%. The Figure below shows first five Eigen modes and their participating masses.

TABLE 25: GOVERNING EIGEN MODE AND THE PARTICIPATING MASS- SIMPLE MODEL 2

MODE	FREQUENCY	EFF.MASS TX	PERCENTAGE
1	0.89326E+01	0.42578E+05	0.78652E+01

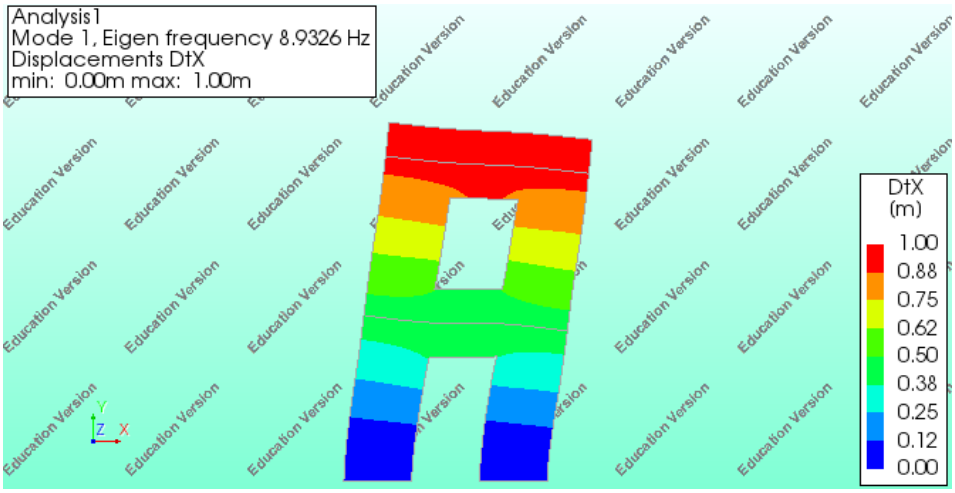

FIGURE 65: GOVERNING EIGEN MODE SIMPLE MODEL 2

RESULTS: STRUCTURAL NONLINEAR ANALYSIS

This part contains the results of the structural nonlinear analysis. The relevant obtained results in this case, are the horizontal deflection, maximum principal strain, observed failure mechanism and the pushover curve.

HORIZONTAL DEFLECTION

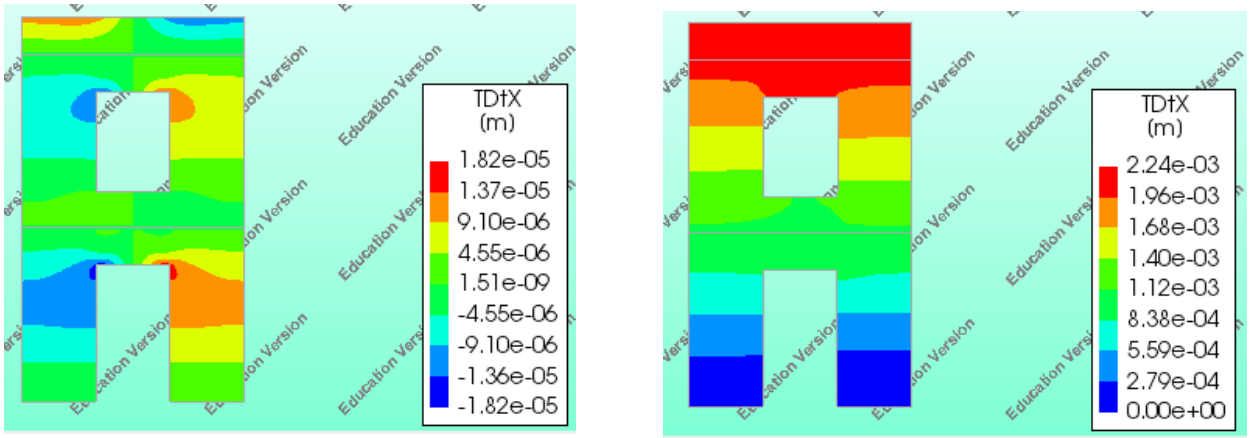

FIGURE 66: HORIZONTAL DEFLECTION STEP 1 (LEFT) , HORIZONTAL DEFLECTION STEP 150 (RIGHT)

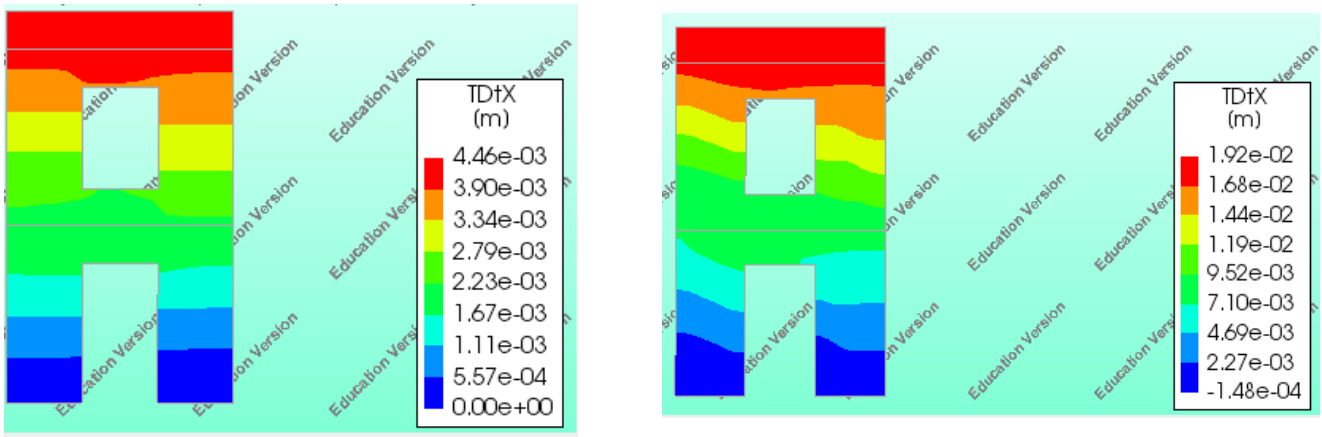

FIGURE 67: HORIZONTAL DEFLECTION STEP 300 (LEFT) , HORIZONTAL DEFLECTION STEP 447 (RIGHT)

MAXIMUM PRINCIPAL STRAIN

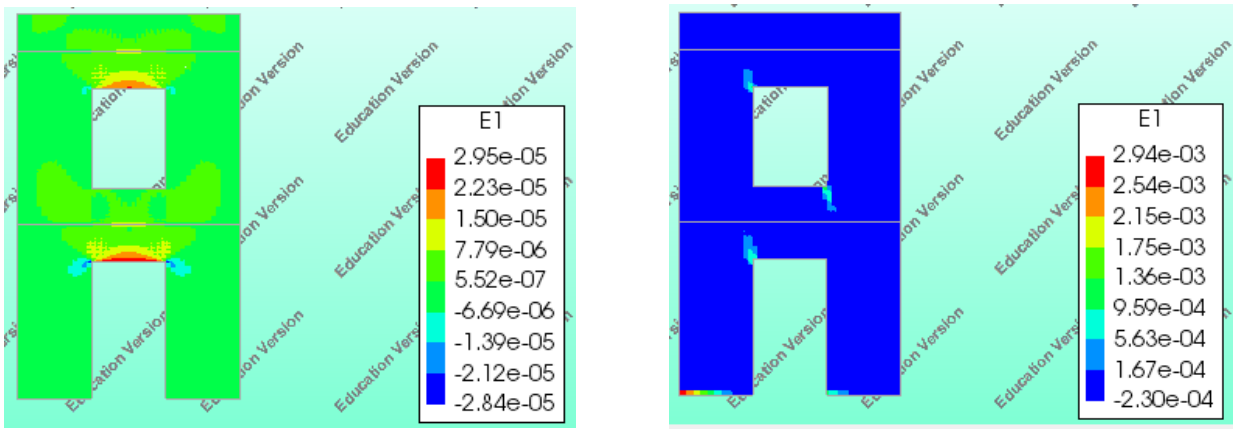

FIGURE 68: MAXIMUM PRINCIPAL STRAIN STEP 1 (LEFT) , MAXIMUM PRINCIPAL STRAIN STEP 150 (RIGHT)

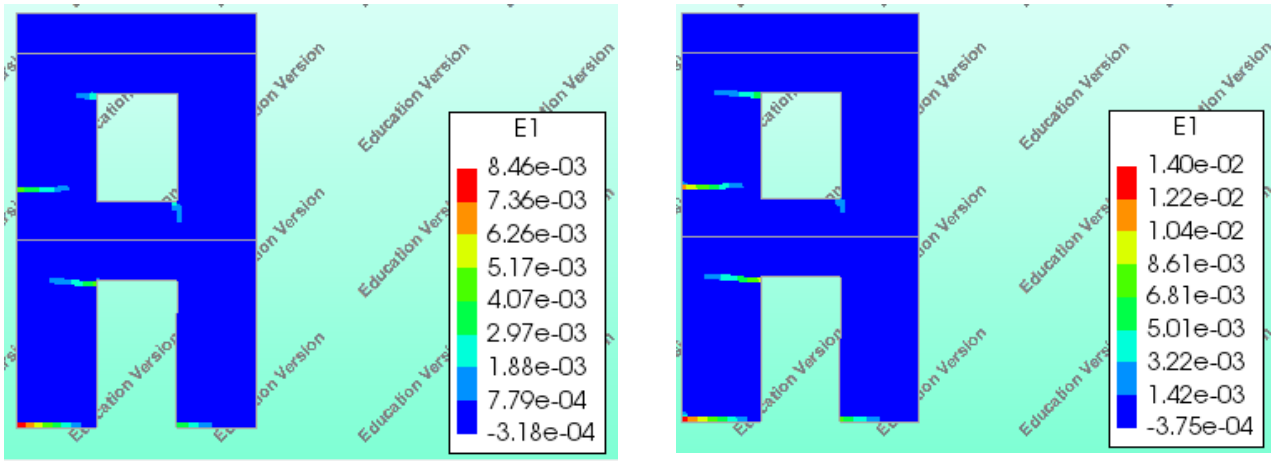

FIGURE 69: MAXIMUM PRINCIPAL STRAIN STEP 300 (LEFT) , MAXIMUM PRINCIPAL STRAIN STEP 447 (RIGHT)

OBSERVED FAILURE MECHANISM

The failure mechanism that is developed during this pushover assessment is mainly the rocking of pier 1 and pier 3. Because this pushover analysis is only applied in one direction and the wall is symmetric, it could be concluded that also pier 2 and 4 will undergo rocking behaviour in the case of the cyclic loading.

PUSHOVER CURVE: SIMPLE MODEL 2

The graph beside shows the pushover curve that is obtained from the results of the analysis in DIANA.

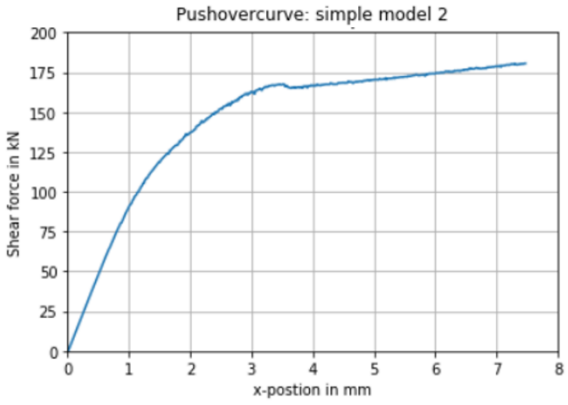

FIGURE 70:PUSHOVER CURVE SIMPLE MODEL 2

14 APPENDIX D: SIMPLE MODEL 2: FULL SLAMA CALCULATIONS

SHEAR CAPACITY OF THE PIERS

The table below shows the shear capacities, drift capacities and the failure mechanisms of each pier.

	Shear capacity	Drift capacity	Failure mechanism
Pier 1	$31977.99N$	0.013	Rocking
Pier 2	$37667.25N$	0.015	Rocking
Pier 3	$18410.51N$	0.015	Rocking
Pier 4	$18410.42N$	0.015	Rocking

PUSHOVER CURVE

The graph below shows the pushover curve that is obtained from the SLaMA calculations.

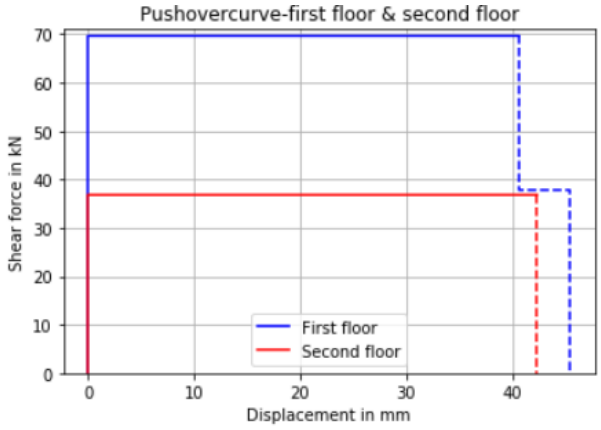

FIGURE 71: PUSHOVER CURVE SIMPLE MODEL 2

ACCELERATION CURVE

The graph below shows the acceleration curve that is obtained from the SLaMA calculations.

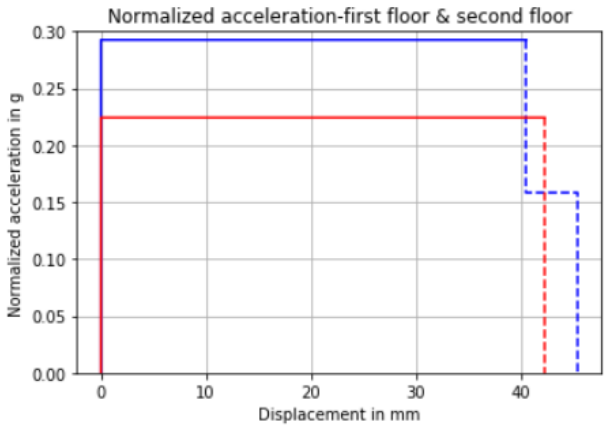

FIGURE 72: ACCELERATION SIMPLE MODEL 2

MAXIMUM BASE SHEAR FORCE

The maximum base shear force is calculated based on the critical acceleration of the second floor. This acceleration is multiplied by the effective masses.

$$V_{base\ shear} = 0.2242363543\ g \cdot (0.68 \cdot m_{2,eff} + 0.32 \cdot m_{1,eff})$$

$$V_{base\ shear} = 53.39\ kN$$

15 APPENDIX E: SIMPLE MODEL 3: FULL DIANA NLPO FEM ANALYSIS

RESULTS: STRUCTURAL EIGENVALUE ANALYSIS

The first analysis that has been made is the structural eigenvalue analysis. This analysis is required to determine the critical Eigen mode and Eigen frequency. The Eigen mode with the highest participating mass is the critical Eigen mode. In this case Eigen mode 1 is the governing Eigen mode and corresponds to a participating mass percentage 82.08%. The Figure below shows first five Eigen modes and their participating masses.

TABLE 26: GOVERNING EIGEN MODE AND THE PARTICIPATING MASS- SIMPLE MODEL 3

MODE	FREQUENCY	EFF.MASS TX	PERCENTAGE	CUM.PERCENT
1	0.95949E+01	0.62246E+05	0.82080E+02	0.82080E+02

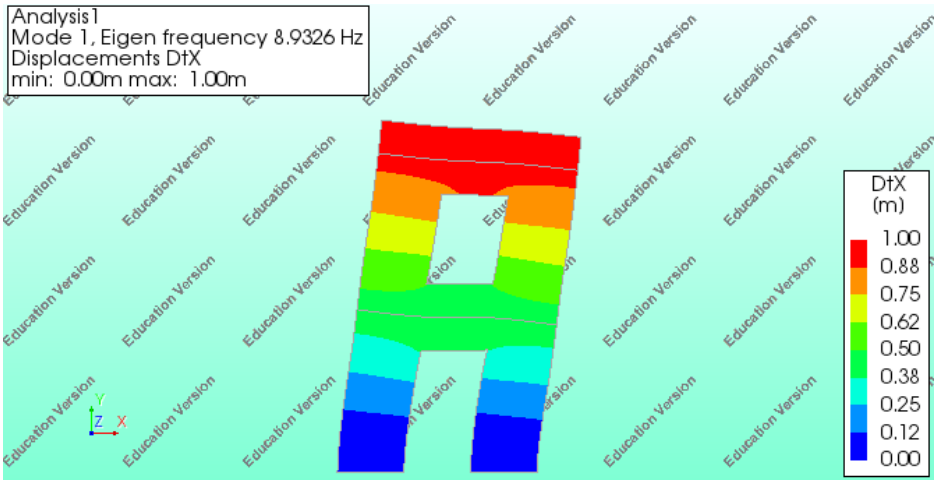

FIGURE 73: GOVERNING EIGEN MODE SIMPLE MODEL 3

RESULTS: STRUCTURAL NONLINEAR ANALYSIS

This part contains the results of the structural nonlinear analysis. The relevant obtained results in this case, are the horizontal deflection, maximum principal strain, observed failure mechanism and the pushover curve.

HORIZONTAL DEFLECTION

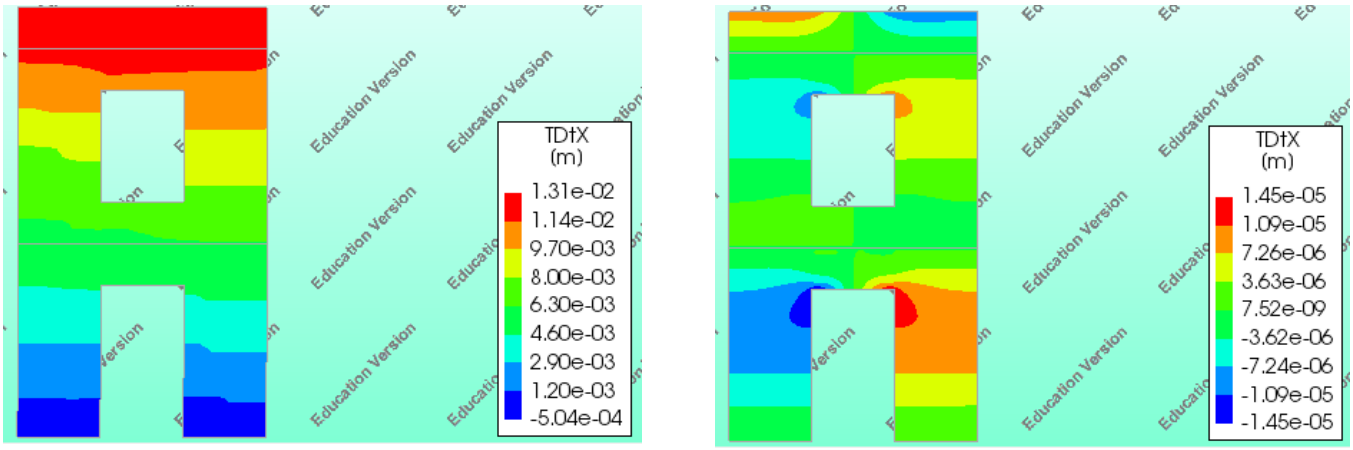

FIGURE 74: HORIZONTAL DEFLECTION STEP 1 (LEFT) , HORIZONTAL DEFLECTION STEP 51 (RIGHT)

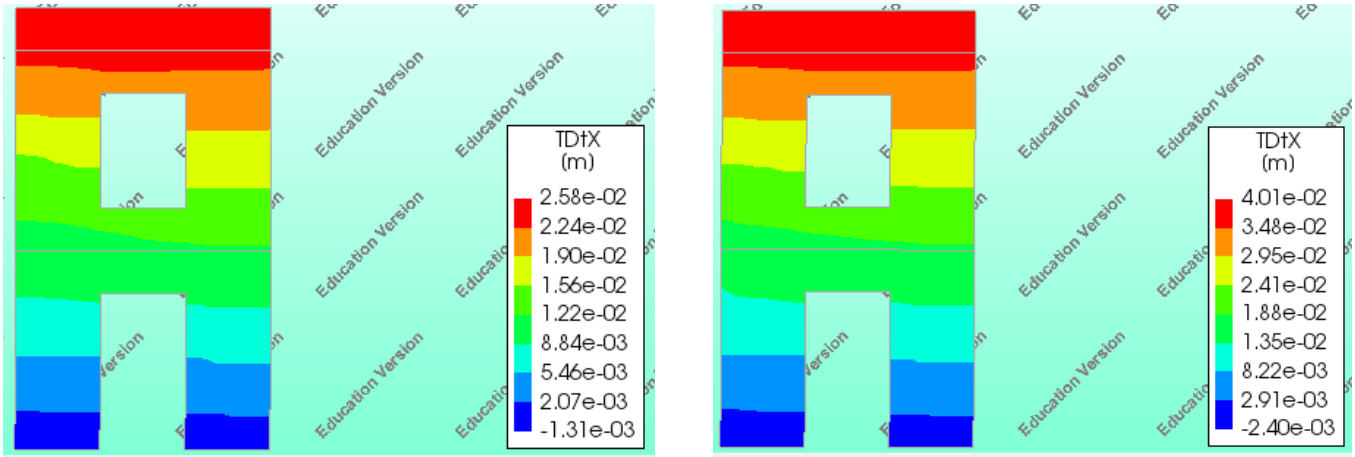

FIGURE 75: HORIZONTAL DEFLECTION STEP 100 (LEFT) , HORIZONTAL DEFLECTION STEP 156 (RIGHT)

MAXIMUM PRINCIPAL STRAIN

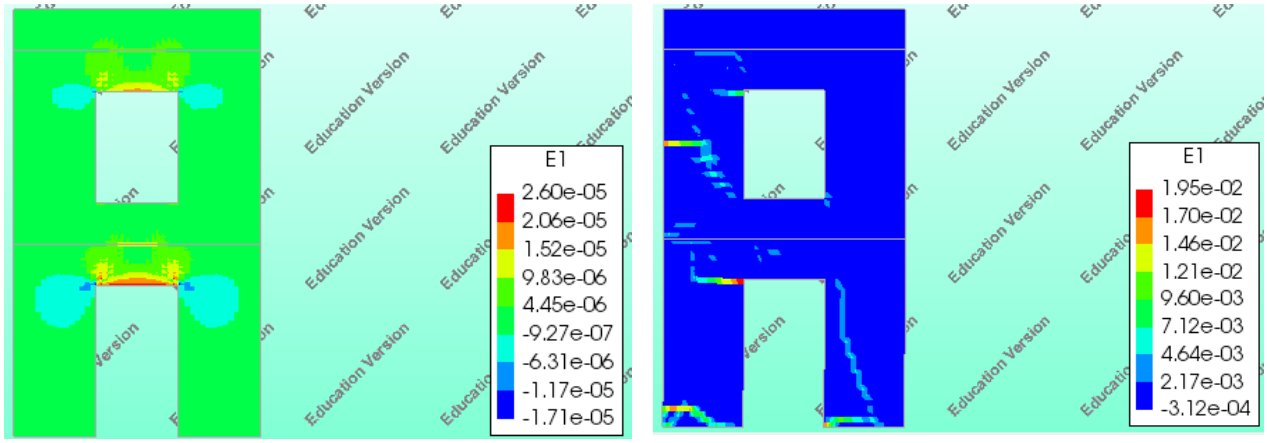

FIGURE 76: MAXIMUM PRINCIPAL STRAIN STEP 1 (LEFT) , MAXIMUM PRINCIPAL STRAIN STEP 51 (RIGHT)

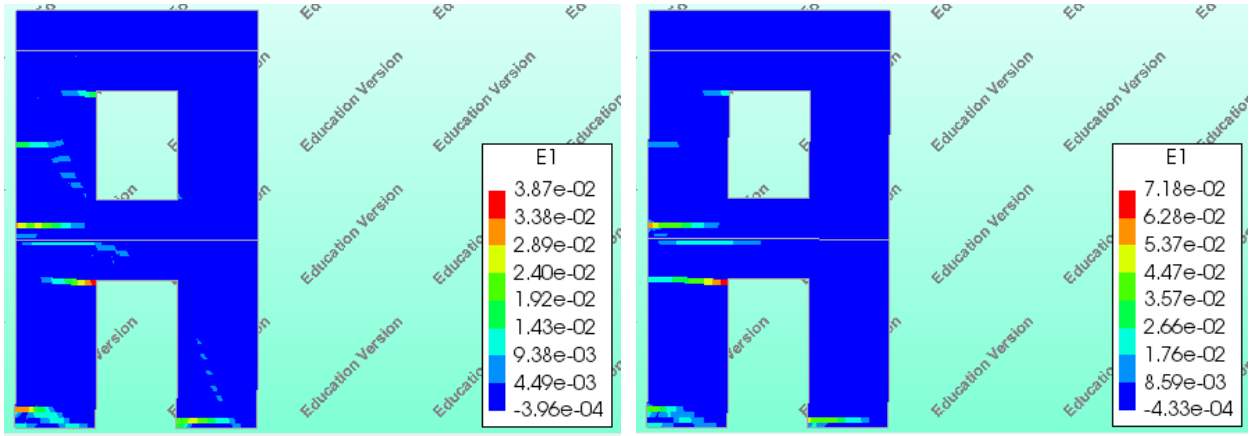

FIGURE 77: MAXIMUM PRINCIPAL STRAIN STEP 100 (LEFT) , MAXIMUM PRINCIPAL STRAIN STEP 156 (RIGHT)

OBSERVED FAILURE MECHANISM

The failure mechanism that is developed during this pushover assessment is mainly the rocking of pier 1 ,2 and 3. But step 51 and step 100 show also the shear failure of pier 2 and 3.

PUSHOVER CURVE: SIMPLE MODEL 3

The graph below shows the pushover curve that is obtained from the results of the analysis in DIANA.

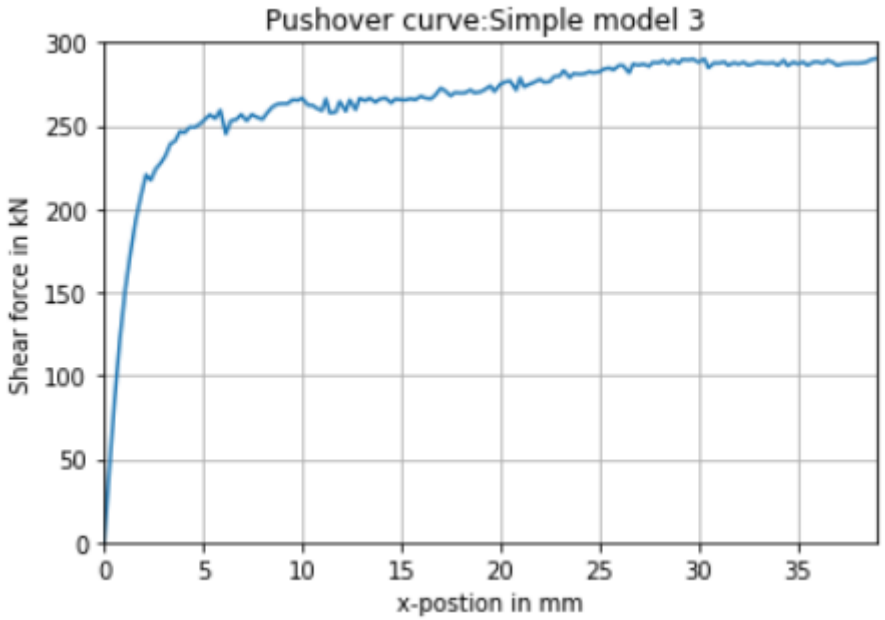

FIGURE 78:PUSHOVER CURVE SIMPLE MODEL 3

16 APPENDIX F: SIMPLE MODEL 3: FULL SLAMA CALCULATIONS

SHEAR CAPACITY OF THE PIERS

The table below shows the shear capacities, drift capacities and the failure mechanisms of each pier.

TABLE 27: OVERVIEW SHEAR AND DRIFT CAPACITY OF EACH PIER

	Shear capacity	Drift capacity	Failure mechanism
Pier 1	125480.30 N	0.012348	Shear (Vbr1)
Pier 2	123429.94 N	0.015187	Rocking
Pier 3	44646.26 N	0.015679	Rocking
Pier 4	44645.87 N	0.015679	Rocking

PUSHOVER CURVE

The graph below shows the pushover curve that is obtained from the SLaMA calculations.

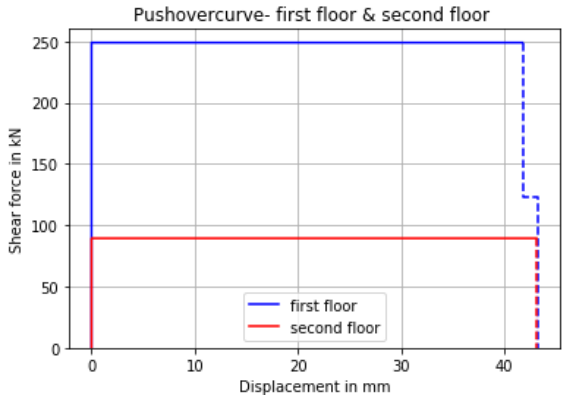

FIGURE 79:PUSHOVER CURVE SIMPLE MODEL 3

ACCELERATION CURVE

The graph below shows the acceleration curve that is obtained from the SLaMA calculations.

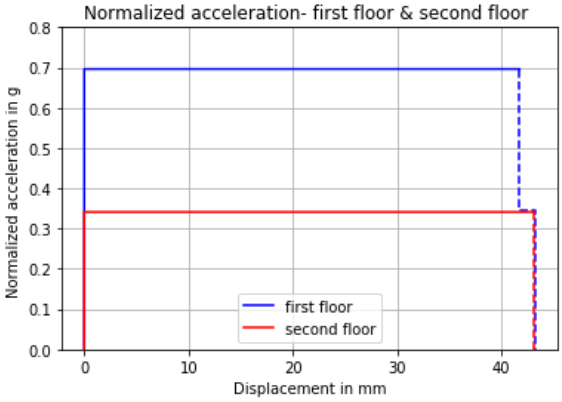

FIGURE 80: ACCELERATION CURVE SIMPLE MODEL 3

MAXIMUM BASE SHEAR FORCE

The maximum base shear force is calculated based on the critical acceleration of the second floor. This acceleration is multiplied by the effective masses.

$$V_{base\ shear} = 0.34115\ g \cdot (0.7 \cdot m_{2,eff} + 0.3 \cdot m_{1,eff})$$

$$V_{base\ shear} = 122.0\ kN$$

17 APPENDIX G: SIMPLE MODEL 4: FULL DIANA NLPO FEM ANALYSIS

RESULTS: STRUCTURAL EIGENVALUE ANALYSIS

The first analysis that has been made is the structural eigenvalue analysis. This analysis is required to determine the critical Eigen mode and Eigen frequency. The Eigen mode with the highest participating mass is the critical Eigen mode. In this case Eigen mode 1 is the governing Eigen mode and corresponds to a participating mass percentage 83.23%. The Figure below shows first five Eigen modes and their participating masses.

TABLE 28: GOVERNING EIGEN MODE AND THE PARTICIPATING MASS- SIMPLE MODEL 4

MODE	FREQUENCY	EFF.MASS TX	PERCENTAGE	CUM.PERCENT
1	0.46062E+02	0.27024E+05	0.8233E+02	0.83233E+02

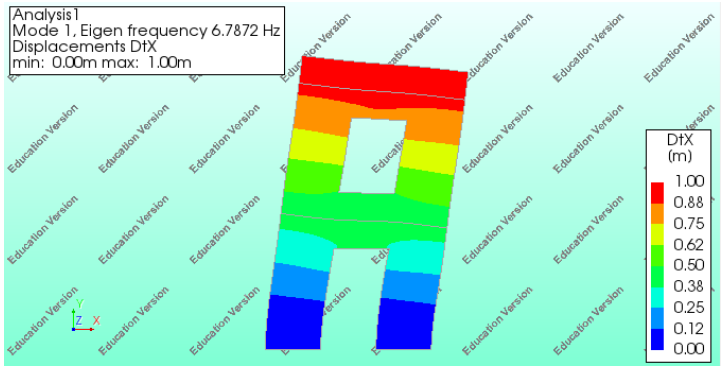

FIGURE 81: THE GOVERNING EIGEN MODE SIMPLE MODEL 4

RESULTS: STRUCTURAL NONLINEAR ANALYSIS

This part contains the results of the structural nonlinear analysis. The relevant obtained results in this case, are the horizontal deflection, maximum principal strain, observed failure mechanism and the pushover curve.

HORIZONTAL DEFLECTION

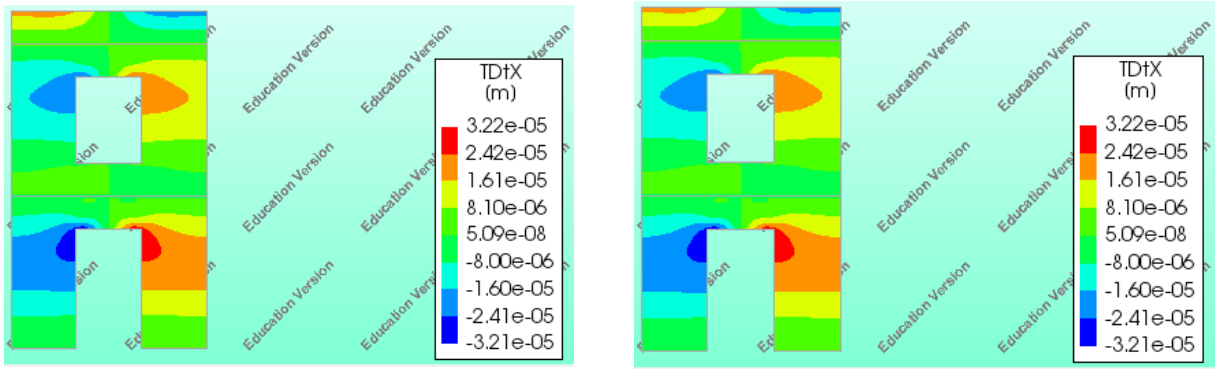

FIGURE 82: HORIZONTAL DEFLECTION STEP 1 (LEFT) , HORIZONTAL DEFLECTION - STEP 20 (RIGHT)

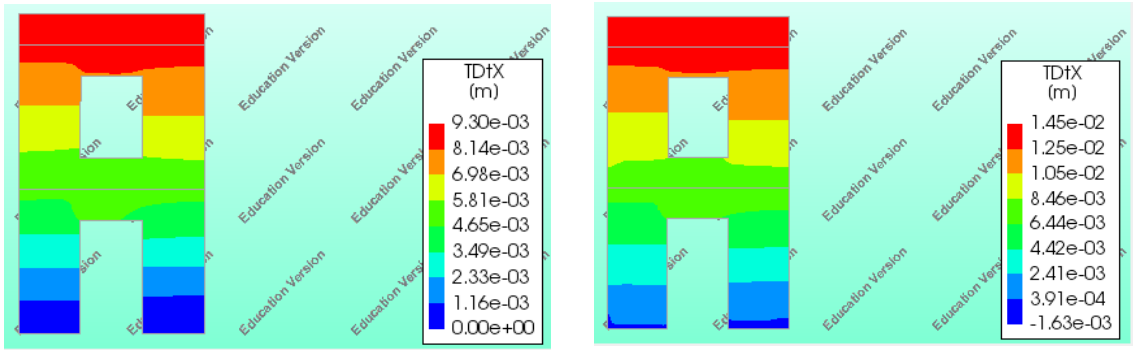

FIGURE 83: HORIZONTAL DEFLECTION STEP 40 (LEFT) , HORIZONTAL DEFLECTION - STEP 62 (RIGHT)

MAXIMUM PRINCIPAL STRAIN

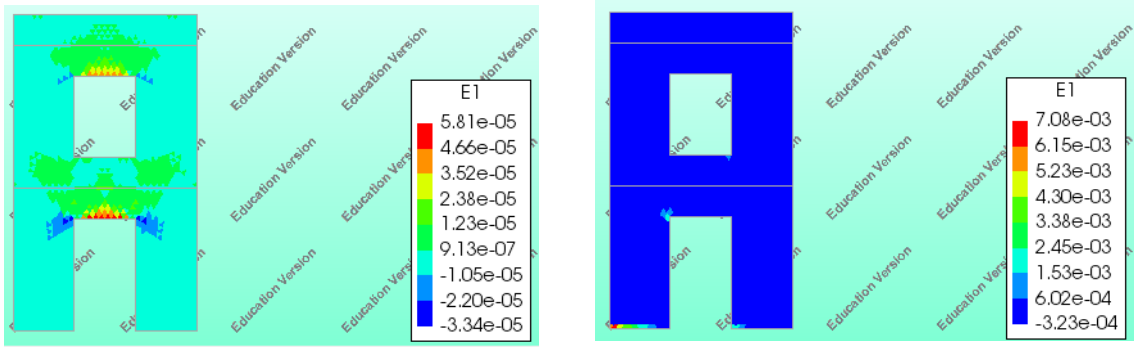

FIGURE 84: MAXIMUM PRINCIPAL STRAIN-LOAD STEP 1 (LEFT) , MAXIMUM PRINCIPAL STRAIN-LOAD STEP 20 (RIGHT)

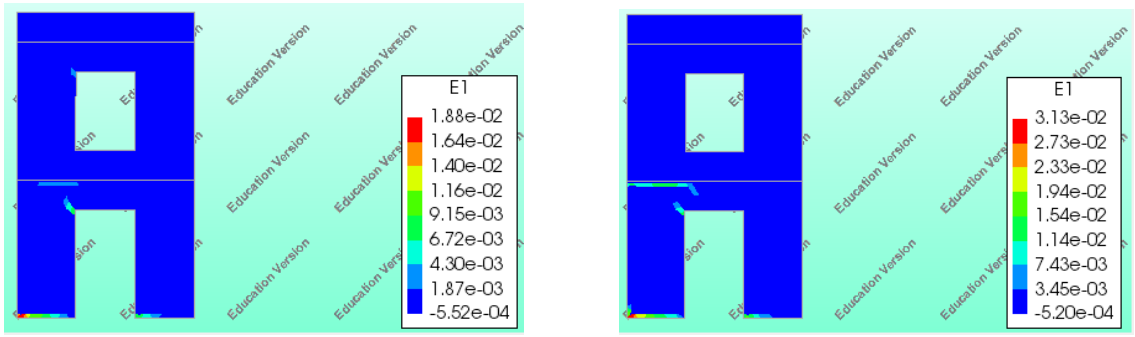

FIGURE 85: MAXIMUM PRINCIPAL STRAIN-LOAD STEP 40 (LEFT) , MAXIMUM PRINCIPAL STRAIN-LOAD STEP 62 (RIGHT)

OBSERVED FAILURE MECHANISM

The failure mechanism that is developed during this pushover assessment is mainly the rocking of pier 1. Because this pushover analysis is only applied in one direction and the wall is symmetric, it could be concluded that also pier 2 will undergo rocking behaviour.

PUSHOVER CURVE: SIMPLE MODEL 4

The graph beside shows the pushover curve that is obtained from the result of the analysis in DIANA.

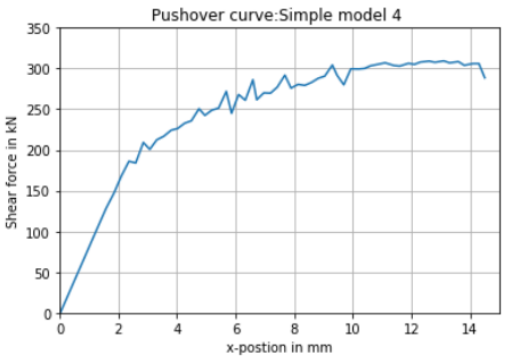

FIGURE 86: PUSHOVER CURVE SIMPLE MODEL 4

18 APPENDIX H: SIMPLE MODEL 4: FULL SLAMA CALCULATIONS

SHEAR CAPACITY OF THE PIERS

The table below shows the shear capacities, drift capacities and the failure mechanisms of each pier.

TABLE 29: OVERVIEW SHEAR AND DRIFT CAPACITY OF EACH PIER

	Shear capacity	Drift capacity	Failure mechanism
Pier 1	62110.07 N	0.012	Rocking
Pier 2	75940.52 N	0.014	Rocking
Pier 3	28079.65 N	0.015	Rocking
Pier 4	28079.40 N	0.015	Rocking

PUSHOVER CURVE

The graph below shows the pushover curve that is obtained from the SLaMA calculations.

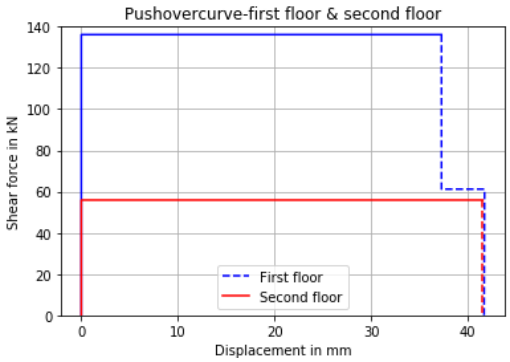

FIGURE 87: PUSHOVER CURVE SIMPLE MODEL 4

ACCELERATION CURVE

The graph below shows the acceleration curve that is obtained from the SLaMA calculations.

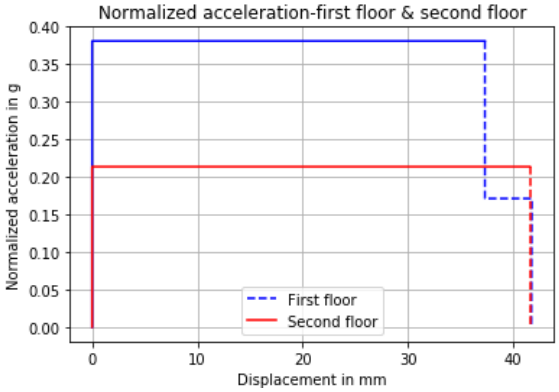

FIGURE 88: ACCELERATION SIMPLE MODEL 5

MAXIMUM BASE SHEAR FORCE

The maximum base shear force is calculated based on the critical acceleration of the second floor. This acceleration is multiplied by the effective masses.

$$V_{base\ shear} = 0.2145675921\ g \cdot (0.7 \cdot m_{2,eff} + 0.3 \cdot m_{1,eff})$$

$$V_{base\ shear} = 76.70\ kN$$

19 APPENDIX I: SIMPLE MODEL 5: FULL DIANA NLPO FEM ANALYSIS

RESULTS: STRUCTURAL EIGENVALUE ANALYSIS

The first analysis that has been made is the structural eigenvalue analysis. This analysis is required to determine the critical Eigen mode and Eigen frequency. The Eigen mode with the highest participating mass is the critical Eigen mode. In this case Eigen mode 1 is the governing Eigen mode and corresponds to a participating mass percentage 83.83%. The Figure below shows first five Eigen modes and their participating masses.

TABLE 30: GOVERNING EIGEN MODE AND THE PARTICIPATING MASS- SIMPLE MODEL 5

MODE	FREQUENCY	EFF.MASS TX	PERCENTAGE	CUM.PERCENT
1	0.61374E+01	0.77774E+05	0.83829E+02	0.83829E+02

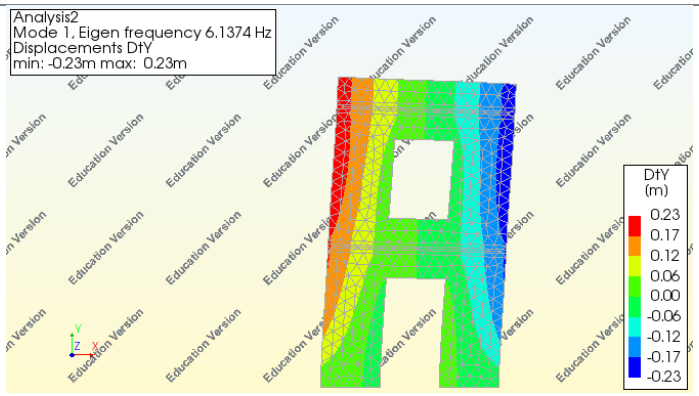

FIGURE 89: GOVERNING EIGEN MODE SINMPLE MODEL 5

RESULTS: STRUCTURAL NONLINEAR ANALYSIS

This part contains the results of the structural nonlinear analysis. The relevant obtained results in this case, are the horizontal deflection, maximum principal strain, observed failure mechanism and the pushover curve.

HORIZONTAL DEFLECTION

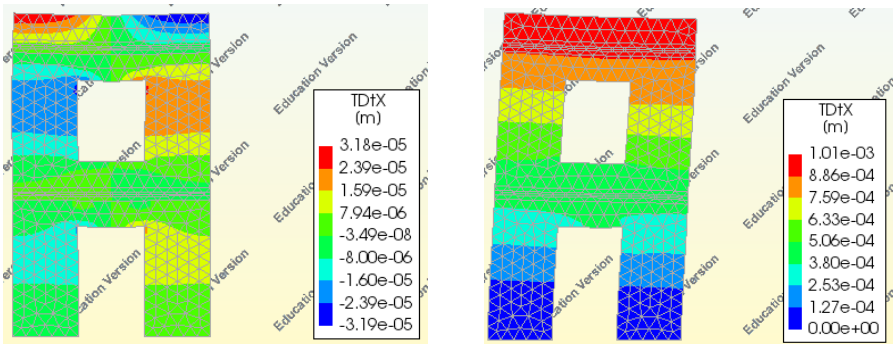

FIGURE 90: HORIZONTAL DEFLECTION STEP 1 (LEFT) , HORIZONTAL DEFLECTION STEP 150 (RIGHT)

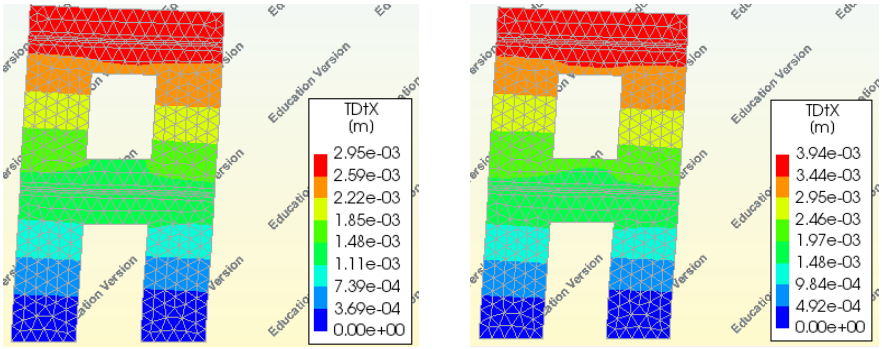

FIGURE 91: HORIZONTAL DEFLECTION STEP 450 (LEFT) , HORIZONTAL DEFLECTION STEP 606 (RIGHT)

MAXIMUM PRINCIPAL STRAIN

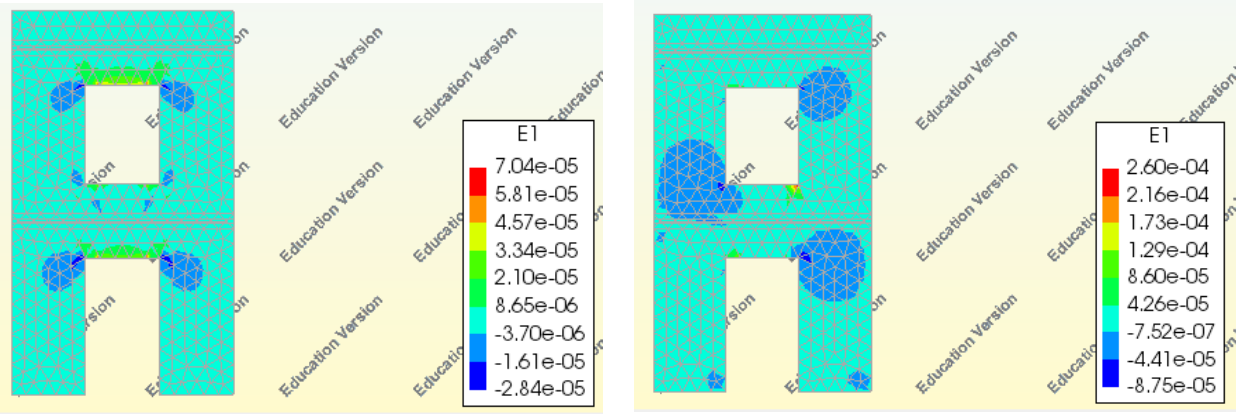

FIGURE 92: MAXIMUM PRINCIPAL STRAIN STEP 1 (LEFT) , MAXIMUM PRINCIPAL STRAIN STEP 150 (RIGHT)

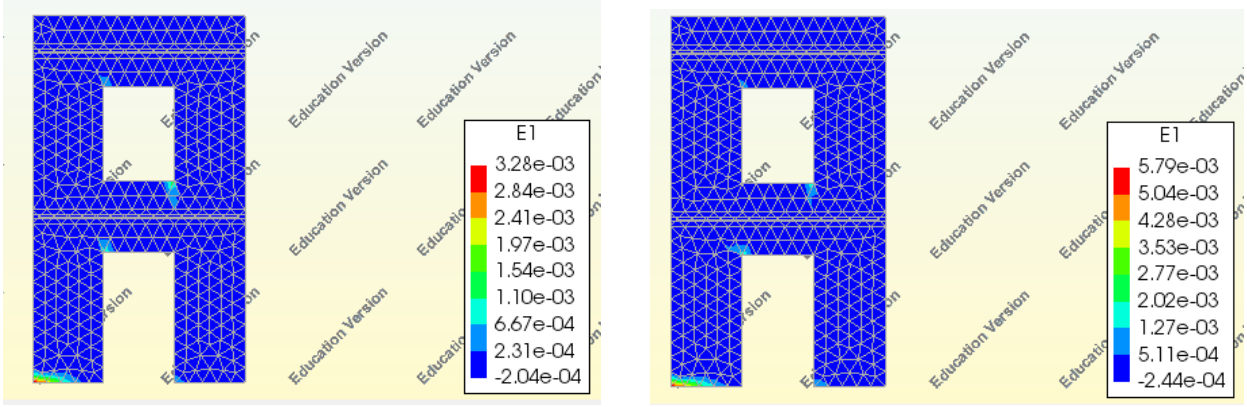

FIGURE 93: MAXIMUM PRINCIPAL STRAIN STEP 450 (LEFT) , MAXIMUM PRINCIPAL STRAIN STEP 606 (RIGHT)

OBSERVED FAILURE MECHANISM

The failure mechanism that is developed during this pushover assessment is mainly the rocking of pier 1. Because this pushover analysis is only applied in one direction and the wall is symmetric, it could be concluded that also pier 2 will undergo rocking behaviour.

PUSHOVER CURVE: SIMPLE MODEL 5

The graph below shows the pushover curve that is obtained from the result of the analysis in DIANA.

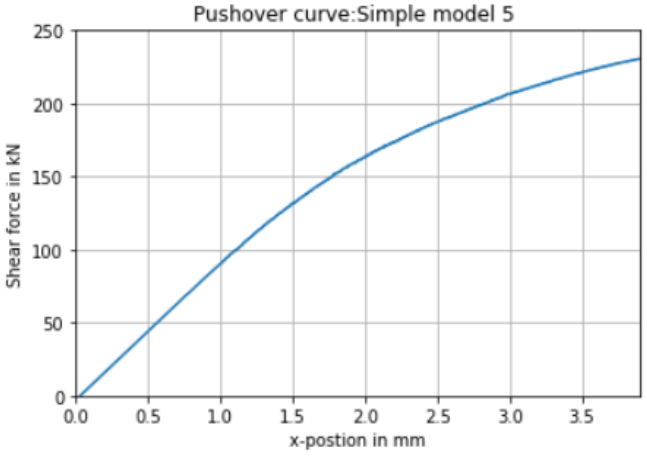

FIGURE 94:PUSHOVER CURVE SIMPLE MODEL 5

20 APPENDIX J: SIMPLE MODEL 5: FULL SLAMA CALCULATIONS

SHEAR CAPACITY OF THE PIERS

The table below shows the shear capacities, drift capacities and the failure mechanisms of each pier.

TABLE 31: OVERVIEW SHEAR AND DRIFT CAPACITY OF EACH PIER

	Shear capacity	**Drift capacity**	**Failure mechanism**
Pier 1	122489.96 N	0.011928275257849686	Rocking
Pier 2	149858.82 N	0.01356097780693261	Rocking
Pier 3	55901.95 N	0.015116072532067334	Rocking
Pier 4	55901.46 N	0.015099473803160027	Rocking

PUSHOVER CURVE

The graph below shows the pushover curve that is obtained from the SLaMA calculations.

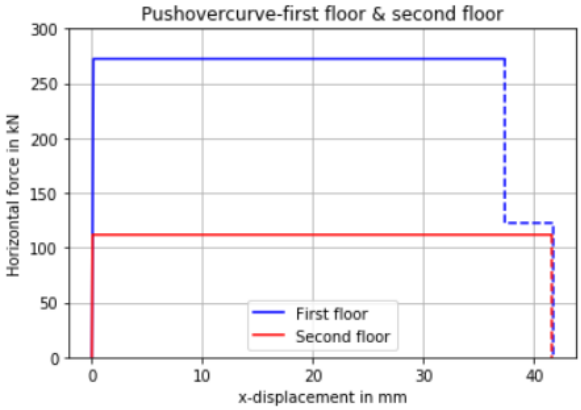

FIGURE 95:PUSHOVER CURVE SIMPLE MODEL 5

ACCELERATION CURVE

The graph below shows the acceleration curve that is obtained from the SLaMA calculations.

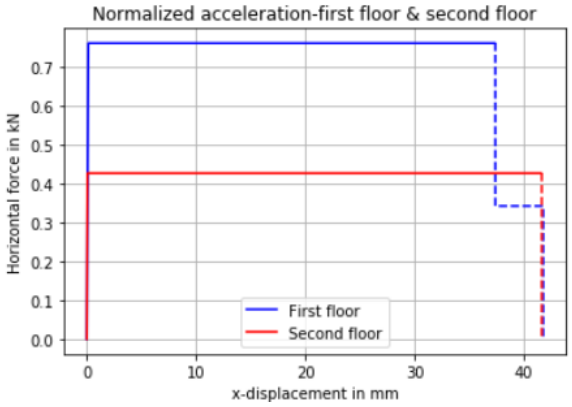

FIGURE 96: ACCELERATION CURVE SIMPLE MODEL 5

MAXIMUM BASE SHEAR FORCE

The maximum base shear force is calculated based on the critical acceleration of the second floor. This acceleration is multiplied by the effective masses.

$$V_{base\ shear} = 0.4271614757\ \ g \cdot (0.7 \cdot m_{2,eff} + 0.3 \cdot m_{1,eff})$$

$$V_{base\ shear} = 152.70\ kN$$

21 APPENDIX K: SIMPLE MODEL 6: FULL DIANA NLPO FEM ANALYSIS

RESULTS: STRUCTURAL EIGENVALUE ANALYSIS

The first analysis that has been made is the structural eigenvalue analysis. This analysis is required to determine the critical Eigen mode and Eigen frequency. The Eigen mode with the highest participating mass is the critical Eigen mode. In this case Eigen mode 1 is the governing Eigen mode and corresponds to a participating mass percentage 80.9%. The Figure below shows first five Eigen modes and their participating masses.

TABLE 32: GOVERNING EIGEN MODE AND THE PARTICIPATING MASS- SIMPLE MODEL 6

MODE	FREQUENCY	EFF.MASS TX	PERCENTAGE	CUM.PERCENT
1	0.74597E+01	0.62000E+05	0.80903E+02	0.80903E+02
2	0.22286E+02	0.10305E+05	0.13447E+02	0.94351E+02
3	0.27794E+02	0.23906E-05	0.31195E-08	0.94351E+02
4	0.44107E+02	0.15305E+01	0.19971E-02	0.94353E+02
5	0.55840E+02	0.92436E-07	0.12062E-09	0.94353E+02

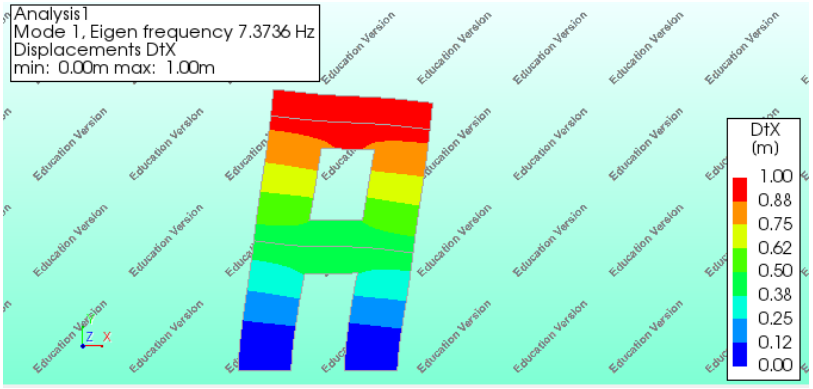

FIGURE 97: GOVERNING EIGEN MODE SIMPLE MODEL 6

RESULTS: STRUCTURAL NONLINEAR ANALYSIS

This part contains the results of the structural nonlinear analysis. The relevant obtained results in this case, are the horizontal deflection, maximum principal strain, observed failure mechanism and the pushover curve.

HORIZONTAL DEFLECTION

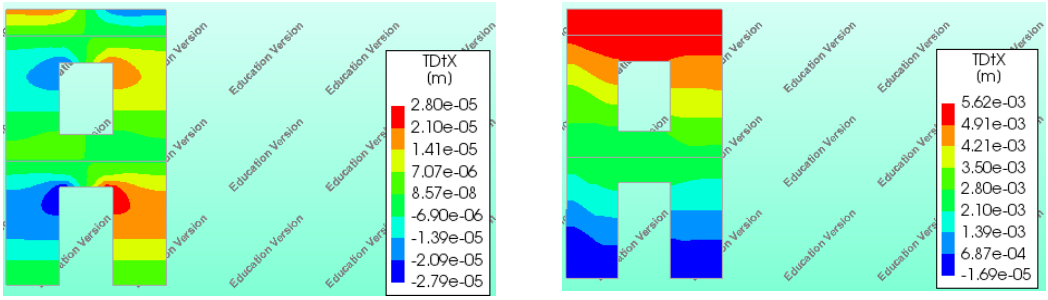

FIGURE 98: HORIZONTAL DEFLECTION STEP 1 (LEFT) , HORIZONTAL DEFLECTION STEP 15 (RIGHT)

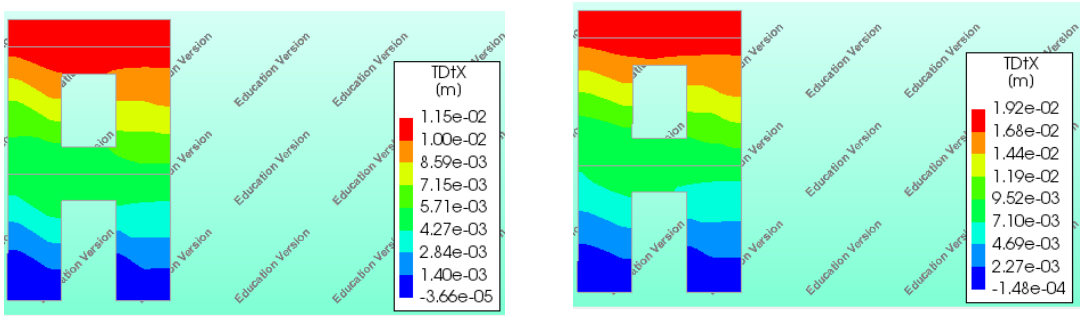

FIGURE 99: HORIZONTAL DEFLECTION STEP 30 (LEFT) , HORIZONTAL DEFLECTION STEP 49 (RIGHT)

MAXIMUM PRINCIPAL STRAIN

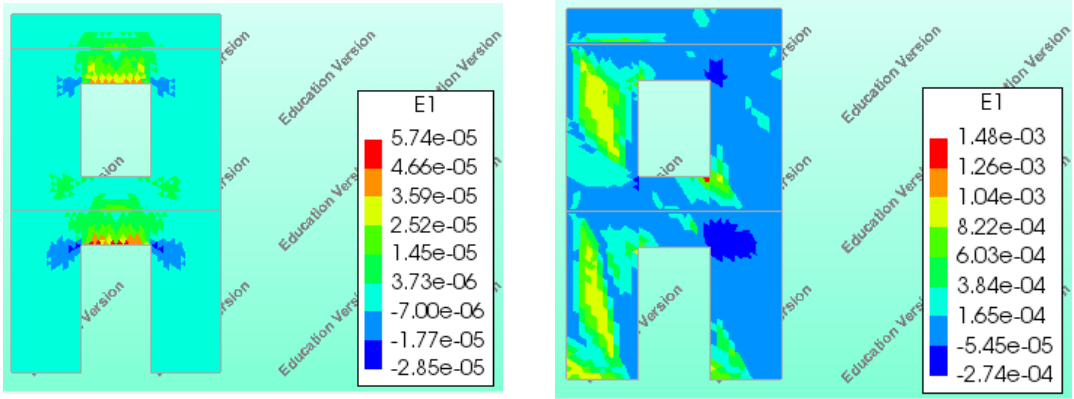

FIGURE 100: MAXIMUM PRINCIPAL STRAIN STEP 1 (LEFT) , MAXIMUM PRINCIPAL STRAIN STEP 15 (RIGHT)

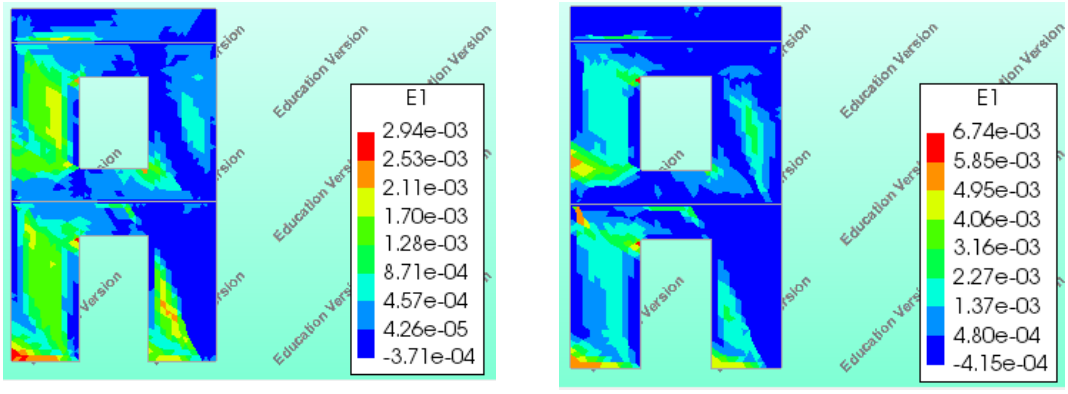

FIGURE 101: MAXIMUM PRINCIPAL STRAIN STEP 30 (LEFT) , MAXIMUM PRINCIPAL STRAIN STEP 49 (RIGHT)

OBSERVED FAILURE MECHANISM

The failure mechanism that is developed during this pushover assessment is a combination of rocking and shear failure of all the piers.

PUSHOVER CURVE: SIMPLE MODEL 6

The graph below shows the pushover curve that is obtained from the result of the analysis in DIANA.

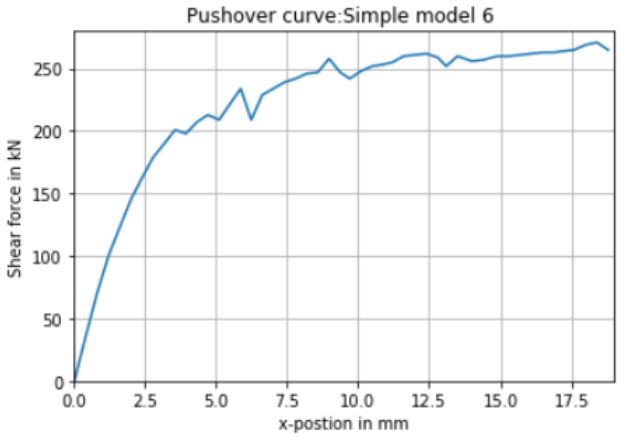

FIGURE 102:PUSHOVER CURVE SIMPLE MODEL 6

22 APPENDIX L: SIMPLE MODEL 6: FULL SLAMA CALCULATIONS

SHEAR CAPACITY OF THE PIERS

The table below shows the shear capacities, drift capacities and the failure mechanisms of each pier.

TABLE 33: OVERVIEW SHEAR AND DRIFT CAPACITY OF EACH PIER

	Shear capacity	Drift capacity	Failure mechanism
Pier 1	61244.98 *N*	0.0119	Rocking
Pier 2	74929.41 *N*	0.0136	Rocking
Pier 3	27950.98*N*	0.0151	Rocking
Pier 4	27950.73 *N*	0.0151	Rocking

PUSHOVER CURVE

The graph below shows the pushover curve that is obtained from the SLaMA calculations.

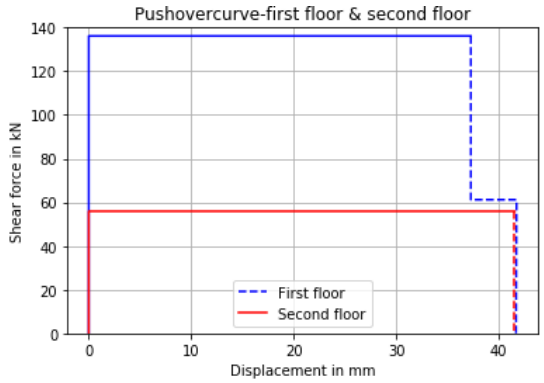

FIGURE 103:PUSHOVER CURVE SIMPLE MODEL 6

ACCELERATION CURVE

The graph below shows the acceleration curve that is obtained from the SLaMA calculations.

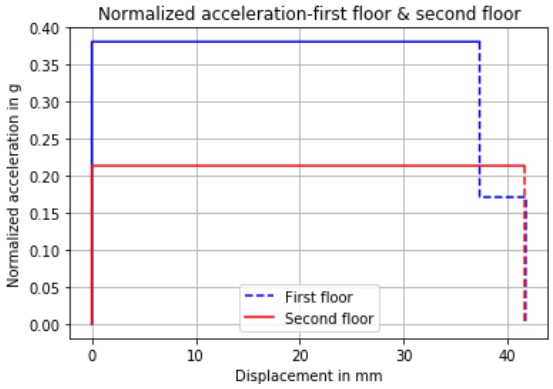

FIGURE 104: ACCELERATION CURVE SIMPLE MODEL 6

MAXIMUM BASE SHEAR FORCE

The maximum base shear force is calculated based on the critical acceleration of the second floor. This acceleration is multiplied by the effective masses.

$$V_{base\ shear} = 0.2135742237\ g \cdot (0.7 \cdot m_{2,eff} + 0.3 \cdot m_{1,eff})$$

$$V_{base\ shear} = 76.35\ kN$$

23 APPENDIX M: CASE STUDY- 2D-1A: FULL DIANA NLPO FEM ANALYSIS

The first analysis that has been made is the structural eigenvalue analysis. This analysis is required to determine the critical Eigen mode and Eigen frequency. The Eigen mode with the highest participating mass is the critical Eigen mode. In this case Eigen mode 1 is the governing Eigen mode and corresponds to a participating mass percentage 55.5%. The Figure below shows first five Eigen modes and their participating masses.

TABLE 34:GOVERNING EIGEN MODE AND THE PARTICIPATING MASS- CASE STUDY-2D-1A

MODE	FREQUENCY	EFF.MASS TX	PERCENTAGE	CUM.PERCENT
1	0.11966E+02	0.51485E+04	0.55482E+02	0.55482E+02

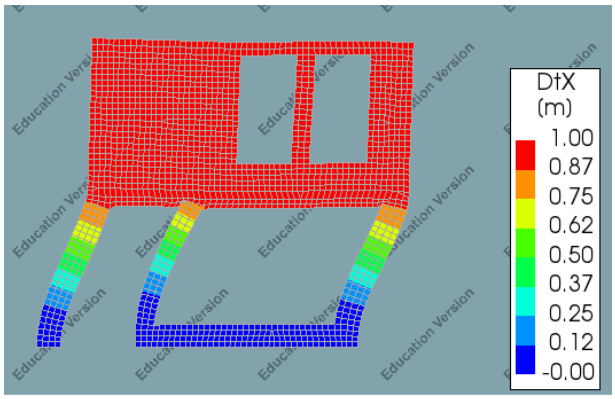

FIGURE 105: THE GOVERNING EIGEN MODE CASE STUDY-2D-1A

RESULTS: STRUCTURAL NONLINEAR ANALYSIS

This part contains the results of the structural nonlinear analysis. The relevant obtained results in this case, are the horizontal deflection, maximum principal strain, observed failure mechanism and the pushover curve.

HORIZONTAL DEFLECTION

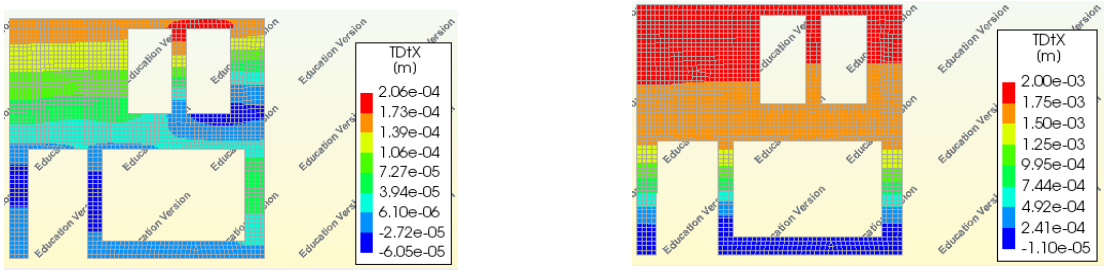

FIGURE 106: HORIZONTAL DEFLECTION STEP 1 (LEFT) , HORIZONTAL DEFLECTION STEP 10 (RIGHT)

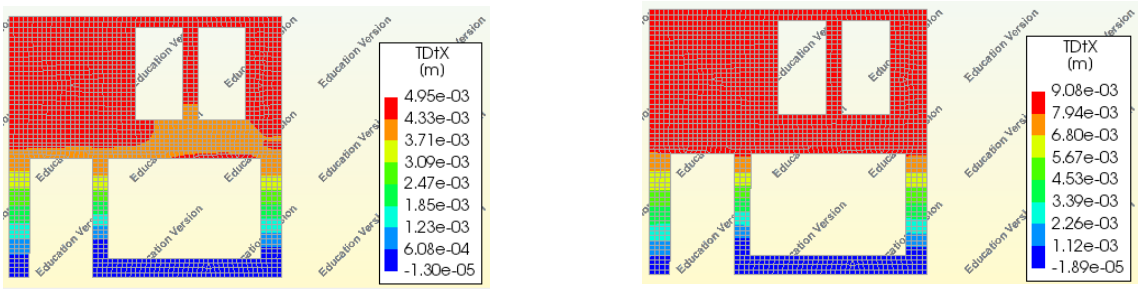

FIGURE 107: HORIZONTAL DEFLECTION STEP 25 (LEFT) , HORIZONTAL DEFLECTION STEP 46 (RIGHT)

MAXIMUM PRINCIPAL STRAIN

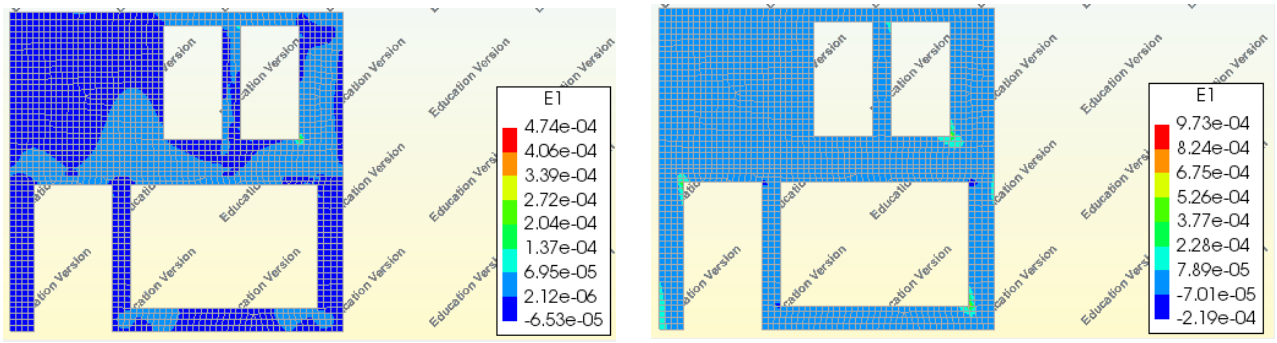

FIGURE 108: MAXIMUM PRINCIPAL STRAIN-LOAD STEP 1 (LEFT) , MAXIMUM PRINCIPAL STRAIN-LOAD STEP 10 (RIGHT)

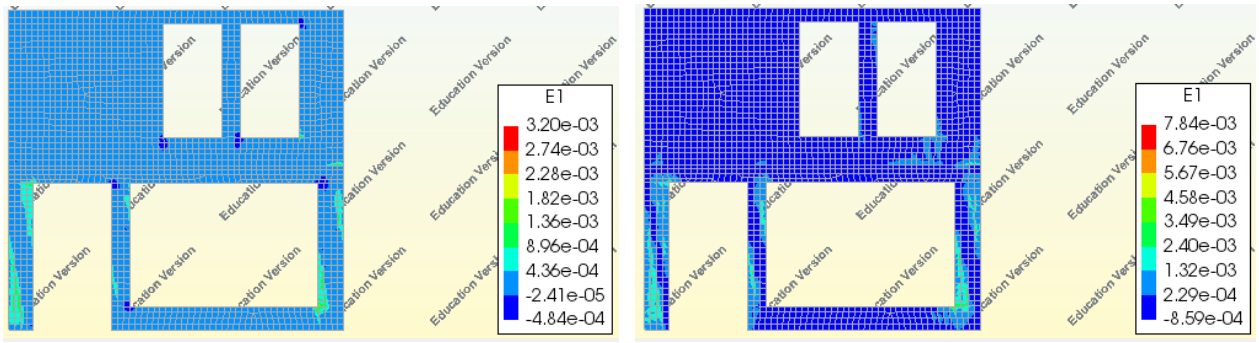

FIGURE 109: MAXIMUM PRINCIPAL STRAIN-LOAD STEP 25 (LEFT) , MAXIMUM PRINCIPAL STRAIN-LOAD STEP 46 (RIGHT)

OBSERVED FAILURE MECHANISM

The failure mechanism that is developed during this pushover assessment is rocking of the piers at the first floor.

PUSHOVER CURVE: CASE STUDY- 2D-1A

The graph below shows the pushover curve that is obtained from the result of the analysis in DIANA.

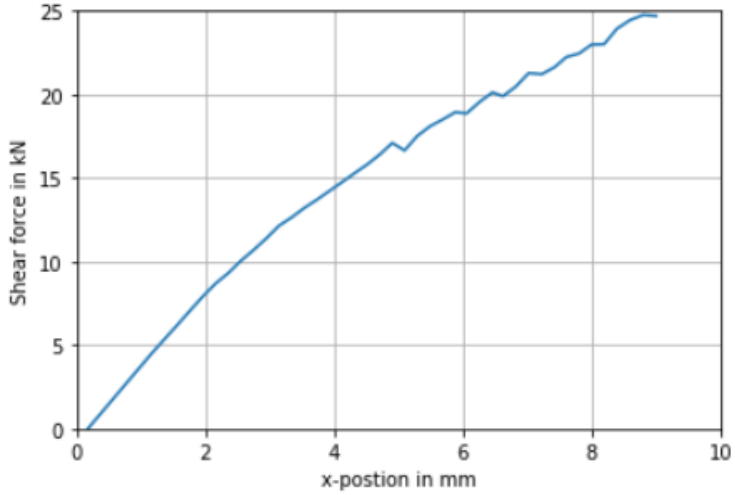

FIGURE 110: PUSHOVER CURVE CASE STUDY-2D-1A

24 APPENDIX N: CASE STUDY- 2D-1B: FULL DIANA NLPO FEM ANALYSIS

RESULTS: STRUCTURAL EIGENVALUE ANALYSIS

The first analysis that has been made is the structural eigenvalue analysis. This analysis is required to determine the critical Eigen mode and Eigen frequency. The Eigen mode with the highest participating mass is the critical Eigen mode. In this case Eigen mode 1 is the governing Eigen mode and corresponds to a participating mass percentage 55.5%. The Figure below shows first five Eigen modes and their participating masses.

TABLE 35: GOVERNING EIGEN MODE AND THE PARTICIPATING MASS- CASE STUDY-2D-1B

MODE	FREQUENCY	EFF.MASS TX	PERCENTAGE	CUM.PERCENT
1	0.11966E+02	0.51485E+04	0.55482E+02	0.55482E+02

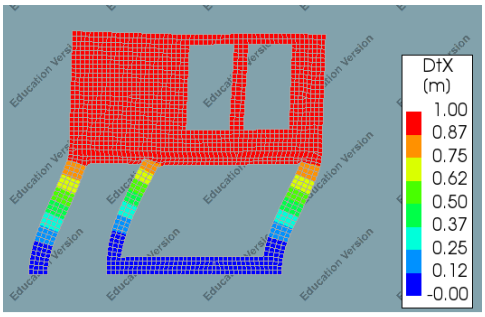

FIGURE 111: GOVERNING EIGEN MODE CASE STUDY-2D-1B

RESULTS:STRUCTURAL NONLINEAR ANALYSIS

This part contains the results of the structural nonlinear analysis. The relevant obtained results in this case, are the horizontal deflection, maximum principal strain, observed failure mechanism and the pushover curve.

HORIZONTAL DEFLECTION

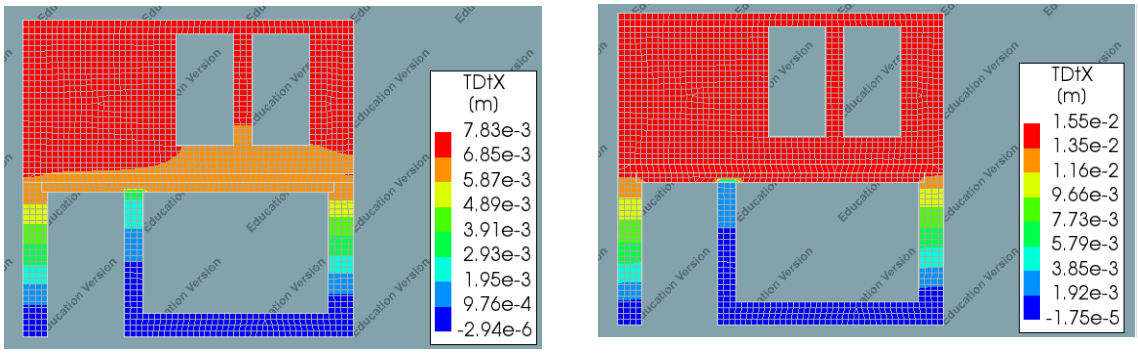

FIGURE 112: HORIZONTAL DEFLECTION STEP 50 (LEFT) , HORIZONTAL DEFLECTION STEP 100 (RIGHT)

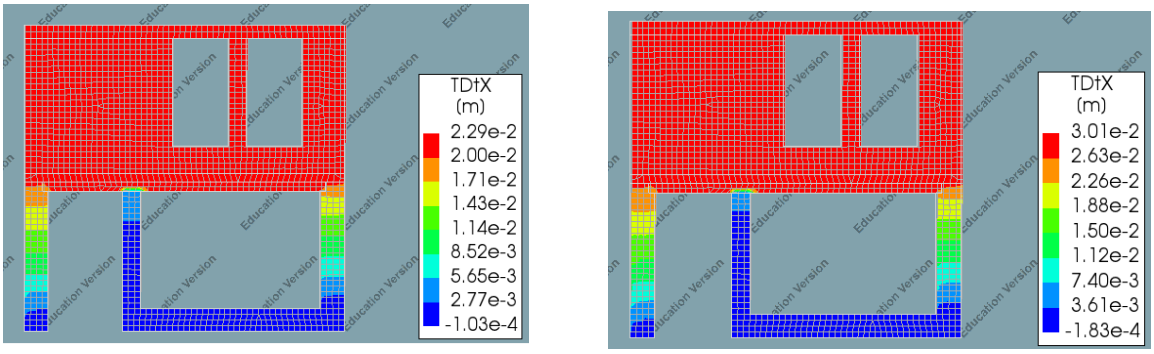

FIGURE 113: HORIZONTAL DEFLECTION STEP 150 (LEFT) , HORIZONTAL DEFLECTION STEP 200 (RIGHT)

MAXIMUM PRINCIPAL STRAIN

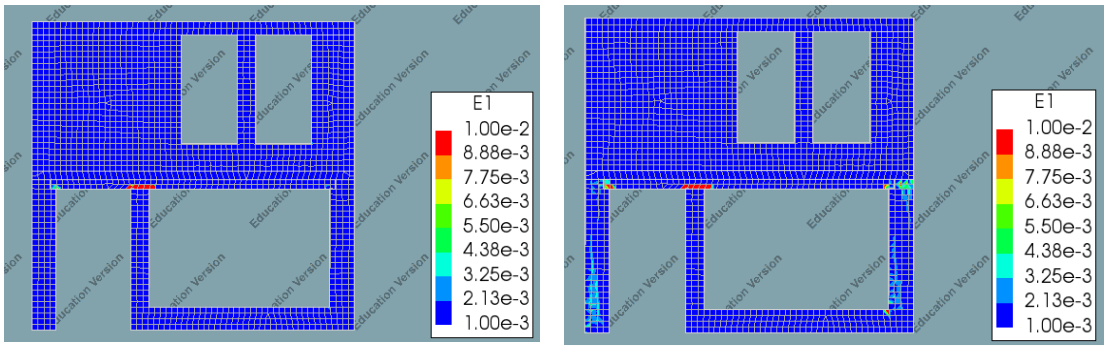

FIGURE 114: MAXIMUM PRINCIPAL STRAIN STEP 50 (LEFT) , MAXIMUM PRINCIPAL STRAIN STEP 100 (RIGHT)

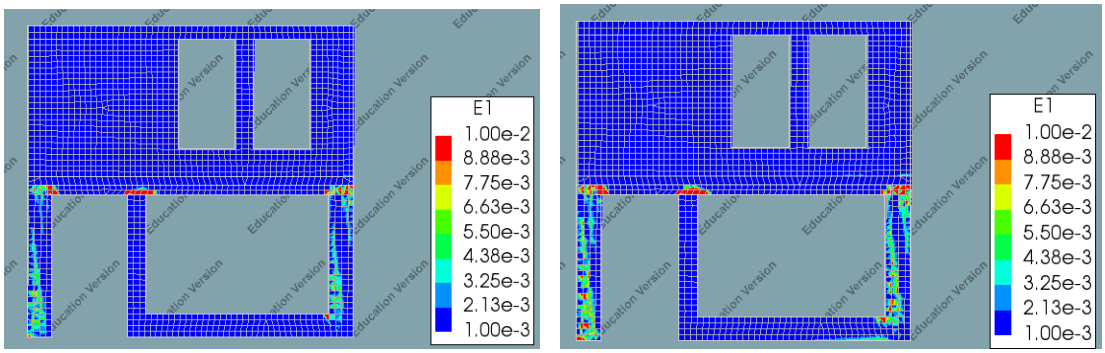

FIGURE 115: MAXIMUM PRINCIPAL STRAIN STEP 150 (LEFT) , MAXIMUM PRINCIPAL STRAIN STEP 200 (RIGHT)

OBSERVED FAILURE MECHANISM

The failure mechanism that is developed during this pushover assessment is rocking of the piers at the first floor.

PUSHOVER CURVE: CASE STUDY- 2D-1B

The graph below shows the pushover curve that is obtained from the result of the analysis in DIANA.

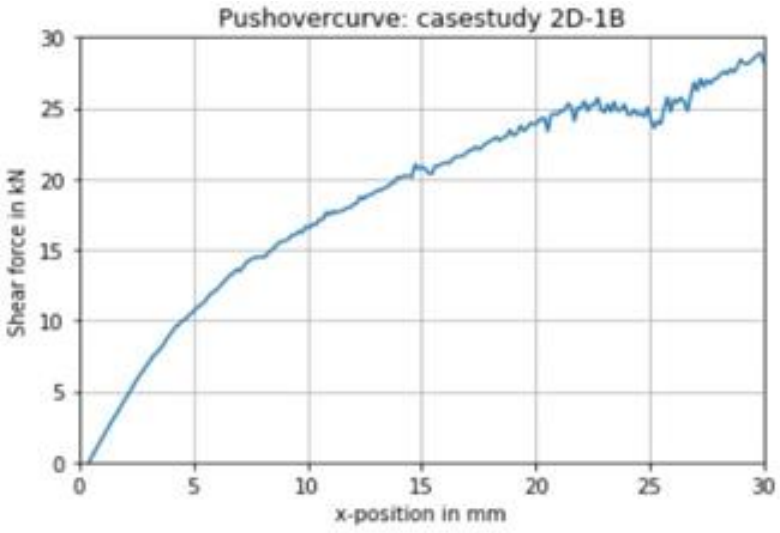

FIGURE 116:PUSHOVER CURVE CASE STUDY-2D-1B

25 APPENDIX O: CASE STUDY- 2D-1A/B: FULL SLAMA CALCULATIONS

SHEAR CAPACITY OF THE PIERS

The table below shows the shear capacities, drift capacities and the failure mechanisms of each pier.

TABLE 36: SHEAR CAPACITIES, DRIFT CAPACITIES AND THE FAILURE MECHANISMS OF EACH PIER

	Shear capacity	Drift capacity	Failure mechanism
Pier 1	2992.7 N	0.00676439	Rocking
Pier 2	1912.32 N	0.00676439	Rocking
Pier 3	3399.68 N	0.00116050	Rocking
Pier 4	23213.23 N	0.01244176	Rocking
Pier 5	289.12 N	0.03688044	Rocking
Pier 6	3918.38 N	0.01807154	Rocking

PUSHOVER CURVE

The graph below shows the pushover curve that is obtained from the SLaMA calculations.

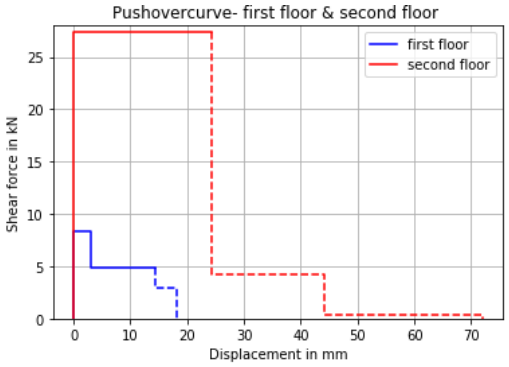

FIGURE 117:PUSHOVER CURVE CASE STUDY-2D-1A/1B

ACCELERATION CURVE

The graph below shows the acceleration curve that is obtained from the SLaMA calculations.

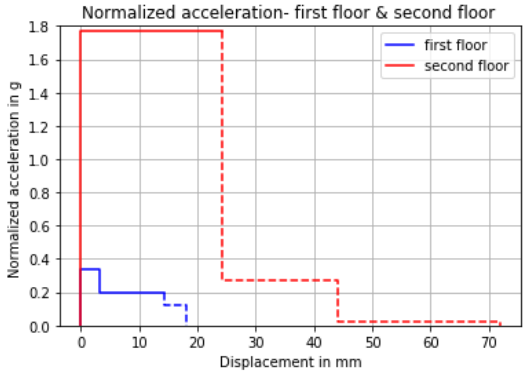

FIGURE 118:ACCELERATION CURVE CASE STUDY-2D-1A/1B

MAXIMUM BASE SHEAR FORCE

The maximum base shear force is calculated based on the critical acceleration of the first floor. This acceleration is multiplied by the effective masses.

$$V_{base\ shear} = 0.337929389\ g \cdot (0.64 \cdot m_{2,eff} + 0.36 \cdot m_{1,eff})$$

$$V_{base\ shear} = 8.3\ kN$$

26 APPENDIX P: CASE STUDY- 2D-2A: FULL DIANA NLPO FEM ANALYSIS

RESULTS: STRUCTURAL EIGENVALUE ANALYSIS

The first analysis that has been made is the structural eigenvalue analysis. This analysis is required to determine the critical Eigen mode and Eigen frequency. The Eigen mode with the highest participating mass is the critical Eigen mode. In this case Eigen mode 1 is the governing Eigen mode and corresponds to a participating mass percentage 90.5%. The Figure below shows first five Eigen modes and their participating masses.

TABLE 37 : GOVERNING EIGEN MODE AND THE PARTICIPATING MASS- CASE STUDY-2D-2A

MODE	FREQUENCY	EFF.MASS TX	PERCENTAGE	CUM.PERCENT
1	0.49806E+01	0.49957E+04	0.90452E+02	0.90452E+02

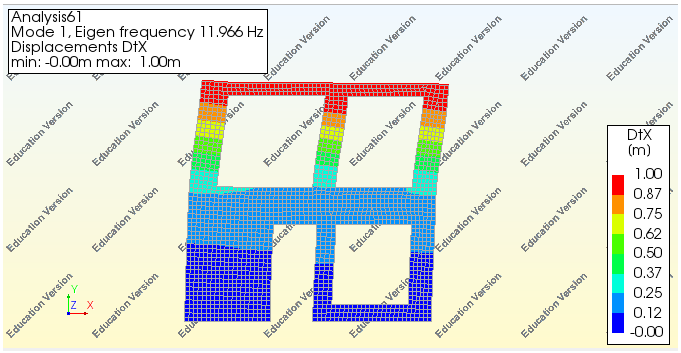

FIGURE 119: THE GOVERNING EIGEN MODE CASE STUDY-2D-2A

RESULTS: STRUCTURAL NONLINEAR ANALYSIS

This part contains the results of the structural nonlinear analysis. The relevant obtained results in this case, are the horizontal deflection, maximum principal strain, observed failure mechanism and the pushover curve.

HORIZONTAL DEFLECTION

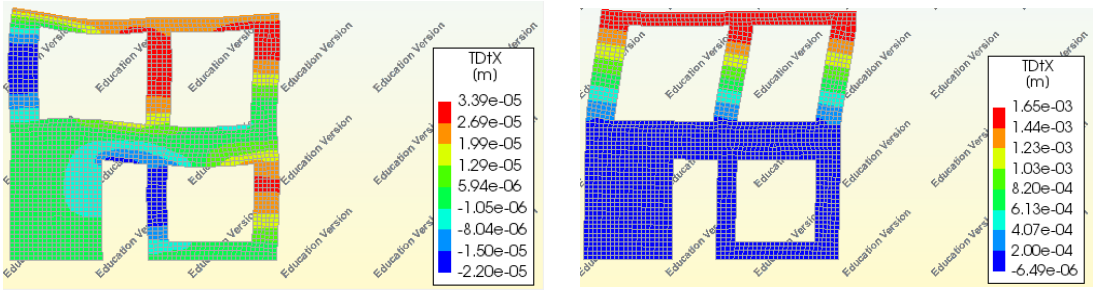

FIGURE 120: HORIZONTAL DEFLECTION STEP 1 (LEFT) , HORIZONTAL DEFLECTION STEP 10 (RIGHT)

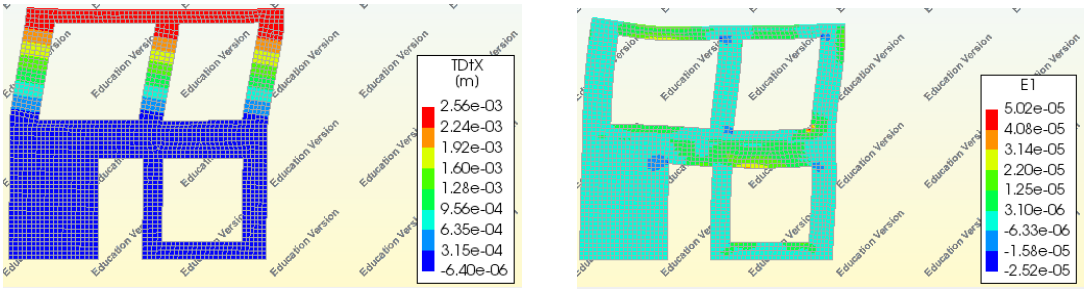

MAXIMUM PRINCIPAL STRAIN

FIGURE 121: HORIZONTAL DEFLECTION STEP 15 (LEFT) , HORIZONTAL DEFLECTION STEP 22 (RIGHT)

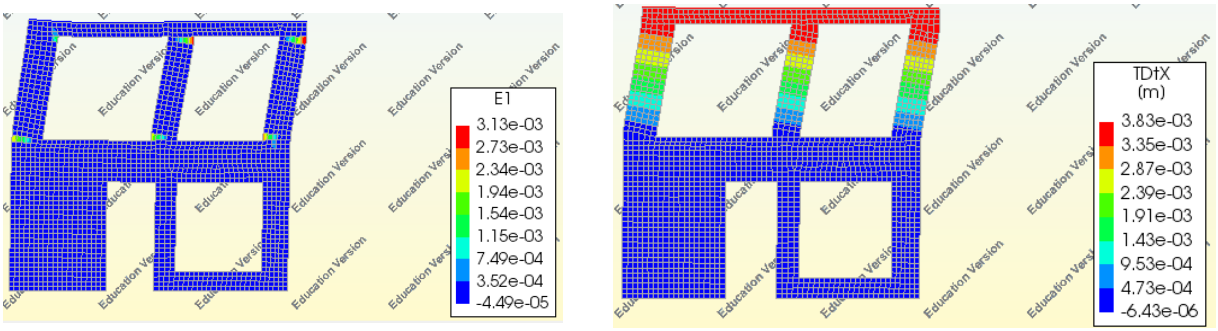

FIGURE 122: MAXIMUM PRINCIPAL STRAIN-LOAD STEP 1 (LEFT) , MAXIMUM PRINCIPAL STRAIN-LOAD STEP 10 (RIGHT)

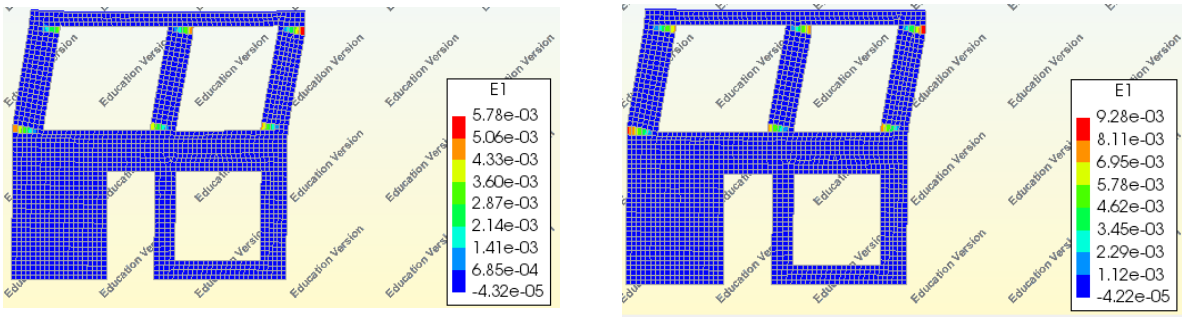

FIGURE 123: MAXIMUM PRINCIPAL STRAIN-LOAD STEP 15 (LEFT) , MAXIMUM PRINCIPAL STRAIN-LOAD STEP 22 (RIGHT)

OBSERVED FAILURE MECHANISM

The failure mechanism that is developed during this pushover assessment is rocking of the piers at the second floor.

PUSHOVER CURVE: CASE STUDY- 2D-2A

The graph below shows the pushover curve that is obtained from the result of the analysis in DIANA.

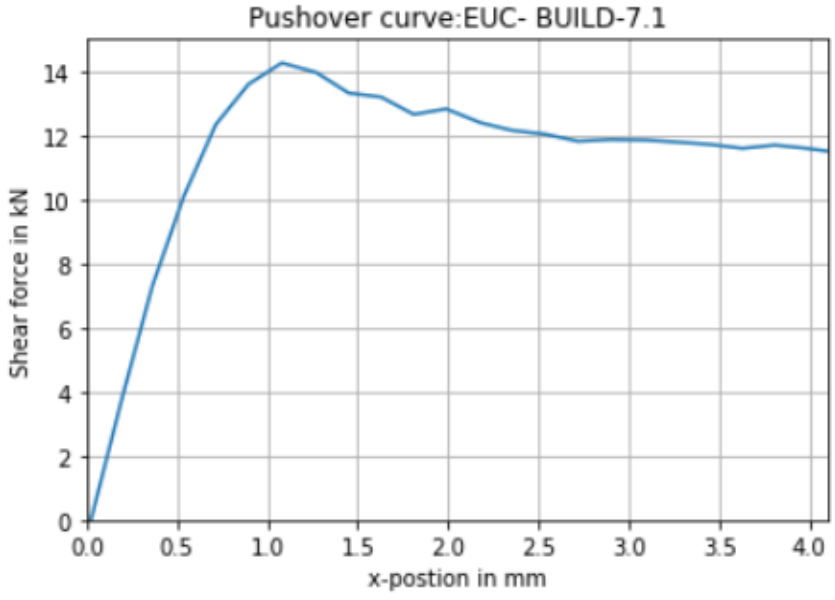

FIGURE 124:PUSHOVER CURVE CASE STUDY-2D-2A

27 APPENDIX Q: CASE STUDY- 2D-2B: FULL DIANA NLPO FEM ANALYSIS

RESULTS: STRUCTURAL EIGENVALUE ANALYSIS

The first analysis that has been made is the structural eigenvalue analysis. This analysis is required to determine the critical Eigen mode and Eigen frequency. The Eigen mode with the highest participating mass is the critical Eigen mode. In this case Eigen mode 1 is the governing Eigen mode and corresponds to a participating mass percentage 90.5%. The Figure below shows first five Eigen modes and their participating masses.

MODE	FREQUENCY	EFF.MASS TX	PERCENTAGE	CUM.PERCENT
1	0.49806E+01	0.49957E+04	0.90452E+02	0.90452E+02

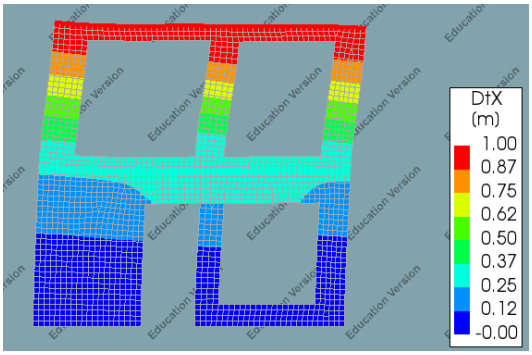

FIGURE 125: GOVERNING EIGEN MODE CASE STUDY-2D-2B

REsults: structural nonlinear analysis

This part contains the results of the structural nonlinear analysis. The relevant obtained results in this case, are the horizontal deflection, maximum principal strain, observed failure mechanism and the pushover curve.

HORZONTAL DEFLECTION

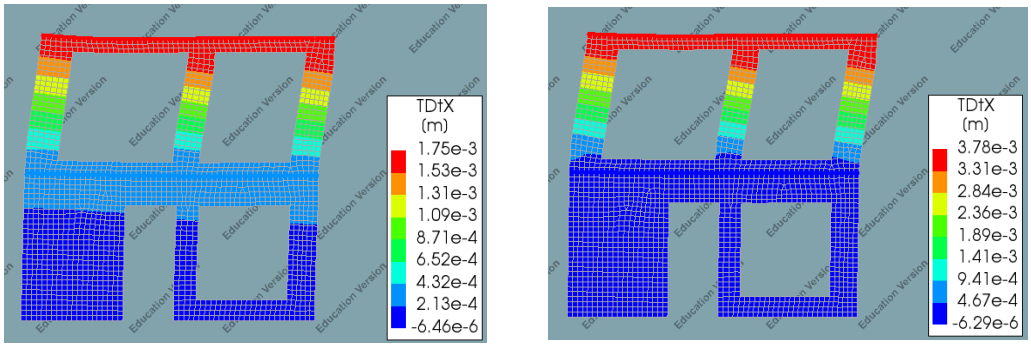

FIGURE 126: HORIZONTAL DEFLECTION STEP 10 (LEFT) , HORIZONTAL DEFLECTION STEP 20 (RIGHT)

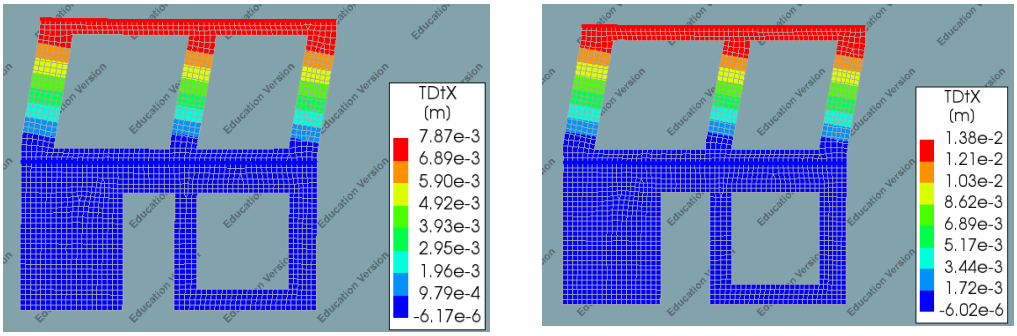

FIGURE 127: HORIZONTAL DEFLECTION STEP 40 (LEFT) , HORIZONTAL DEFLECTION STEP 68 (RIGHT)

MAXIMUM PRINCIPAL STRAIN

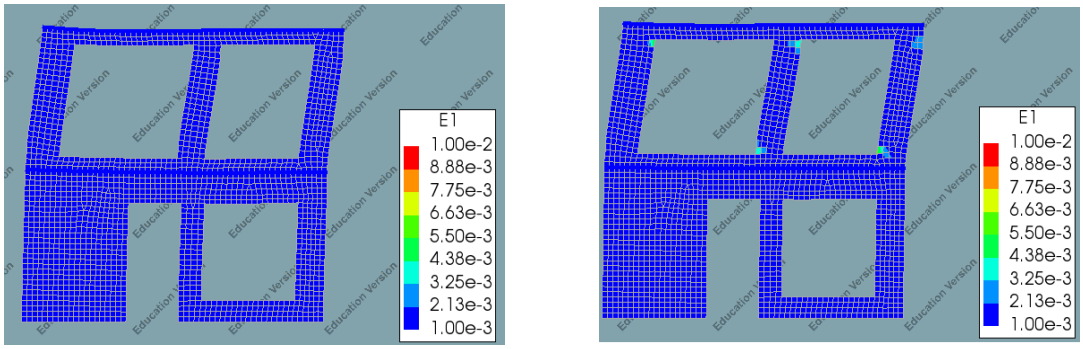

FIGURE 128: MAXIMUM PRINCIPAL STRAIN STEP 10 (LEFT) , MAXIMUM PRINCIPAL STRAIN STEP 20 (RIGHT)

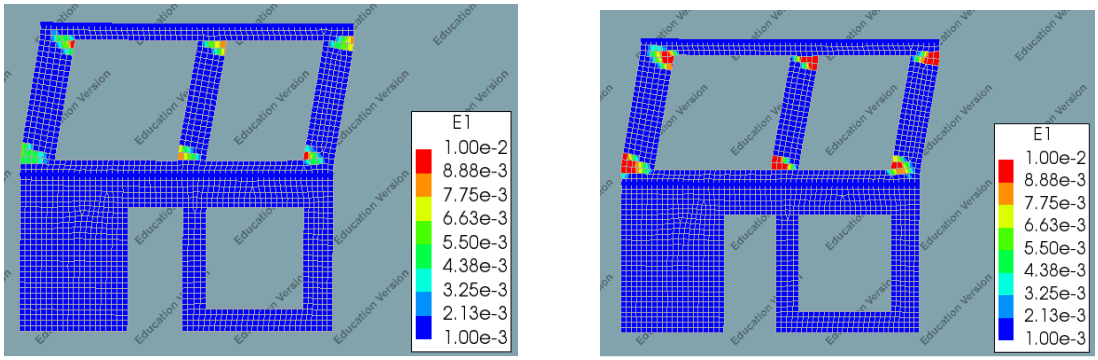

FIGURE 129: MAXIMUM PRINCIPAL STRAIN STEP 40 (LEFT) , MAXIMUM PRINCIPAL STRAIN STEP 68 (RIGHT)

OBSERVED FAILURE MECHANISM

The failure mechanism that is developed during this pushover assessment is rocking of the piers at the second floor.

PUSHOVER CURVE: CASE STUDY- 2D-2B

The graph below shows the pushover curve that is obtained from the result of the analysis in DIANA.

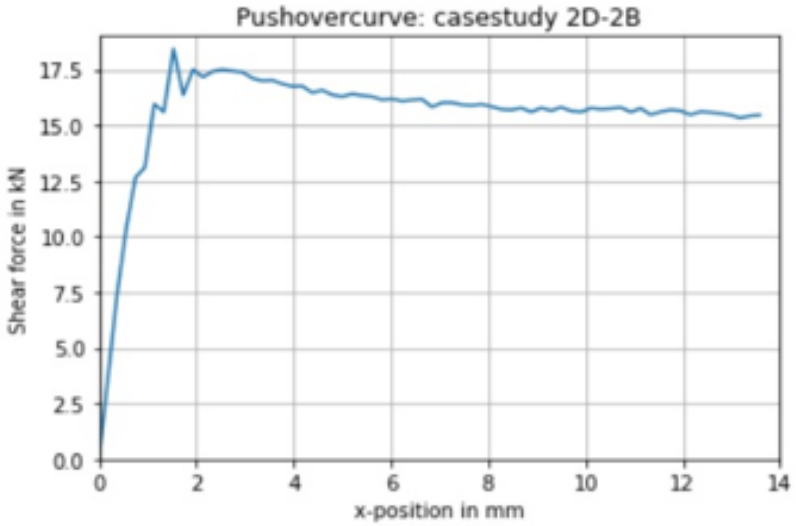

FIGURE 130: PUSHOVER CURVE CASE STUDY-2D-2B

28 APPENDIX R: CASE STUDY- 2D-2A/B: FULL SLAMA CALCULATIONS

SHEAR CAPACITY OF THE PIERS

The table below shows the shear capacities, drift capacities and the failure mechanisms of each pier.

TABLE 38: SHEAR CAPACITIES, DRIFT CAPACITIES AND THE FAILURE MECHANISMS OF EACH PIER

	Shear capacity	**Drift capacity**	**Failure mechanism**
Pier 1	11403.76 N	0.013	Rocking
Pier 2	2390.22 N	0.018	Rocking
Pier 3	3317.66 N	0.017	Rocking
Pier 4	2003.51 N	0.024	Rocking
Pier 5	1592.94 N	0.024	Rocking
Pier 6	1427.77 N	0.023	Rocking

PUSHOVER CURVE

The graph below shows the pushover curve that is obtained from the SLaMA calculations.

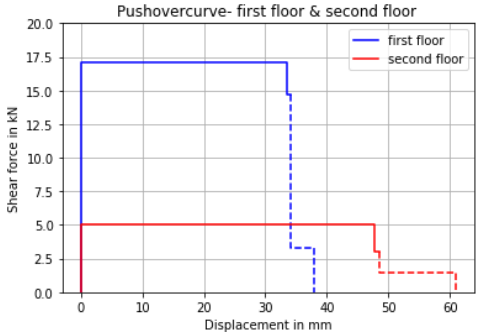

FIGURE 131:PUSHOVER CURVE CASE STUDY-2D-2A/B

ACCELERATION CURVE

The graph below shows the acceleration curve that is obtained from the SLaMA calculations.

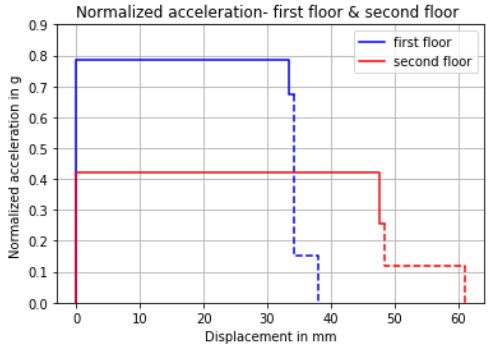

FIGURE 132: ACCELERATION CURVE CASE STUDY-2D-2A/B

MAXIMUM BASE SHEAR FORCE

The maximum base shear force is calculated based on the critical acceleration of the second floor. This acceleration is multiplied by the effective masses.

$$V_{base\ shear} = 0.42\ g \cdot (0.62 \cdot m_{2,eff} + 0.38 \cdot m_{1,eff})$$

$$V_{base\ shear} = 9.3\ kN$$

29 APPENDIX S: CASE STUDY-3D-MODEL-DOUBLE RC-FLOORS FULL DIANA NLPO FEM ANALYSIS

3D-MODEL-DOUBLE RC-FLOORS- DIAGONAL STAIRCASE

RESULTS: STRUCTURAL EIGENVALUE ANALYSIS

The first analysis that has been made is the structural eigenvalue analysis. This analysis is required to determine the critical Eigen mode and Eigen frequency. The Eigen mode with the highest participating mass is the critical Eigen mode. In this case Eigen mode 1 is the governing Eigen mode and corresponds to a participating mass percentage 84.2%. The Figure below shows first five Eigen modes and their participating masses.

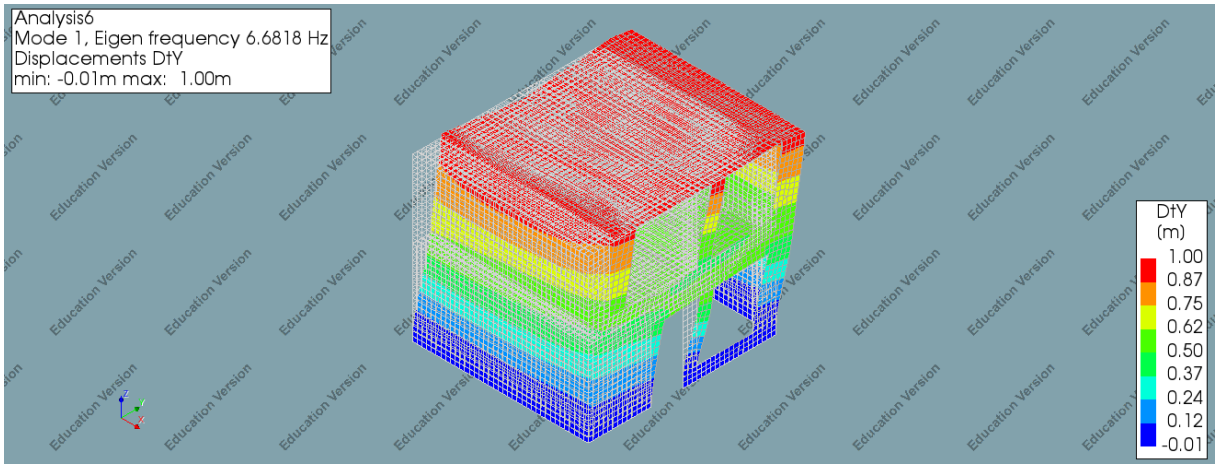

FIGURE 133: GOVERNING EIGEN MODE – 3D-MODEL-DOUBLE RC- FLOORS- DS

TABLE 39: GOVERNING EIGEN MODE AND THE PARTICIPATING MASS- 3D-MODEL-DOUBLE RC- FLOORS- DS

MODE	FREQUENCY	EFF.MASS TX	PERCENTAGE	CUM.PERCENT
1	0.66817+01	0.37092E+04	0.84232E+02	0.84232E+02

RESULTS: STRUCTURAL NONLINEAR ANALYSIS

This part contains the results of the structural nonlinear analysis. The relevant obtained results in this case, are the horizontal deflection, maximum principal strain, observed failure mechanism and the pushover curve.

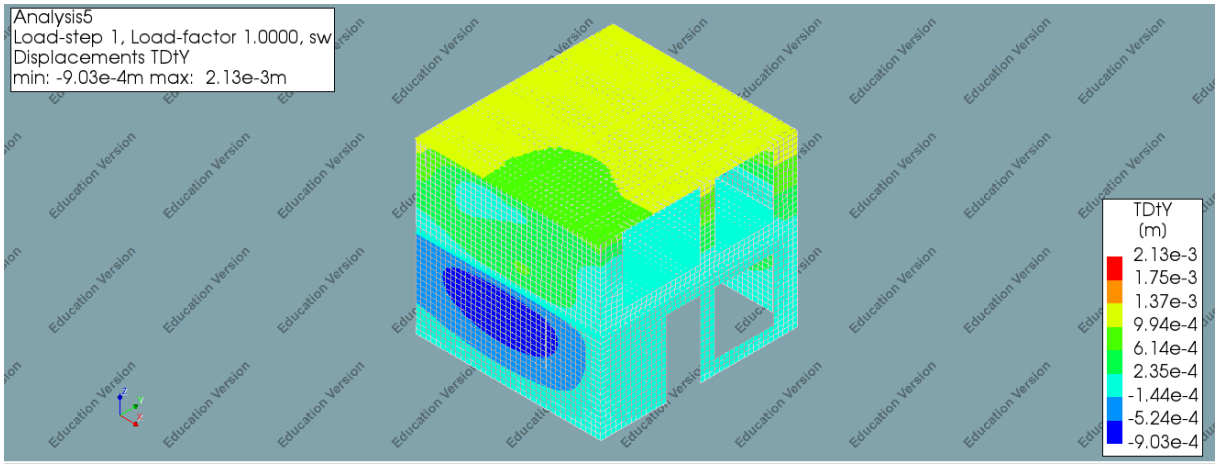

FIGURE 134: DEFLECTION IN THE Y-DIRECTION – STEP 1- 3D-VIEW 1

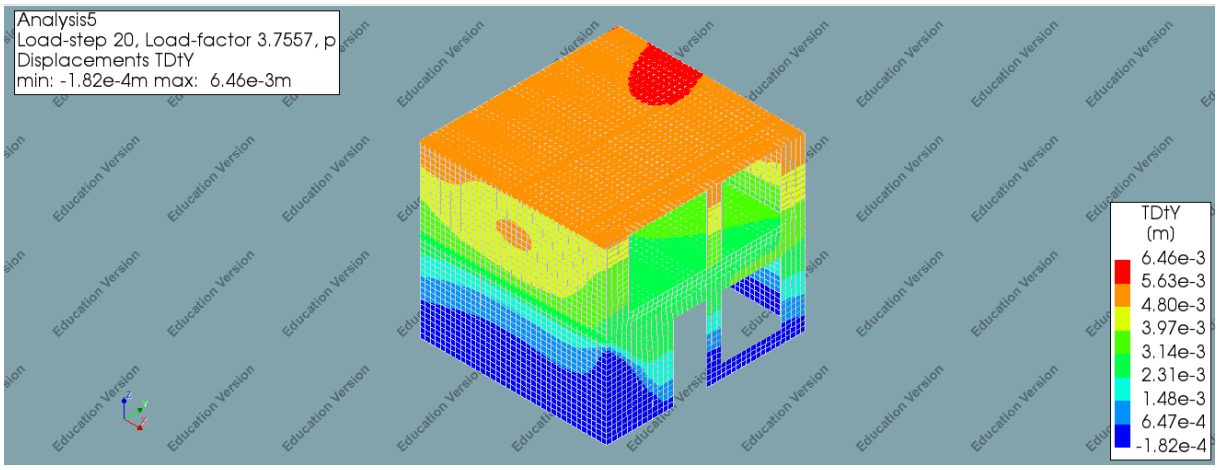

FIGURE 135: DEFLECTION IN THE Y-DIRECTION – STEP 20- 3D-VIEW 1

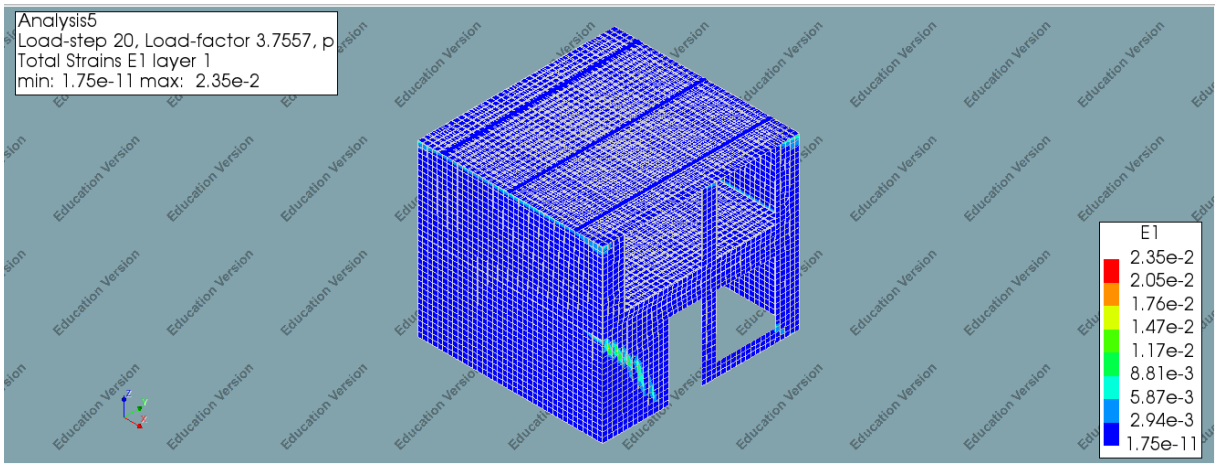

FIGURE 136: MAXIMUM PRINCIPAL STRAIN – STEP 20- 3D-VIEW 1

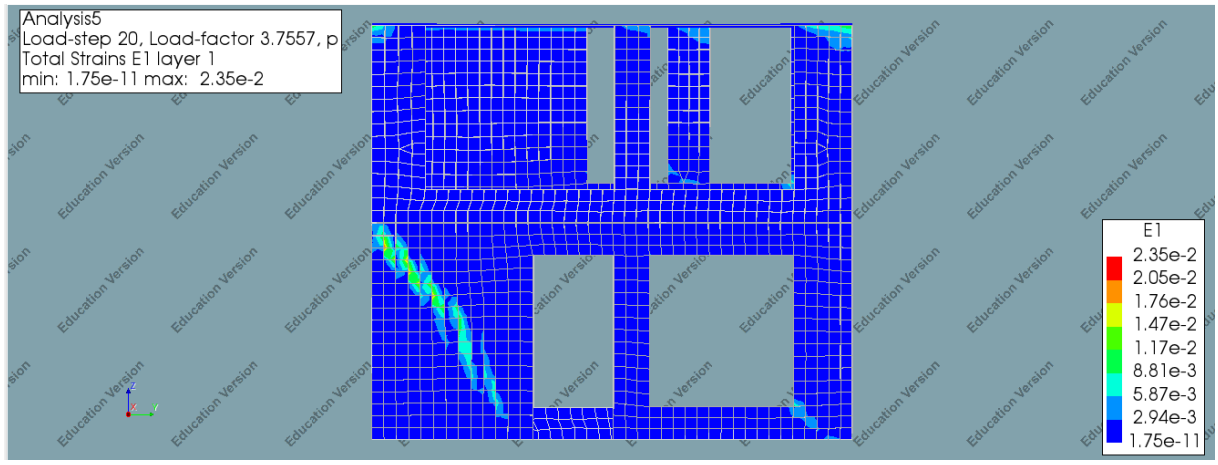

FIGURE 137: MAXIMUM PRINCIPAL STRAIN – STEP 20- SIDE-VIEW 1

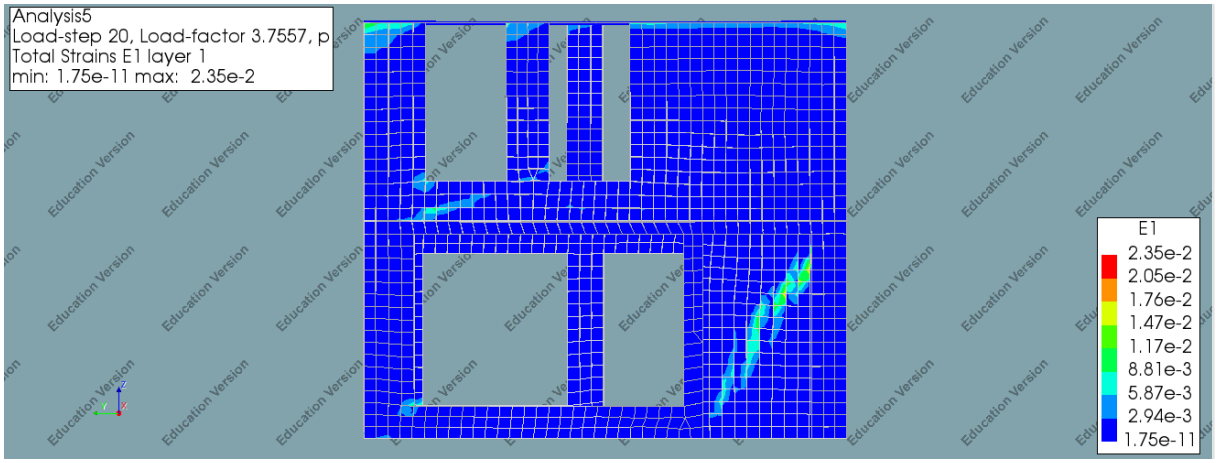

FIGURE 138: MAXIMUM PRINCIPAL STRAIN – STEP 20- SIDE-VIEW 2

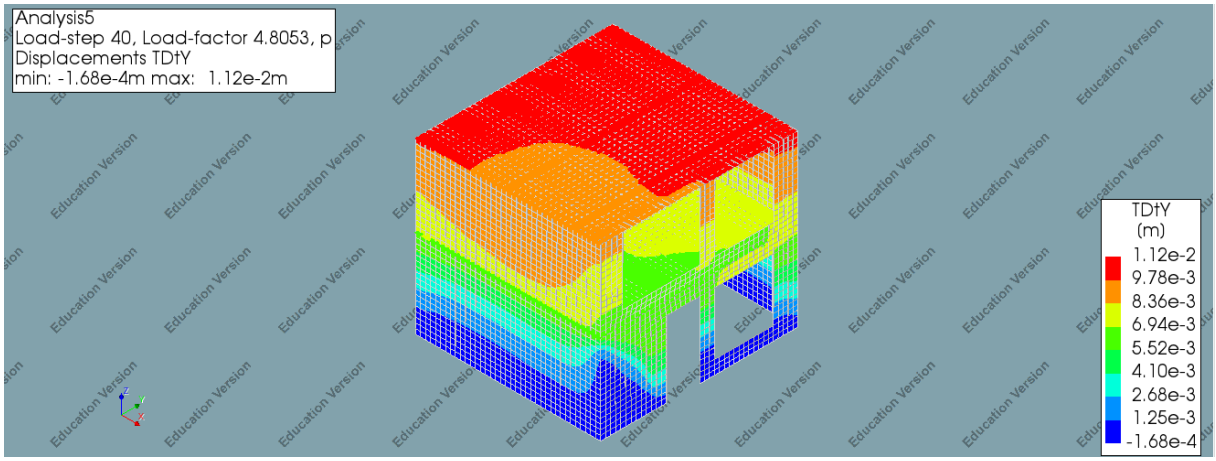

FIGURE 139: DEFLECTION IN THE Y-DIRECTION – STEP 20- 3D-VIEW 1

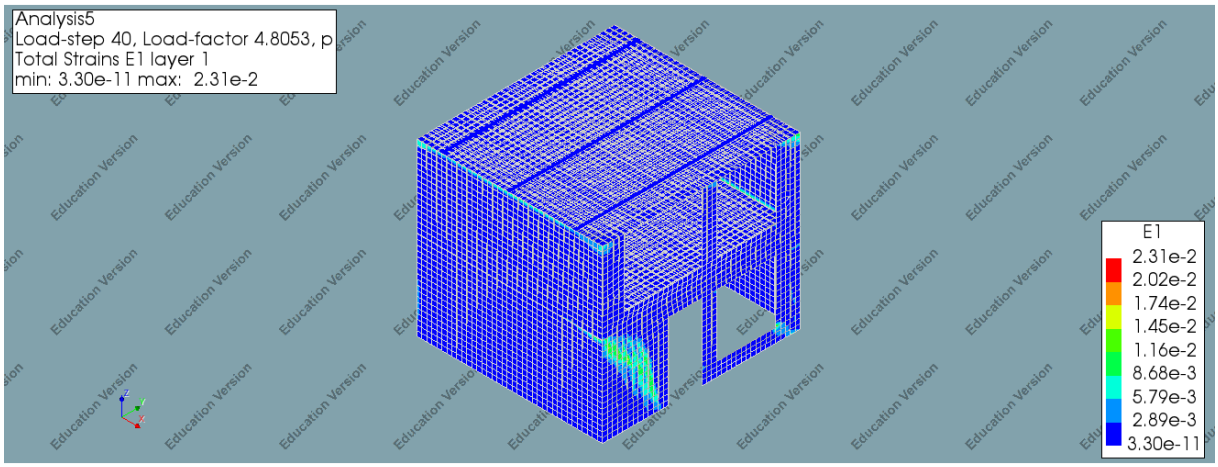

FIGURE 140: MAXIMUM PRINCIPAL STRAIN – STEP 40- 3D-VIEW 1

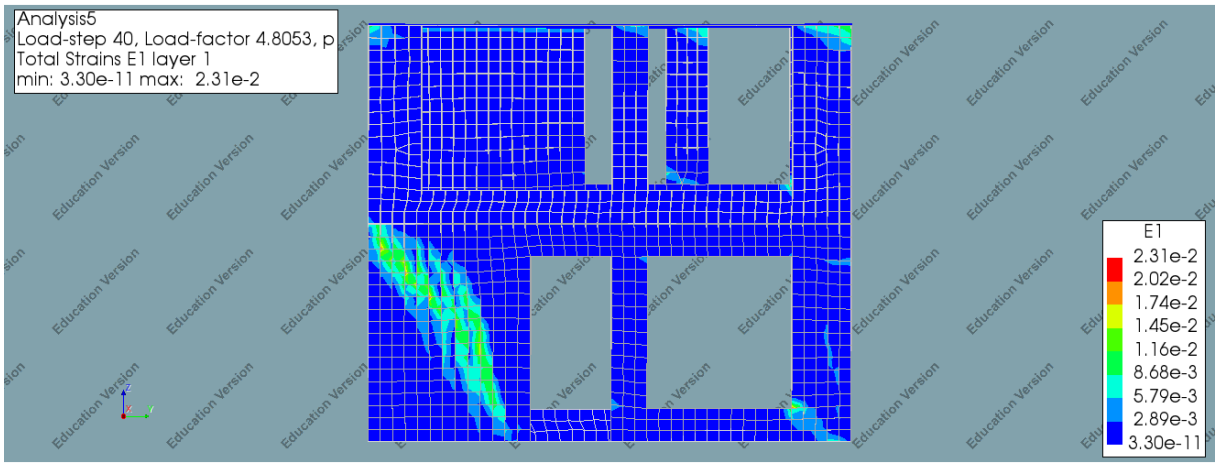

FIGURE 141: MAXIMUM PRINCIPAL STRAIN – STEP 40- SIDE-VIEW 1

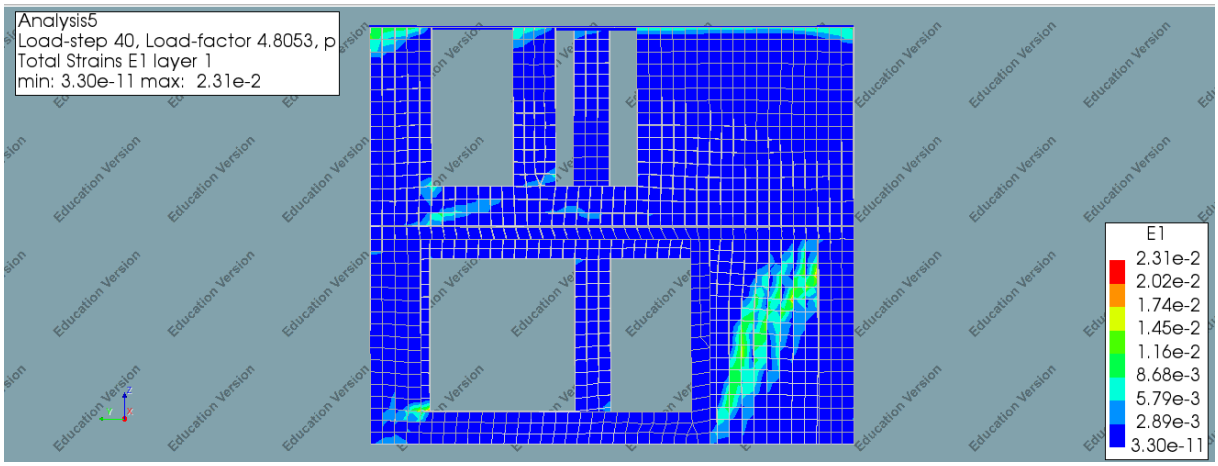

FIGURE 142: MAXIMUM PRINCIPAL STRAIN – STEP 40- SIDE-VIEW 2

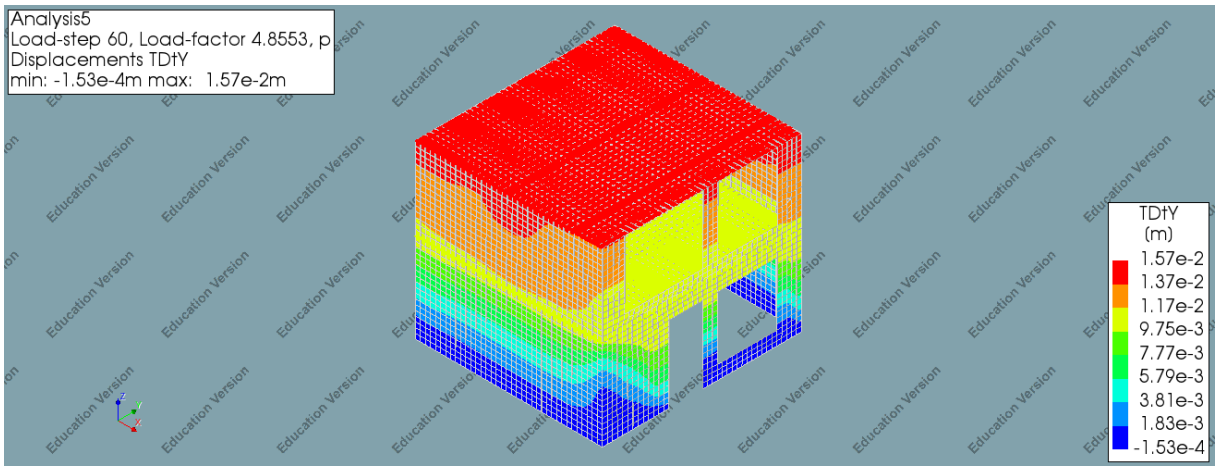

FIGURE 143: DEFLECTION IN THE Y-DIRECTION – STEP 60- 3D-VIEW 1

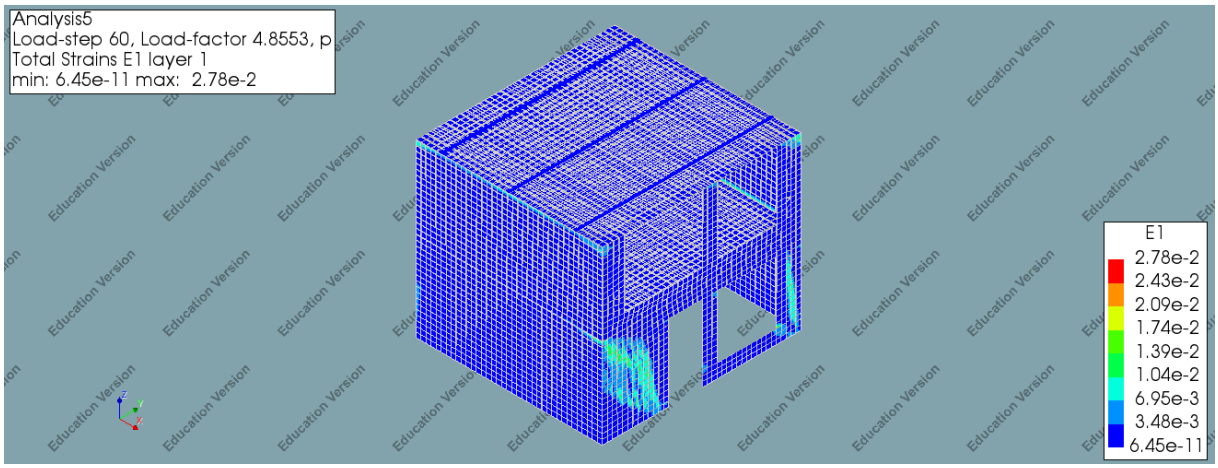

FIGURE 144: MAXIMUM PRINCIPAL STRAIN – STEP 60- 3D-VIEW 1

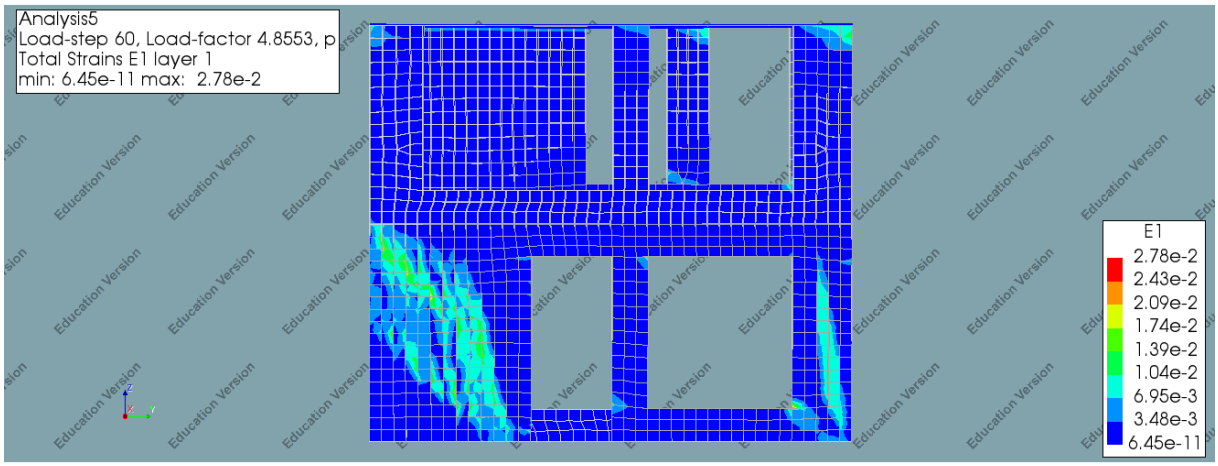

FIGURE 145: MAXIMUM PRINCIPAL STRAIN – STEP 60- SIDE-VIEW 1

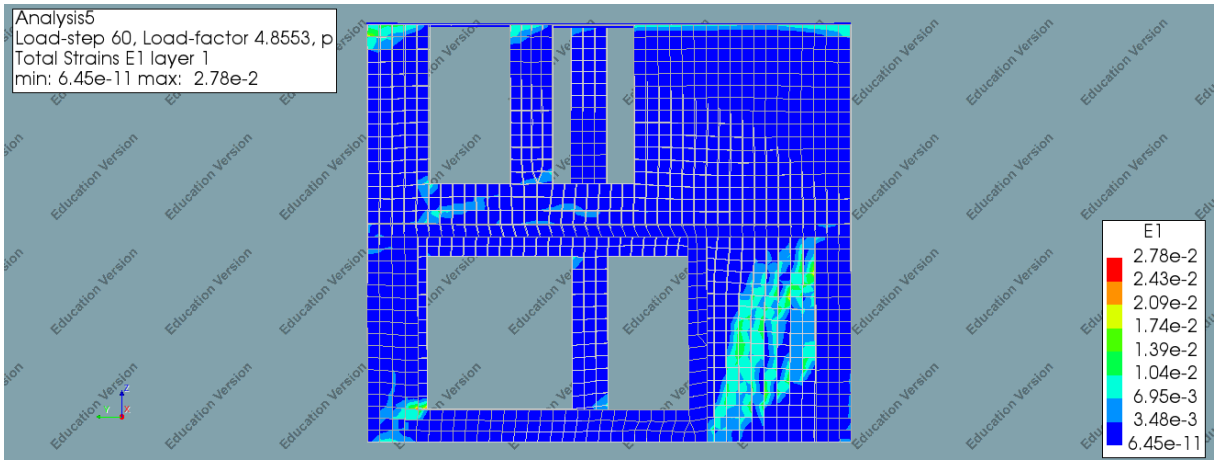

FIGURE 146: MAXIMUM PRINCIPAL STRAIN – STEP 60- SIDE-VIEW 2

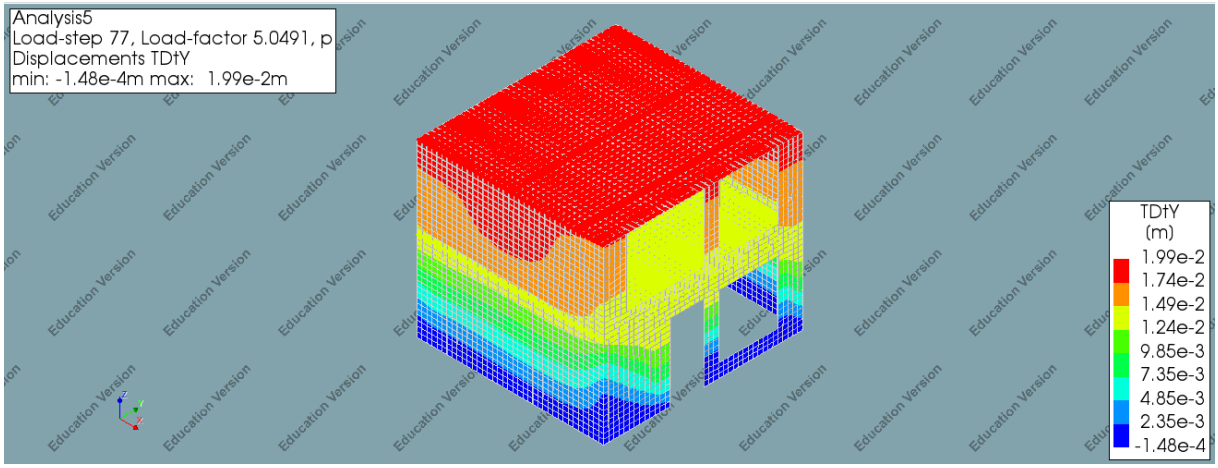

FIGURE 147: DEFLECTION IN THE Y-DIRECTION – STEP 77- 3D-VIEW 1

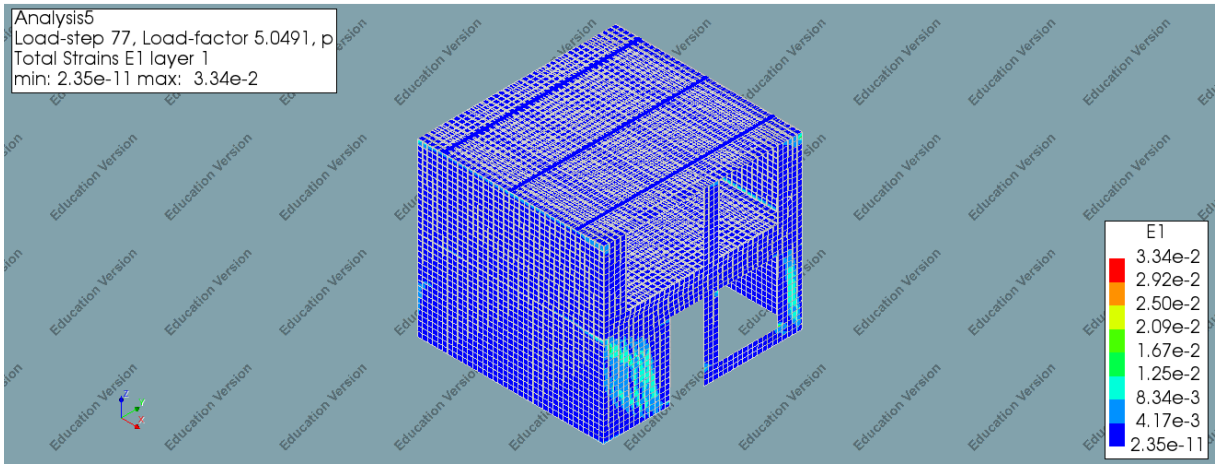

FIGURE 148: MAXIMUM PRINCIPAL STRAIN – STEP 77- 3D-VIEW 1

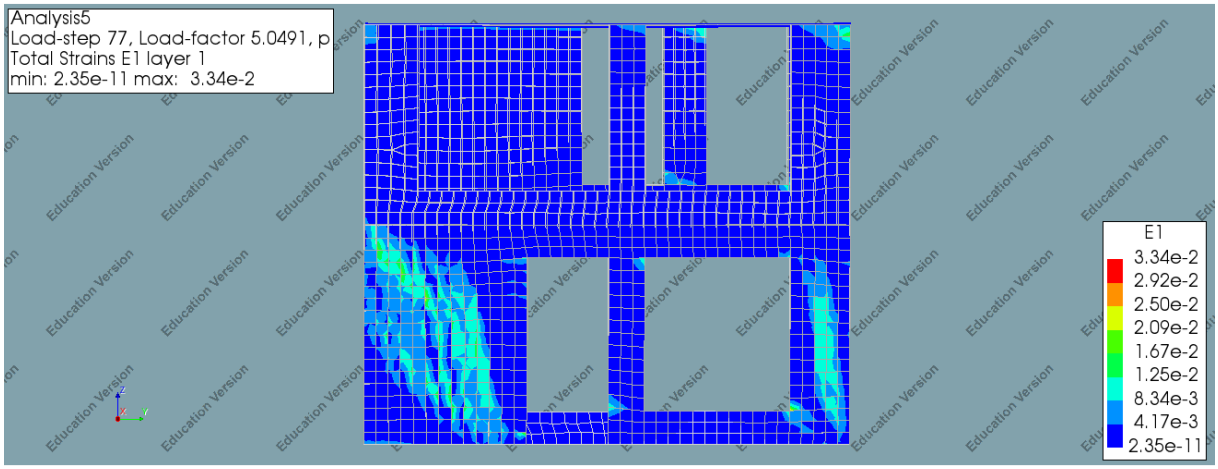

FIGURE 149: MAXIMUM PRINCIPAL STRAIN – STEP 77-SIDE -VIEW 1

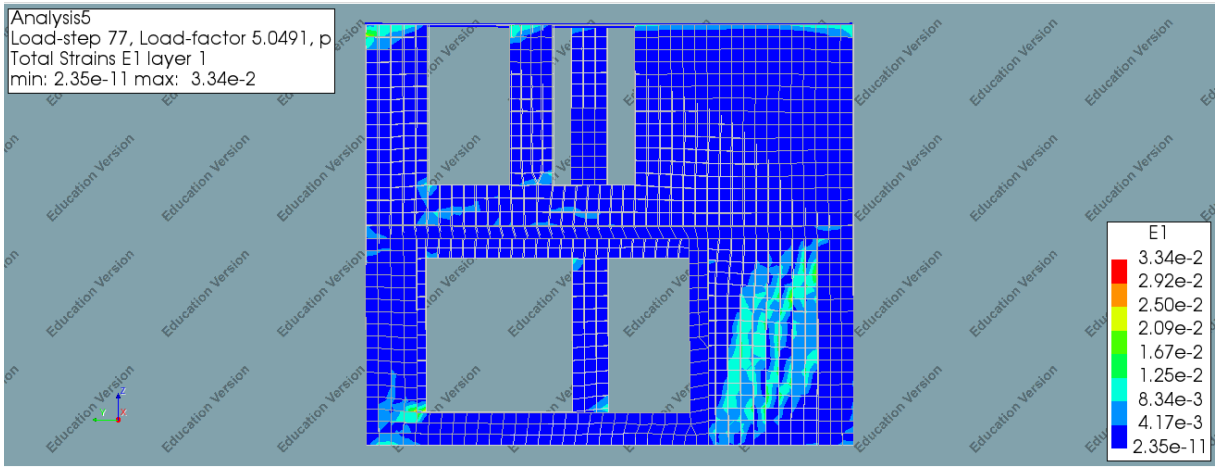

FIGURE 150: MAXIMUM PRINCIPAL STRAIN – STEP 77- SIDE-VIEW 2

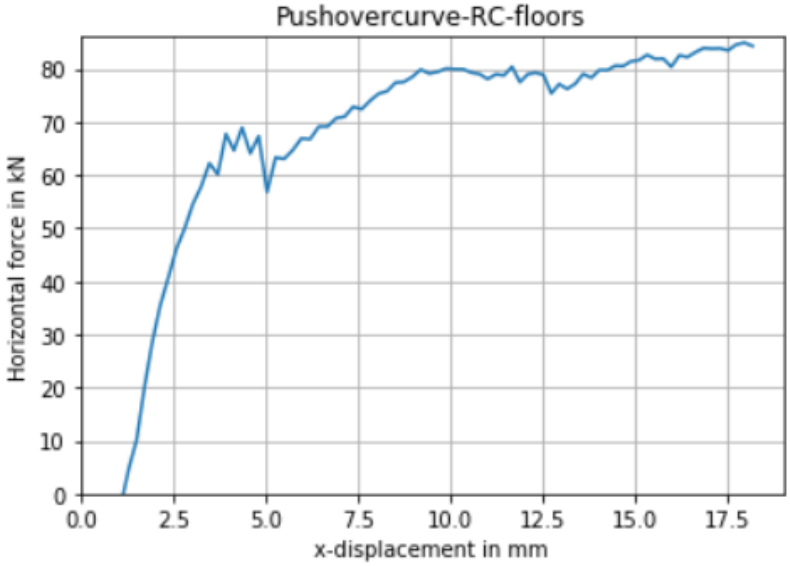

FIGURE 151:PUSHOVER CURVE CASE STUDY-3D-MODEL-DOUBLE RC FLOORS-DS

3D-MODEL-DOUBLE RC-FLOORS- HJ

RESULTS: STRUCTURAL EIGENVALUE ANALYSIS

The first analysis that has been made is the structural eigenvalue analysis. This analysis is required to determine the critical Eigen mode and Eigen frequency. The Eigen mode with the highest participating mass is the critical Eigen mode. In this case Eigen mode 1 is the governing Eigen mode and corresponds to a participating mass percentage 84.2%. The Figure below shows first five Eigen modes and their participating masses.

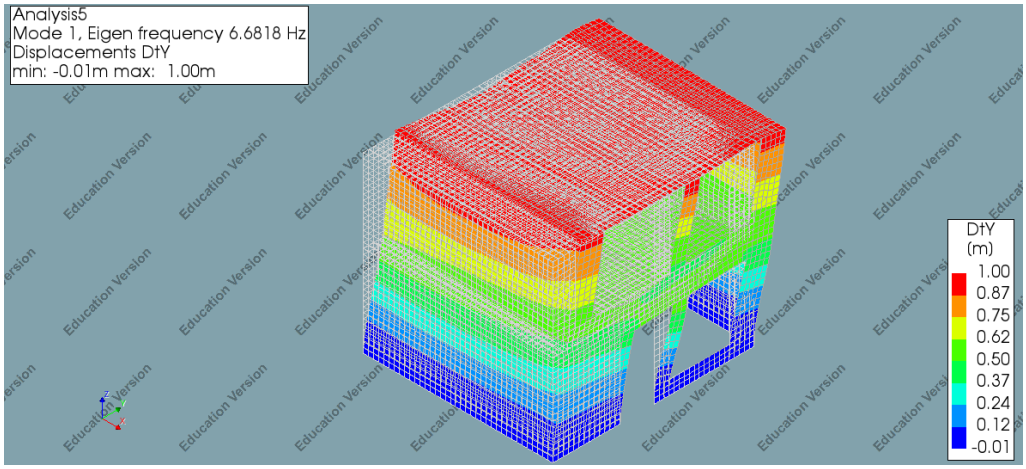

FIGURE 152: GOVERNING EIGEN MODE – 3D-MODEL-DOUBLE RC- FLOORS- HJ

TABLE 40: GOVERNING EIGEN MODE AND THE PARTICIPATING MASS- 3D-MODEL-DOUBLE RC- FLOORS- HJ

MODE	FREQUENCY	EFF.MASS TX	PERCENTAGE	CUM.PERCENT
1	0.66818+01	0.37091E+04	0.84232E+02	0.84232E+02

RESULTS: STRUCTURAL NONLINEAR ANALYSIS

This part contains the results of the structural nonlinear analysis. The relevant obtained results in this case, are the horizontal deflection, maximum principal strain, observed failure mechanism and the pushover curve.

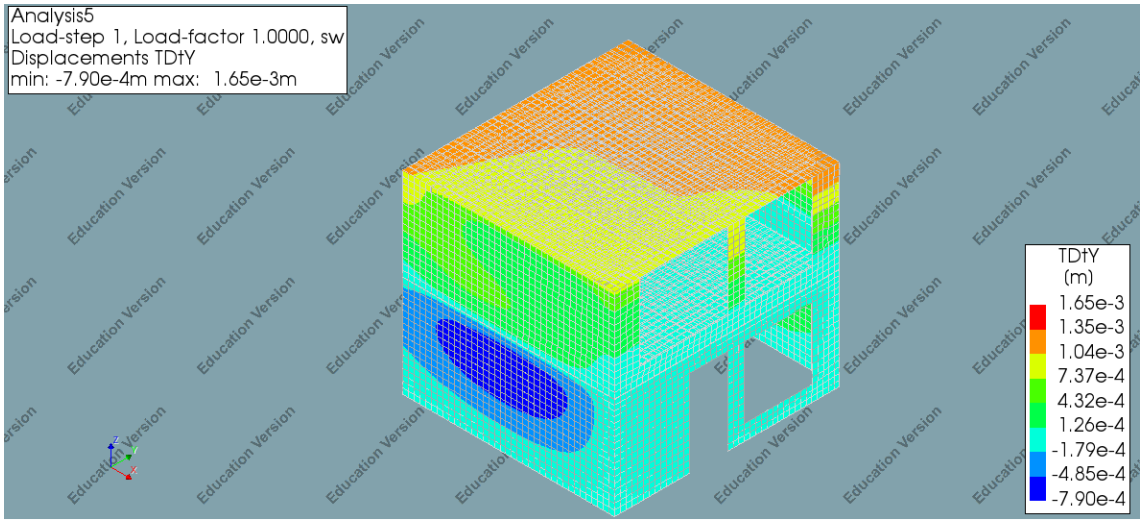

FIGURE 153: DEFLECTION IN THE Y-DIRECTION – STEP 1- 3D-VIEW 1

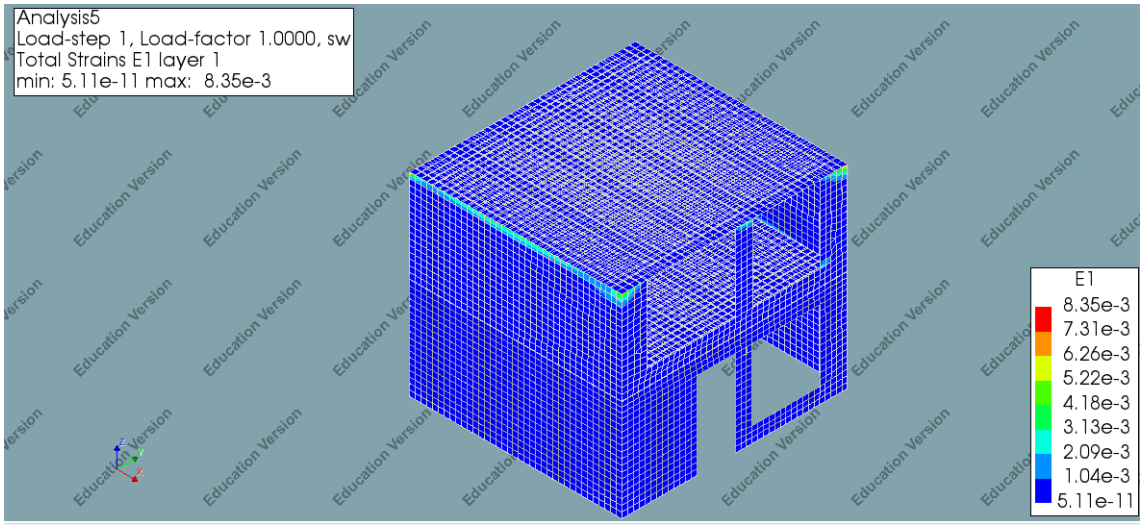

FIGURE 154: MAXIMUM PRINCIPAL STRAIN – STEP 1- 3D-VIEW 1

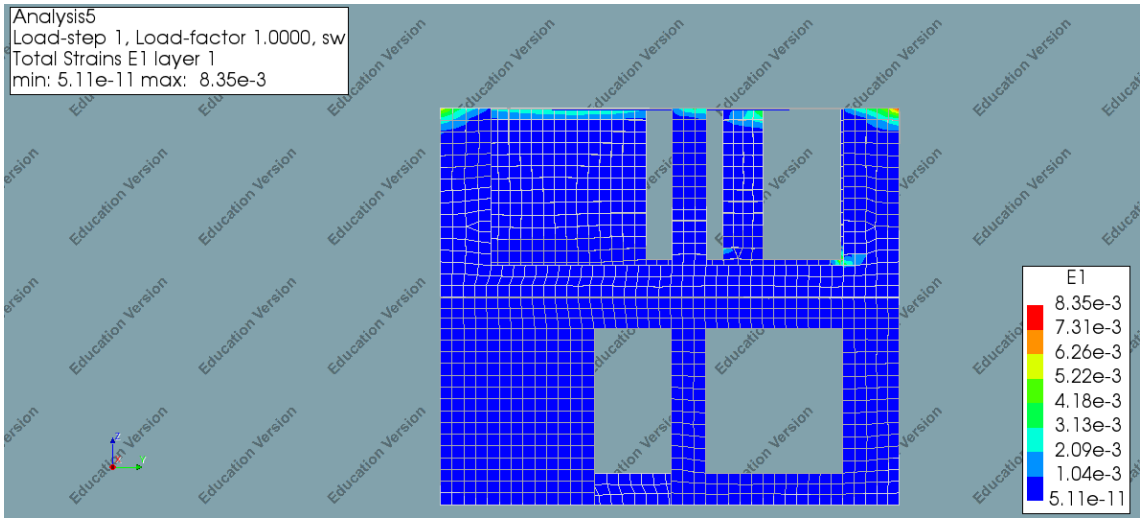

FIGURE 155: MAXIMUM PRINCIPAL STRAIN – STEP 1- SIDE-VIEW 1

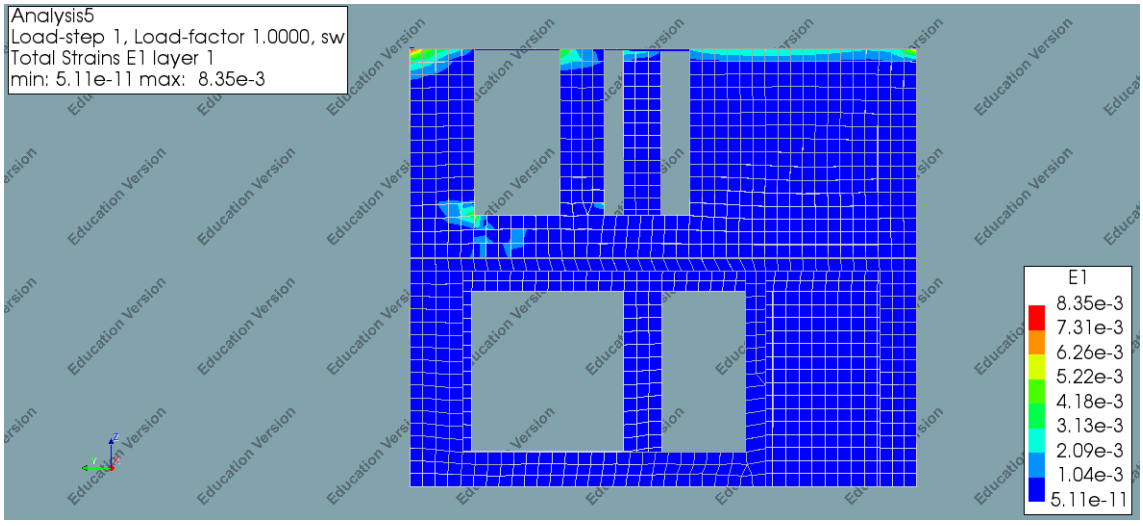

FIGURE 156: MAXIMUM PRINCIPAL STRAIN – STEP 1- SIDE-VIEW 2

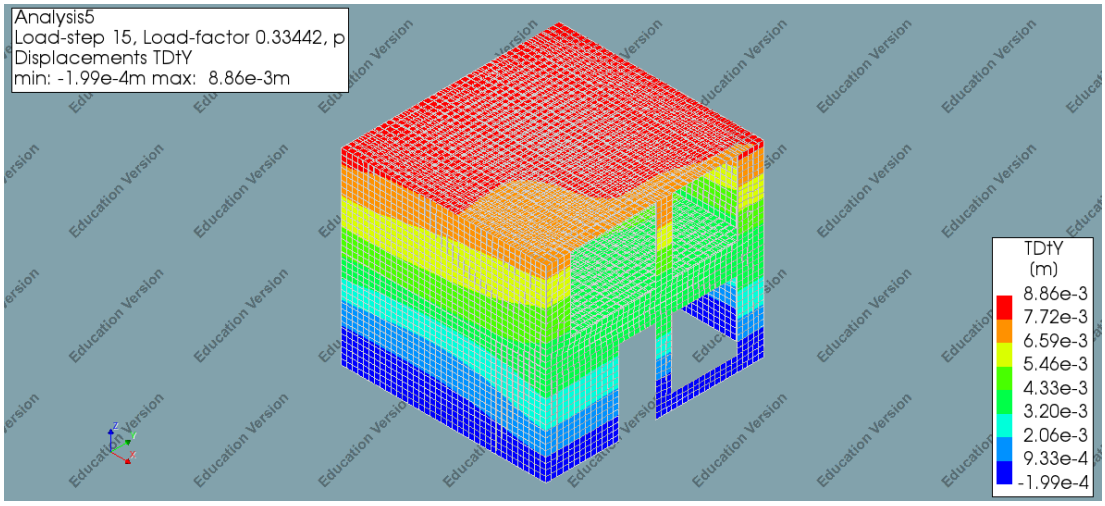

FIGURE 157: DEFLECTION IN THE Y-DIRECTION – STEP 15- 3D-VIEW 1

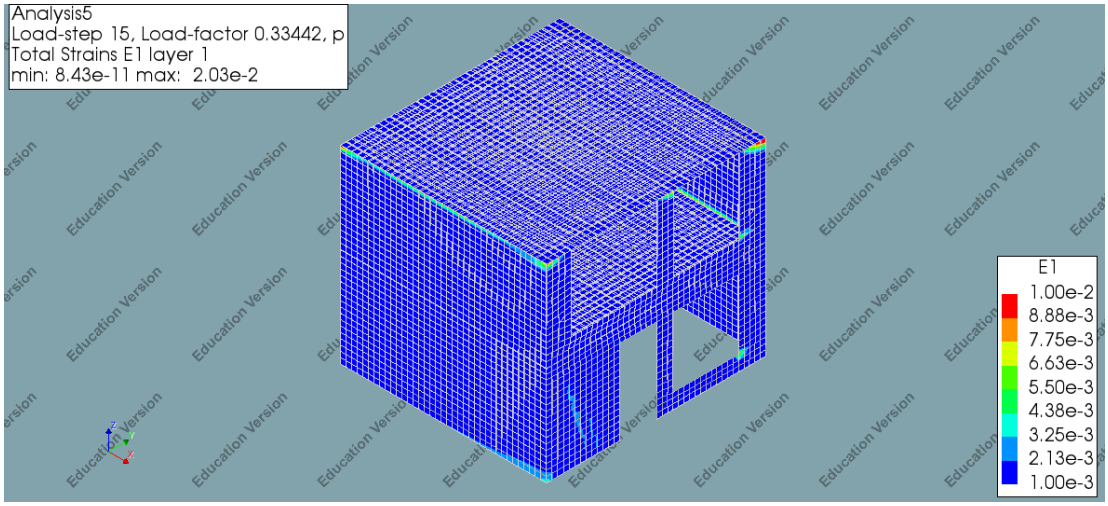

FIGURE 158: MAXIMUM PRINCIPAL STRAIN – STEP 15- 3D-VIEW 1

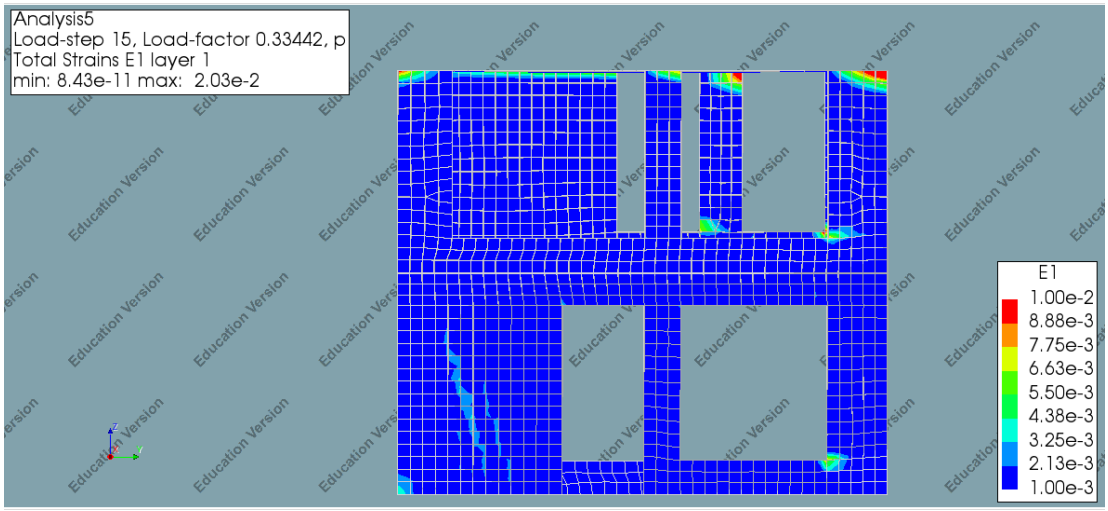

FIGURE 159: MAXIMUM PRINCIPAL STRAIN – STEP 15- SIDE-VIEW 1

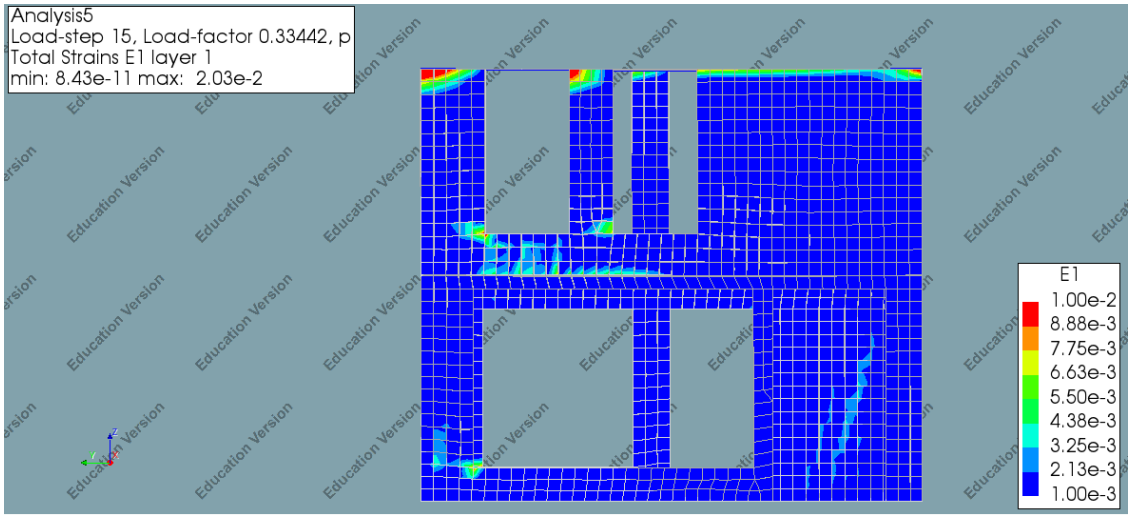

FIGURE 160: MAXIMUM PRINCIPAL STRAIN – STEP 15- SIDE-VIEW 2

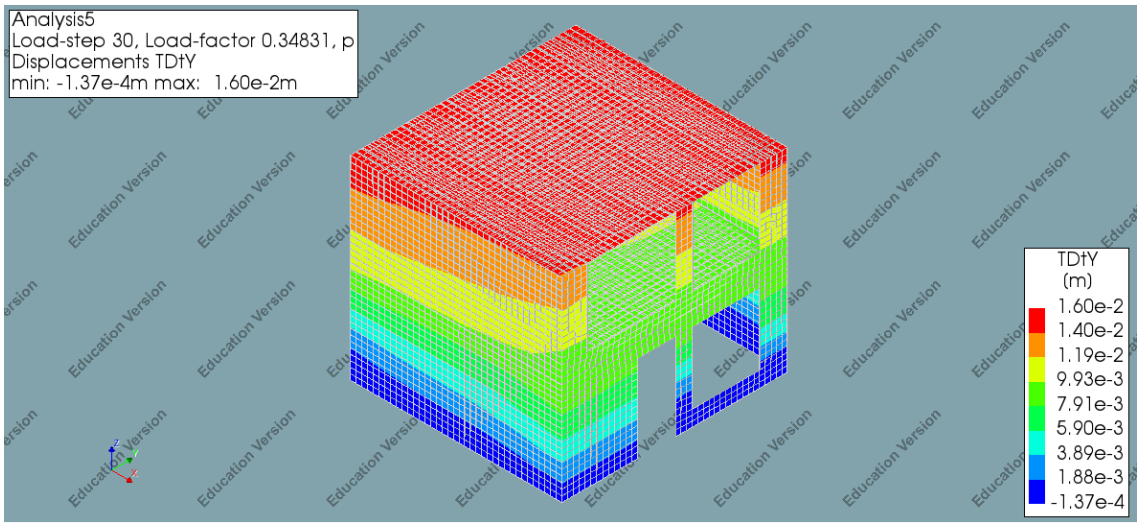

FIGURE 161: DEFLECTION IN THE Y-DIRECTION – STEP 30- 3D-VIEW 1

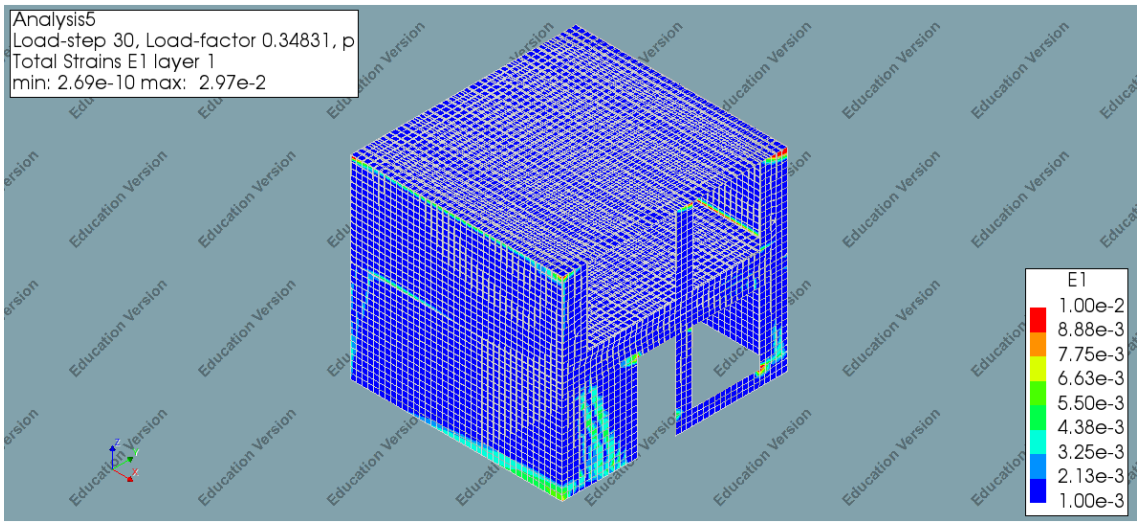

FIGURE 162: MAXIMUM PRINCIPAL STRAIN – STEP 30- 3D-VIEW 1

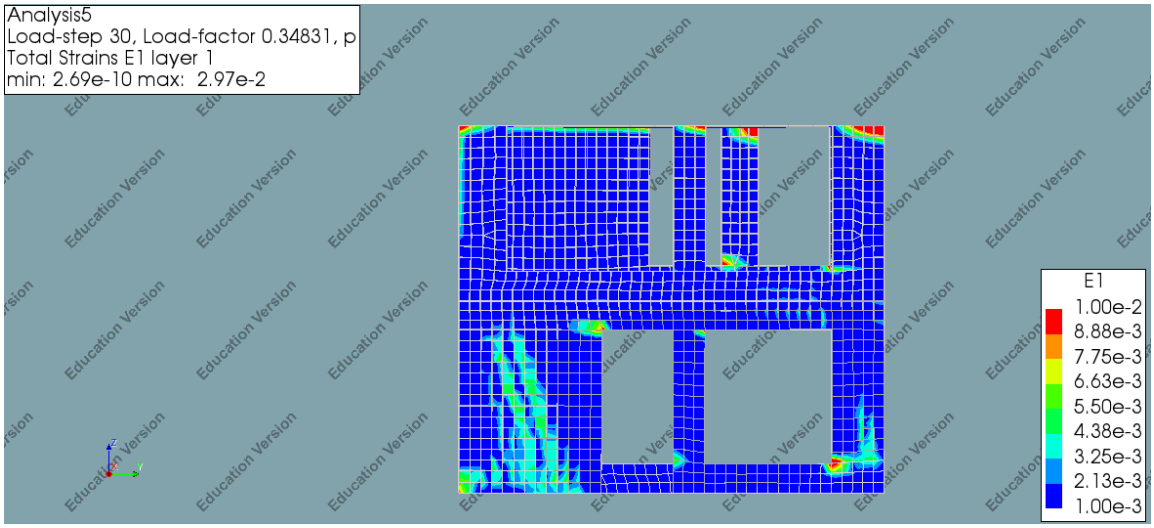

FIGURE 163: MAXIMUM PRINCIPAL STRAIN – STEP 30- SIDE-VIEW 1

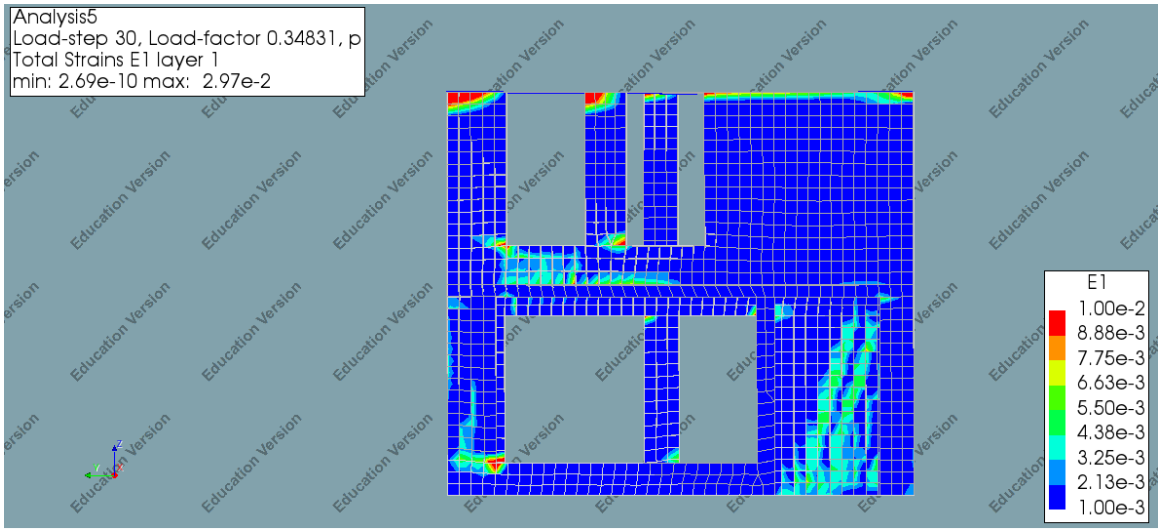

FIGURE 164: MAXIMUM PRINCIPAL STRAIN – STEP 30- SIDE-VIEW 2

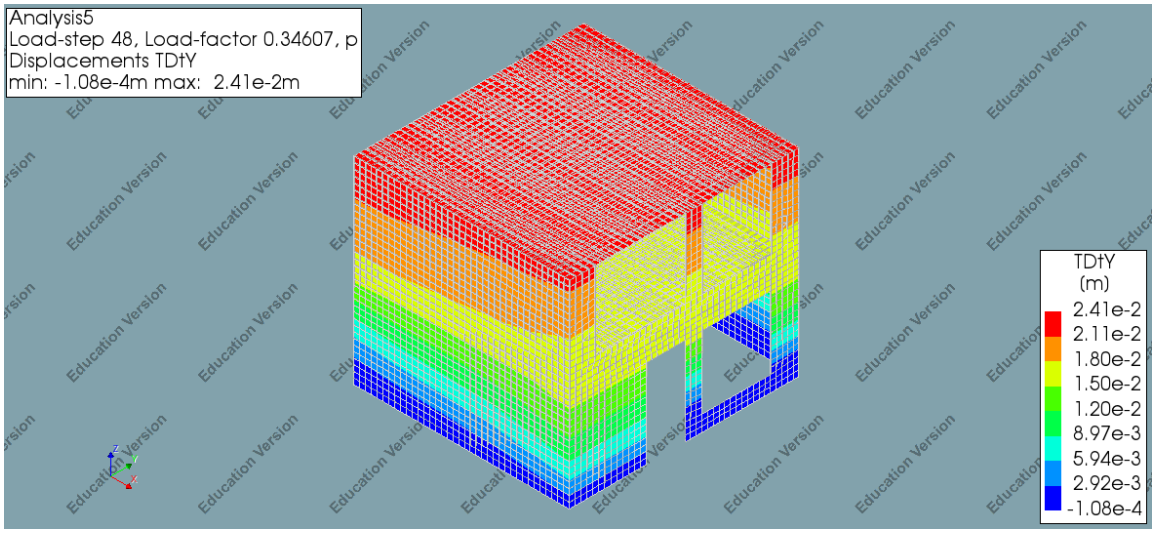

FIGURE 165: DEFLECTION IN THE Y-DIRECTION – STEP 48- 3D-VIEW 1

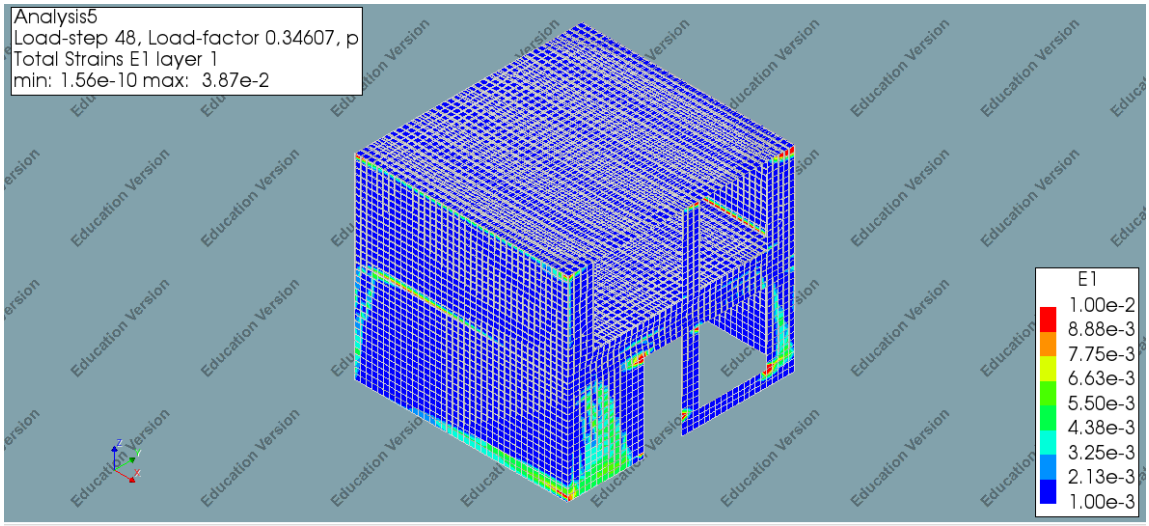

FIGURE 166: MAXIMUM PRINCIPAL STRAIN – STEP 40- 3D-VIEW 1

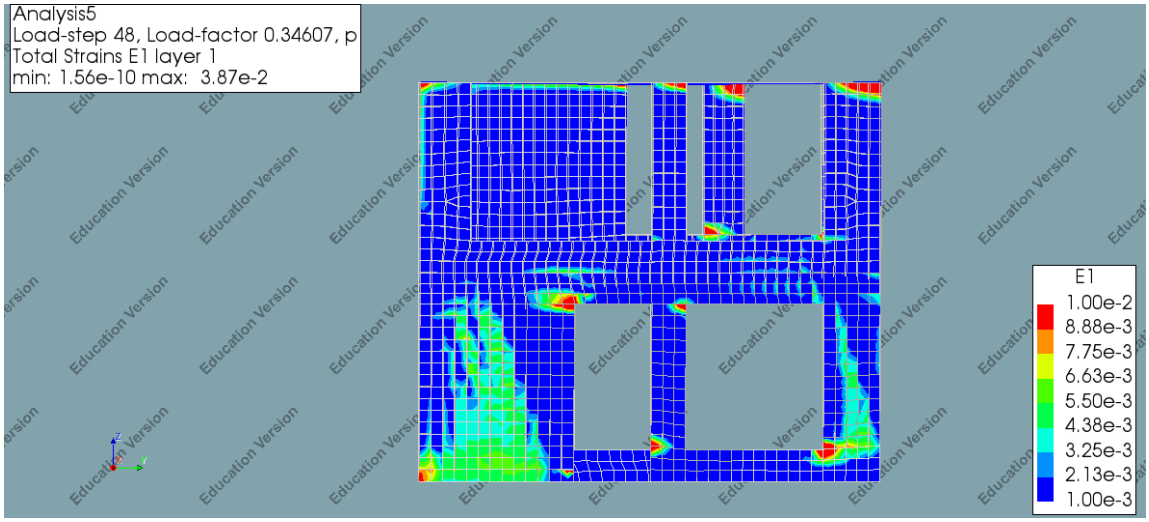

FIGURE 167: MAXIMUM PRINCIPAL STRAIN – STEP 48- SIDE-VIEW 1

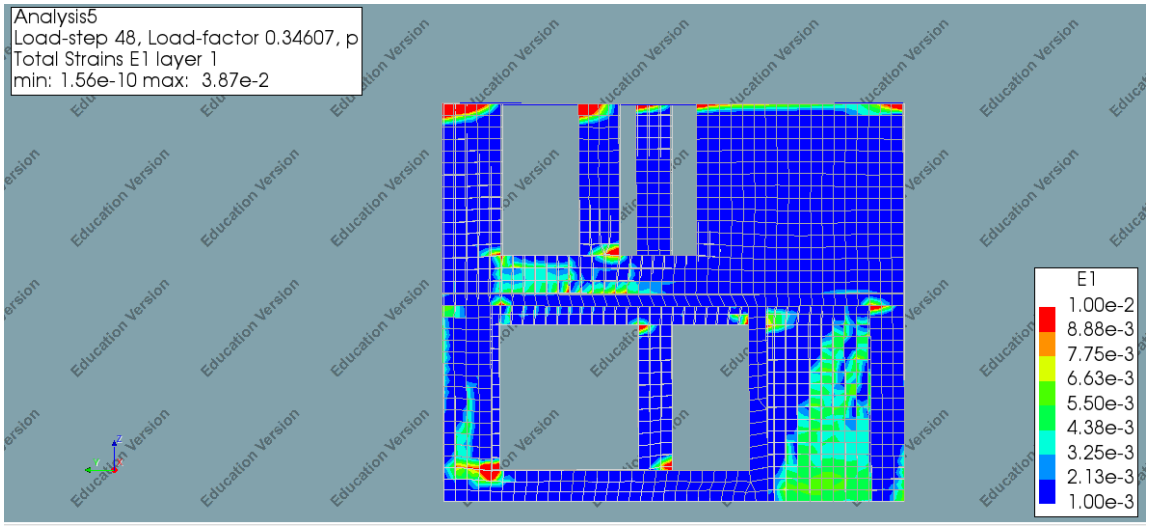

FIGURE 168: MAXIMUM PRINCIPAL STRAIN – STEP 48- SIDE-VIEW 2

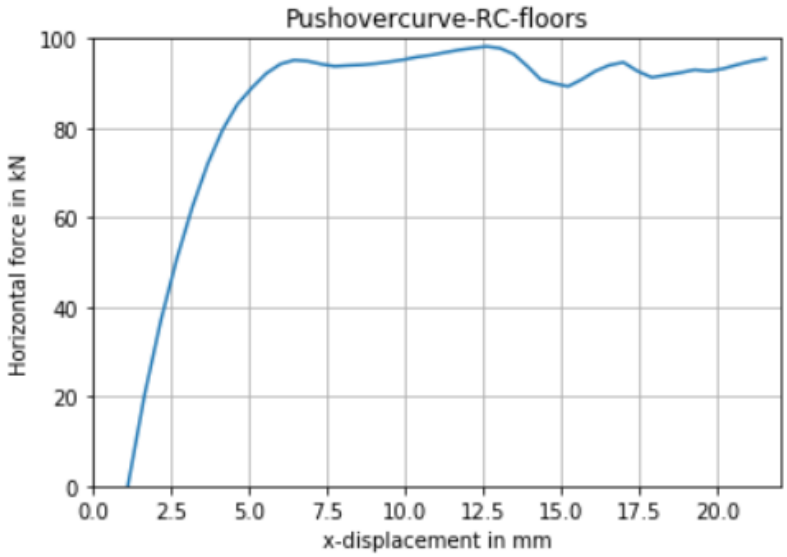

FIGURE 169:PUSHOVER CURVE 3D-MODEL-DOUBLE RC-FLOORS- HJ

3D-MODEL-DOUBLE RC-FLOORS- DIRECT

RESULTS: STRUCTURAL EIGENVALUE ANALYSIS

The first analysis that has been made is the structural eigenvalue analysis. This analysis is required to determine the critical Eigen mode and Eigen frequency. The Eigen mode with the highest participating mass is the critical Eigen mode. In this case Eigen mode 1 is the governing Eigen mode and corresponds to a participating mass percentage 84.2%. The Figure below shows first five Eigen modes and their participating masses.

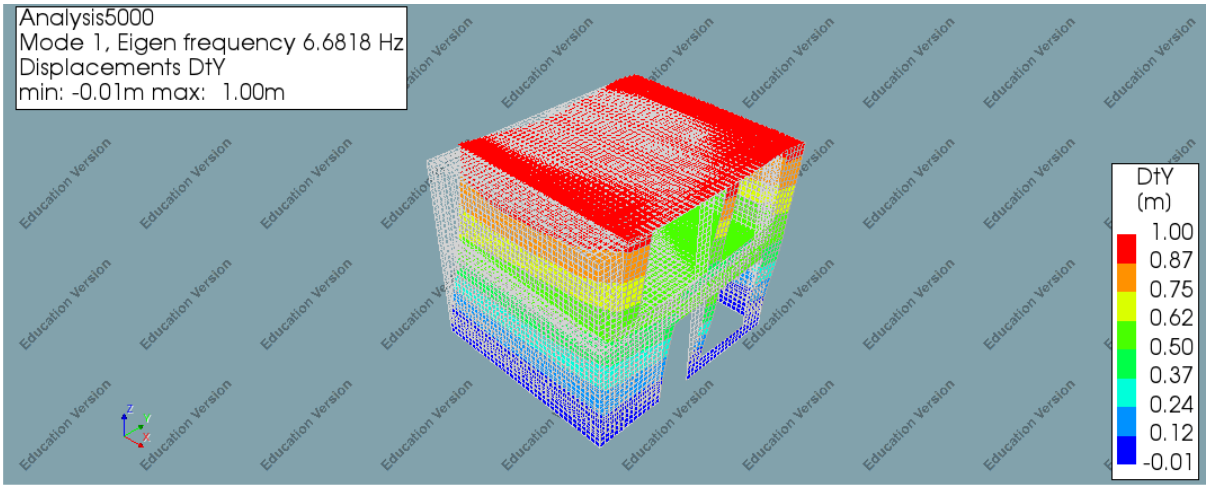

FIGURE 170: GOVERNING EIGEN MODE – 3D-MODEL-DOUBLE RC- FLOORS- DIRECT

TABLE 41: GOVERNING EIGEN MODE AND THE PARTICIPATING MASS- 3D-MODEL-DOUBLE RC- FLOORS- DIRECT

MODE	FREQUENCY	EFF.MASS TX	PERCENTAGE	CUM.PERCENT
1	0.66818+01	0.37091E+04	0.84232E+02	0.84232E+02

RESULTS: STRUCTURAL NONLINEAR ANALYSIS

This part contains the results of the structural nonlinear analysis. The relevant obtained results in this case, are the horizontal deflection, maximum principal strain, observed failure mechanism and the pushover curve.

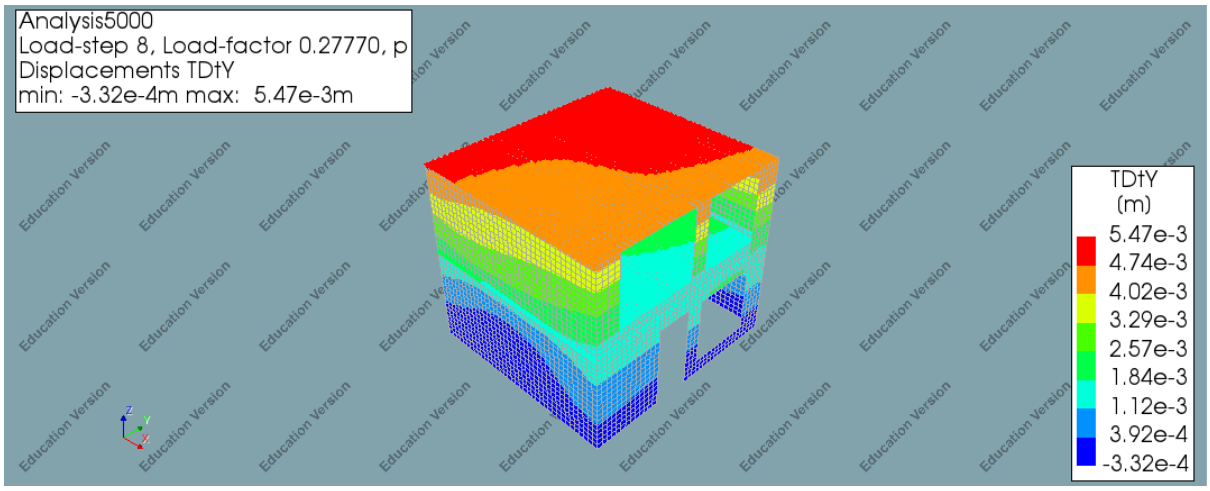

FIGURE 171: DEFLECTION IN THE Y-DIRECTION – STEP 8- 3D-VIEW 1

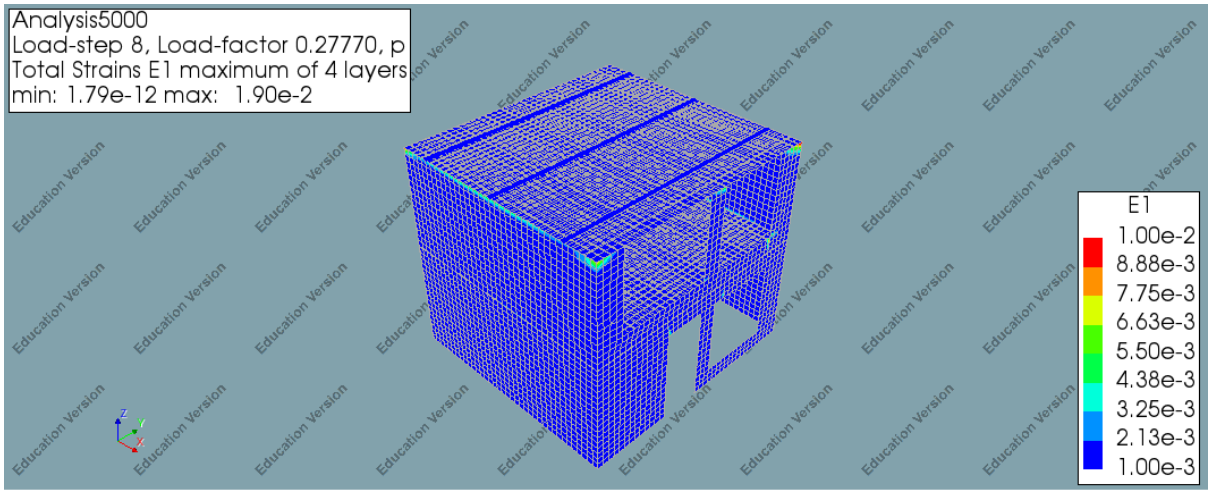

FIGURE 172: MAXIMUM PRINCIPAL STRAIN – STEP 8- 3D-VIEW 1

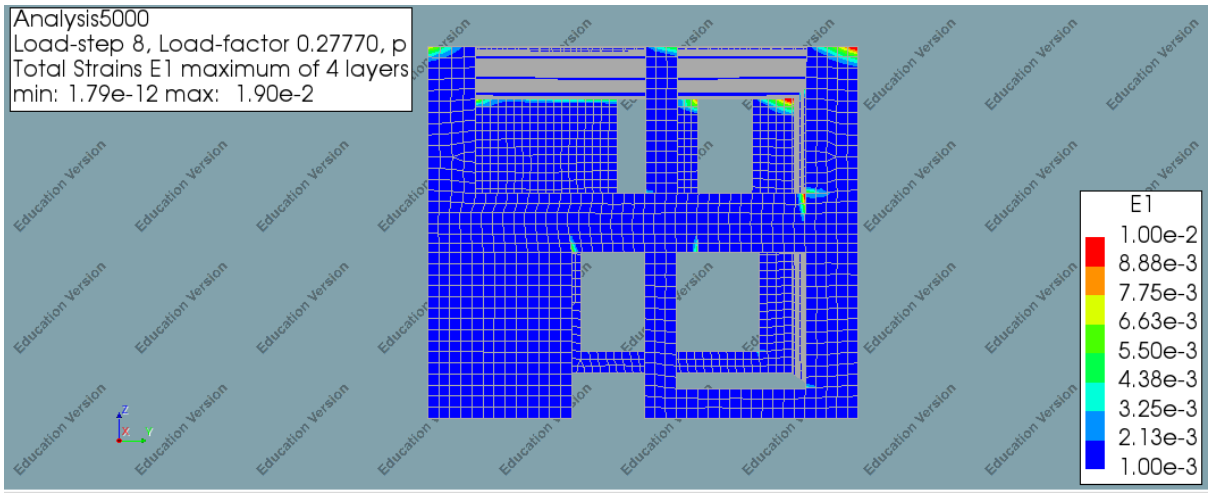

FIGURE 173: MAXIMUM PRINCIPAL STRAIN – STEP 8- SIDE-VIEW 1

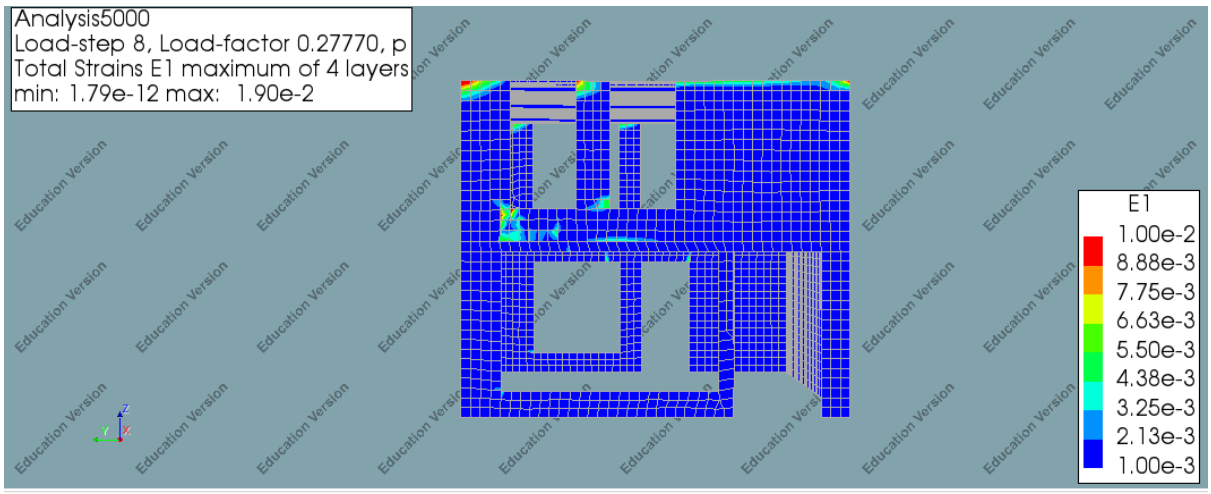

FIGURE 174: MAXIMUM PRINCIPAL STRAIN – STEP 8- SIDE-VIEW 2

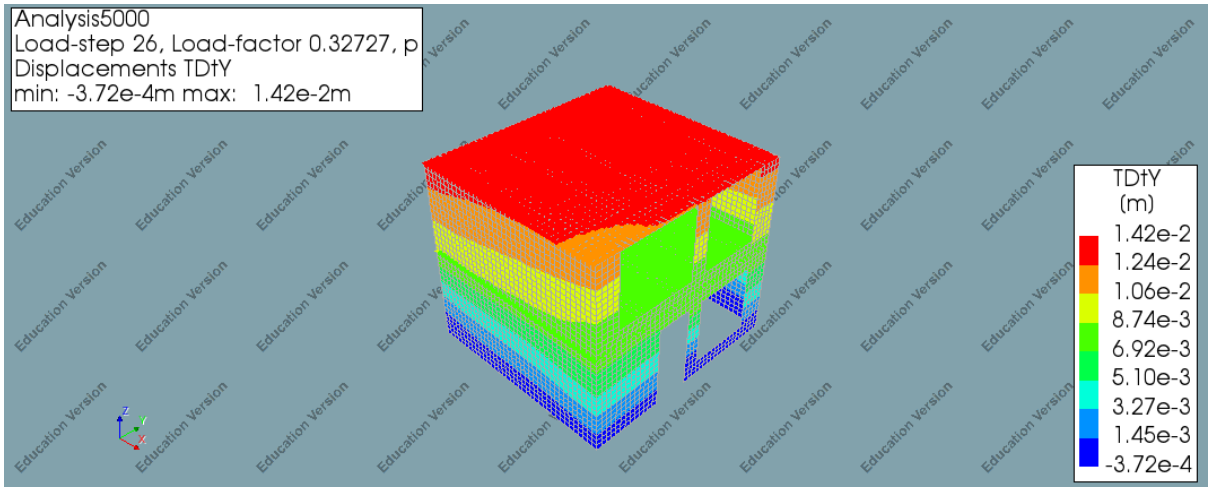

FIGURE 175: DEFLECTION IN THE Y-DIRECTION – STEP 26- 3D-VIEW 1

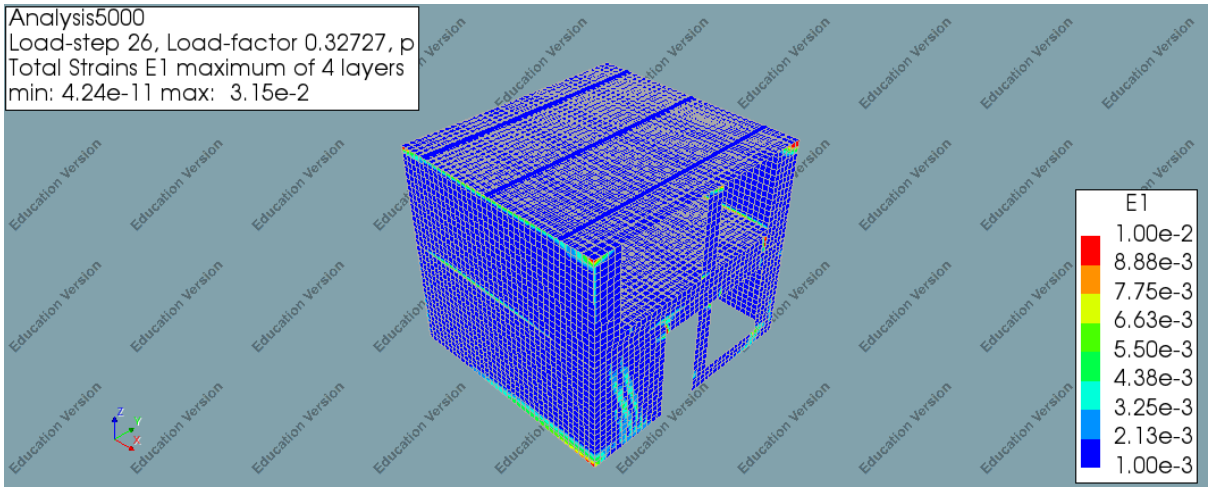

FIGURE 176: MAXIMUM PRINCIPAL STRAIN – STEP 26- 3D-VIEW 1

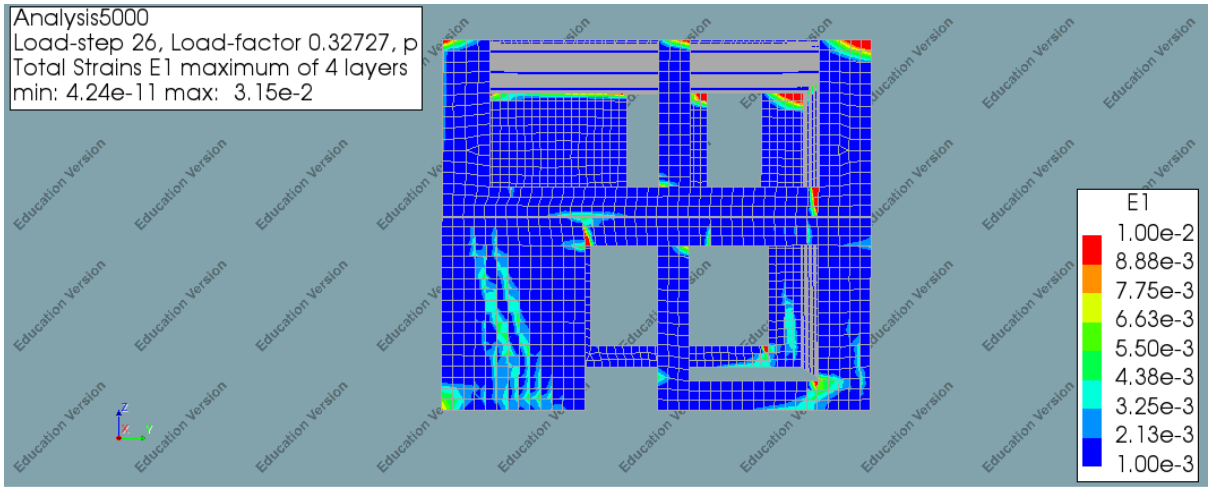

FIGURE 177: MAXIMUM PRINCIPAL STRAIN – STEP 26- SIDE-VIEW 1

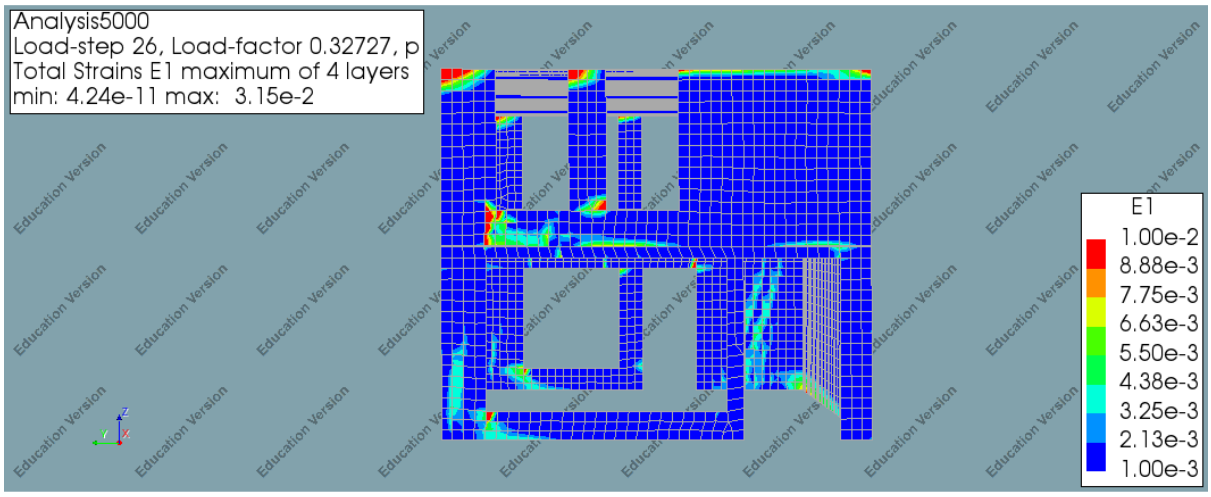

FIGURE 178: MAXIMUM PRINCIPAL STRAIN – STEP 26- SIDE-VIEW 2

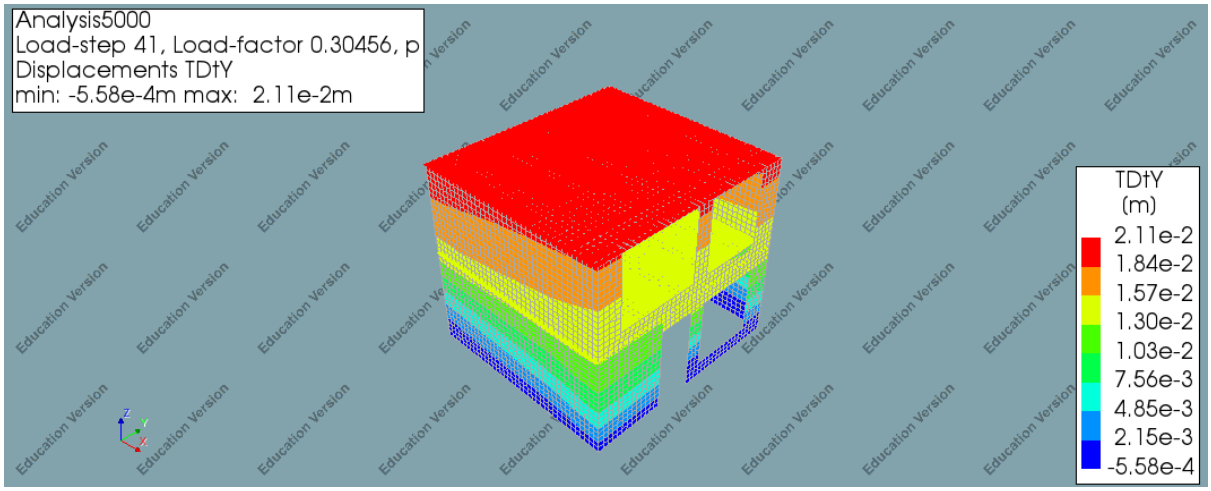

FIGURE 179: DEFLECTION IN THE Y-DIRECTION – STEP 41- 3D-VIEW 1

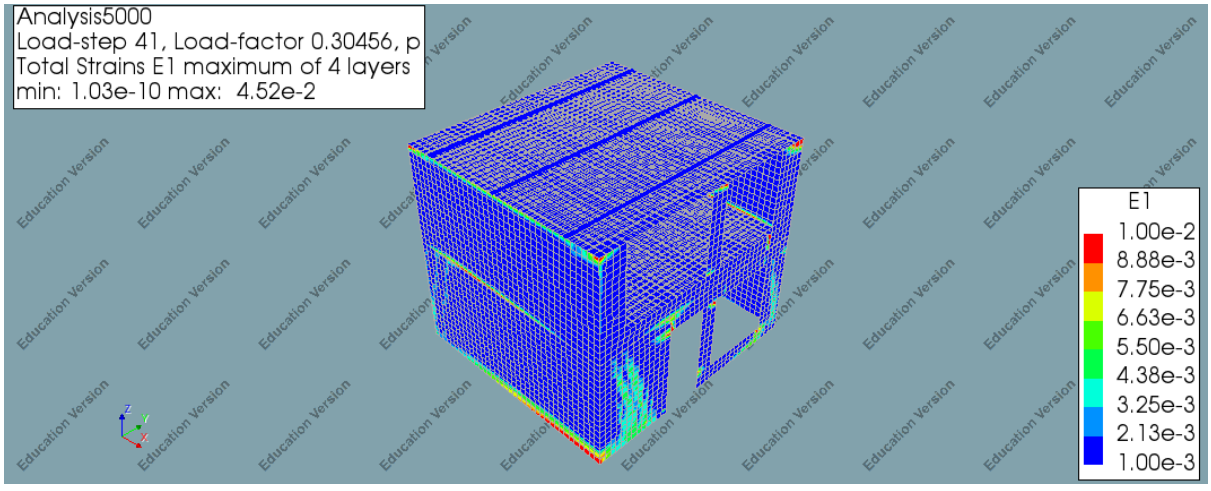

FIGURE 180: MAXIMUM PRINCIPAL STRAIN – STEP 41- 3D-VIEW 1

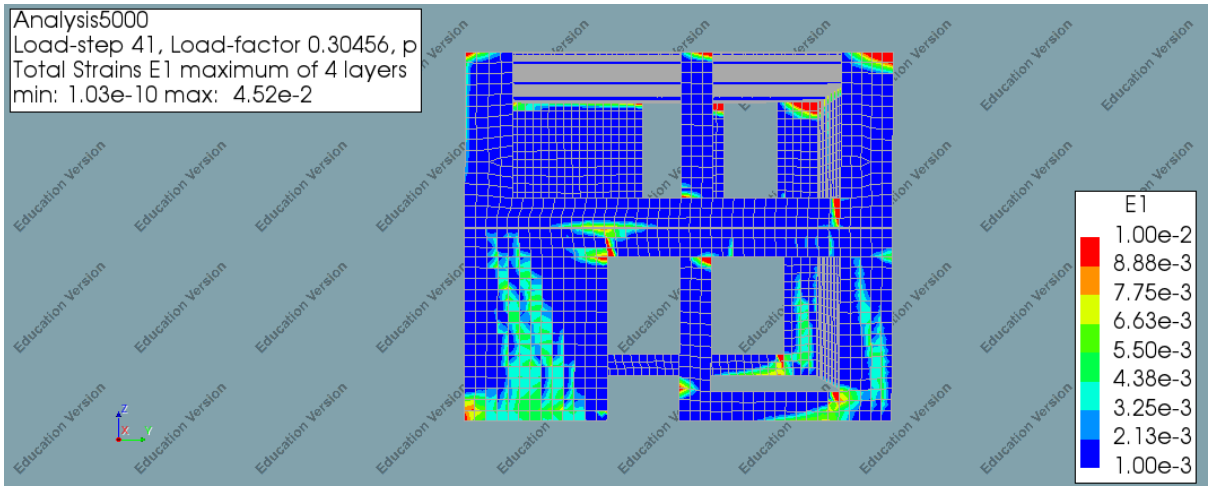

FIGURE 181: MAXIMUM PRINCIPAL STRAIN – STEP 41- SIDE-VIEW 1

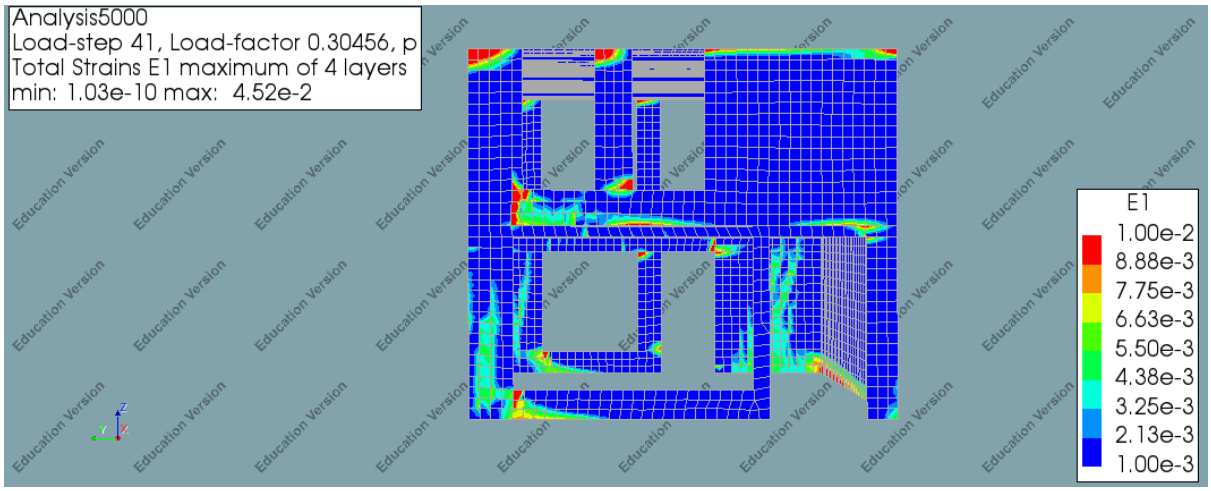

FIGURE 182: MAXIMUM PRINCIPAL STRAIN – STEP 41- SIDE-VIEW 2

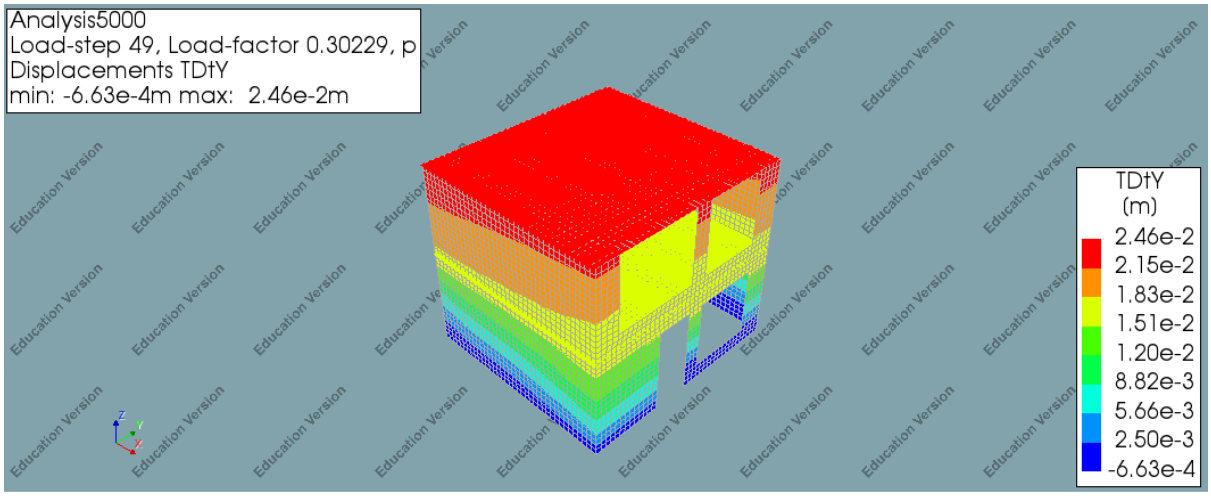

FIGURE 183: DEFLECTION IN THE Y-DIRECTION – STEP 49- 3D-VIEW 1

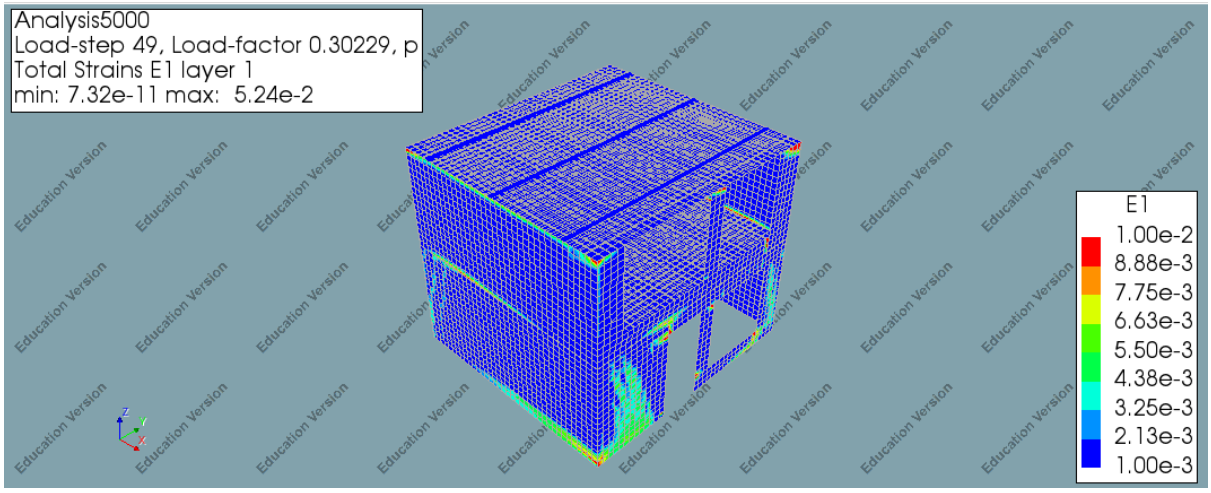

FIGURE 184: MAXIMUM PRINCIPAL STRAIN – STEP 49- 3D-VIEW 1

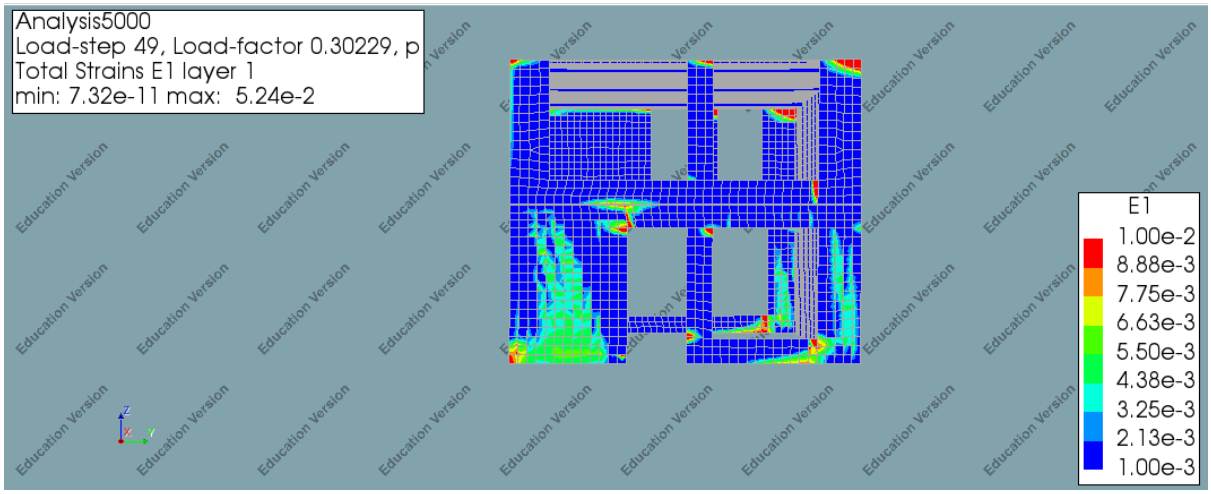

FIGURE 185: MAXIMUM PRINCIPAL STRAIN – STEP 49- SIDE-VIEW 1

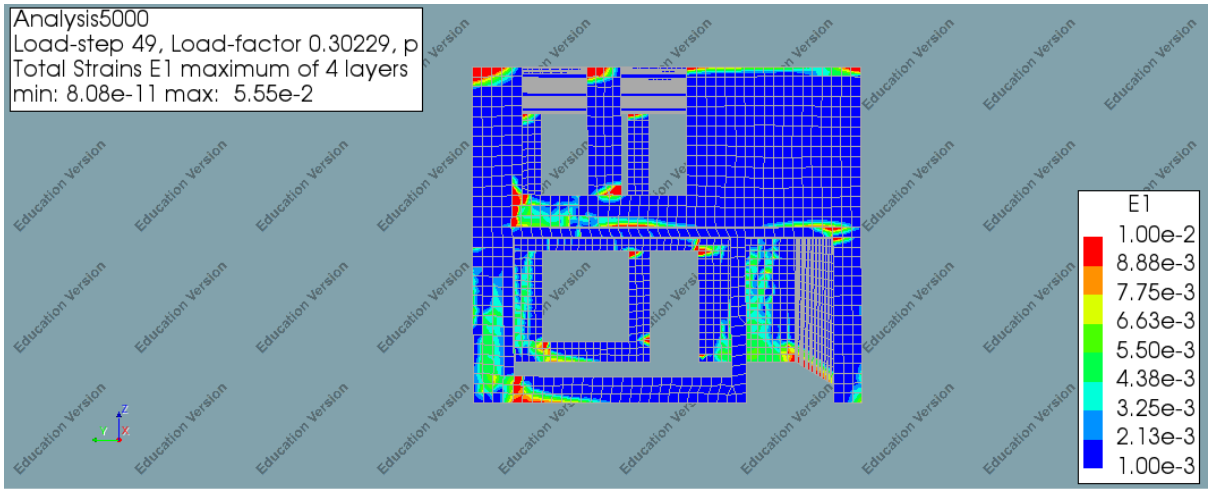

FIGURE 186: MAXIMUM PRINCIPAL STRAIN – STEP 49- SIDE-VIEW 2

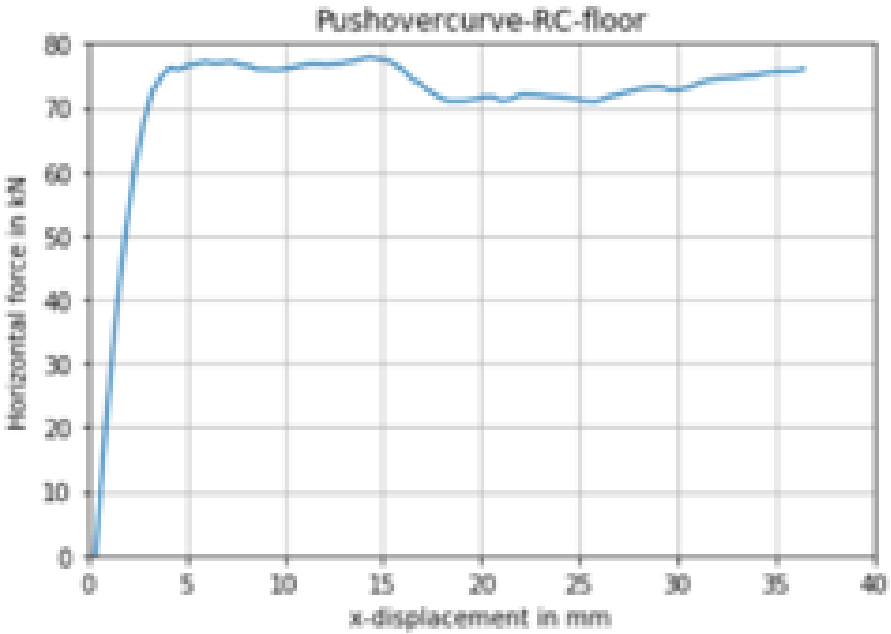

FIGURE 187: PUSHOVER CURVE 3D-MODEL-DOUBLE RC-FLOORS- DIRECT

3D-MODEL-DOUBLE TIMBER FLOOR-DS

RESULTS: STRUCTURAL EIGENVALUE ANALYSIS

The first analysis that has been made is the structural eigenvalue analysis. This analysis is required to determine the critical Eigen mode and Eigen frequency. The Eigen mode with the highest participating mass is the critical Eigen mode. In this case Eigen mode 1 is the governing Eigen mode and corresponds to a participating mass percentage 54%. The Figure below shows first five Eigen modes and their participating masses.

MODE	FREQUENCY	EFF.MASS TX	PERCENTAGE	CUM.PERCENT
1	0.38446+01	0.12892E+04	0.54177E+02	0.54177E+02

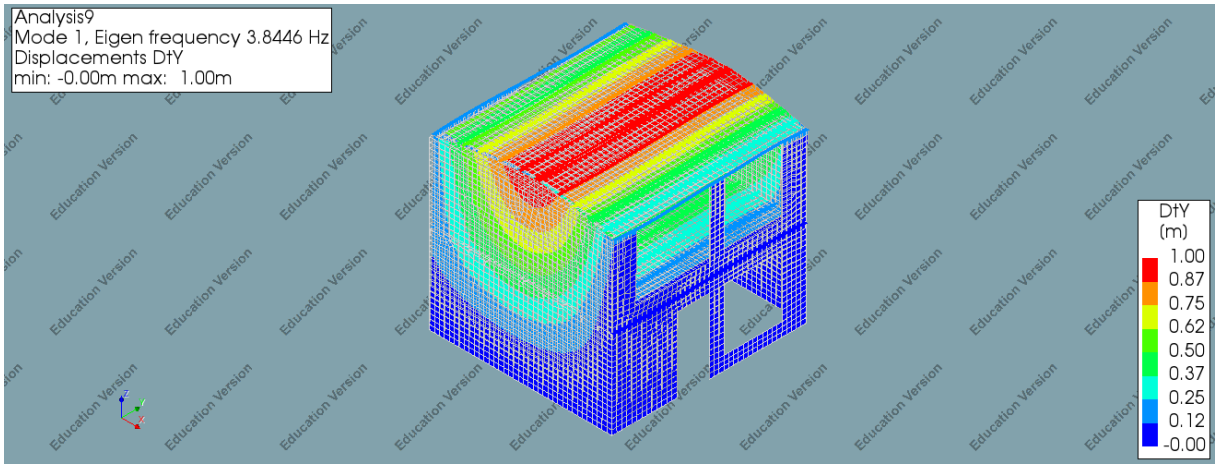

FIGURE 188: GOVERNING EIGEN MODE – 3D-MODEL-DOUBLE TIMBER - FLOORS- DS

RESULTS: STRUCTURAL NONLINEAR ANALYSIS

This part contains the results of the structural nonlinear analysis. The relevant obtained results in this case, are the horizontal deflection, maximum principal strain, observed failure mechanism and the pushover curve.

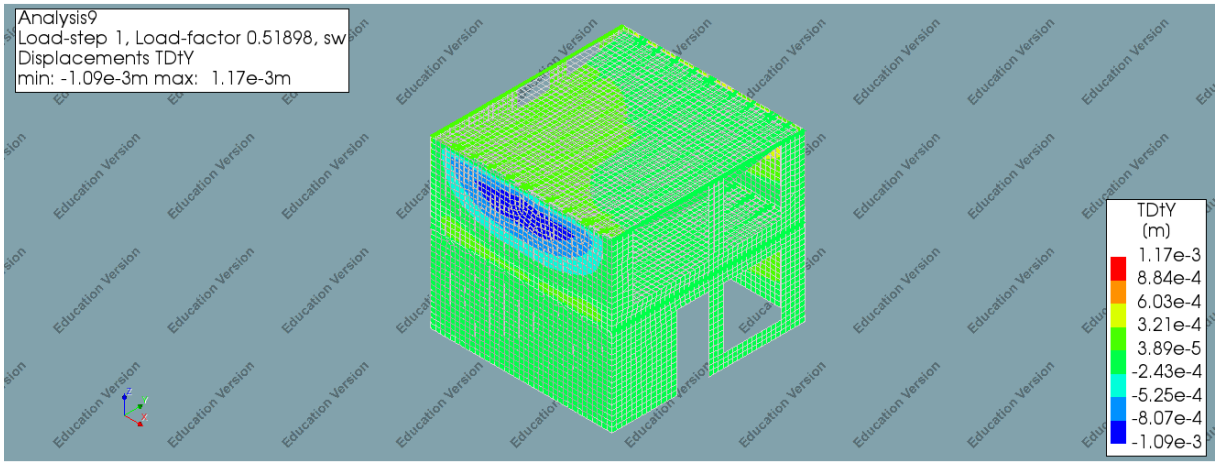

FIGURE 189: DEFLECTION IN THE Y-DIRECTION – STEP 1- 3D-VIEW 1

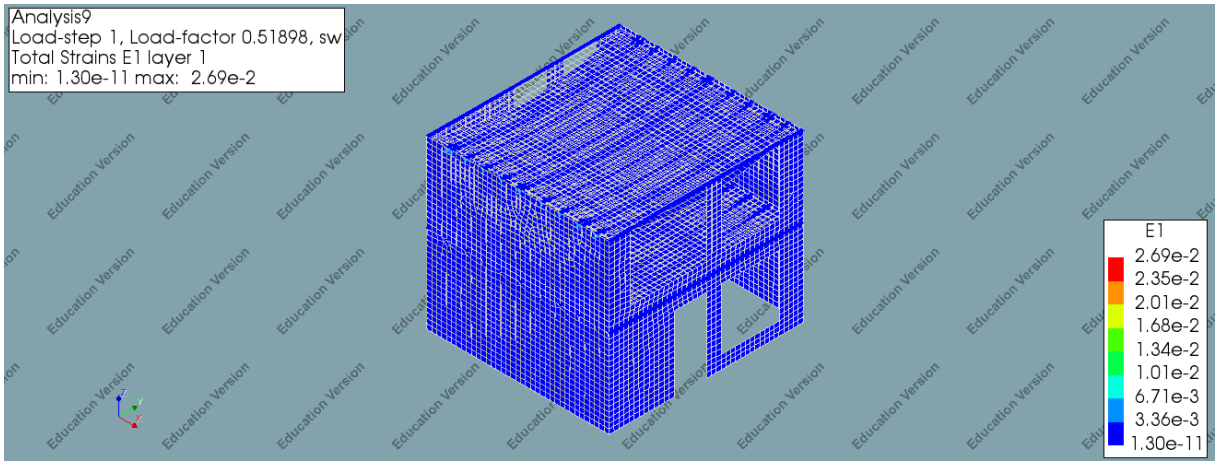

FIGURE 190: MAXIMUM PRINCIPAL STRAIN – STEP 1- 3D-VIEW 1

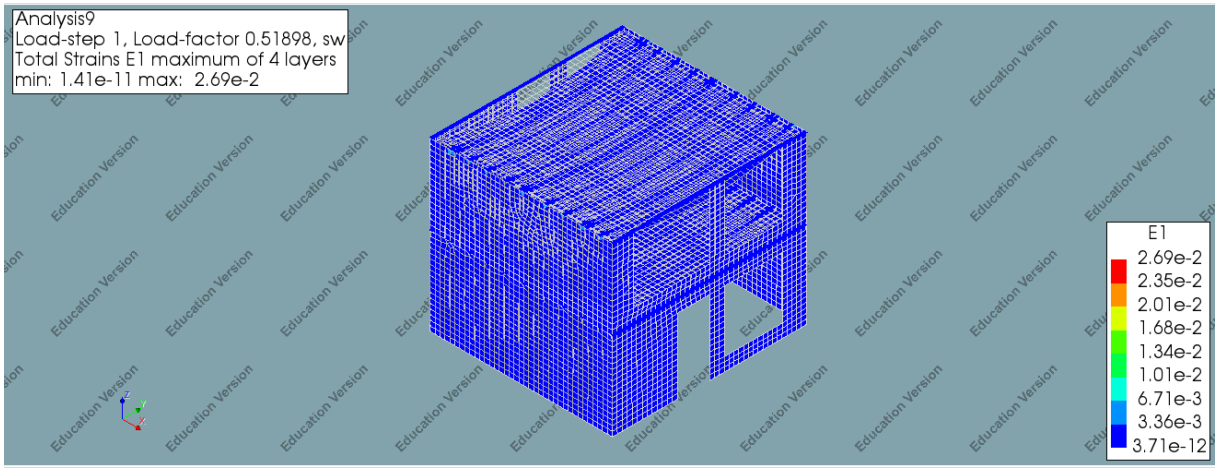

FIGURE 191: MAXIMUM PRINCIPAL STRAIN – STEP 1- 3D-VIEW 1

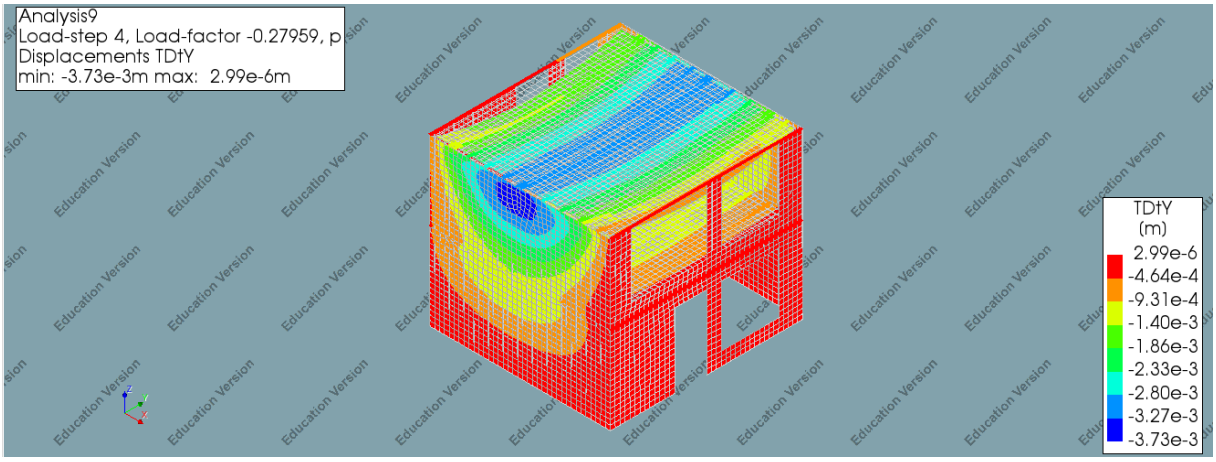

FIGURE 192: DEFLECTION IN THE Y-DIRECTION – STEP 4- 3D-VIEW 1

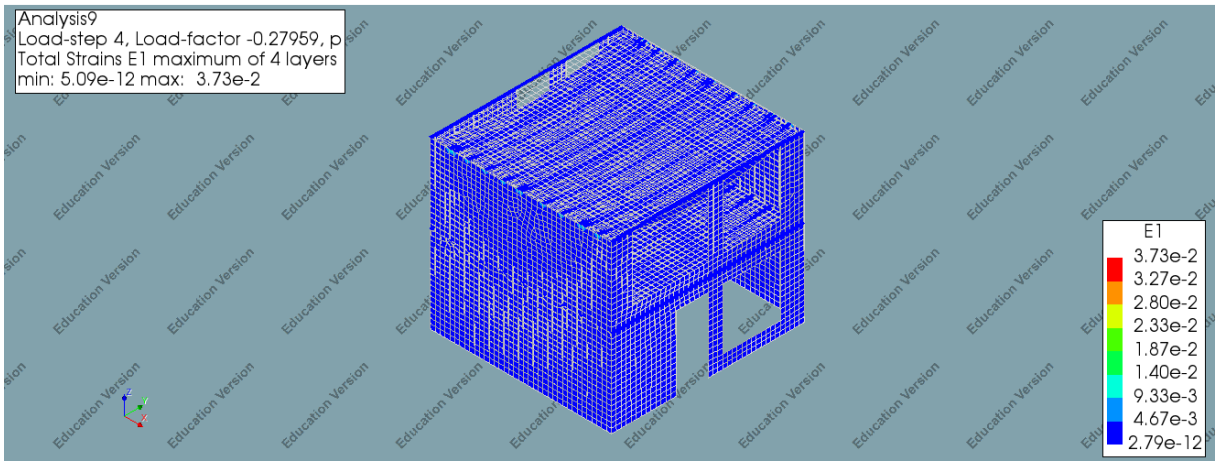

FIGURE 193: MAXIMUM PRINCIPAL STRAIN – STEP 4- 3D-VIEW 1

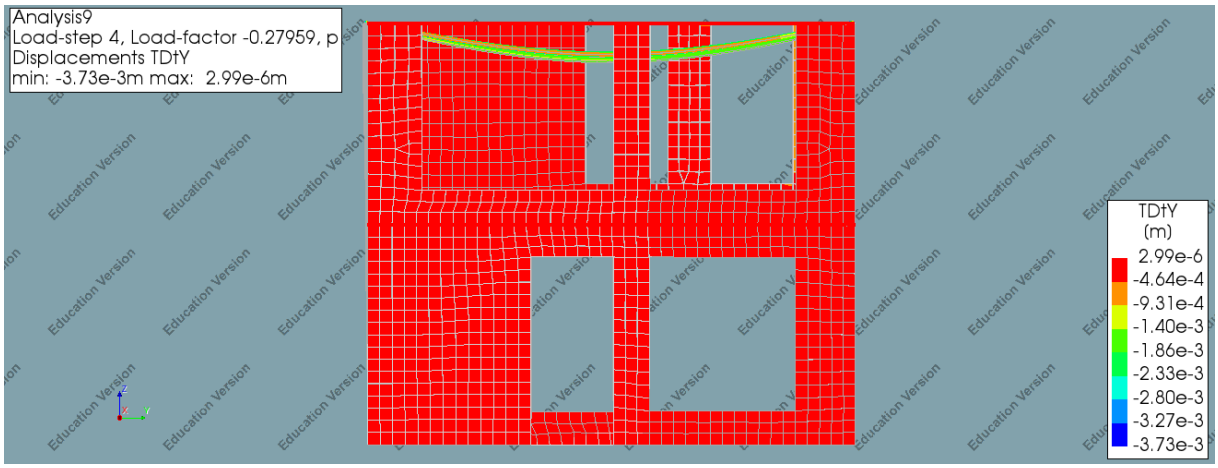

FIGURE 194: DEFLECTION IN THE Y-DIRECTION – STEP 4- 3D-VIEW 1

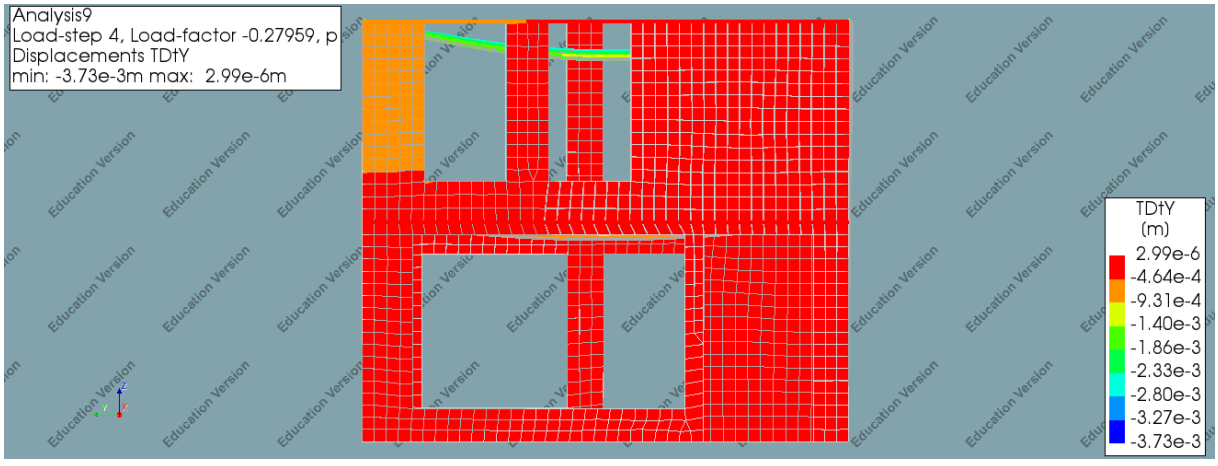

FIGURE 195: DEFLECTION IN THE Y-DIRECTION – STEP 4- 3D-VIEW 1

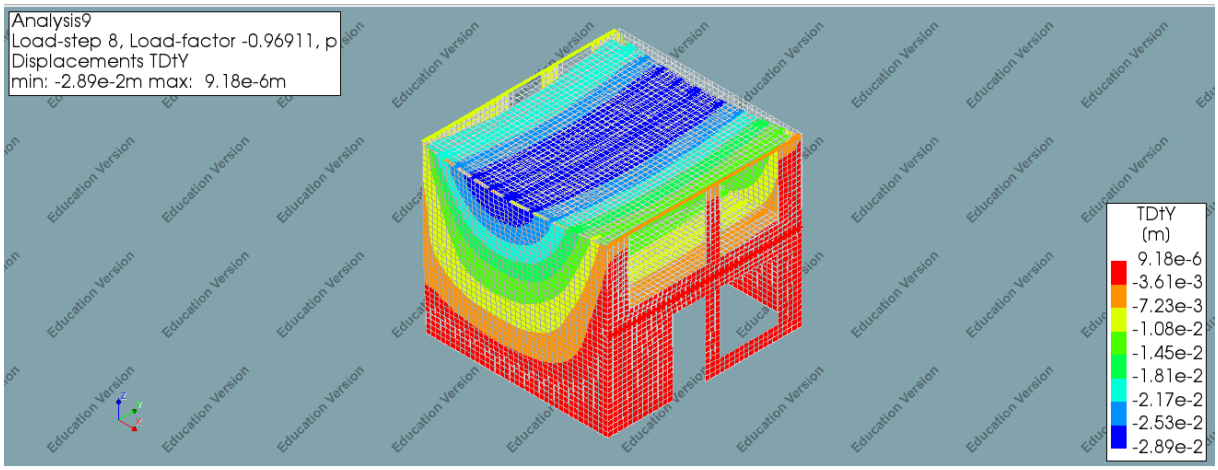

FIGURE 196: DEFLECTION IN THE Y-DIRECTION – STEP 8- 3D-VIEW 1

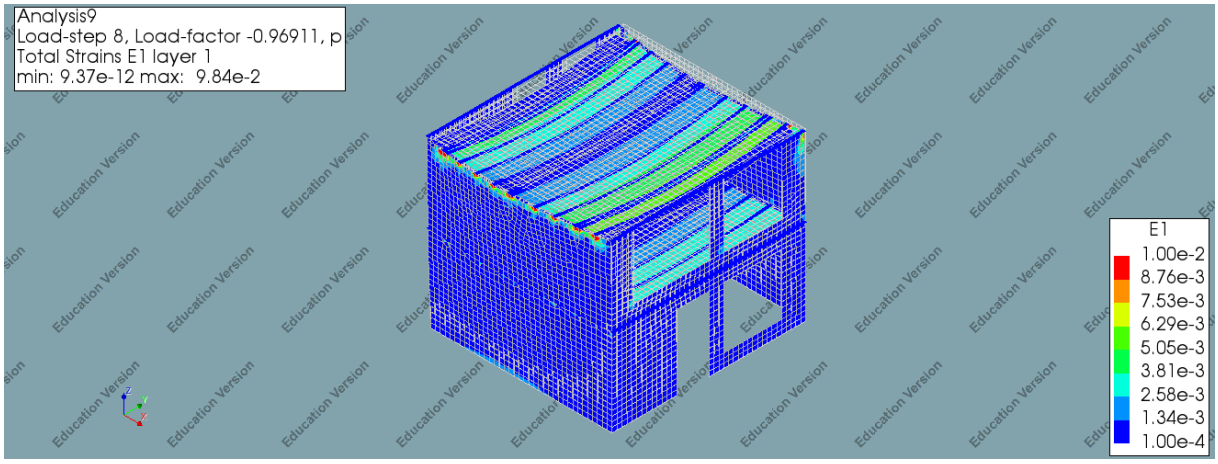

FIGURE 197: MAXIMUM PRINCIPAL STRAIN – STEP 8- 3D-VIEW 1

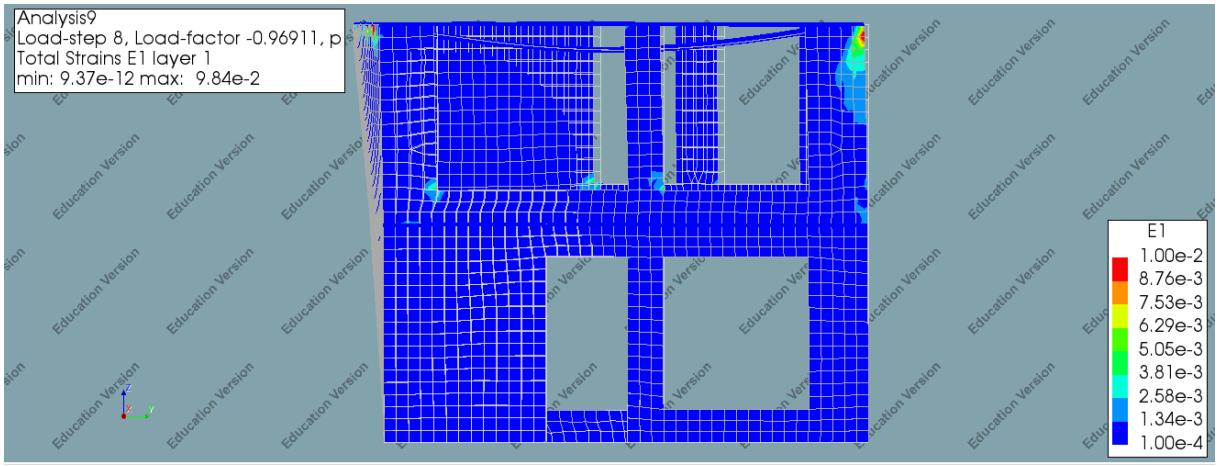

FIGURE 198: MAXIMUM PRINCIPAL STRAIN – STEP 8- SIDE-VIEW 1

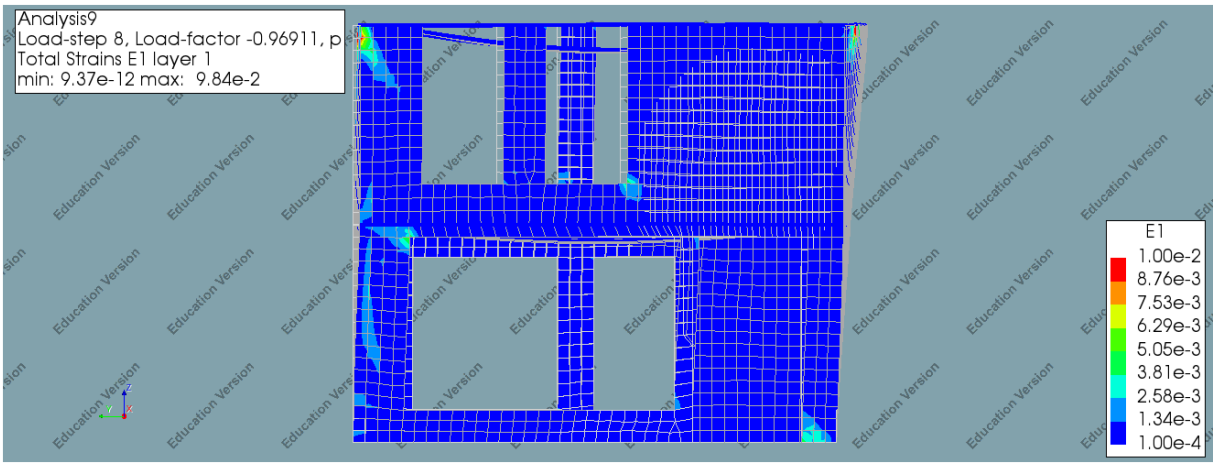

FIGURE 199: MAXIMUM PRINCIPAL STRAIN – STEP 8- SIDE-VIEW 1

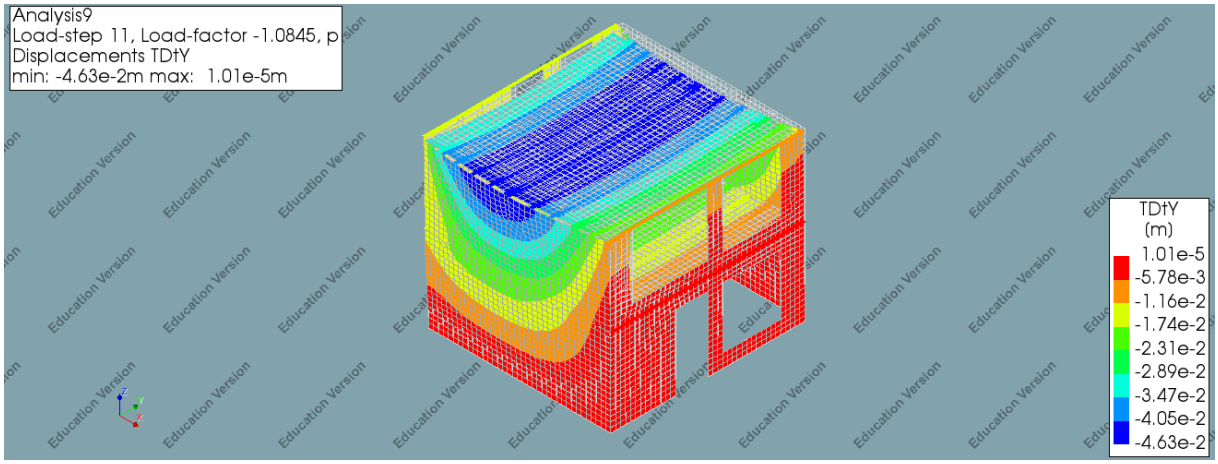

FIGURE 200: DEFLECTION IN THE Y-DIRECTION – STEP 11- 3D-VIEW 1

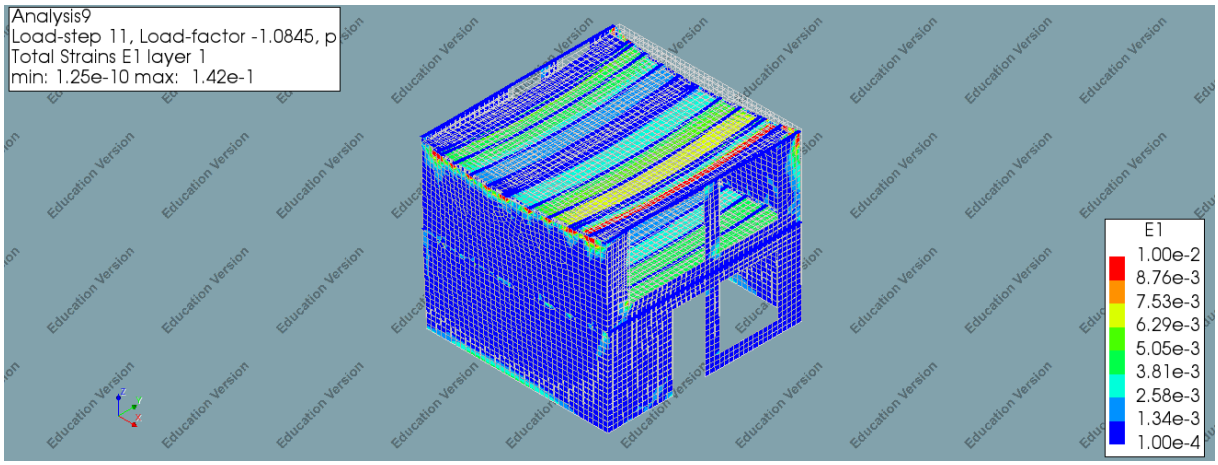

FIGURE 201: MAXIMUM PRINCIPAL STRAIN – STEP 11-3D -VIEW 1

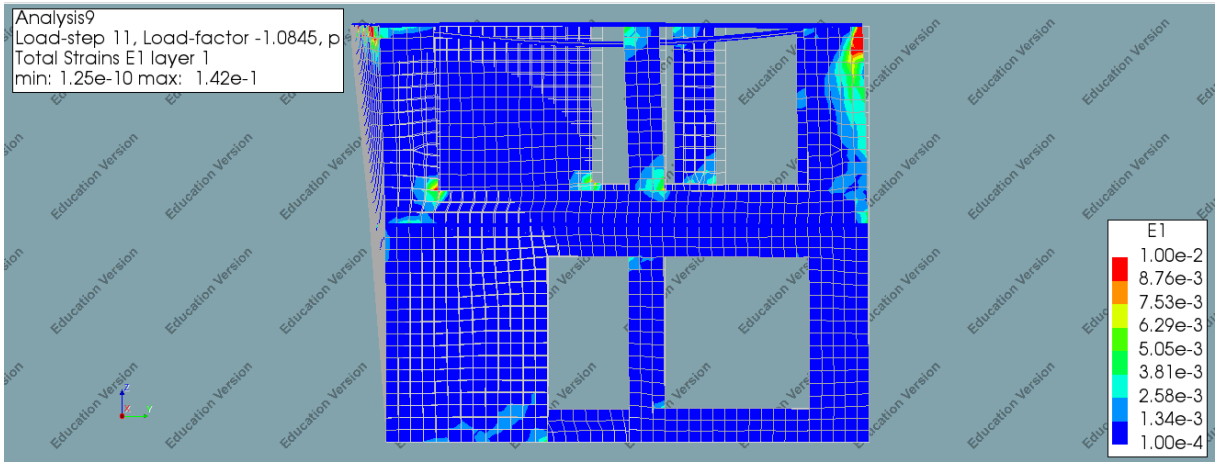

FIGURE 202: MAXIMUM PRINCIPAL STRAIN – STEP 11- SIDE-VIEW 1

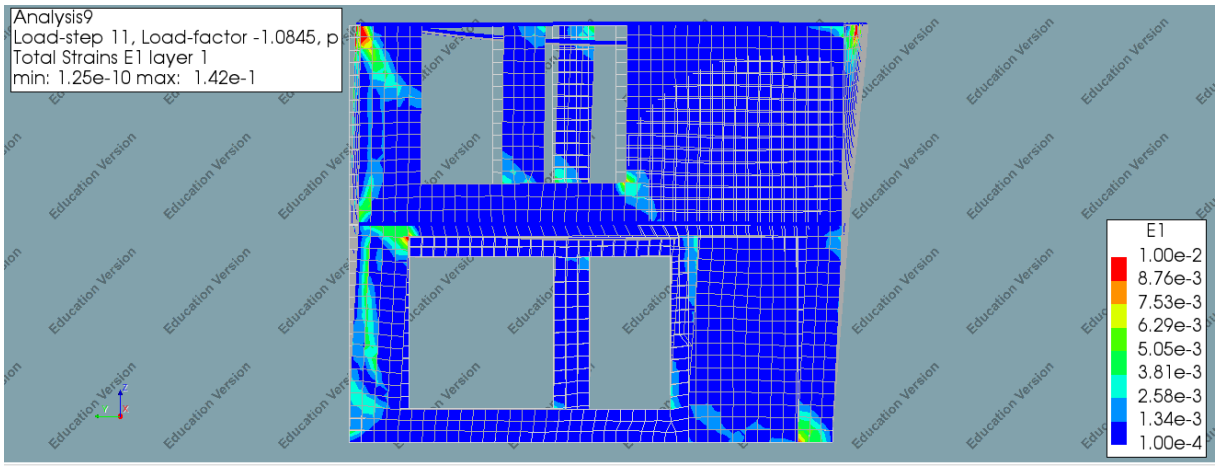

FIGURE 203: MAXIMUM PRINCIPAL STRAIN – STEP 11- SIDE-VIEW 1

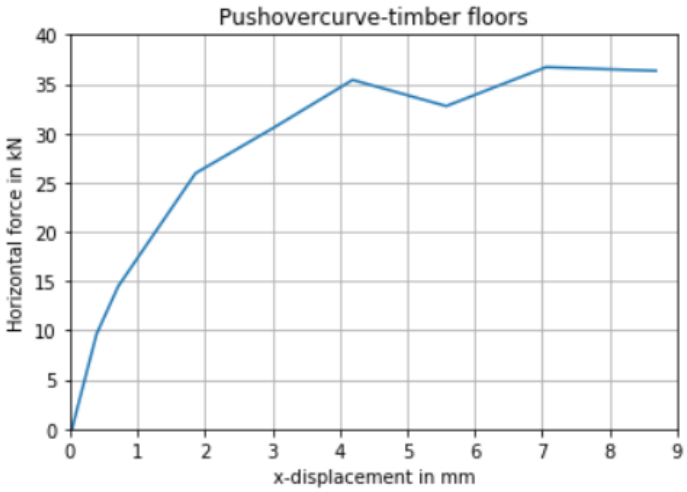

FIGURE 204: PUSHOVER CURVE 3D MODEL DOUBLE TIMBER FLOOR-DS

3D-MODEL-DOUBLE TIMBER FLOOR-HJ

RESULTS: STRUCTURAL EIGENVALUE ANALYSIS

The first analysis that has been made is the structural eigenvalue analysis. This analysis is required to determine the critical Eigen mode and Eigen frequency. The Eigen mode with the highest participating mass is the critical Eigen mode. In this case Eigen mode 1 is the governing Eigen mode and corresponds to a participating mass percentage 54%. The Figure below shows first five Eigen modes and their participating masses.

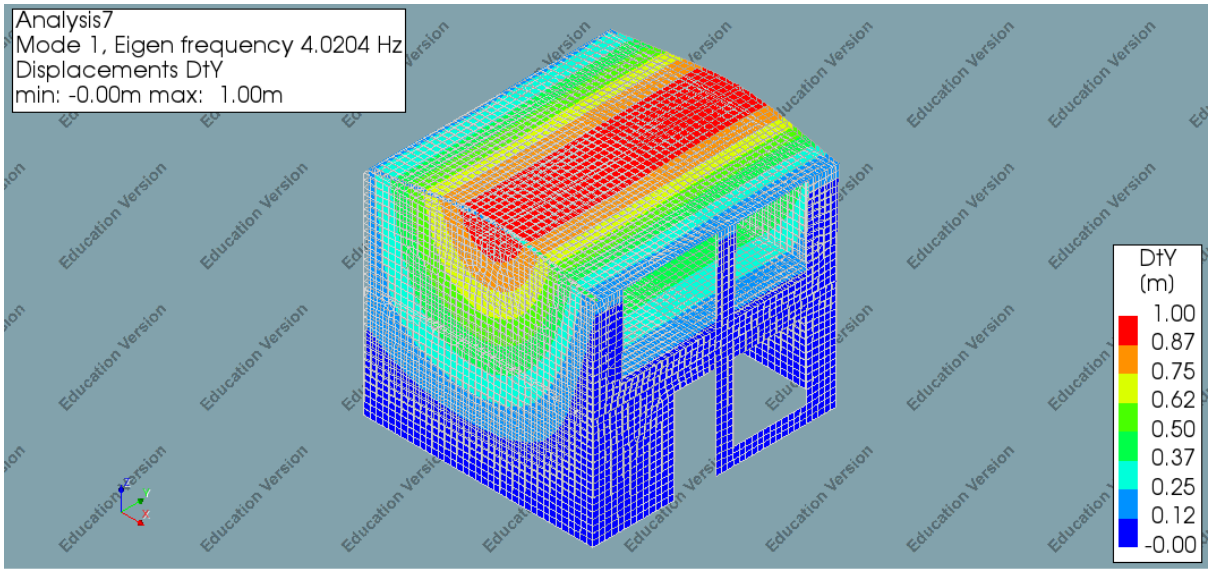

FIGURE 205: GOVERNING EIGEN MODE – 3D-MODEL-DOUBLE TIMBER - FLOORS- HJ

TABLE 42: GOVERNING EIGEN MODE AND PARTICIPATING MASS – 3D-MODEL-DOUBLE TIMBER - FLOORS- HJ

MODE	FREQUENCY	EFF.MASS TX	PERCENTAGE	CUM.PERCENT
1	0.40204+01	0.13018E+04	0.54424E+02	0.54424E+02

RESULTS: STRUCTURAL NONLINEAR ANALYSIS

This part contains the results of the structural nonlinear analysis. The relevant obtained results in this case, are the horizontal deflection, maximum principal strain, observed failure mechanism and the pushover curve.

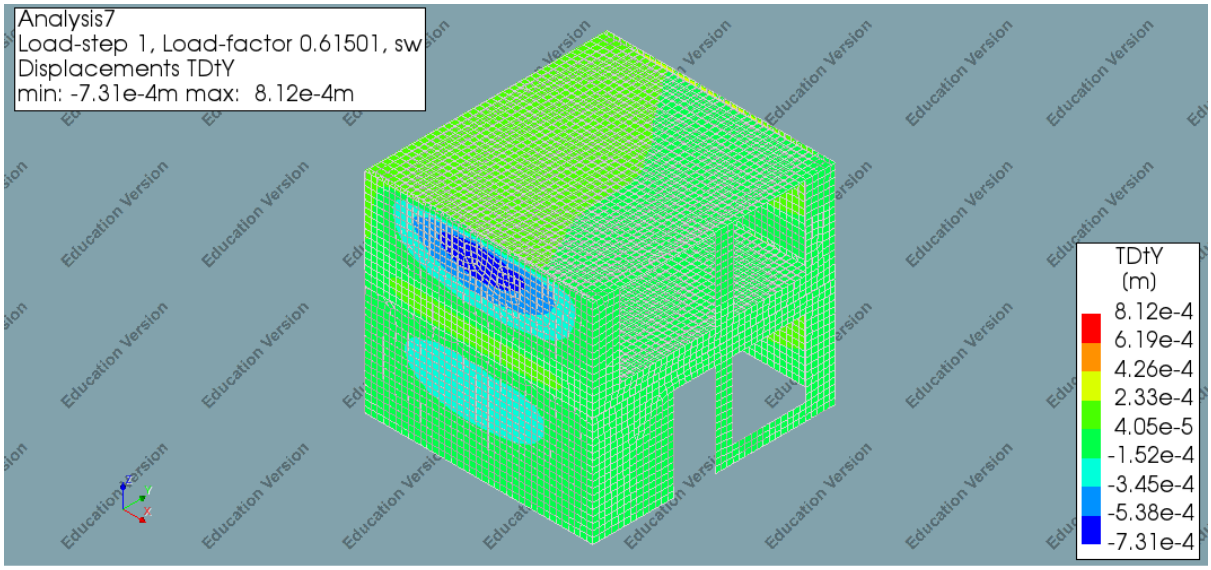

FIGURE 206: DEFLECTION IN THE Y-DIRECTION – STEP 1- 3D-VIEW 1

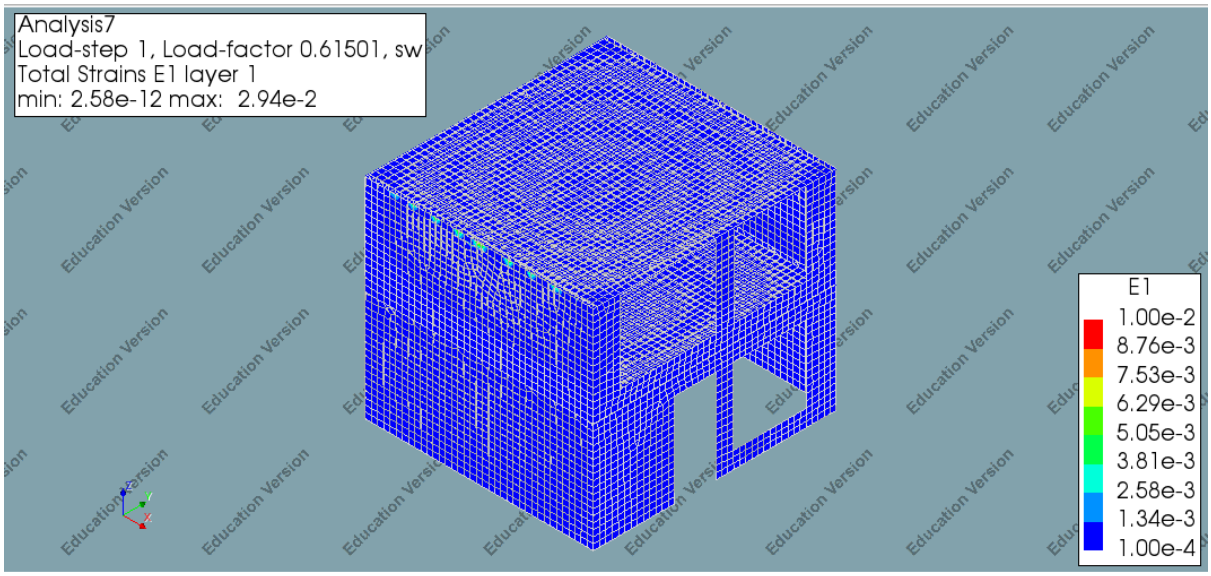

FIGURE 207: MAXIMUM PRINCIPAL STRAIN – STEP 1- 3D-VIEW 1

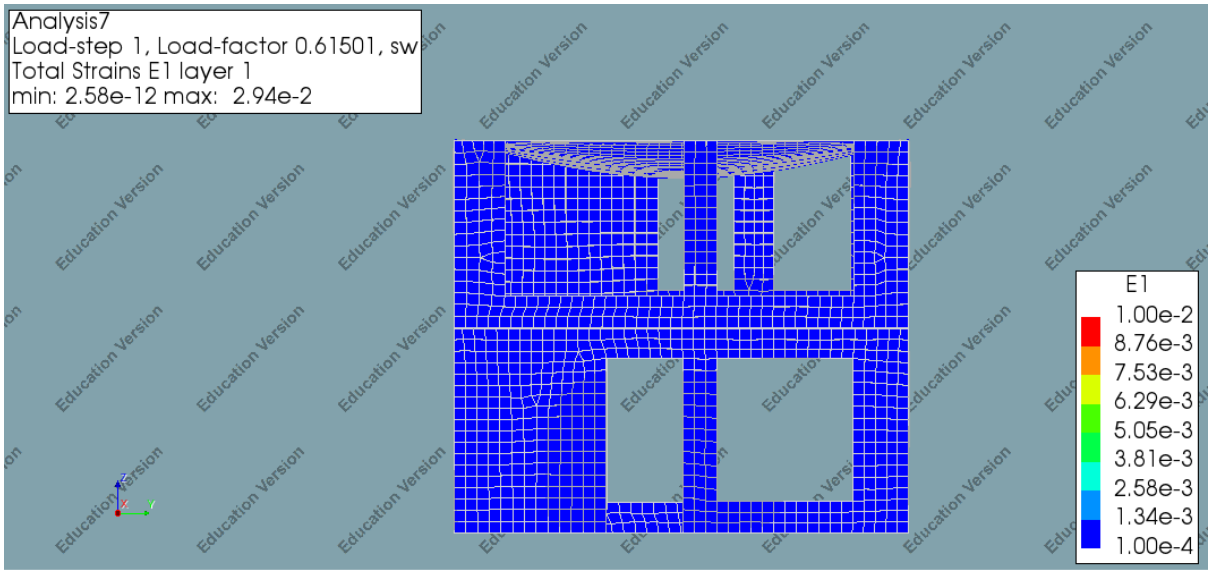

FIGURE 208: MAXIMUM PRINCIPAL STRAIN – STEP 1- SIDE-VIEW 1

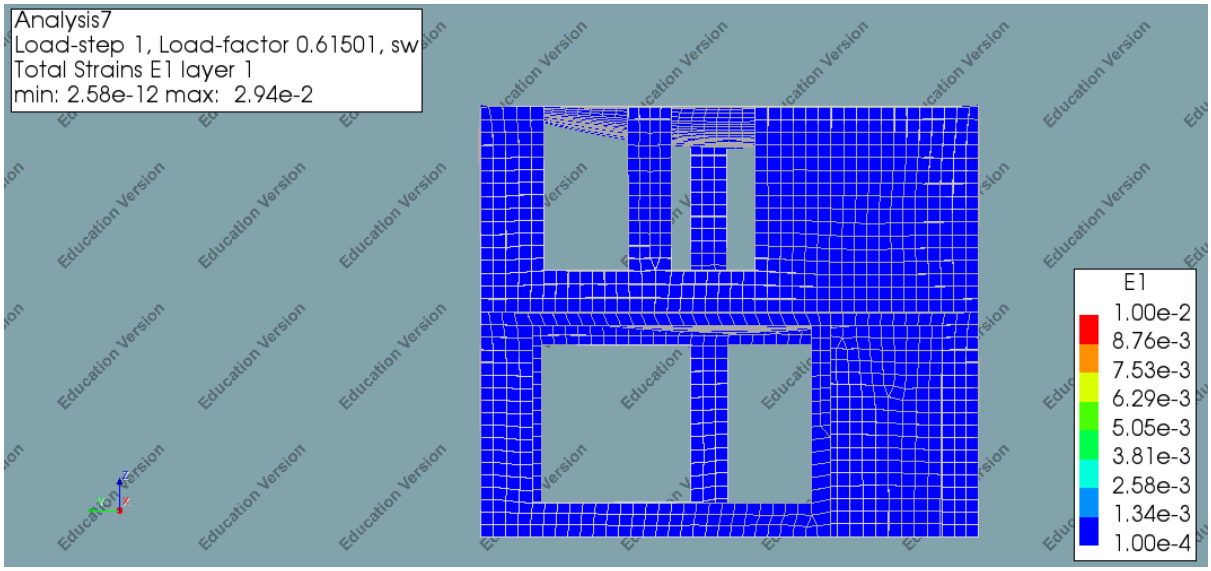

FIGURE 209: MAXIMUM PRINCIPAL STRAIN – STEP 1- SIDE-VIEW 2

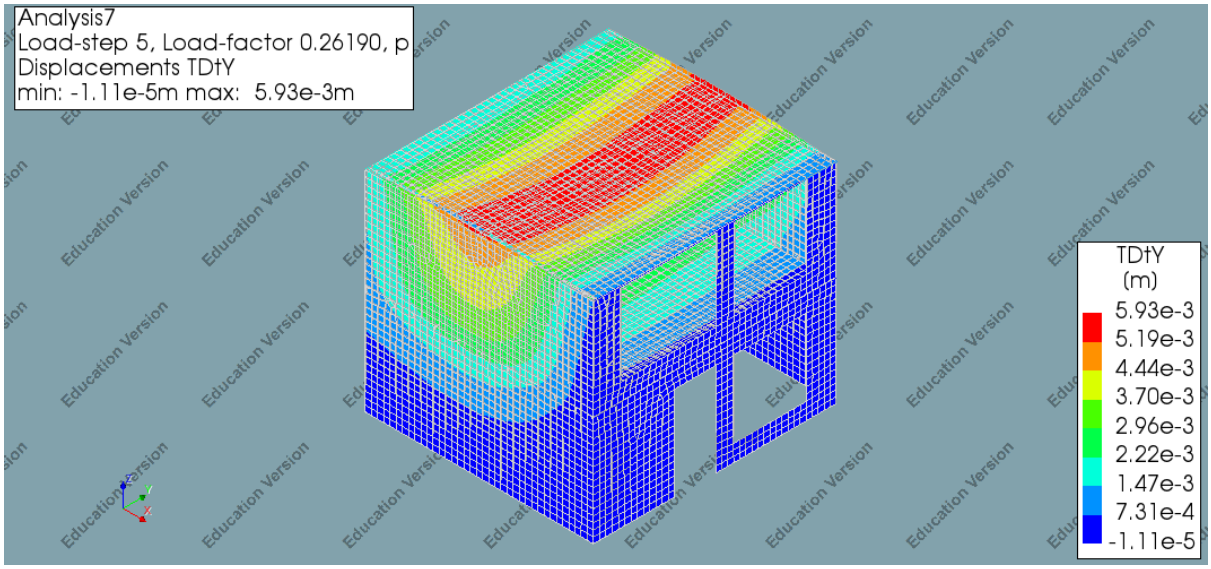

FIGURE 210: DEFLECTION IN THE Y-DIRECTION – STEP 5- 3D-VIEW 1

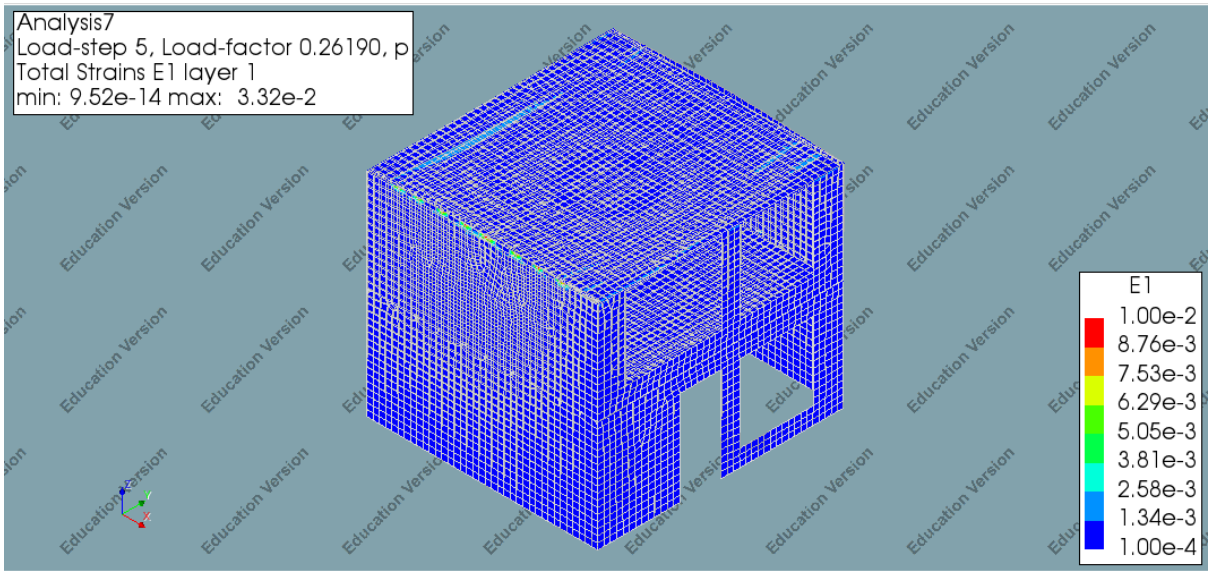

FIGURE 211: MAXIMUM PRINCIPAL STRAIN – STEP 5- 3D-VIEW 1

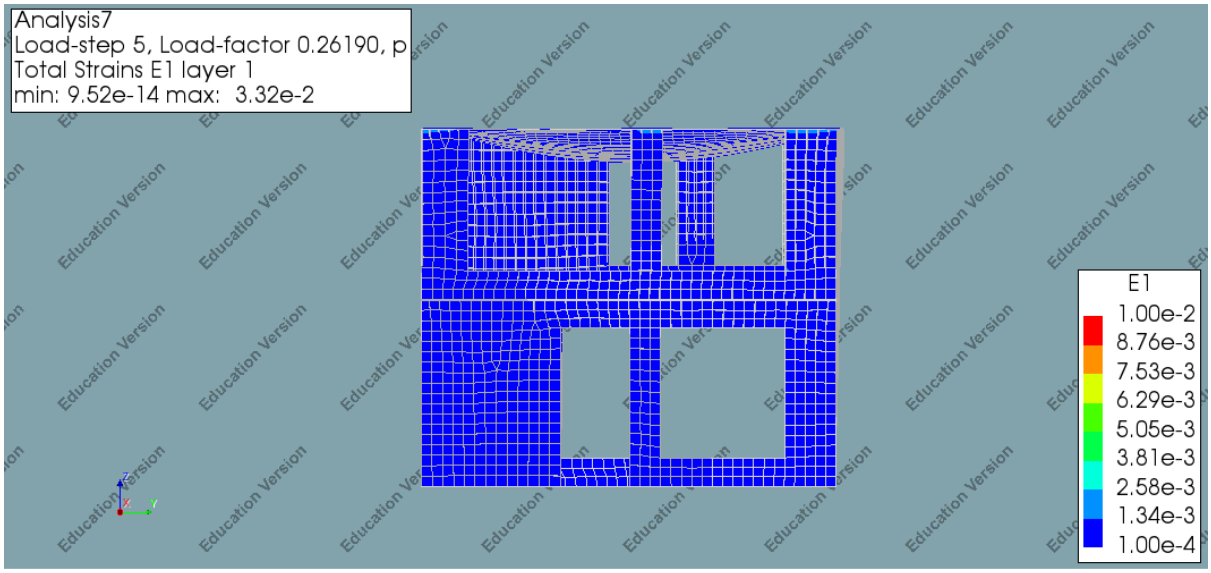

FIGURE 212: MAXIMUM PRINCIPAL STRAIN – STEP 5- SIDE-VIEW 1

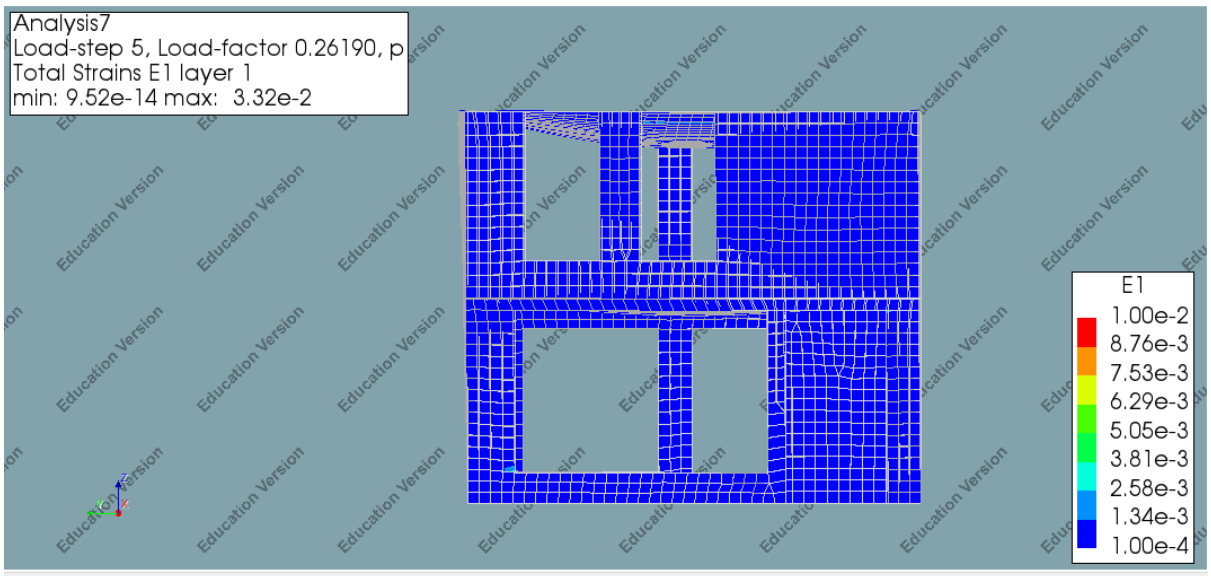

FIGURE 213: MAXIMUM PRINCIPAL STRAIN – STEP 5- SIDE-VIEW 2

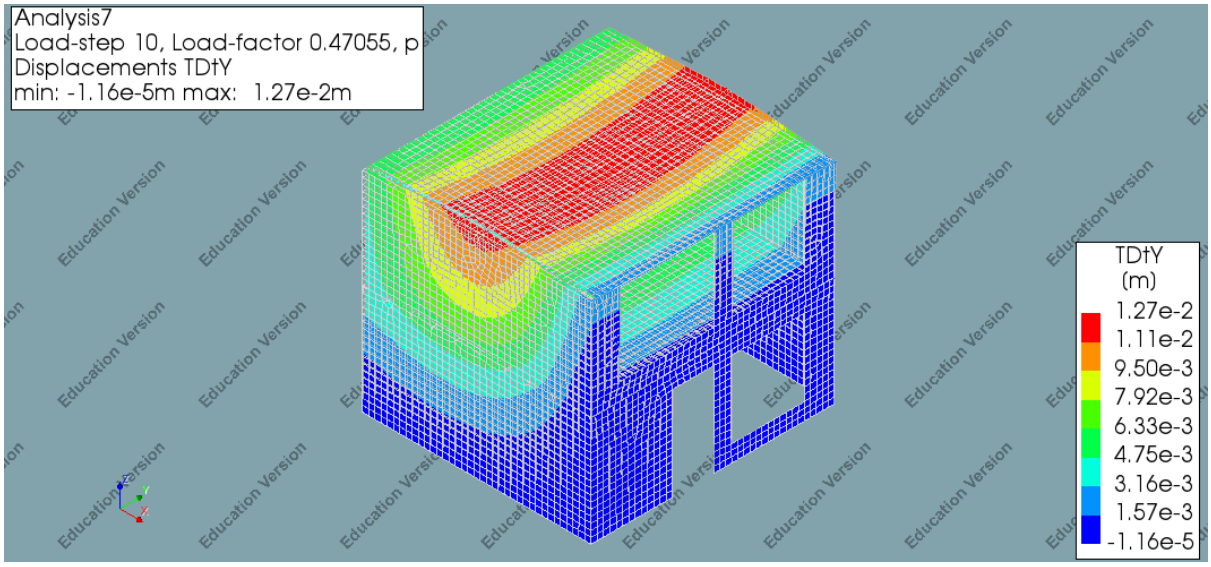

FIGURE 214: DEFLECTION IN THE Y-DIRECTION – STEP 10- 3D-VIEW 1

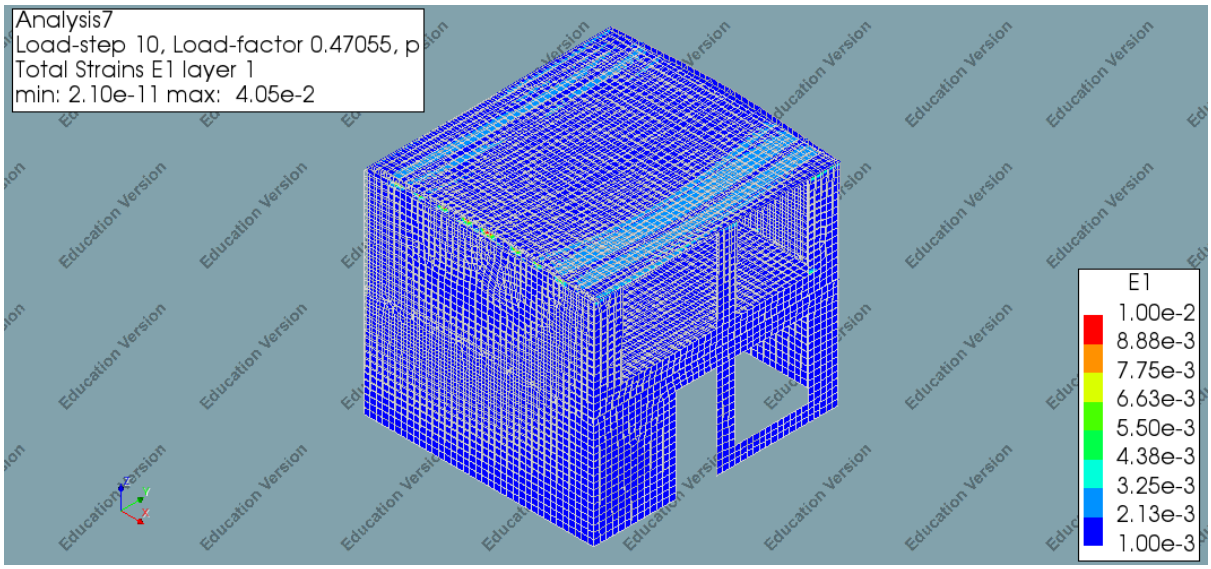

FIGURE 215: MAXIMUM PRINCIPAL STRAIN – STEP 10- 3D-VIEW 1

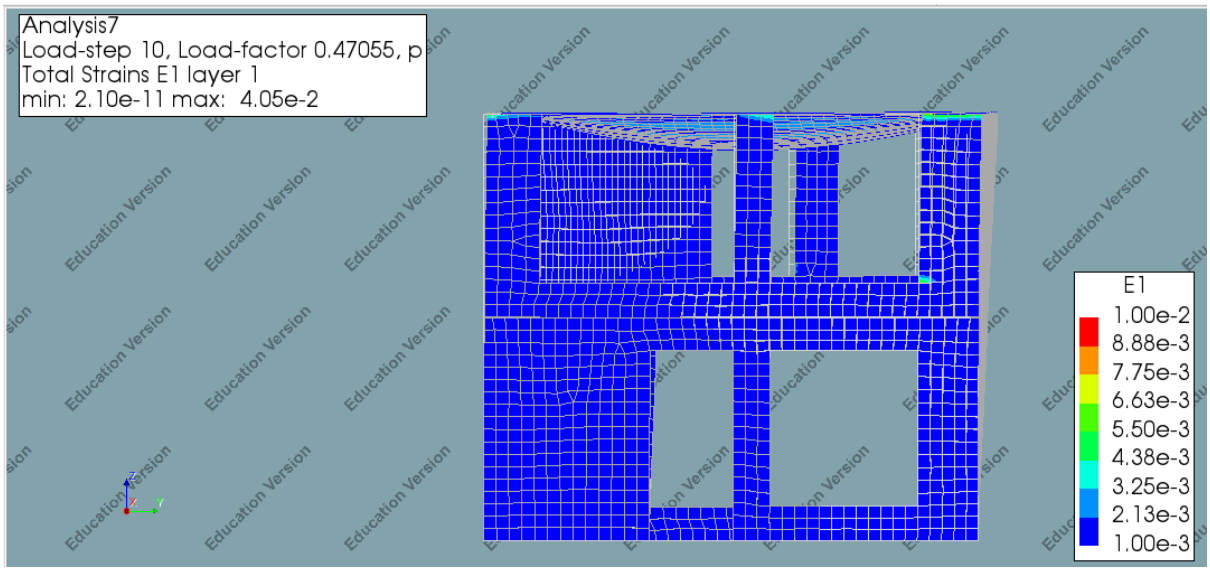

FIGURE 216: MAXIMUM PRINCIPAL STRAIN – STEP 10- SIDE-VIEW 1

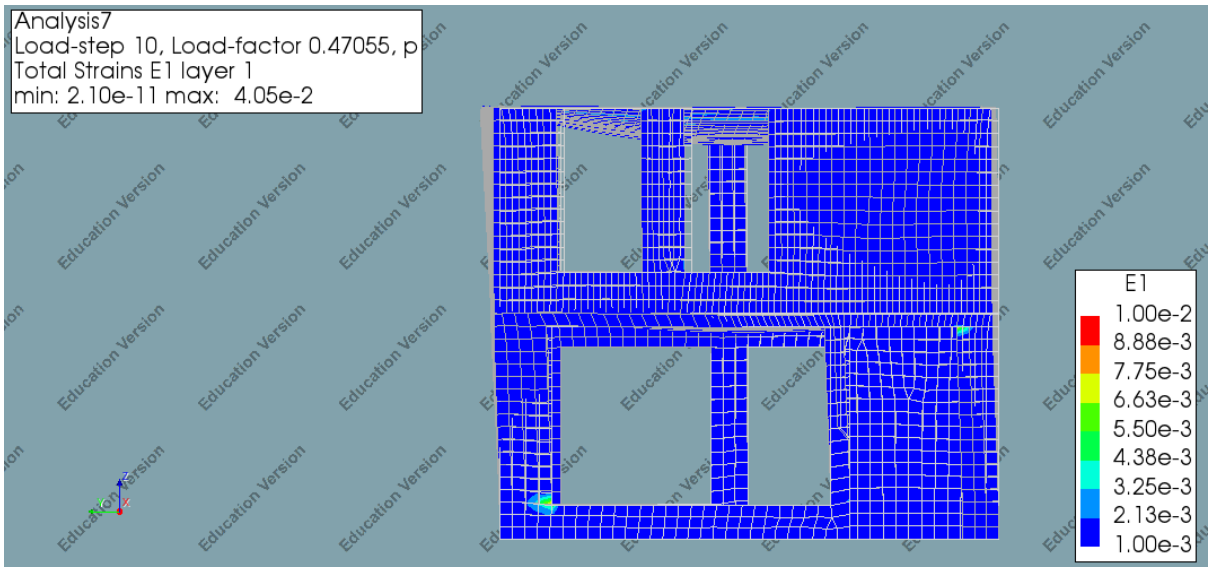

FIGURE 217: MAXIMUM PRINCIPAL STRAIN – STEP 10- SIDE-VIEW 2

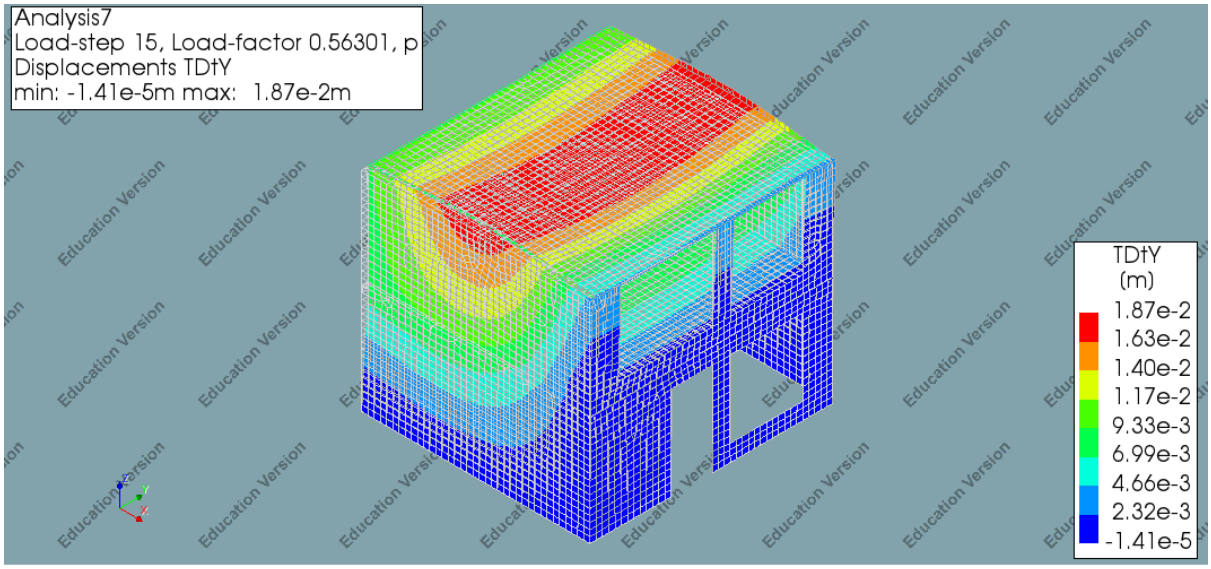

FIGURE 218: DEFLECTION IN THE Y-DIRECTION – STEP 15- 3D-VIEW 1

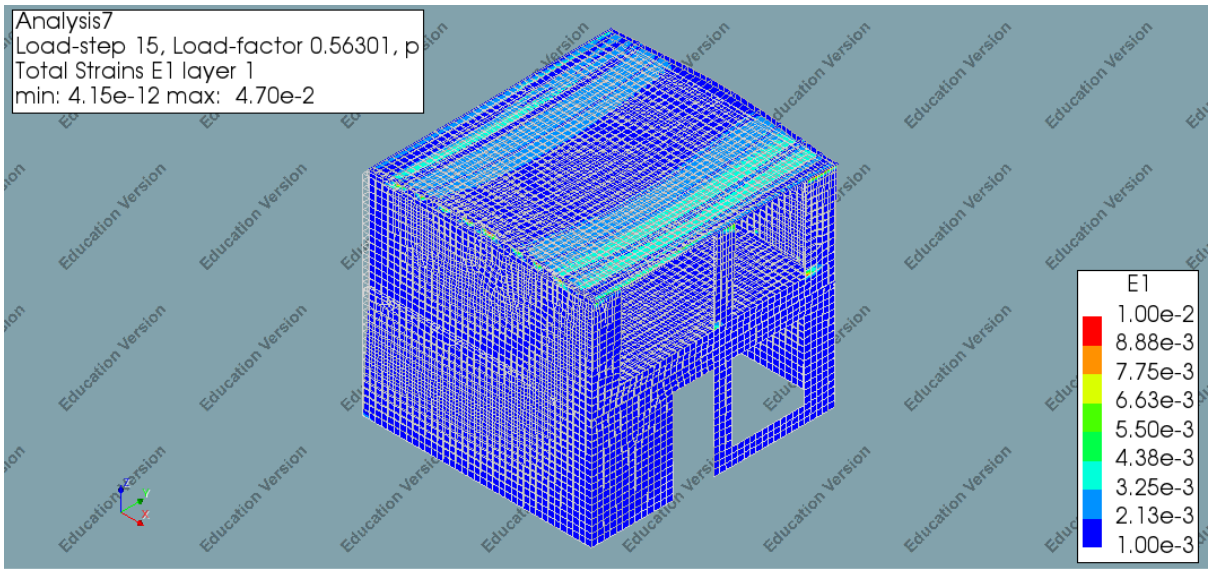

FIGURE 219: MAXIMUM PRINCIPAL STRAIN – STEP 15- 3D-VIEW 1

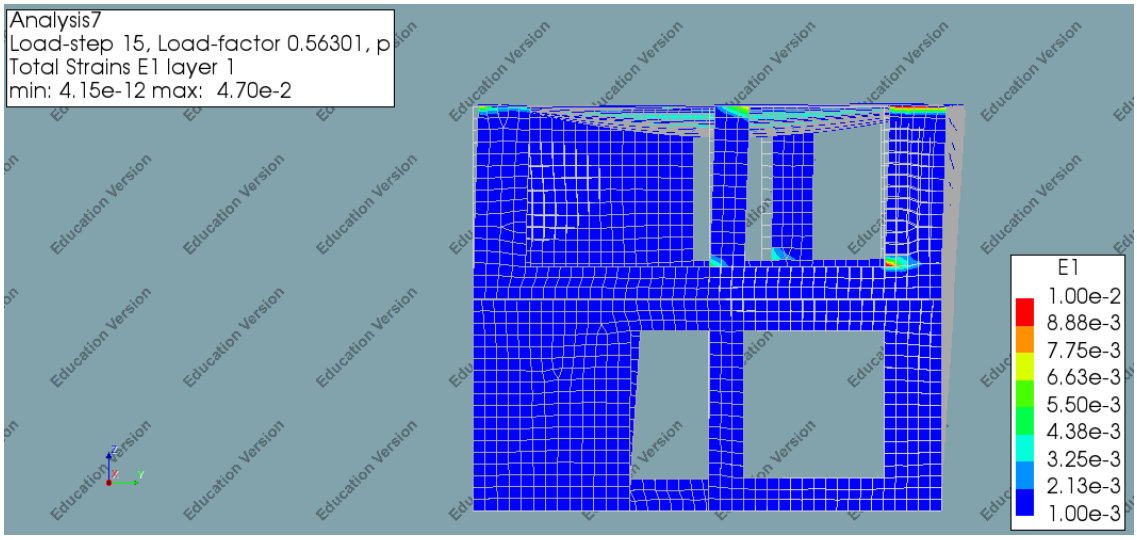

FIGURE 220: MAXIMUM PRINCIPAL STRAIN – STEP 15- SIDE-VIEW 1

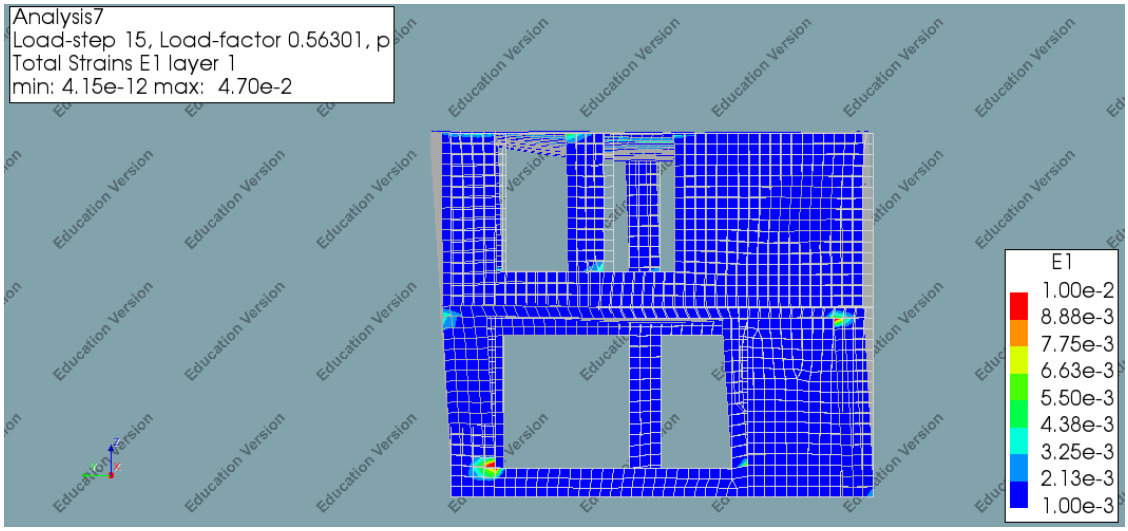

FIGURE 221: MAXIMUM PRINCIPAL STRAIN – STEP 15- SIDE-VIEW 2

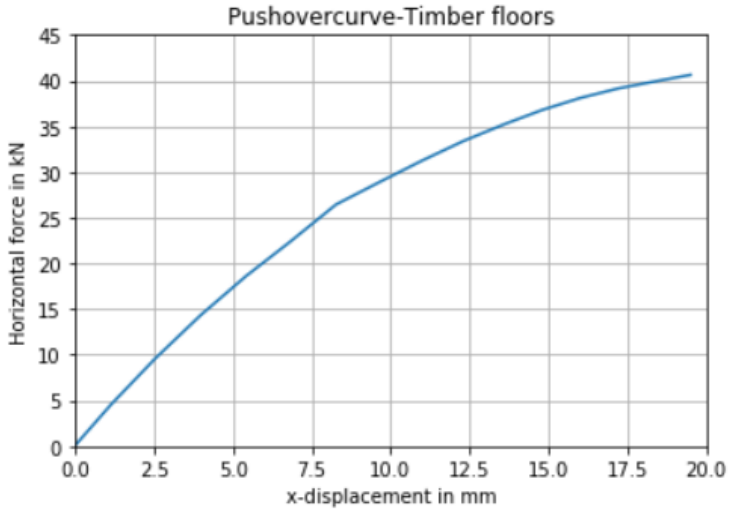

FIGURE 222: PUSHOVER CURVE 3D MODEL DOUBLE TIMBER FLOOR-HJ

RESULTS: STRUCTURAL EIGENVALUE ANALYSIS

The first analysis that has been made is the structural eigenvalue analysis. This analysis is required to determine the critical Eigen mode and Eigen frequency. The Eigen mode with the highest participating mass is the critical Eigen mode. In this case Eigen mode 1 is the governing Eigen mode and corresponds to a participating mass percentage 54%. The Figure below shows first five Eigen modes and their participating masses.

TABLE 43: GOVERNING EIGEN MODE AND PARTICIPATING MASS – 3D-MODEL-DOUBLE TIMBER - FLOORS- DIRECT

MODE	FREQUENCY	EFF.MASS TX	PERCENTAGE	CUM.PERCENT
1	0.40204E+01	0.13018E+04	0.54424E+02	0.54424E+02

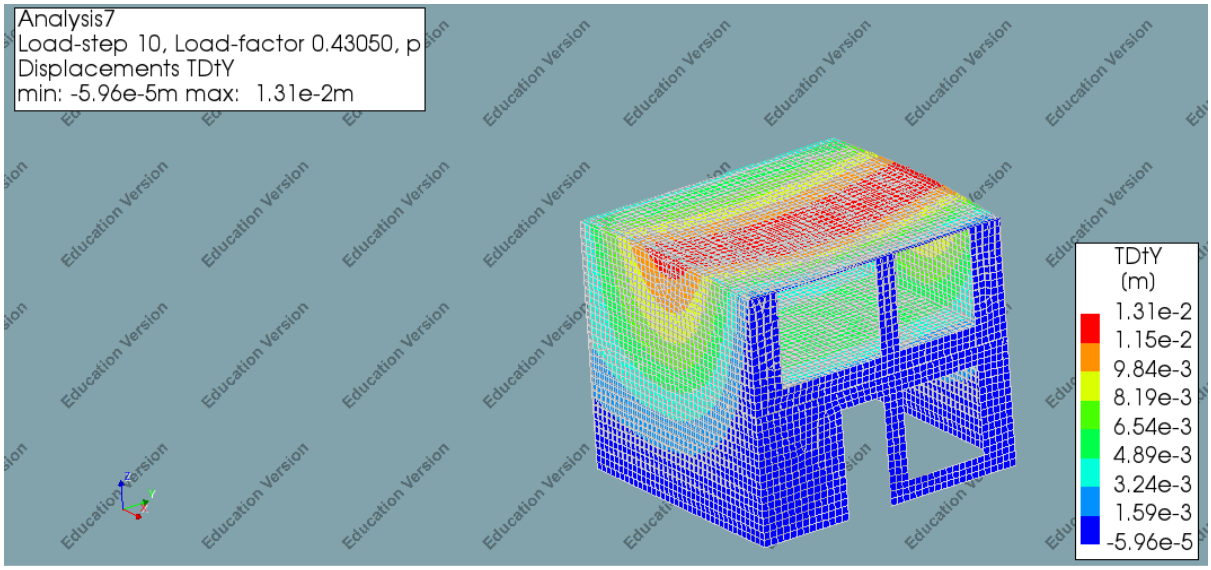

FIGURE 223: GOVERNING EIGEN MODE – 3D-MODEL-DOUBLE TIMBER - FLOORS- DIRECT

RESULTS: STRUCTURAL NONLINEAR ANALYSIS

This part contains the results of the structural nonlinear analysis. The relevant obtained results in this case, are the horizontal deflection, maximum principal strain, observed failure mechanism and the pushover curve.

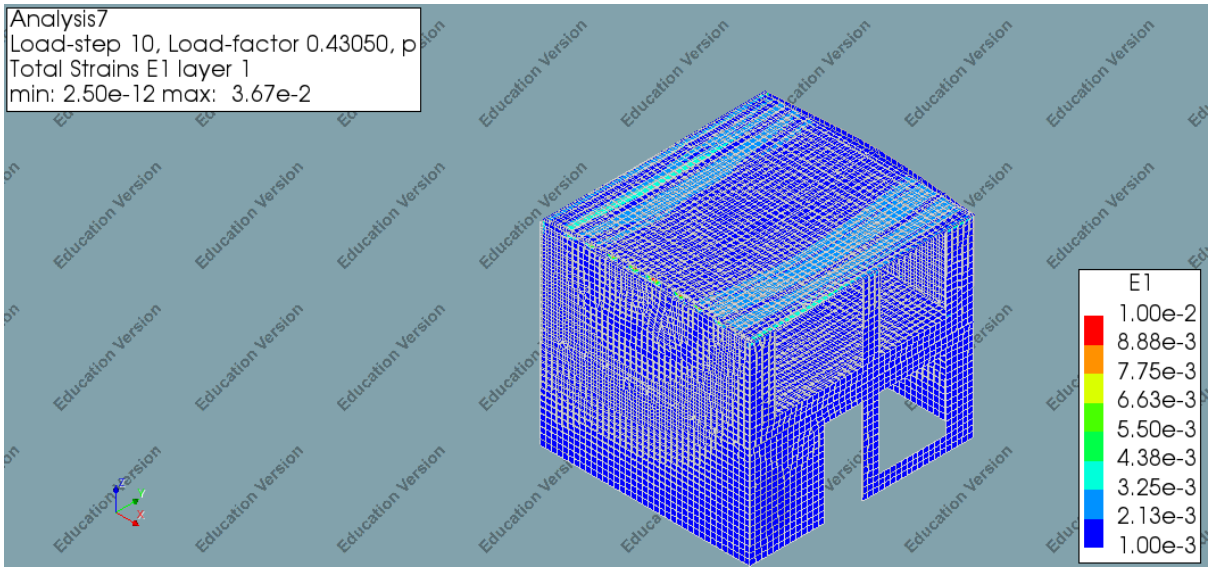

FIGURE 224: MAXIMUM PRINCIPAL STRAIN – STEP 10- 3D-VIEW 1

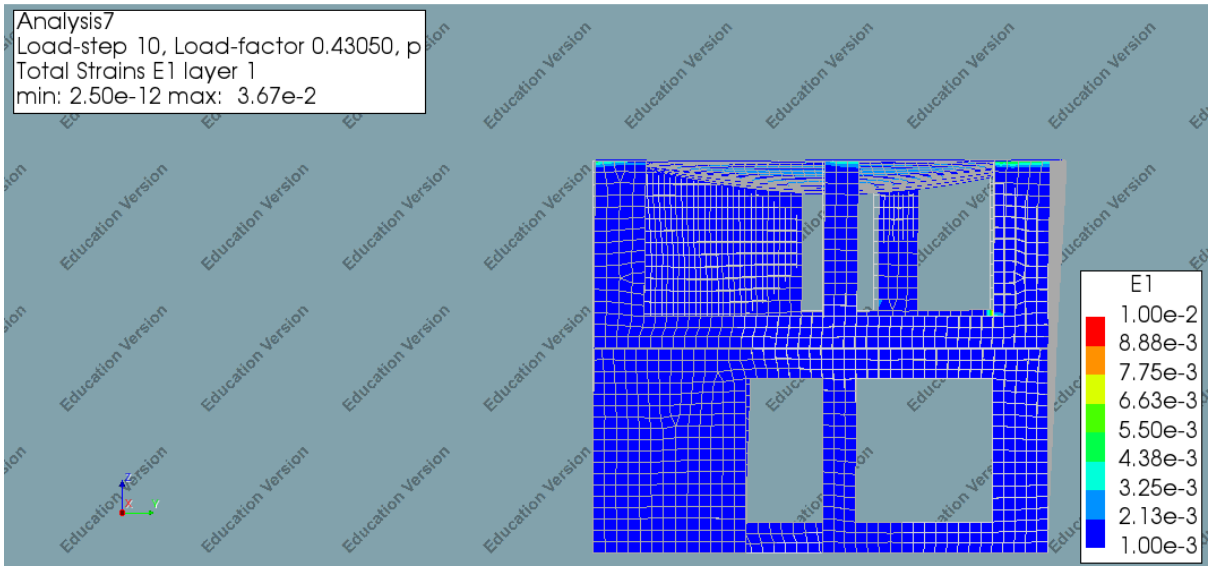

FIGURE 225: MAXIMUM PRINCIPAL STRAIN – STEP 10- SIDE-VIEW 1

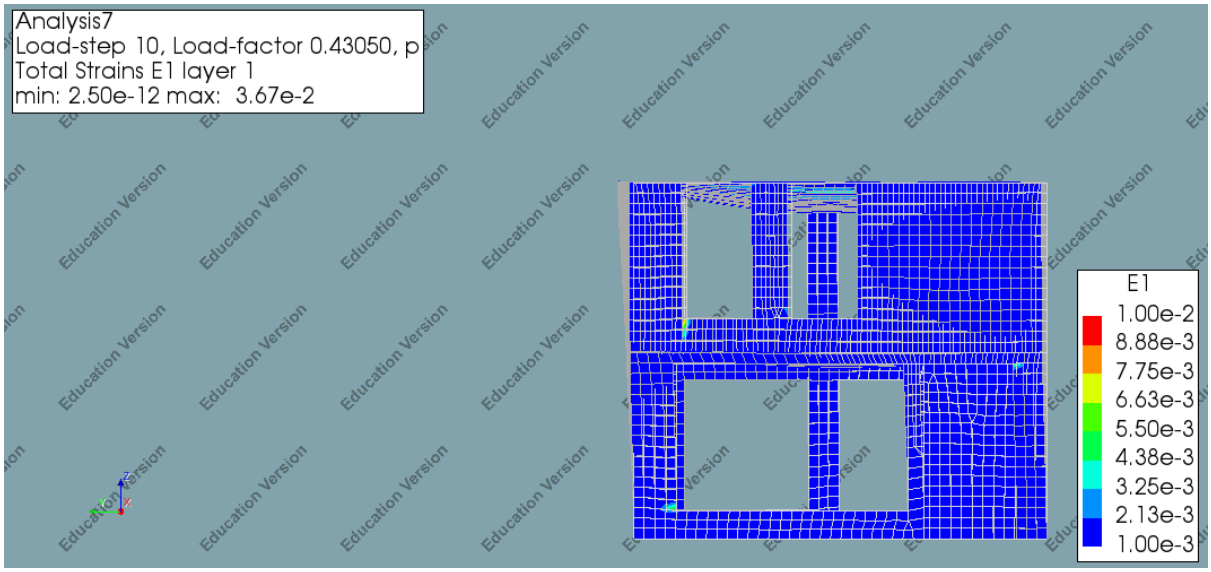

FIGURE 226: MAXIMUM PRINCIPAL STRAIN – STEP 10- SIDE-VIEW 2

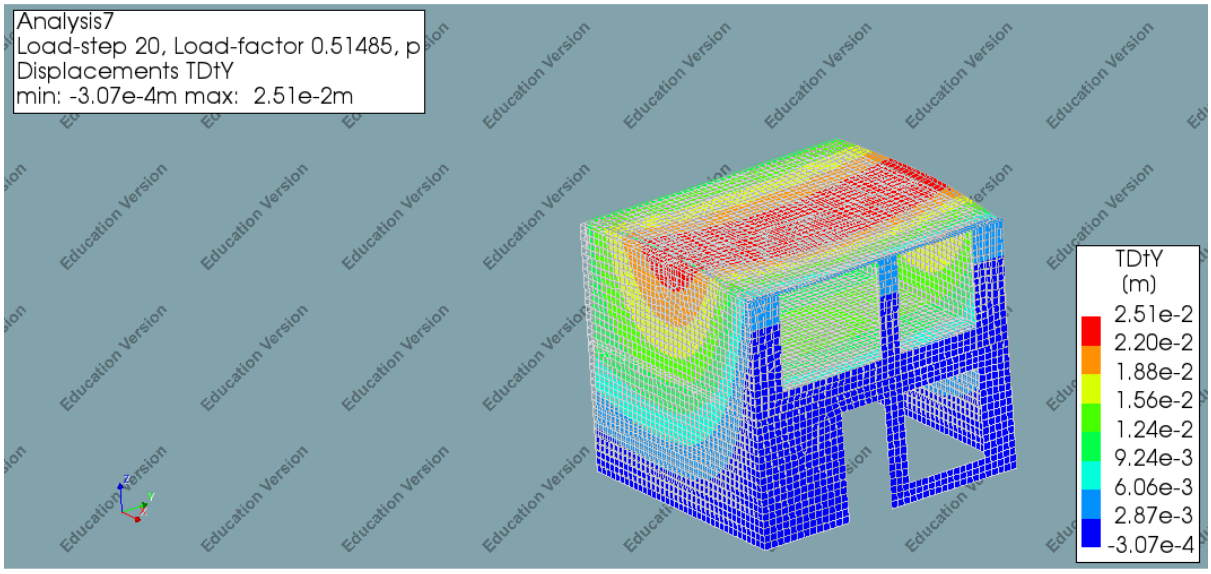

FIGURE 227: DEFLECTION IN THE Y-DIRECTION – STEP 20- 3D-VIEW 1

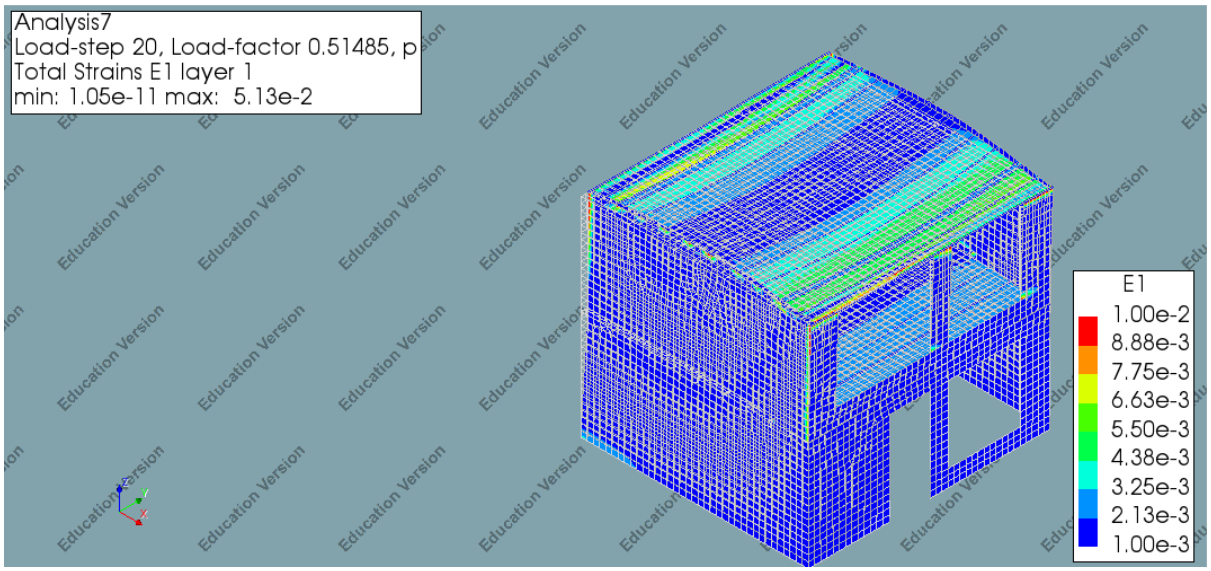

FIGURE 228: MAXIMUM PRINCIPAL STRAIN – STEP 20- 3D-VIEW 1

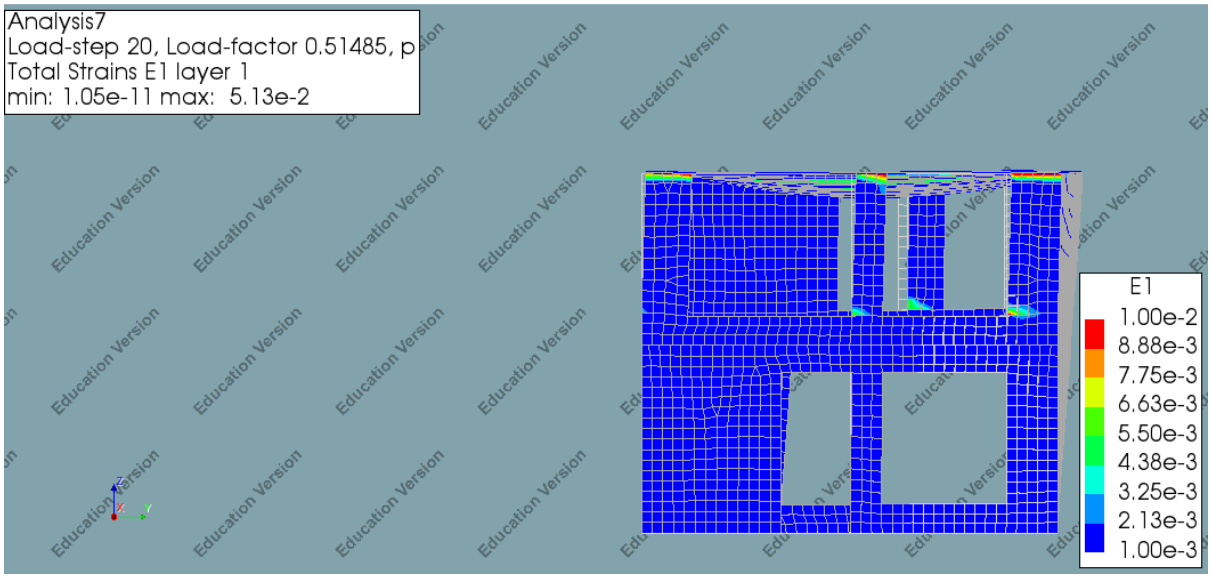

FIGURE 229: MAXIMUM PRINCIPAL STRAIN – STEP 20- SIDE-VIEW 1

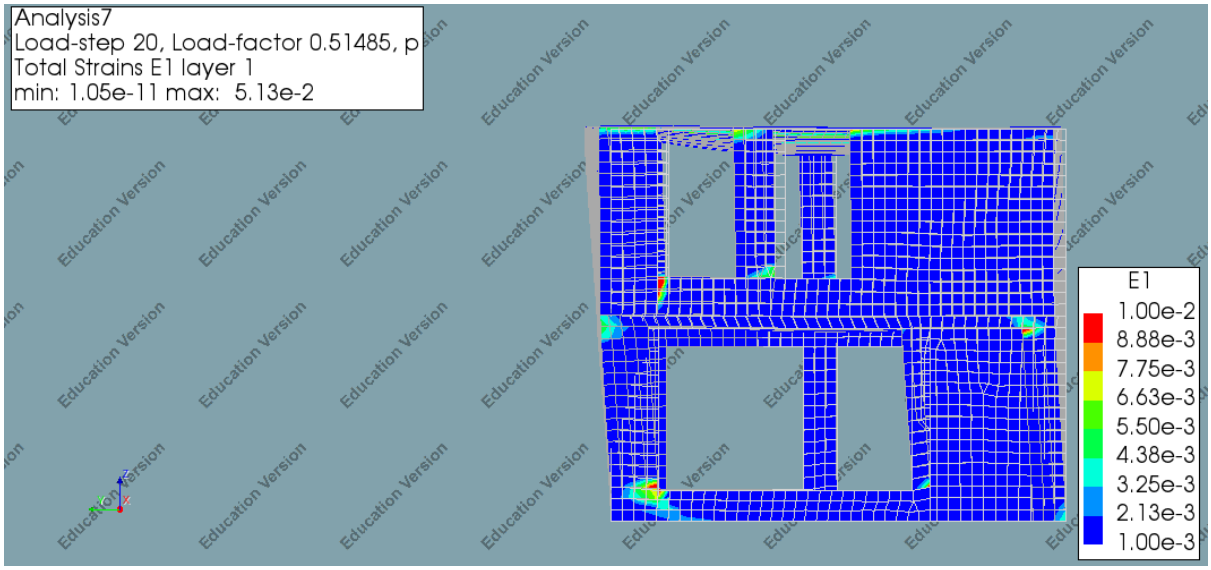

FIGURE 230: MAXIMUM PRINCIPAL STRAIN – STEP 20- SIDE-VIEW 2

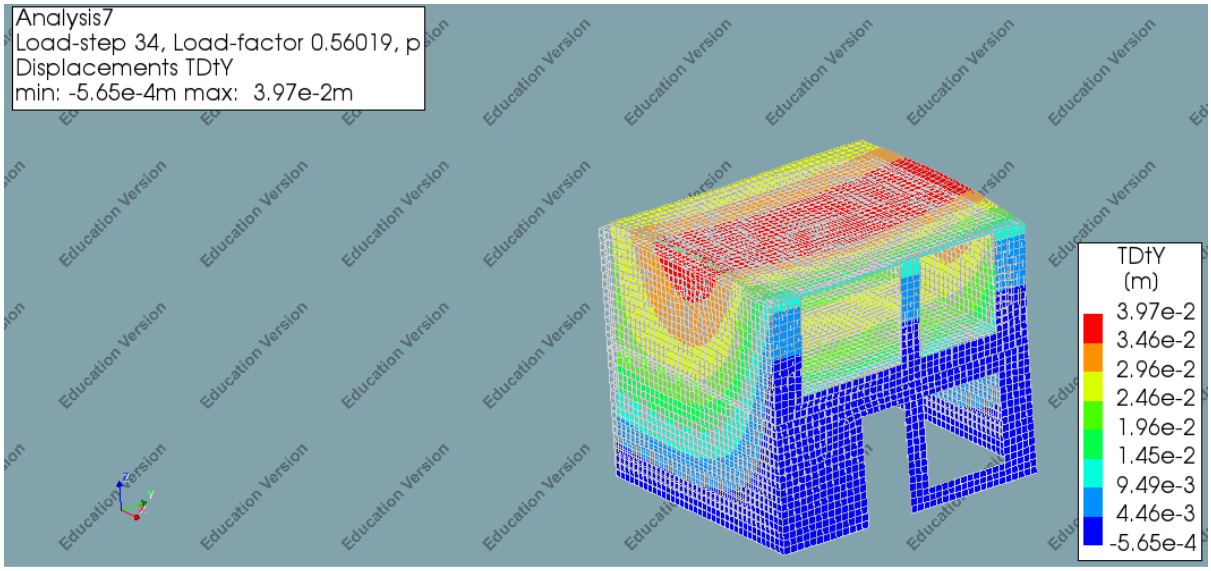

FIGURE 231: DEFLECTION IN THE Y-DIRECTION – STEP 34- 3D-VIEW 1

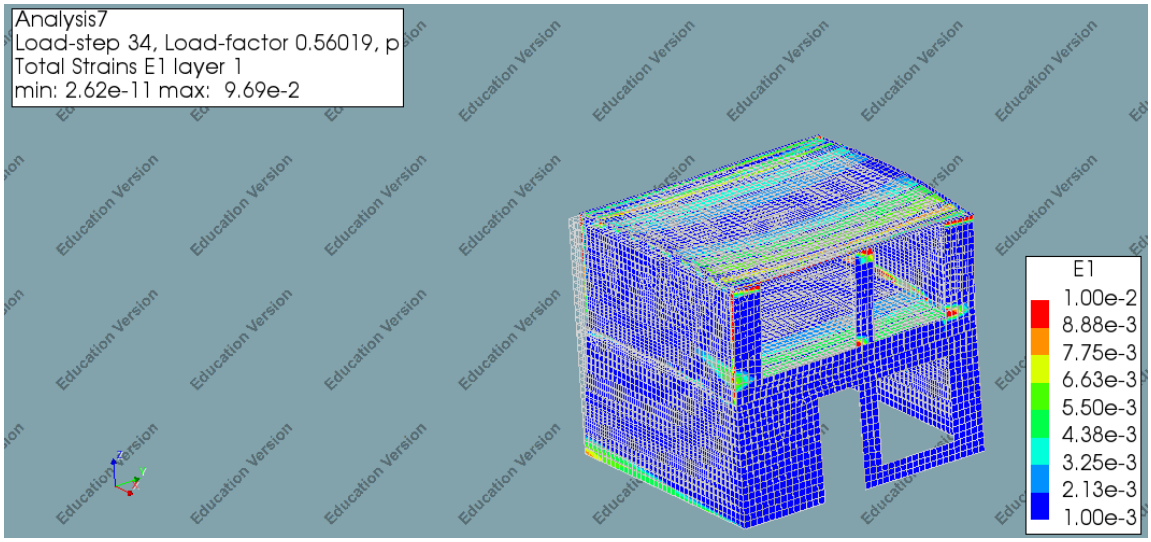

FIGURE 232: MAXIMUM PRINCIPAL STRAIN – STEP 34- 3D-VIEW 1

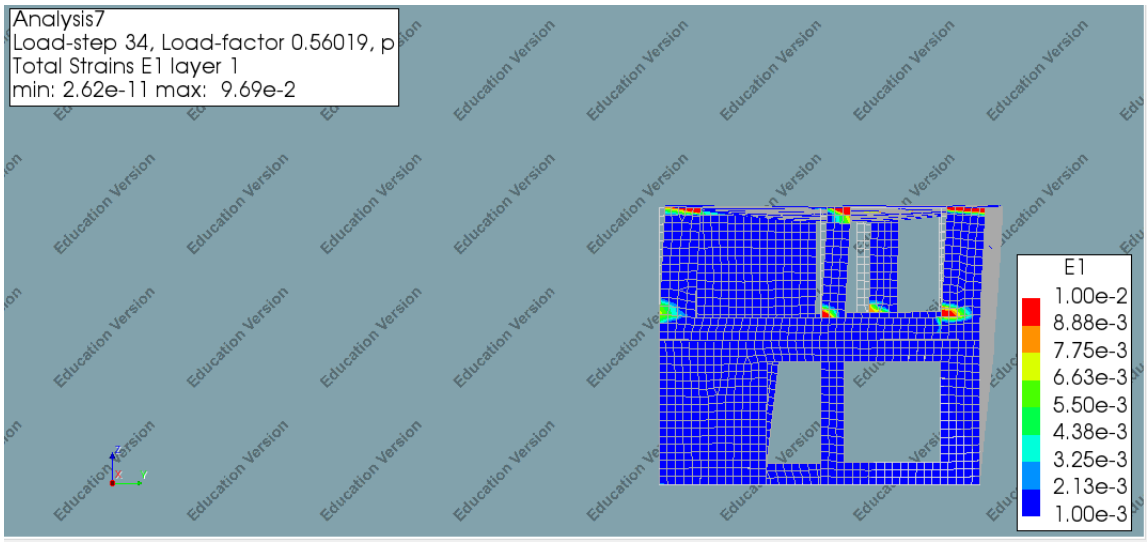

FIGURE 233: MAXIMUM PRINCIPAL STRAIN – STEP 34- SIDE-VIEW 1

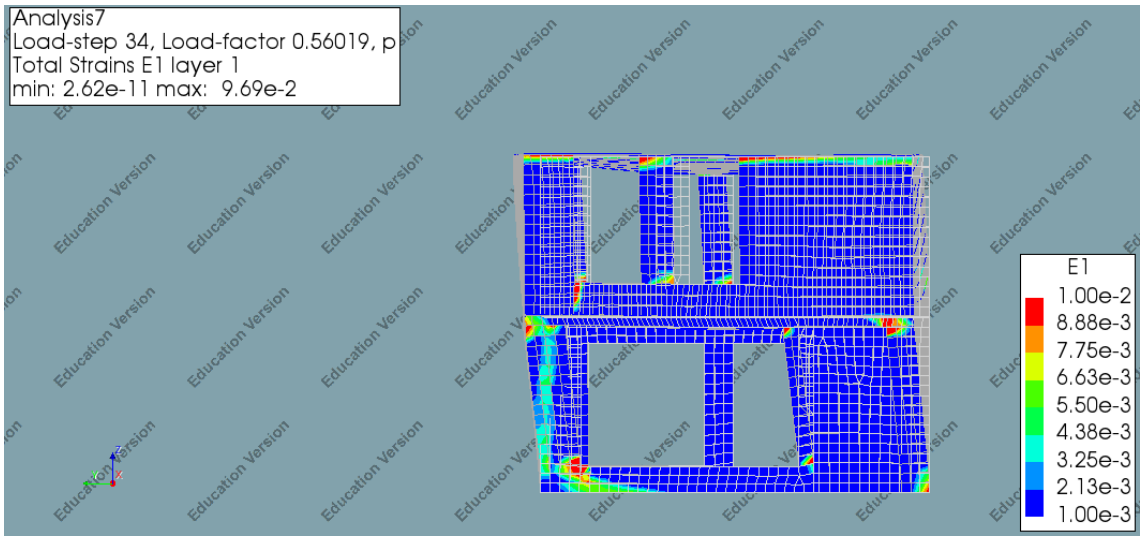

FIGURE 234: MAXIMUM PRINCIPAL STRAIN – STEP 20- SIDE-VIEW 2

30 APPENDIX T: CASE STUDY-3D ASSESSMENT PHASE: FULL SLAMA CALCULATIONS

This part gives an overview of the results of the SLaMA calculation for both unreinforced masonry buildings, that have been analysed in the DIANA FEM assessment. The SLaMA approach that is followed in this assessment is like the approach used in the 2D assessment phase. The effective heights of the piers have been determined based on the effective height method of Moon (Moon F. , 2004). The axial force at the top of the piers are extracted from FEM resuls after applying the self-weight on the structure. Therefore, is the starting point of both assessment methods equal. The flange contribution has been considered in both SLaMA calculations in the way the Moon (Moon F. , 2004) proposed. This chapter gives an overview of the most important results of the SLaMA method.

3D-MODEL-DOUBLE RC-FLOORS

TABLE 44: AXIAL FORCE AT THE TOP OF EACH PIERS

Number of pier	Axial force at the top of the piers	Length	Height
Pier 1	14566.01	1.99	2.28
Pier 2	25148.88	0.44	1.87
Pier 3	5163.08 +4941.5= 10104.5 N	0.73	2.28
Pier 4	6179.14	0.66	2.03
Pier 5	13603.71	0.44	2.03
Pier 6	2217 +3917= 6134 N	0.72	2.44
Pier 7	7139 +6828= 13967 N	0.45	2.68
Pier 8	28128.5	0.33	2.12
Pier 9	9418.6	0.62	2.52
Pier 10	11502+3615=15117 N	2.66	1.95
Pier 11	8292.58	0.52	1.95
Pier 12	772.35	0.76	2.44

The calculations below show the resulting shear capacities, displacement capacities and the predicted failure mechanism of each pier in the different walls.

```
# Shear capacity wall
print(Vr)
print(np.sum(Vr))
print(uNC)
```

```
[18613.37642373  5526.6576831   4094.80238803  1517.72330133
  3771.5733924   2926.97558411]
36451.108772707026
[0.0171  0.01496 0.01824 0.02144 0.01696 0.02016]
```

```
# Failure mechanisms piers
print(Failure)
```

```
['Sliding shear a', 'Rocking', 'Rocking', 'Rocking', 'Rocking', 'Rocking']
```

```
# Shear capacity wall
print(Vr)
print(np.sum(Vr))
print(uNC)
```

```
[ 2762.54426182  3087.30161345  2722.45746195 28377.01186587
  2618.9175      1323.63498737]
40891.86769046269
[0.01624  0.01624  0.01952  0.014625 0.0156   0.01952 ]
```

```
# Failure mechanisms piers
print(Failure)
```

```
['Rocking', 'Rocking', 'Rocking', 'Sliding shear a', 'Rocking', 'Rocking']
```

TABLE 45: TABLE EFFECTIVE MASS, MAXIMUM BASE SHEAR FORCE CALCULATION

	Mass masonry	Mass floor	Mass loading	Total mass	Factor	V	a
First floor	10172.53kg	12727.76kg 189.37 201.59		23291.25	0.4	**36430.73 N**	0.18278856 g
Second floor	4014.69 kg	12727.76kg 189.37 201.59	1200kg	18333.41	0.6		0.37845061 g

```
# Failure mechanisms piers
print(Failure)
```

```
['Sliding shear a', 'Rocking', 'Rocking', 'Rocking', 'Rocking', 'Rocking']
```

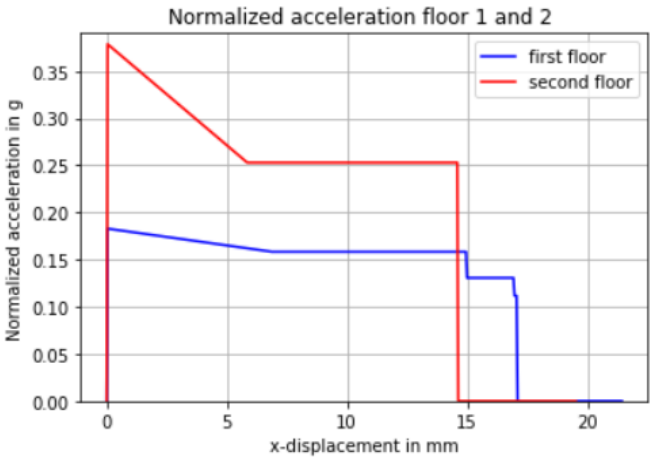

FIGURE 235: ACCELERATION CURVE

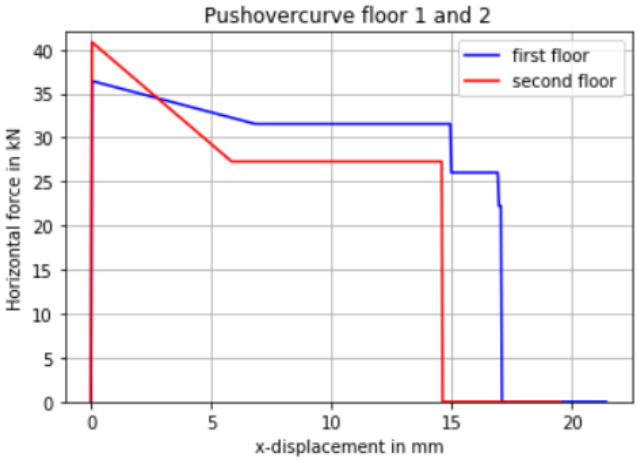

FIGURE 236:PUSHOVER CURVE

3D-MODEL-DOUBLE TIMBER FLOOR

TABLE 46: TABLE EFFECTIVE MASS, MAXIMUM BASE SHEAR FORCE CALCULATION

	Mass masonry	Mass floor	Mass loading	Total mass	Factor	V	a
First floor	10172.53kg	1789.84kg+940.9kg		12903.27	0.45	7.4 kN	0.09028508 g
Second floor	4014.69 kg	1789.84kg+940.9*kg	1200kg	7945.43	0.55	9 kN	0.26832391 g

TABLE 47: AXIAL FORCE AT THE TOP OF EACH PIER

Number of pier	Axial force at the top of the piers	**Length**	**Height**
Pier 1	2623 N	1.99	2.28
Pier 2	2516 N	0.44	1.87
Pier 3	2327 N+4941.5N=	0.73	2.28
Pier 4	0	0.66	2.03
Pier 5	0	0.44	2.03
Pier 6	3917 N	0.72	2.44
Pier 7	2182 N+6828 N=	0.45	2.68
Pier 8	5074 N	0.33	2.12
Pier 9	2698 N	0.62	2.52
Pier 10	3615 N	2.66	1.95
Pier 11	0	0.52	1.95
Pier 12	0	0.76	2.44

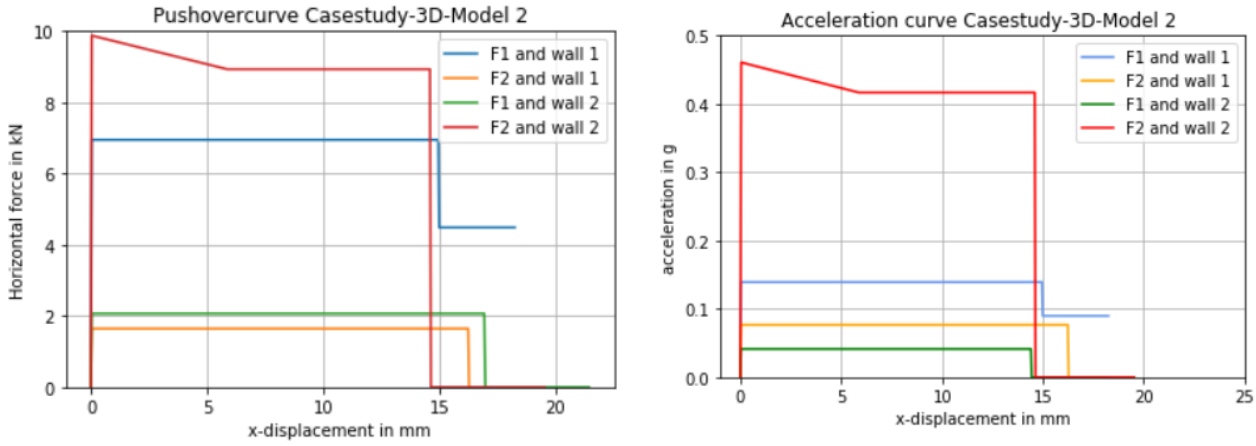

FIGURE 237: PUSHOVER CURVE (LEFT) ACCELERATION CURVE (RIGHT)

The calculations below show the resulting shear capacities, displacement capacities and the predicted failure mechanism of each pier in the different walls.

Wall 1

```
# Failure mechanisms piers
print(Failure)
```

```
['Rocking', 'Rocking', 'Rocking', 'Sliding shear a', 'Rocking', 'Rocking']
```

```
# Shear capacity wall
print(Vr)
print(np.sum(Vr))
print(uNC)
```

```
[ 410.8988597   182.62171542 1049.24445446 9067.51319486  255.14443027
  543.99558267]
11509.418237385216
[0.01624  0.01624  0.01952  0.014625 0.0156   0.01952 ]
```

Wall 2

```
# Failure mechanisms piers
print(Failure)
```

```
['Rocking', 'Rocking', 'Rocking', 'Rocking', 'Rocking', 'Rocking']
```

```
# Shear capacity wall
print(Vr)
print(np.sum(Vr))
print(uNC)
```

```
[4853.93417926  471.18236658 1622.77917157  901.53682548  479.19594082
  684.62656861]
9013.255052312868
[0.01824 0.01496 0.01824 0.02144 0.01696 0.02016]
```

31 APPENDIX U: DISCUSSION- CHANGING AXIAL FORCE SM1

The Figures below show the changing distributed normal force in 4 steps during pushover analysis within DIANA. The results are obtained from the DIANA FEM analysis of simple model 1. This change of the normal distributed forces at the top of the piers are similar for all the simple models.

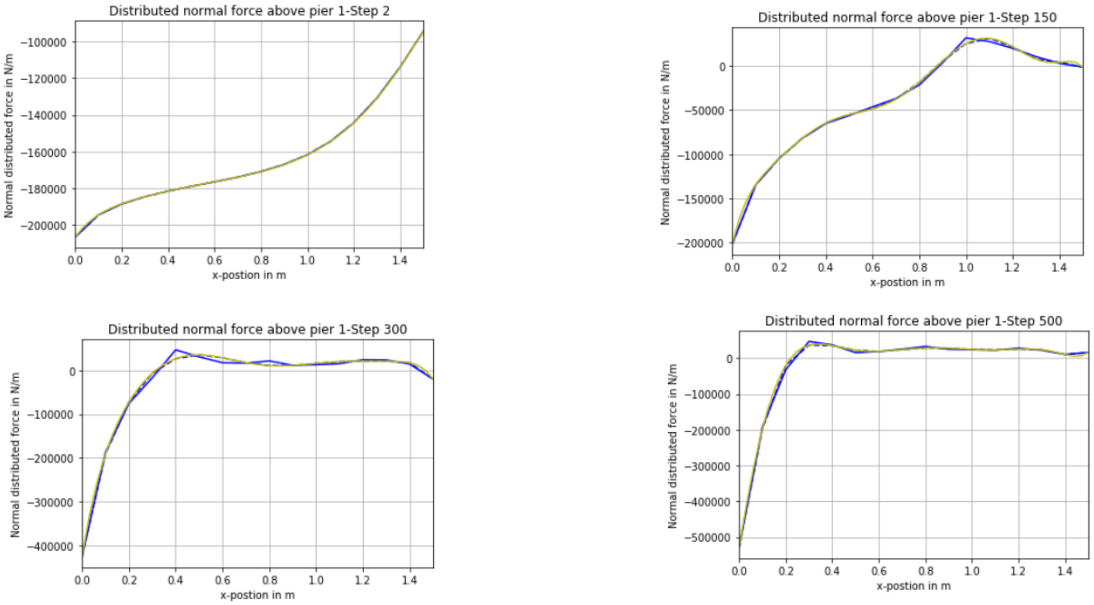

FIGURE 238: CHANGING AXIAL FORCE AT THE TOP OF PIER 1

TABLE 48: CHANGING AXIAL FORCE AT THE TOP OF PIER 1

Pier 1	Normal force-compression	Eccentricity	Normal force-tension	Eccentricity
Step 2	-261399.53 N	0.74 m	-	-
Step 150	-63736.64 N	0.29 m	9663.77 N	1.12m
Step 300	-45606.21 N	0.086 m	21982.09 N	0.83 m
Step 500	-45100.67 N	0.063m	30184.34 N	0.80 m

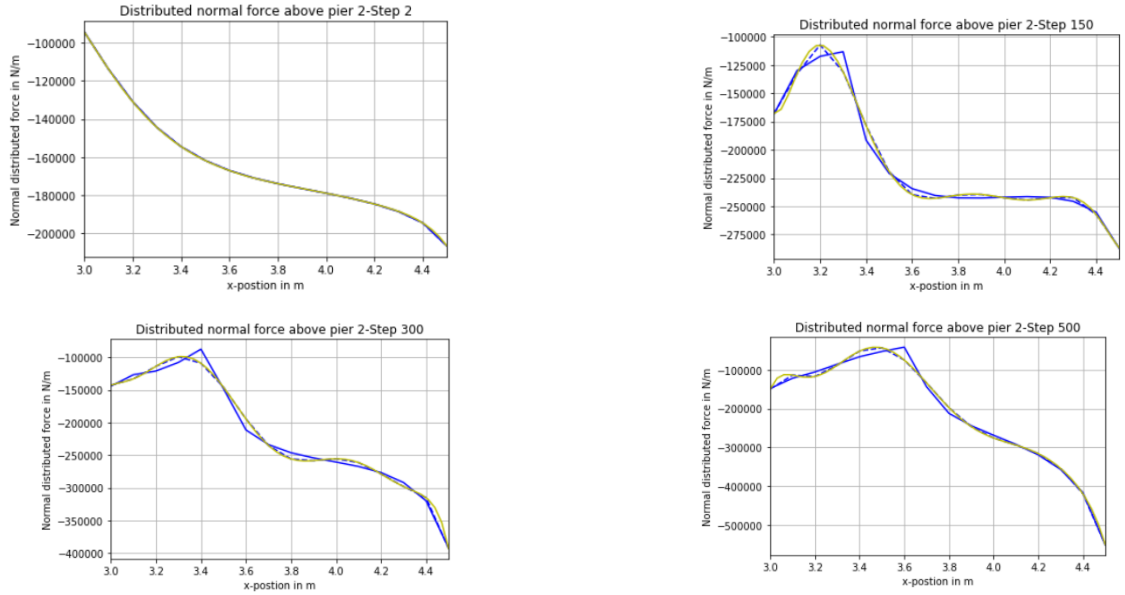

FIGURE 239: CHANGING AXIAL FORCE AT THE TOP OF PIER 2

TABLE 49: CHANGING AXIAL FORCE AT THE TOP OF PIER 2

Pier 2	Normal force-compression	Eccentricity	Normal force-tension	Eccentricity
Step 2	-247228.85 N	3.81 m	-	-
Step 150	-318550.20 N	3.84 m	-	-
Step 300	-320737.77 N	4.00 m	-	-
Step 500	-305378.52 N	4.00 m	-	-

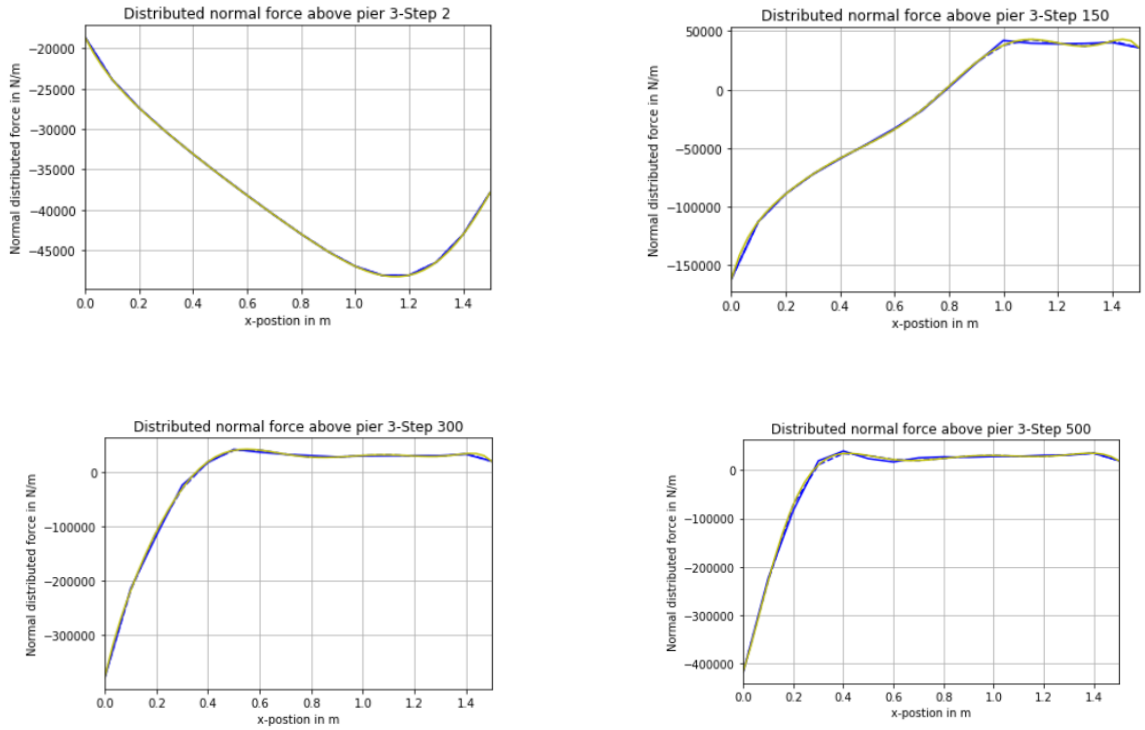

FIGURE 240: CHANGING AXIAL FORCE AT THE TOP OF PIER 3

TABLE 50: CHANGING AXIAL FORCE AT THE TOP OF PIER 3

Pier 3	Normal force-compression	Eccentricity	Normal force-tension	Eccentricity
Step 2	-57945.06 N	0.83 m	-	-
Step 150	-50565.65 N	0.26 m	24613.58 N	1.19 m
Step 300	-52600.03 N	0.10 m	35947.95 N	0.93 m
Step 500	-49413.56 N	0.08 m	34181.55	0.92 m

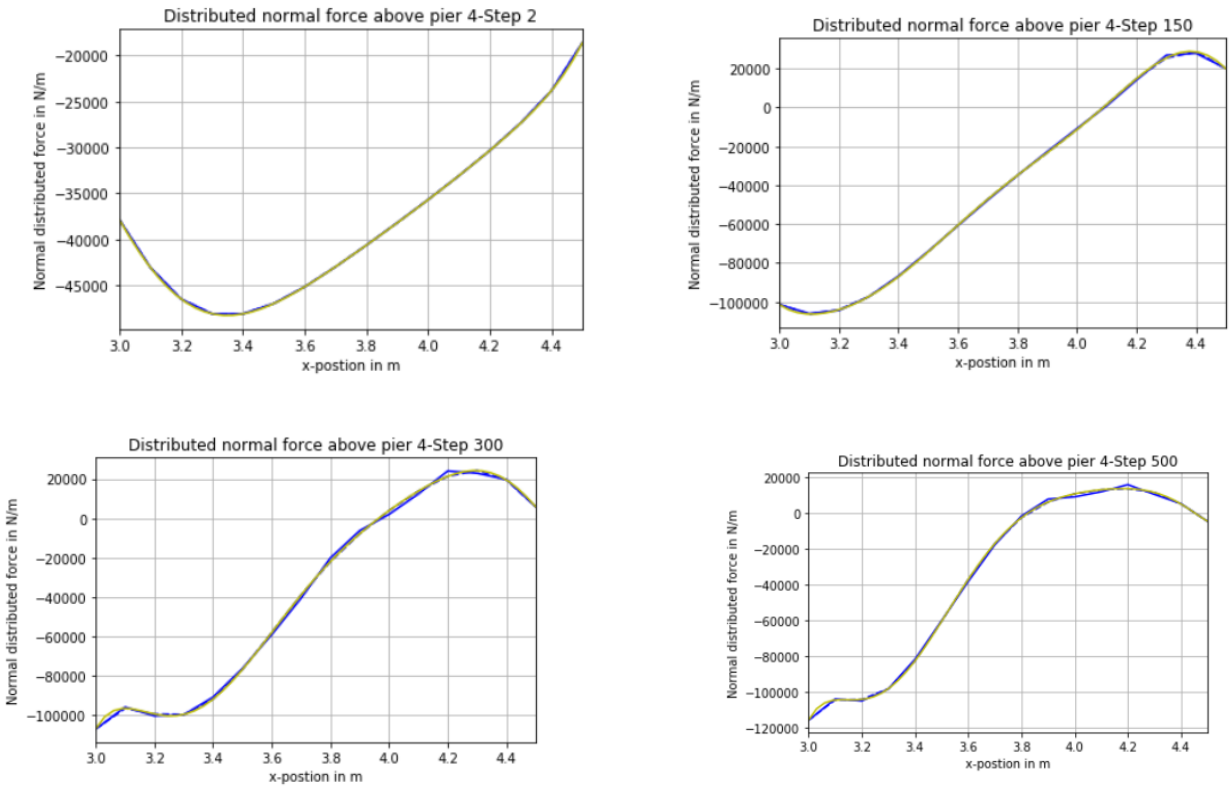

FIGURE 241: CHANGING AXIAL FORCE AT THE TOP OF PIER 4

TABLE 51: CHANGING AXIAL FORCE AT THE TOP OF PIER 4

Pier 4	Normal force-compression	Eccentricity	Normal force-tension	Eccentricity
Step 2	-57944.13 N	3.67 m	-	-
Step 150	-69818.86 N	3.38 m	8239.47 N	4.34 m
Step 300	-64251.32 N	3.35 m	8683.78 N	4.26 m
Step 500	-56308.42 N	3.29 m	5992.59 N	4.14 m

32 APPENDIX V: DISCUSSION- CHANGING AXIAL FORCE CASE STUDY- 2D-1A

The Figures and the table below show the changing distributed normal force at the top of the piers of Case study1.

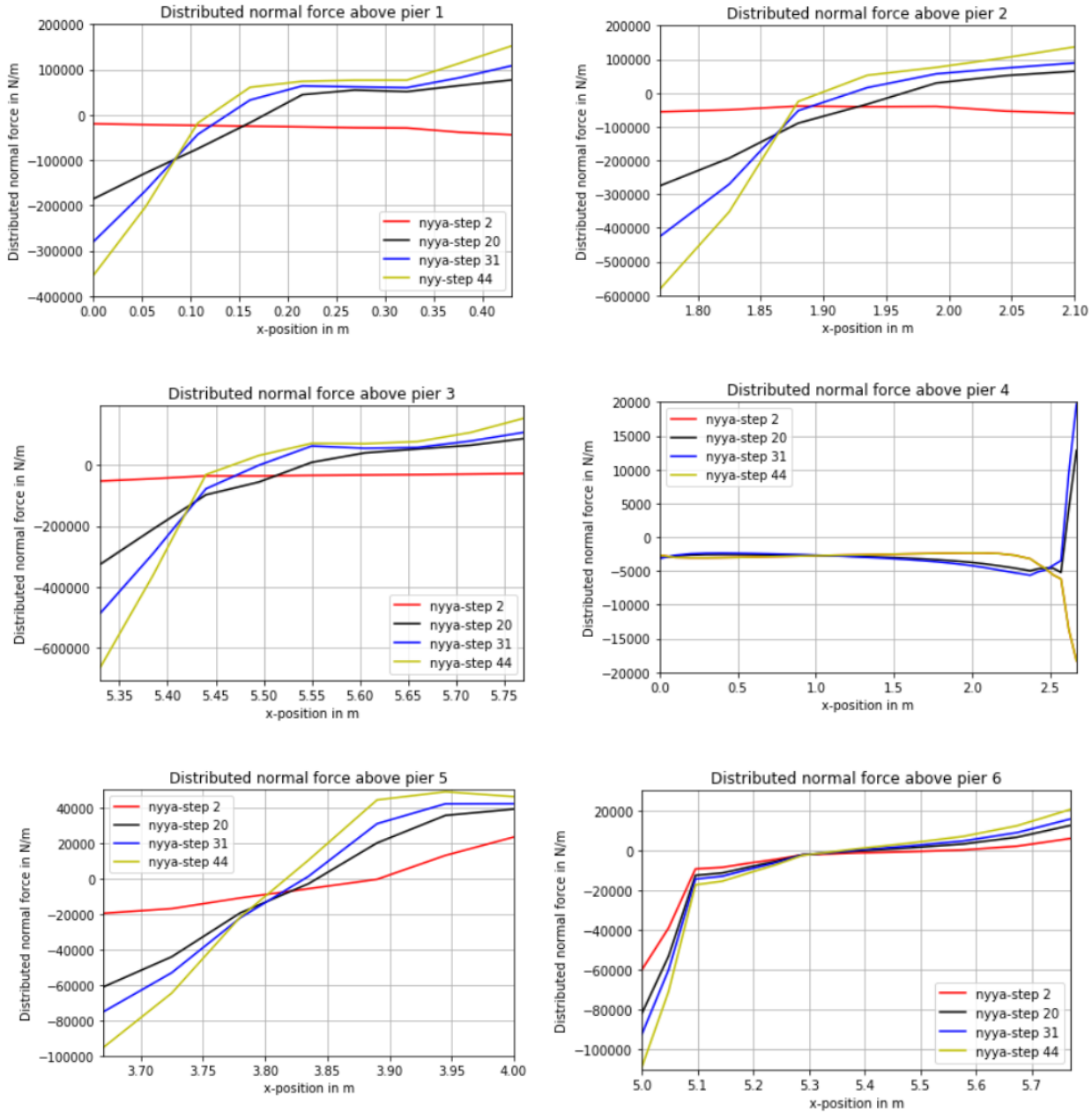

FIGURE 242: CHANGING AXIAL FORCE AT THE TOP OF EACH PIER

33 TABLE LIST

TABLE 1: MATERIAL PROPERTIES CLAY MASONRY-PRE 1945 33
TABLE 2: MATERIAL PROPERTIES CLAY MASONRY-POST 1945 34
TABLE 3: MATERIAL PROPERTIES CALCIUM SILICATE-PRE 1985 35
TABLE 4: MATERIAL PROPERTIES CLAY-PRE 1945- DIFFERENT TENSILE STREGNTH 36
TABLE 5: PARTICIPATING MASSES 38
TABLE 6: MAXIMUM BASE SHEAR FORCE AND PREDICTED FAILURE MECHANISMS 47
TABLE 7: COMPARISON MAXIMUM BASE SHEAR FORCE 48
TABLE 8: COMPARISON PREDICTED FAILURE MECHANISMS 49
TABLE 9: COMPARISON DISPLACEMENT CAPACITY 50
TABLE 10: PREDICTED FAILURE MECHANISM 55
TABLE 11: SUMMURIZED RESULTS OF 3D-MODEL-DOUBLE TIMBER FLOORS 59
TABLE 12: PREDICTED FAILURE MECHANISM 62
TABLE 13: MAXIMUM BASE SHEAR FORCE AND THE DISPLACEMENT CAPACITY 62
TABLE 14: COMPARISON PREDICTED FAILURE MECHANISM 63
TABLE 15: COMPARISON PREDICTED FAILURE MECHANISM 64
TABLE 16: COMPARISON MAXIMUM BASE SHEAR FORCE 65
TABLE 17: COMPARISON DISPLACEMENT CAPACITY 65
TABLE 18: CHANGING AXIAL FORCE AT THE TOP OF THE PIERS OF SIMPLE MODEL 1 66
TABLE 19: CHANGING AXIAL FORCE AT THE TOP OF THE PIERS OF CASE STUDY-2D-1A 67
TABLE 20: AXIAL FORCE AT THE BASE OF THE PIERS OF SIMPLE MODEL 1 68
TABLE 21: NEW CALCULATED SHEAR CAPACITIES OF THE PIERS AT SIMPLE MODEL 1 68
TABLE 22: NEW SLAMA CALCULATION BASED ON THE CHANGING AXIAL FORCES 69
TABLE 23: GOVERNING EIGEN MODE AND THE PARTICIPATING MASS 85
TABLE 24: OVERVIEW SHEAR AND DRIFT CAPACITY OF EACH PIER 88
TABLE 25: GOVERNING EIGEN MODE AND THE PARTICIPATING MASS- SIMPLE MODEL 2 89
TABLE 26: GOVERNING EIGEN MODE AND THE PARTICIPATING MASS- SIMPLE MODEL 3 93
TABLE 27: OVERVIEW SHEAR AND DRIFT CAPACITY OF EACH PIER 96
TABLE 28: GOVERNING EIGEN MODE AND THE PARTICIPATING MASS- SIMPLE MODEL 4 97
TABLE 29: OVERVIEW SHEAR AND DRIFT CAPACITY OF EACH PIER 99
TABLE 30: GOVERNING EIGEN MODE AND THE PARTICIPATING MASS- SIMPLE MODEL 5 100
TABLE 31: OVERVIEW SHEAR AND DRIFT CAPACITY OF EACH PIER 102
TABLE 32: GOVERNING EIGEN MODE AND THE PARTICIPATING MASS- SIMPLE MODEL 6 103
TABLE 33: OVERVIEW SHEAR AND DRIFT CAPACITY OF EACH PIER 106
TABLE 34:GOVERNING EIGEN MODE AND THE PARTICIPATING MASS- CASE STUDY-2D-1A 107
TABLE 35: GOVERNING EIGEN MODE AND THE PARTICIPATING MASS- CASE STUDY-2D-1B 109
TABLE 36: SHEAR CAPACITIES, DRIFT CAPACITIES AND THE FAILURE MECHANISMS OF EACH PIER 111
TABLE 37 : GOVERNING EIGEN MODE AND THE PARTICIPATING MASS- CASE STUDY-2D-2A 112
TABLE 38: SHEAR CAPACITIES, DRIFT CAPACITIES AND THE FAILURE MECHANISMS OF EACH PIER 116
TABLE 39: GOVERNING EIGEN MODE AND THE PARTICIPATING MASS- 3D-MODEL-DOUBLE RC-FLOORS- DS 117
TABLE 40: GOVERNING EIGEN MODE AND THE PARTICIPATING MASS- 3D-MODEL-DOUBLE RC-FLOORS- HJ 124
TABLE 41: GOVERNING EIGEN MODE AND THE PARTICIPATING MASS- 3D-MODEL-DOUBLE RC-FLOORS- DIRECT 131
TABLE 43: GOVERNING EIGEN MODE AND PARTICIPATING MASS – 3D-MODEL-DOUBLE TIMBER - FLOORS- HJ 144
TABLE 44: GOVERNING EIGEN MODE AND PARTICIPATING MASS – 3D-MODEL-DOUBLE TIMBER - FLOORS- DIRECT 153
TABLE 45: AXIAL FORCE AT THE TOP OF EACH PIERS 159

TABLE 46: TABLE EFFECTIVE MASS, MAXIMUM BASE SHEAR FORCE CALCULATION 160
TABLE 47: TABLE EFFECTIVE MASS, MAXIMUM BASE SHEAR FORCE CALCULATION 161
TABLE 48: AXIAL FORCE AT THE TOP OF EACH PIER 161
TABLE 49: CHANGING AXIAL FORCE AT THE TOP OF PIER 1 163
TABLE 50: CHANGING AXIAL FORCE AT THE TOP OF PIER 2 164
TABLE 51: CHANGING AXIAL FORCE AT THE TOP OF PIER 3 164
TABLE 52: CHANGING AXIAL FORCE AT THE TOP OF PIER 4 165

34 FIGURE LIST

FIGURE 1: ASSUMED MECHANICAL MODEL ROCKING FAILURE (MAGENES, 1997) 6
FIGURE 2: FORCE-DRIFT DIAGRAM ACCORDING TO THE NPR9998 9
FIGURE 3: FORCE-DRIFT DIAGRAM ACCORDING TO THE NPR9998 12
FIGURE 4: TIMBER BEAM-PLANK CONNECTION: B-RIGID DEFORMATION, C-SHEAR DEFORMATION AND D-FLEXURAL DEFORMATION. (A. Brignola & S. Podestà, 2008) 12
FIGURE 5: OVERVIEW OF THE DIFFERENT TYPE OF FLANGES (FRANKLIN L.MOON, 2006) 14
FIGURE 6: EFFECTIVE HEIGTH APPROACH (Moon F. Y., 2006) 15
FIGURE 7: CRACKING BEHAVIOUR ENGINEERING MASONRY MODEL (Schreppers, Garofano, Messali, & Rots, 2017) 18
FIGURE 8: COMPRESSIVE BEHAVIOUR OF ENGINEERING MASONRY MODEL (Schreppers, Garofano, Messali, & Rots, 2017) 19
FIGURE 9: SHEAR BEHAVIOUR OF ENGINEERING MASONRY MODEL (Schreppers, Garofano, Messali, & Rots, 2017) 20
FIGURE 10: LINEAR TENSILE SOFTENING CURVE (LEFT) AND PARABOLIC COMPRESSION CURVE (RIGHT) (DIANA FEA) 22
FIGURE 11: SM 1-CLAY<1945, SM2, SM- CLAY>1945 *FROM LEFT TO RIGHT* 24
FIGURE 12: SM4 CS<1985, SM5, SM6- CLAY- TENSILE CASE FROM LEFT TO RIGHT 24
FIGURE 13: CASE STUDY-2D-1A , CASE STUDY-2D-2A 25
FIGURE 14: CASE STUDY-2D-1B , CASE STUDY-2D-2B 25
FIGURE 15: 3D MODELS CONCRETE FLOOR, TIMBER FLOOR *FROM LEFT TO RIGHT* 26
FIGURE 16: PIER LOCATIONS 3D MODEL 26
FIGURE 17: FLOOR PLANS, EUCENTRE EXAMPLES (M. Miglietta, 2019) 26
FIGURE 18: EIGENMODE SM1 UNTILL SM4,SM6 (LEFT) AND EIGENMODE SM5 (RIGHT) 38
Figure 19:EIGENMODE CASESTUDY 2D-1A & 1B(LEFT) AND EIGENMODE CASESTUDY 2D-2A & 2B (RIGHT) 38
Figure 20:SM1-ULTIMATE DISPLACEMENT(LEFT) AND SM2-ULTIMATE DISPLACEMENT (RIGHT) 39
Figure 21:SM3-ULTIMATE DISPLACEMENT(LEFT) AND SM4-ULTIMATE DISPLACEMENT (RIGHT) 39
Figure 22: SM5-ULTIMATE DISPLACEMENT (LEFT) AND SM6-ULTIMATE DISPLACEMENT(RIGHT) 39
FIGURE 23: CASESTUDY 2D-1A-ULTIMATE DISPLACEMENT (LEFT) AND CASESTUDY 2D-2A-ULTIMATE DISPLACEMENT(RIGHT) 40
FIGURE 24: CASESTUDY 2D-1B-ULTIMATE DISPLACEMENT (LEFT) AND CASESTUDY 2D-2B-ULTIMATE DISPLACEMENT (RIGHT) 40
FIGURE 25: SM1-MAXIMUM PRINCIPAL STRAIN (LEFT) AND SM2-MAXIMUM PRINCIPAL STRAIN (RIGHT) 41
FIGURE 26: SM3-MAXIMUM PRINCIPAL STRAIN (LEFT) AND SM4-MAXIMUM PRINCIPAL STRAIN (RIGHT) 41
FIGURE 27: SM5-MAXIMUM PRINCIPAL STRAIN (LEFT) AND SM6-MAXIMUM PRINCIPAL STRAIN (RIGHT) 41
FIGURE 28: CASESTUDY 2D-1A MAXIMUM PRINCIPAL STRAIN (LEFT) AND CASESTUDY 2D-2A-MAXIMUM PRINCIPAL STRAIN (RIGHT) 42
FIGURE 29: CASESTUDY 2D-1B MAXIMUM PRINCIPAL STRAIN (LEFT) AND CASESTUDY 2D-2B-MAXIMUM PRINCIPAL STRAIN (RIGHT) 42
FIGURE 30: PUSHOVER CURVE SM1 AND SM2 *LEFT TO RIGHT* 43
FIGURE 31: PUSHOVER CURVE SM3 AND SM4 *LEFT TO RIGHT* 43
FIGURE 32: PUSHOVER CURVE SM5 AND SM6 *LEFT TO RIGHT* 43
FIGURE 33: PUSHOVER CURVE CASE STUDY 2D-1A, CASESTUDY 2D-2A, *LEFT TO RIGHT* 44
FIGURE 34: PUSHOVER CURVE CASE STUDY 2D-1B, CASESTUDY 2D-2B, *LEFT TO RIGHT* 44
FIGURE 35: ACCELERATION CURVES SM1,SM2 *LEFT TO RIGHT* 45

FIGURE 36: ACCELERATION CURVES SM3,SM4 *LEFT TO RIGHT* 45
FIGURE 37: ACCELERATION CURVES SM5,SM6 *LEFT TO RIGHT* 45
FIGURE 38: ACCELERATION CURVES CASE STUDY 2D-1A, CASESTUDY 2D-2A, *LEFT TO RIGHT* . 45
FIGURE 39: ACCELERATION CURVES CASE STUDY 2D-1B, CASESTUDY 2D-2B, *LEFT TO RIGHT* . 46
FIGURE 40: EIGENMODE 1, 84% PARTICIPATING MASS 51
Figure 41: displacement in the y-direction of model-3D-double RC floors-DS (left), model model-3D-double RC floors -HJ (middle) and model- model-3D-double RC floors -Direct(right). 52
FIGURE 42: MODEL-3D-DOUBLE RC FLOORS-DS-OPTION (LEFT), MODEL-3D-DOUBLE RC FLOORS-HJ-OPTION (MIDDLE), MODEL-3D-DOUBLE RC FLOORS- DIRECT-OPTION (RIGHT) 53
FIGURE 43: PUSHOVER CURVE 3D-MODEL-DOUBLE RC- DS,HJ &DIRECT LEFT TO RIGHT 54
FIGURE 44: EIGENMODE 3D-MODEL-DOUBLE TIMBER FLOORS, 54% PART. MASS 56
FIGURE 45: 3D-MODEL-DOUBLE TIMBER FLOORS-DS(LEFT), 3D-MODEL-DOUBLE TIMBER FLOORS-HJ (MIDDLE), 3D-MODEL-DOUBLE TIMBER FLOORS-DIRECT (RIGHT)..... 57
FIGURE 46: 3D-MODEL-DOUBLE TIMBER FLOORS -DS (LEFT), 3D-MODEL-DOUBLE TIMBER FLOORS-HJ(MIDDLE), 3D-MODEL-DOUBLE TIMBER FLOORS-DIRECT (RIGHT)..... 58
FIGURE 47: PUSHOVER CURVE 3D-MODEL-DOUBLE TIMBER FLOORS -DS, HJ, DIRECT LEFT TO RIGHT 59
Figure 48: PUSHOVER CURVE 3D-Model-double TIMBER FLOORS (LEFT) AND THE ACCELERATION CURVE 3D-Model-double TIMBER-FLOORS (rIGHT) 61
Figure 49: PUSHOVER CURVE 3D-Model-double RC FLOORS (LEFT) AND THE ACCELERATION CURVE 3D-Model-double RC-FLOORS (rIGHT)..... 61
FIGURE 50: SHEAR CAPACITY AS FUNCTION OF AXIAL FORCE AT THE OF THE PIER (Lagomarsino, 2013)..... 69
FIGURE 51: MODEL WITH RIGID BEAM-WALL CONNECTION 73
FIGURE 52: MODEL WITH HINGED BEAM-WALL CONNECTION 73
FIGURE 53: FINAL STEP IN THE PUSHOVER ANALYSIS OF THE 3D MODEL WITH RC-FLOORS 76
FIGURE 54: SIDEVIEW 3D MODEL WITH RC-FLOORS 77
FIGURE 55: ONE STEP BEFORRE FINAL STEP IN THE PUSHOVER ANALYSIS OF THE 3D MODEL WITH RC-FLOORS 79
FIGURE 56: FINAL STEP IN THE PUSHOVER ANALYSIS OF THE 3D MODEL WITH RC-FLOORS 79
FIGURE 57: THE GOVERNING EIGEN MODE 85
Figure 58: HORIZONTAL DEFLECTION STEP 1 (LEFT) , HORIZONTAL DEFLECTION STEP 150 (RIGHT) 86
Figure 59: HORIZONTAL DEFLECTION STEP 300 (LEFT) , HORIZONTAL DEFLECTION STEP 500 (RIGHT) 86
Figure 60: MAXIMUM PRINCIPAL STRAIN-LOAD STEP 1 (LEFT) , MAXIMUM PRINCIPAL STRAIN-LOAD STEP 150 (RIGHT) 86
Figure 61: MAXIMUM PRINCIPAL STRAIN-LOAD STEP 300 (LEFT) , MAXIMUM PRINCIPAL STRAIN-LOAD STEP 500 (RIGHT) 86
FIGURE 62:PUSHOVER CURVE SIMPLE MODEL 1 87
FIGURE 63:PUSHOVER CURVE SIMPLE MODEL 1 88
FIGURE 64: ACCELERATION CURVE SIMPLE MODEL 1..... 88
FIGURE 65: GOVERNING EIGEN MODE SIMPLE MODEL 2 89
Figure 66: HORIZONTAL DEFLECTION STEP 1 (LEFT) , HORIZONTAL DEFLECTION STEP 150 (RIGHT) 90
Figure 67: HORIZONTAL DEFLECTION STEP 300 (LEFT) , HORIZONTAL DEFLECTION STEP 447 (RIGHT) 90
Figure 68: MAXIMUM PRINCIPAL STRAIN STEP 1 (LEFT) , MAXIMUM PRINCIPAL STRAIN STEP 150 (RIGHT) 91
Figure 69: MAXIMUM PRINCIPAL STRAIN STEP 300 (LEFT) , MAXIMUM PRINCIPAL STRAIN STEP 447 (RIGHT) 91
FIGURE 70:PUSHOVER CURVE SIMPLE MODEL 2 91

FIGURE 71: PUSHOVER CURVE SIMPLE MODEL 2 92
FIGURE 72: ACCELERATION SIMPLE MODEL 2 92
FIGURE 73: GOVERNING EIGEN MODE SIMPLE MODEL 3 93
Figure 74: HORIZONTAL DEFLECTION STEP 1 (LEFT) , HORIZONTAL DEFLECTION STEP 51 (RIGHT) 94
Figure 75: HORIZONTAL DEFLECTION STEP 100 (LEFT) , HORIZONTAL DEFLECTION STEP 156 (RIGHT) 94
Figure 76: MAXIMUM PRINCIPAL STRAIN STEP 1 (LEFT) , MAXIMUM PRINCIPAL STRAIN STEP 51 (RIGHT) 94
Figure 77: MAXIMUM PRINCIPAL STRAIN STEP 100 (LEFT) , MAXIMUM PRINCIPAL STRAIN STEP 156 (RIGHT) 95
FIGURE 78:PUSHOVER CURVE SIMPLE MODEL 3 95
FIGURE 79:PUSHOVER CURVE SIMPLE MODEL 3 96
FIGURE 80: ACCELERATION CURVE SIMPLE MODEL 3 96
FIGURE 81: THE GOVERNING EIGEN MODE SIMPLE MODEL 4 97
Figure 82: HORIZONTAL DEFLECTION STEP 1 (LEFT) , HORIZONTAL DEFLECTION - STEP 20 (RIGHT) 97
Figure 83: HORIZONTAL DEFLECTION STEP 40 (LEFT) , HORIZONTAL DEFLECTION - STEP 62 (RIGHT) 98
Figure 84: MAXIMUM PRINCIPAL STRAIN-LOAD STEP 1 (LEFT) , MAXIMUM PRINCIPAL STRAIN-LOAD STEP 20 (RIGHT) 98
Figure 85: MAXIMUM PRINCIPAL STRAIN-LOAD STEP 40 (LEFT) , MAXIMUM PRINCIPAL STRAIN-LOAD STEP 62 (RIGHT) 98
FIGURE 86: PUSHOVER CURVE SIMPLE MODEL 4 98
FIGURE 87: PUSHOVER CURVE SIMPLE MODEL 4 99
FIGURE 88: ACCELERATION SIMPLE MODEL 5 99
FIGURE 89: GOVERNING EIGEN MODE SINMPLE MODEL 5 100
Figure 90: HORIZONTAL DEFLECTION STEP 1 (LEFT) , HORIZONTAL DEFLECTION STEP 150 (RIGHT) 100
Figure 91: HORIZONTAL DEFLECTION STEP 450 (LEFT) , HORIZONTAL DEFLECTION STEP 606 (RIGHT) 100
Figure 92: MAXIMUM PRINCIPAL STRAIN STEP 1 (LEFT) , MAXIMUM PRINCIPAL STRAIN STEP 150 (RIGHT) 101
Figure 93: MAXIMUM PRINCIPAL STRAIN STEP 450 (LEFT) , MAXIMUM PRINCIPAL STRAIN STEP 606 (RIGHT) 101
FIGURE 94:PUSHOVER CURVE SIMPLE MODEL 5 101
FIGURE 95:PUSHOVER CURVE SIMPLE MODEL 5 102
FIGURE 96: ACCELERATION CURVE SIMPLE MODEL 5 102
FIGURE 97: GOVERNING EIGEN MODE SIMPLE MODEL 6 103
Figure 98: HORIZONTAL DEFLECTION STEP 1 (LEFT) , HORIZONTAL DEFLECTION STEP 15 (RIGHT) 104
Figure 99: HORIZONTAL DEFLECTION STEP 30 (LEFT) , HORIZONTAL DEFLECTION STEP 49 (RIGHT) 104
Figure 100: MAXIMUM PRINCIPAL STRAIN STEP 1 (LEFT) , MAXIMUM PRINCIPAL STRAIN STEP 15 (RIGHT) 104
Figure 101: MAXIMUM PRINCIPAL STRAIN STEP 30 (LEFT) , MAXIMUM PRINCIPAL STRAIN STEP 49 (RIGHT) 104
FIGURE 102:PUSHOVER CURVE SIMPLE MODEL 6 105
FIGURE 103:PUSHOVER CURVE SIMPLE MODEL 6 106
FIGURE 104: ACCELERATION CURVE SIMPLE MODEL 6 106
FIGURE 105: THE GOVERNING EIGEN MODE CASE STUDY-2D-1A 107

Figure 106: HORIZONTAL DEFLECTION STEP 1 (LEFT) , HORIZONTAL DEFLECTION STEP 10 (RIGHT) 107
Figure 107: HORIZONTAL DEFLECTION STEP 25 (LEFT) , HORIZONTAL DEFLECTION STEP 46 (RIGHT) 107
Figure 108: MAXIMUM PRINCIPAL STRAIN-LOAD STEP 1 (LEFT) , MAXIMUM PRINCIPAL STRAIN-LOAD STEP 10 (RIGHT) 108
Figure 109: MAXIMUM PRINCIPAL STRAIN-LOAD STEP 25 (LEFT) , MAXIMUM PRINCIPAL STRAIN-LOAD STEP 46 (RIGHT) 108
FIGURE 110: PUSHOVER CURVE CASE STUDY-2D-1A 108
FIGURE 111: GOVERNING EIGEN MODE CASE STUDY-2D-1B 109
Figure 112: HORIZONTAL DEFLECTION STEP 50 (LEFT) , HORIZONTAL DEFLECTION STEP 100 (RIGHT) 109
Figure 113: HORIZONTAL DEFLECTION STEP 150 (LEFT) , HORIZONTAL DEFLECTION STEP 200 (RIGHT) 109
Figure 114: MAXIMUM PRINCIPAL STRAIN STEP 50 (LEFT) , MAXIMUM PRINCIPAL STRAIN STEP 100 (RIGHT) 110
Figure 115: MAXIMUM PRINCIPAL STRAIN STEP 150 (LEFT) , MAXIMUM PRINCIPAL STRAIN STEP 200 (RIGHT) 110
FIGURE 116:PUSHOVER CURVE CASE STUDY-2D-1B 110
FIGURE 117:PUSHOVER CURVE CASE STUDY-2D-1A/1B 111
FIGURE 118:ACCELERATION CURVE CASE STUDY-2D-1A/1B 111
FIGURE 119: THE GOVERNING EIGEN MODE CASE STUDY-2D-2A 112
Figure 120: HORIZONTAL DEFLECTION STEP 1 (LEFT) , HORIZONTAL DEFLECTION STEP 10 (RIGHT) 112
Figure 121: HORIZONTAL DEFLECTION STEP 15 (LEFT) , HORIZONTAL DEFLECTION STEP 22 (RIGHT) 112
Figure 122: MAXIMUM PRINCIPAL STRAIN-LOAD STEP 1 (LEFT) , MAXIMUM PRINCIPAL STRAIN-LOAD STEP 10 (RIGHT) 113
Figure 123: MAXIMUM PRINCIPAL STRAIN-LOAD STEP 15 (LEFT) , MAXIMUM PRINCIPAL STRAIN-LOAD STEP 22 (RIGHT) 113
FIGURE 124:PUSHOVER CURVE CASE STUDY-2D-2A 113
FIGURE 125: GOVERNING EIGEN MODE CASE STUDY-2D-2B 114
Figure 126: HORIZONTAL DEFLECTION STEP 10 (LEFT) , HORIZONTAL DEFLECTION STEP 20 (RIGHT) 114
Figure 127: HORIZONTAL DEFLECTION STEP 40 (LEFT) , HORIZONTAL DEFLECTION STEP 68 (RIGHT) 114
Figure 128: MAXIMUM PRINCIPAL STRAIN STEP 10 (LEFT) , MAXIMUM PRINCIPAL STRAIN STEP 20 (RIGHT) 115
Figure 129: MAXIMUM PRINCIPAL STRAIN STEP 40 (LEFT) , MAXIMUM PRINCIPAL STRAIN STEP 68 (RIGHT) 115
FIGURE 130: PUSHOVER CURVE CASE STUDY-2D-2B 115
FIGURE 131:PUSHOVER CURVE CASE STUDY-2D-2A/B 116
FIGURE 132: ACCELERATION CURVE CASE STUDY-2D-2A/B 116
FIGURE 133: GOVERNING EIGEN MODE – 3D-MODEL-DOUBLE RC- FLOORS- DS 117
FIGURE 134: DEFLECTION IN THE Y-DIRECTION – STEP 1- 3D-VIEW 1 117
FIGURE 135: DEFLECTION IN THE Y-DIRECTION – STEP 20- 3D-VIEW 1 118
FIGURE 136: MAXIMUM PRINCIPAL STRAIN – STEP 20- 3D-VIEW 1 118
FIGURE 137: MAXIMUM PRINCIPAL STRAIN – STEP 20- SIDE-VIEW 1 118
FIGURE 138: MAXIMUM PRINCIPAL STRAIN – STEP 20- SIDE-VIEW 2 119
FIGURE 139: DEFLECTION IN THE Y-DIRECTION – STEP 20- 3D-VIEW 1 119
FIGURE 140: MAXIMUM PRINCIPAL STRAIN – STEP 40- 3D-VIEW 1 119
FIGURE 141: MAXIMUM PRINCIPAL STRAIN – STEP 40- SIDE-VIEW 1 120

FIGURE 142: MAXIMUM PRINCIPAL STRAIN – STEP 40- SIDE-VIEW 2 120
FIGURE 143: DEFLECTION IN THE Y-DIRECTION – STEP 60- 3D-VIEW 1 120
FIGURE 144: MAXIMUM PRINCIPAL STRAIN – STEP 60- 3D-VIEW 1 121
FIGURE 145: MAXIMUM PRINCIPAL STRAIN – STEP 60- SIDE-VIEW 1 121
FIGURE 146: MAXIMUM PRINCIPAL STRAIN – STEP 60- SIDE-VIEW 2 121
FIGURE 147: DEFLECTION IN THE Y-DIRECTION – STEP 77- 3D-VIEW 1 122
FIGURE 148: MAXIMUM PRINCIPAL STRAIN – STEP 77- 3D-VIEW 1 122
FIGURE 149: MAXIMUM PRINCIPAL STRAIN – STEP 77-SIDE -VIEW 1 122
FIGURE 150: MAXIMUM PRINCIPAL STRAIN – STEP 77- SIDE-VIEW 2 123
FIGURE 151:PUSHOVER CURVE CASE STUDY-3D-MODEL-DOUBLE RC FLOORS-DS 123
FIGURE 152: GOVERNING EIGEN MODE – 3D-MODEL-DOUBLE RC- FLOORS- HJ 124
FIGURE 153: DEFLECTION IN THE Y-DIRECTION – STEP 1- 3D-VIEW 1 124
FIGURE 154: MAXIMUM PRINCIPAL STRAIN – STEP 1- 3D-VIEW 1 125
FIGURE 155: MAXIMUM PRINCIPAL STRAIN – STEP 1- SIDE-VIEW 1 125
FIGURE 156: MAXIMUM PRINCIPAL STRAIN – STEP 1- SIDE-VIEW 2 125
FIGURE 157: DEFLECTION IN THE Y-DIRECTION – STEP 15- 3D-VIEW 1 126
FIGURE 158: MAXIMUM PRINCIPAL STRAIN – STEP 15- 3D-VIEW 1 126
FIGURE 159: MAXIMUM PRINCIPAL STRAIN – STEP 15- SIDE-VIEW 1 126
FIGURE 160: MAXIMUM PRINCIPAL STRAIN – STEP 15- SIDE-VIEW 2 127
FIGURE 161: DEFLECTION IN THE Y-DIRECTION – STEP 30- 3D-VIEW 1 127
FIGURE 162: MAXIMUM PRINCIPAL STRAIN – STEP 30- 3D-VIEW 1 127
FIGURE 163: MAXIMUM PRINCIPAL STRAIN – STEP 30- SIDE-VIEW 1 128
FIGURE 164: MAXIMUM PRINCIPAL STRAIN – STEP 30- SIDE-VIEW 2 128
FIGURE 165: DEFLECTION IN THE Y-DIRECTION – STEP 48- 3D-VIEW 1 128
FIGURE 166: MAXIMUM PRINCIPAL STRAIN – STEP 40- 3D-VIEW 1 129
FIGURE 167: MAXIMUM PRINCIPAL STRAIN – STEP 48- SIDE-VIEW 1 129
FIGURE 168: MAXIMUM PRINCIPAL STRAIN – STEP 48- SIDE-VIEW 2 129
FIGURE 169:PUSHOVER CURVE 3D-MODEL-DOUBLE RC-FLOORS- HJ 130
FIGURE 170: GOVERNING EIGEN MODE – 3D-MODEL-DOUBLE RC- FLOORS- DIRECT 131
FIGURE 171: DEFLECTION IN THE Y-DIRECTION – STEP 8- 3D-VIEW 1 131
FIGURE 172: MAXIMUM PRINCIPAL STRAIN – STEP 8- 3D-VIEW 1 132
FIGURE 173: MAXIMUM PRINCIPAL STRAIN – STEP 8- SIDE-VIEW 1 132
FIGURE 174: MAXIMUM PRINCIPAL STRAIN – STEP 8- SIDE-VIEW 2 132
FIGURE 175: DEFLECTION IN THE Y-DIRECTION – STEP 26- 3D-VIEW 1 133
FIGURE 176: MAXIMUM PRINCIPAL STRAIN – STEP 26- 3D-VIEW 1 133
FIGURE 177: MAXIMUM PRINCIPAL STRAIN – STEP 26- SIDE-VIEW 1 133
FIGURE 178: MAXIMUM PRINCIPAL STRAIN – STEP 26- SIDE-VIEW 2 134
FIGURE 179: DEFLECTION IN THE Y-DIRECTION – STEP 41- 3D-VIEW 1 134
FIGURE 180: MAXIMUM PRINCIPAL STRAIN – STEP 41- 3D-VIEW 1 134
FIGURE 181: MAXIMUM PRINCIPAL STRAIN – STEP 41- SIDE-VIEW 1 135
FIGURE 182: MAXIMUM PRINCIPAL STRAIN – STEP 41- SIDE-VIEW 2 135
FIGURE 183: DEFLECTION IN THE Y-DIRECTION – STEP 49- 3D-VIEW 1 135
FIGURE 184: MAXIMUM PRINCIPAL STRAIN – STEP 49- 3D-VIEW 1 136
FIGURE 185: MAXIMUM PRINCIPAL STRAIN – STEP 49- SIDE-VIEW 1 136
FIGURE 186: MAXIMUM PRINCIPAL STRAIN – STEP 49- SIDE-VIEW 2 136
FIGURE 187: PUSHOVER CURVE 3D-MODEL-DOUBLE RC-FLOORS- DIRECT 137
FIGURE 188: GOVERNING EIGEN MODE – 3D-MODEL-DOUBLE TIMBER - FLOORS- DS 138
FIGURE 189: DEFLECTION IN THE Y-DIRECTION – STEP 1- 3D-VIEW 1 138
FIGURE 190: MAXIMUM PRINCIPAL STRAIN – STEP 1- 3D-VIEW 1 139
FIGURE 191: MAXIMUM PRINCIPAL STRAIN – STEP 1- 3D-VIEW 1 139
FIGURE 192: DEFLECTION IN THE Y-DIRECTION – STEP 4- 3D-VIEW 1 139
FIGURE 193: MAXIMUM PRINCIPAL STRAIN – STEP 4- 3D-VIEW 1 140

FIGURE 194: DEFLECTION IN THE Y-DIRECTION – STEP 4- 3D-VIEW 1 140
FIGURE 195: DEFLECTION IN THE Y-DIRECTION – STEP 4- 3D-VIEW 1 140
FIGURE 196: DEFLECTION IN THE Y-DIRECTION – STEP 8- 3D-VIEW 1 141
FIGURE 197: MAXIMUM PRINCIPAL STRAIN – STEP 8- 3D-VIEW 1 141
FIGURE 198: MAXIMUM PRINCIPAL STRAIN – STEP 8- SIDE-VIEW 1 141
FIGURE 199: MAXIMUM PRINCIPAL STRAIN – STEP 8- SIDE-VIEW 1 142
FIGURE 200: DEFLECTION IN THE Y-DIRECTION – STEP 11- 3D-VIEW 1 142
FIGURE 201: MAXIMUM PRINCIPAL STRAIN – STEP 11-3D -VIEW 1 142
FIGURE 202: MAXIMUM PRINCIPAL STRAIN – STEP 11- SIDE-VIEW 1 143
FIGURE 203: MAXIMUM PRINCIPAL STRAIN – STEP 11- SIDE-VIEW 1 143
FIGURE 204: PUSHOVER CURVE 3D MODEL DOUBLE TIMBER FLOOR-DS 143
FIGURE 205: GOVERNING EIGEN MODE – 3D-MODEL-DOUBLE TIMBER - FLOORS- HJ 144
FIGURE 206: DEFLECTION IN THE Y-DIRECTION – STEP 1- 3D-VIEW 1 145
FIGURE 207: MAXIMUM PRINCIPAL STRAIN – STEP 1- 3D-VIEW 1 145
FIGURE 208: MAXIMUM PRINCIPAL STRAIN – STEP 1- SIDE-VIEW 1 146
FIGURE 209: MAXIMUM PRINCIPAL STRAIN – STEP 1- SIDE-VIEW 2 146
FIGURE 210: DEFLECTION IN THE Y-DIRECTION – STEP 5- 3D-VIEW 1 147
FIGURE 211: MAXIMUM PRINCIPAL STRAIN – STEP 5- 3D-VIEW 1 147
FIGURE 212: MAXIMUM PRINCIPAL STRAIN – STEP 5- SIDE-VIEW 1 148
FIGURE 213: MAXIMUM PRINCIPAL STRAIN – STEP 5- SIDE-VIEW 2 148
FIGURE 214: DEFLECTION IN THE Y-DIRECTION – STEP 10- 3D-VIEW 1 149
FIGURE 215: MAXIMUM PRINCIPAL STRAIN – STEP 10- 3D-VIEW 1 149
FIGURE 216: MAXIMUM PRINCIPAL STRAIN – STEP 10- SIDE-VIEW 1 150
FIGURE 217: MAXIMUM PRINCIPAL STRAIN – STEP 10- SIDE-VIEW 2 150
FIGURE 218: DEFLECTION IN THE Y-DIRECTION – STEP 15- 3D-VIEW 1 151
FIGURE 219: MAXIMUM PRINCIPAL STRAIN – STEP 15- 3D-VIEW 1 151
FIGURE 220: MAXIMUM PRINCIPAL STRAIN – STEP 15- SIDE-VIEW 1 152
FIGURE 221: MAXIMUM PRINCIPAL STRAIN – STEP 15- SIDE-VIEW 2 152
FIGURE 222: PUSHOVER CURVE 3D MODEL DOUBLE TIMBER FLOOR-HJ 152
FIGURE 223: GOVERNING EIGEN MODE – 3D-MODEL-DOUBLE TIMBER - FLOORS- DIRECT 153
FIGURE 224: MAXIMUM PRINCIPAL STRAIN – STEP 10- 3D-VIEW 1 154
FIGURE 225: MAXIMUM PRINCIPAL STRAIN – STEP 10- SIDE-VIEW 1 154
FIGURE 226: MAXIMUM PRINCIPAL STRAIN – STEP 10- SIDE-VIEW 2 155
FIGURE 227: DEFLECTION IN THE Y-DIRECTION – STEP 20- 3D-VIEW 1 155
FIGURE 228: MAXIMUM PRINCIPAL STRAIN – STEP 20- 3D-VIEW 1 156
FIGURE 229: MAXIMUM PRINCIPAL STRAIN – STEP 20- SIDE-VIEW 1 156
FIGURE 230: MAXIMUM PRINCIPAL STRAIN – STEP 20- SIDE-VIEW 2 157
FIGURE 231: DEFLECTION IN THE Y-DIRECTION – STEP 34- 3D-VIEW 1 157
FIGURE 232: MAXIMUM PRINCIPAL STRAIN – STEP 34- 3D-VIEW 1 158
FIGURE 233: MAXIMUM PRINCIPAL STRAIN – STEP 34- SIDE-VIEW 1 158
FIGURE 234: MAXIMUM PRINCIPAL STRAIN – STEP 20- SIDE-VIEW 2 158
FIGURE 235: ACCELERATION CURVE 160
FIGURE 236:PUSHOVER CURVE 160
Figure 237: PUSHOVER CURVE (LEFT) ACCELERATION CURVE (RIGHT) 161
FIGURE 238: CHANGING AXIAL FORCE AT THE TOP OF PIER 1 163
FIGURE 239: CHANGING AXIAL FORCE AT THE TOP OF PIER 2 163
FIGURE 240: CHANGING AXIAL FORCE AT THE TOP OF PIER 3 164
FIGURE 241: CHANGING AXIAL FORCE AT THE TOP OF PIER 4 165
FIGURE 242: CHANGING AXIAL FORCE AT THE TOP OF EACH PIER 166